Shaping and Modelling Electronically Excited States of Indoles

Inaugural-Dissertation

zur Erlangung des Doktorgrades

der Mathematisch-Naturwissenschaftlichen Fakultät

der Heinrich-Heine-Universität Düsseldorf

vorgelegt von

Christian Brand

aus Eckernförde

Düsseldorf, Februar 2013

aus dem Institut für Physikalische Chemie I
der Heinrich-Heine-Universität Düsseldorf

Gedruckt mit der Genehmigung der
Mathematisch-Naturwissenschaftlichen Fakultät der
Heinrich-Heine-Universität Düsseldorf

Referent: Prof. Dr. Michael Schmitt
Korreferent: Prof. Dr. Karl Kleinermanns

Tag der mündlichen Prüfung: 23. Januar 2013

Studenten kommen von der Schule im festen Glauben, dass sie nahezu alles wissen, und Jahre später gehen sie mit der Gewissheit ab, praktisch nichts zu wissen. Wo ist das Wissen geblieben? In der Universität natürlich, wo es sorgfältig getrocknet und gelagert wird. Deswegen bezeichnet man Universitäten als Horte des Wissens.

Terry Pratchett - Die Gelehrten der Scheibenwelt

Contents

Symbols and Abbreviations

1C-R2PI	1-colour resonant 2-photon ionization
5CI	5-cyanoindole
5FI	5-fluoroindole
5MOI	5-methoxyindole
6MOI	6-methoxyindole
6-311G(d,p)	Pople's basis set of triple zeta quality
$\sim$	has the same normal distribution as
$\sphericalangle$	angle
$\forall$	for all
$[x, y]$	commutator, $x^{-1}y^{-1}yx =$ neutral element
ϵ_0	vacuum permittivity
ϵ	is a member of
ϕ, θ	polar angles
χ_T, θ_T, ϕ_T	reorientation angles
χ_m	vibrational wave function of the state m
$\hat{\vec{\mu}}_e$	electronic transition dipole moment
μ	permanent dipole moment
τ	lifetime
ϕ	torsional angle
ν	frequency
$\boldsymbol{\Phi}$	rotation matrix
κ	parameter of asymmetry according to Ray [1]
λ_g	direction cosines between the main inertial axes g and the torsional axis
λ	wavelength
$\boldsymbol{\Lambda}$	matrix containing the non-adiabatic coupling elements
Λ_{ji}	elements of the matrix $\boldsymbol{\Lambda}$
σ	index to distinguish the sublevels of a torsional level

ψ	wave function
∇_i	nabla operator, ∂/∂_i
ω	angular velocity
a, b, c	main inertial axes
a_i, b_i, c_i	internal coordinates in the PAS
a. u.	atomic units
amu	atomic mass unit
A, B, C	rotational constants
$A_{J\tau M}$	asymmetric top wave function
Å	Ångström, $1\text{Å}=10^{-10}$ m
AD	analog digital
Ar^+	Argon-ion
BBO	β-barium borate
BH-LYP	a DFT functional by Becke [2]
BSSE	basis set superposition error
CASPT2	complete-active-space second-order perturbation theory
CASSCF	complete-active-space self-consistent-field
CI	conical intersection *or* configuration interaction
CIS	configuration interaction singles
CC2	approximate second order coupled cluster
cc-pVTZ	correlation consistent polarized valence triple zeta basis set
CMA-ES	evolutionary strategy including covariance matrix adaptation
C_n	n-fold axis of rotation
CNDO	complete neglect of diatomic overlap
CSF	configuration state function
cw	continuous wave
$\mathfrak{D}$	Wigner matrix [3]
D	Debye
DF	dispersed fluorescence
DFT	density functional theory
DFT/MRCI	density-functional theory multi-reference configuration-interaction
DR2	derandomized evolutionary strategy
e	elementary charge $e= 1.602\ 176\ 565(35) \cdot 10^{-19}$ C [1]

---

[1]*2010 CODATA recommended values*: elementary charge. National Institute of Standards and Technology. Retrieved 2012-09-04

e_{ijk}	permutation symbol
E	energy
ES	Evolutionary Strategy
eV	electron volt, 1 eV=1.602 176 565(35) $\cdot$ 10^{-19} J [2]
exp.	experimental
f	focal distance
F	reduced torsional constant
$\mathbf{F}_{ji}$	non-adiabatic derivative couplings
FDIR	fluorescence dip IR spectroscopy (ground state)
FDIRS	fluorescence dip IR spectroscopy (excited state)
FC	Franck-Condon
FCHT	Franck-Condon-Herzberg-Teller
FSR	free spectral range
FWHM	full width at half maximum
$\mathcal{F}$	finesse
G_ν	Gauss function
G_{ji}	scalar couplings
GA	Genetic Algorithms
h	Planck constant, $h = 6.626\ 069\ 57(29) \cdot 10^{-34}$ Js [3]
$\hbar$	$h/2\pi$
H	Hamilton function
$\widehat{\mathbf{H}}$	Hamiltonian
HOMO	highest occupied molecular orbital
HRLIF	high resolution laser induced fluorescence
HT	Herzberg-Teller
i	counting index (*or* $\sqrt{-1}$)
$I_\alpha\ (\alpha = a, b, c)$	principle moment of inertia
$\widetilde{\mathbf{I}}$	moment of inertia tensor
IAM	internal axis method
INDO/S-CI	intermediate neglect of differential overlap configuration interaction
IR	infrared
ΔI	inertial defect
J	rotational quantum number

---

[2] *2010 CODATA recommended values*: electron volt. National Institute of Standards and Technology. Retrieved 2012-09-04

[3] *2010 CODATA recommended values*: Planck constant. National Institute of Standards and Technology. Retrieved 2012-09-04

K	quantum number defining the orientation of $\widehat{\mathbf{J}}$ onto the molecule-fixed coordinate system *or* Kelvin
K_a, K_c	pseudo quantum numbers according to Mulliken [4]
KDP	potassium dihydrogen phosphate
KS	Kohn-Sham
$L(\nu)$	Lorentzian profile
$^1L_b, {}^1L_a$	electronically excited states in the nomenclature of Platt [5]
LIF	laser induced fluorescence
LUMO	lowest unoccupied molecular orbital
MP2	Møller-Plesset perturbation theory
m_i	mass of the particle i
$\mathcal{N}$	normal distribution
NBO	natural bond orbital
Nd:YAG	An yttrium aluminium garnet doped with Nd^{3+}
$\widehat{\mathbf{O}}$	operator
O^+, O^-	submatrices odd in K
$\widehat{p}$	total angular momentum of the internal top
P, Q, R	branches in a rotationally resolved spectrum
$\mathbf{P}_{tot}$	overall angular momentum
P_α	angular momentum of a rotation around the axis α
P_b	backing pressure
PAM	principle axis method
PAS	principle axis system
PEA	2-phenylethylamine
PES	potential energy surface
PC	personal computer
PVC	polyvinyl chloride
Q_i	normal coordinate i
QSAR	quantitative structure-activity relationship
r	distance
$\mathbf{R}_i$	coordinate of a nuclei i
R_{ab}	distance between the particles a and b
^{R} and ^{L}	right- and lefthanded
R2PI	resonant 2-photon ionization
RICC2	CC2 including the resolution of the identity
RIDIRS	resonant ion-dip infrared spectroscopy

$\mathbb{R}$	real numbers
S_0	electronic ground state
S_1	first electronically excited state
S_2	second electronically excited state
$\mathbf{S}^{-1}$	rotational matrix
SCS	Spin-component scaling
SFB	Sonderforschungsbereich
S^{nm}	line strength of a transition between the states n and m
SOS	scaled opposite-spin
SVLF	single vibronic level fluorescence
x^T	transposed vector or matrix
T	kinetic energy
T_1, T_2	temperatures in a molecular beam
$\mathbf{T}$	reorientation matrix
$T_\perp$	temperature perpendicular to the stream velocity in a jet
$T_\parallel$	temperature parallel to the stream velocity in a jet
TDM	transition dipole moment
TOFMS	time-of-flight mass spectrometer
TRA	tryptamine
Trp	tryptophan
TU	Technische Universität
$\mathbf{U}$	unitary matrix
$\mathbf{U}_J = \mathbf{U}_J^{-1}$	Wang matrix
UV	ultraviolet
v	principle torsion quantum number
V	potential energy
$V(\nu)$	Voigt profile
W	perturbation coefficient
W_{nm}	transition probability
x, y, z	molecule-fixed cartesian coordinates
X, Y, Z	space-fixed cartesian coordinates
Z_a	nuclear charge
ZPE	zero-point-energy

Introduction

The intrinsic fluorescence of proteins provides valuable information on both its structure and dynamics. It allows to monitor folding and unfolding processes [6–8] and substrate binding [9] as well as to reconstruct energy transfer between aromatic amino acids [10] and investigate the local surrounding of the chromophore [11–13]. There are three fluorescing amino acids in proteins: phenylalanine, tyrosine and tryptophan, shown in Figure 1. All of them are relatively rare in proteins, so usually only a small number of fluorophores contributes to the spectrum [9].[4] Tryptophan is most important regarding fluorescence spectroscopy, which has a number of reasons. First of all, it is the most abundant aromatic amino acid with around 1 mole%. Furthermore, it has the largest extinction coefficient, it is very sensitive to quenching processes [15, 16] and it can be excited leaving the other amino acids in their electronic ground state. The most outstanding features are due to its electronically excited states. Tryptophan has two near-degenerate excited singlet states, referred to as the ^1L_a and the ^1L_b in the nomenclature of Platt [5], adapted to tryptophan by Weber [17]. While the ^1L_b state is lowest in energy in apolar surroundings and has a structured emission spectrum, interactions with polar groups or molecules may reverse the energetic order, and the ^1L_a state becomes lowest in energy. This is mainly due to the excited state dipole moments [9]: excitation to the ^1L_a state enhances the excited state dipole moment significantly more than excitation to the ^1L_b does. Thus, favorable dipole-dipole interactions lower its energy and provoke the observed changes. Quite in contrast to the one of the ^1L_b, the emission spectrum of the ^1L_a state in solution is rather broad and lacks distinct features. To illustrate this, the fluorescence spectra of tryptophan's chromophore indole in both cyclohexane and ethanol are shown in Figure 2.

Making statements regarding the local surroundings in proteins requires detailed

---

[4]The fourth aromatic amino acid, histidine, exhibits an molecular extinction coefficient which is lower by an order of magnitude [14]. Hence it does not contribute significantly to the fluorescence spectrum and is neglected.
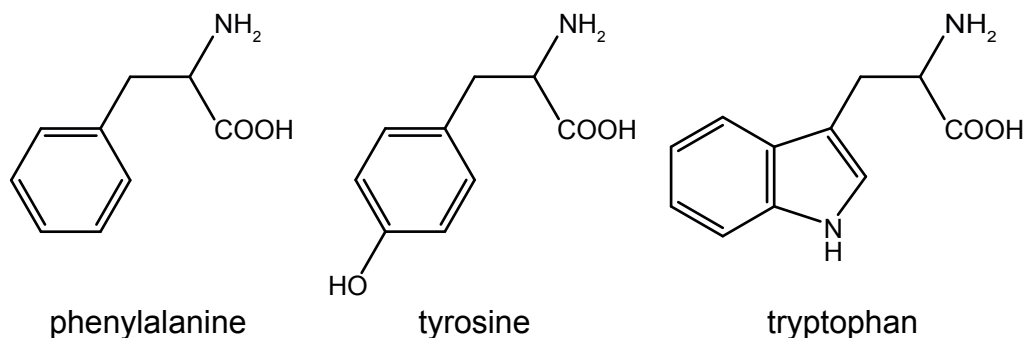
Figure 1: Natural aromatic amino acids important for fluorescence measurements.

understanding of the photophysics of its components. This can be quite complicated: proteins are far from being simple systems, and the interactions of amino acids among themselves and with solvents are always present. One way to circumvent these problems is to investigate small components in the gas phase. The advantage of this approach is an exclusion of unwanted interactions and thus the possibility to obtain information about the unperturbed molecule. Recording the absorption spectra at rotational resolution opens the way to a very precise understanding of structure and dynamics regarding the substances. From the interpretation of the rotational lines it is possible to determine the rotational constants in both electronic states with high precision. As the geometry of a molecule can be deduced from these constants, we get detailed information on the shape and its changes upon excitation. Furthermore, these changes allow an unambiguous assignment of the electronic state observed, in the present case either the ^1L_a or the ^1L_b state, and contain information on couplings between them. If present, the conformational space can be investigated, and the influence of internal motions be conceived. Additionally, statements regarding the orientation of the transition dipole moment vector and the excited state lifetime can be made.

This thesis aims to increase knowledge on tryptophan's chromophore indole by examining itself along with several derivatives using *rotationally resolved laser induced fluorescence spectroscopy* and compare the results to high level quantum chemical calculations. We start our investigations with a theoretical work on the photophysics of indole in Chapter 6. Here we take a first look at the lowest excited singlet states in the bare chromophore and elaborate the interactions between them. It lays the foundation for the subsequent chapters. In the further progress of this thesis, we increase the complexity of the investigated systems by introducing different side groups at different positions of the chromophore. These may alter the photophysics considerably compared to indole itself, depending on its characteristics. The study
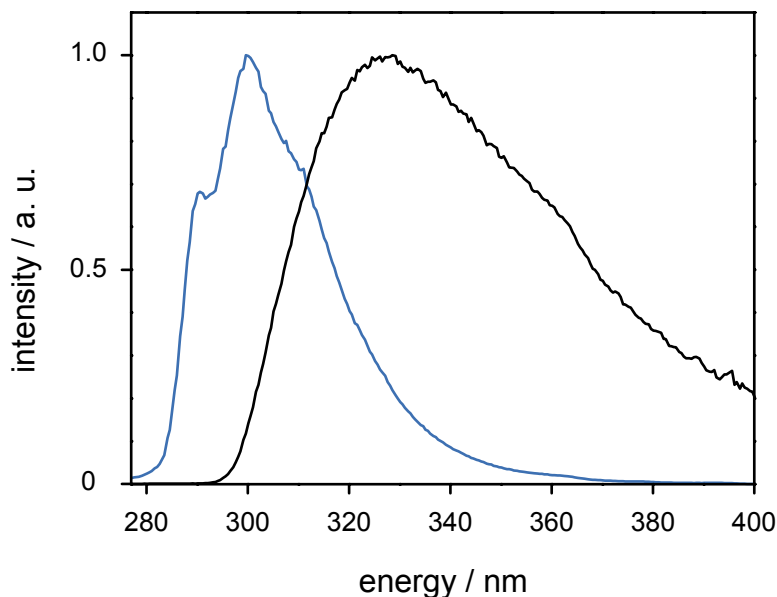
Figure 2: Fluorescence emission spectra of indole in cyclohexane (blue) and ethanol (black) in the energy range between 275 and 400 nm. The fluorescence intensity is normalized to 1.0.

on 5-cyanoindole (cf. Figure 3) is presented in Chapter 8, the influence of a fluorine atom at position 5 is subject to Chapter 9. 5-Methoxyindole has one of the largest energy gaps between the ^1L_a and ^1L_b states and is therefore an excellent candidate to look for a change of vibronic coupling compared to indole. The results of the high resolution investigations are given in Chapter 10. In the ensuing chapter we modify the position of the methoxy group from 5 to 6, and investigate the photophysical consequences (Chapter 11). Attaching an ethylamino side chain at position 3 (for numbering cf. Figure 3) to indole brings us to the neurotransmitter tryptamine. The importance of its conformational space becomes obvious by way of comparison to tryptophan: Conformational changes induced by the flexible side chain are believed to be responsible for double exponential decay of tryptophan in water [18, 19]. This behaviour was previously attributed to emission from both electronic states, the ^1L_a and the ^1L_b [20]. Therefore, knowledge of the favoured conformers is of great assistance, when emission phenomena are to be discussed. Additionally, the amino group can act as a kind of intramolecular solvent. In Chapter 13 the influence of the experimentally determined conformers of tryptamine on the orientation of the transition dipole moment vector is discussed and compared in depth to 2-phenylethylamin (ethylaminobenzene). The largest system investigated is the hormone melatonin (N-acetyl-5-methoxytryptamine). In Chapter 14 its conformational space and internal motions are presented. This way we increase the complexity of the systems step by step and use information gathered to describe qualitative changes. All investigated systems are depicted in Figure 3.

The experimental setup for rotationally resolved laser induced fluorescence is in-
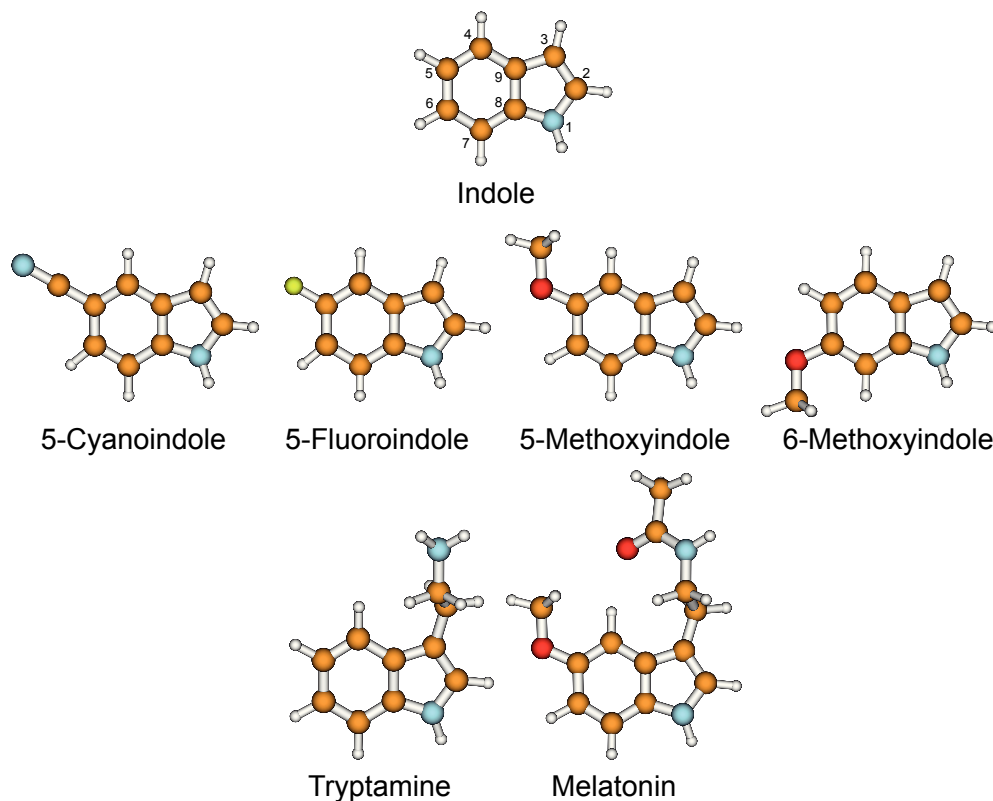
Figure 3: Overview on the molecular systemes investigated in this thesis

troduced in Chapter 3, which states the essentials of tunable continuous wave laser generation, frequency doubling and molecular beam technique needed to understand the experimental basics. Analysis of the recorded spectra is done using evolutionary algorithms, and the results are always compared to *ab initio* calculations. The Chapters 4 and 5 provide a general insight to both fields. Quite important in respect to couplings between electronic states are the Born-Oppenheimer approximation and its violations, which are discussed in Chapter 2. However, this publication will start with a review of quantum-mechanics regarding molecular rotations, both internal and overall.

1. Theoretical Background

As the interpretation of rotational transitions is essential to this work, we will start with the derivation of the Hamiltonian for a rigid rotor. A rigid rotor is a hypothetical molecule which exhibits neither internal motions nor centrifugal distortions. In a subsequent section a special class of internal motions, namely internal rotation, will be introduced, leading to more complex spectra. Further sections will give an introduction to rovibronic line intensities and shapes.

1.1 The Rigid Rotor Hamiltonian

Derivation of the quantum mechanical description of molecular rotors can be easily performed, starting from its classical expressions and then extending these to quantum mechanics according to the correspondence principle. We will start by the approximation of the rigid rotor, assuming that the geometry of the molecule is constant for a given electronic state and that vibrationally induced changes can be neglected. This initial approximation is valid as long as no large amplitude motion, like internal rotation, is involved. Regarding the literature about rotations in quantum mechanics, there are excellent works covering this field, like the publications from Gordy and Cook [21], Kroto [22], Hollas [23], Mulliken [4], Dennison [24] and King, Hainer, and Cross [25], which provide the foundation for the following section.

A reasonable starting point is to consider a molecule containing n atoms rotating in free space around an arbitrary axis α. The angular momentum P_α of this rotation depends on the angular velocity ω and the moment of inertia I:

$$P_\alpha = I_\alpha \omega_\alpha \tag{1.1}$$

This moment of inertia I_α is a function of the masses m_i of the nuclei and their

distance $r_{i\alpha}$ perpendicular to the axis α:

$$I_\alpha = \sum_{i=1}^{n} m_i r_{i\alpha}^2 \tag{1.2}$$

Generalization to rotations around up to three orthogonal axes requires the moment of inertia to be extended to be a tensor $\widetilde{\mathbf{I}}$, describing the three-dimensional geometry of the system.

$$\widetilde{\mathbf{I}} = \begin{pmatrix} I_{xx} & I_{xy} & I_{xz} \\ I_{yx} & I_{yy} & I_{yz} \\ I_{zx} & I_{zy} & I_{zz} \end{pmatrix} \tag{1.3}$$

The diagonal elements of this symmetric tensor are called the *moments of inertia*, while the off-diagonal elements are the *products of inertia*.

$$
\begin{aligned}
I_{xx} &= \sum_{i=1}^{n} m_i \left(y_i^2 + z_i^2 \right) & I_{xy} &= I_{yx} = -\sum_{i=1}^{n} m_i x_i y_i \\
I_{yy} &= \sum_{i=1}^{n} m_i \left(x_i^2 + z_i^2 \right) & I_{yz} &= I_{zy} = -\sum_{i=1}^{n} m_i y_i z_i \\
I_{zz} &= \sum_{i=1}^{n} m_i \left(x_i^2 + y_i^2 \right) & I_{zx} &= I_{xz} = -\sum_{i=1}^{n} m_i z_i x_i
\end{aligned}
\tag{1.4}
$$

Considering the components of the angular velocity ω as a three-dimensional column vector ($\vec{\omega} = (\omega_x \quad \omega_y \quad \omega_z)^T$), the angular momentum becomes $\mathbf{P}_{tot} = \widetilde{\mathbf{I}}\vec{\omega}$. The positional coordinates x, y and z used so far refer to an arbitrarily oriented orthogonal coordinate system fixed in the frame of the molecule. To facilitate the treatment of rotations $\widetilde{\mathbf{I}}$ can be diagonalized by the means of a *similarity transformation* using the unitary matrix $\mathbf{U}$.

$$\mathbf{U}^{-1} \begin{pmatrix} I_{xx} & I_{xy} & I_{xz} \\ I_{yx} & I_{yy} & I_{yz} \\ I_{zx} & I_{zy} & I_{zz} \end{pmatrix} \mathbf{U} = \begin{pmatrix} I_x & 0 & 0 \\ 0 & I_y & 0 \\ 0 & 0 & I_z \end{pmatrix} \tag{1.5}$$

A similarity transformation can be regarded as a change of basis functions within a given function space [26]. With respect to cartesian coordinate systems exhibiting a common center of mass $\mathbf{S}$, diagonalization can be achieved as well by rotating the coordinate system around the three Eulerian angles θ, ϕ, and χ, following the definition of Wilson, Decius, and Cross [27]. The resulting orientation of the axes coincides with the eigenvectors of the matrix $\widetilde{\mathbf{I}}$. This method can also be used to

convert the molecule-fixed coordinate system, which rotates with the frame of the molecule, into the laboratory-fixed one, in which, for instance, the direction of the exciting radiation source is defined. The example given below transfers the space-fixed axes X, Y and Z into the molecule-fixed ones (x, y, z), cf. Figure 1.1.

The sequence of rotations is [27]:

1. Turning around the Z axis by the angle ϕ, thus rotating X and Y onto X' and Y',

2. Rotation around Y' by the angle θ, so that Z and X' are rotated onto z and X'',

3. Finally, rotating the axes around z by the angle χ, achieving the final orientation x, y, z.

All of these rotations can be described by a matrix. Multiplication of the three matrices yields the *overall rotation matrix* $\boldsymbol{\Phi}$

$$
\begin{pmatrix} x \\ y \\ z \end{pmatrix} = \boldsymbol{\Phi} \begin{pmatrix} X \\ Y \\ Z \end{pmatrix}
\tag{1.6}
$$

with

$$
\begin{aligned}
\boldsymbol{\Phi} &= \begin{pmatrix} \cos\chi & \sin\chi & 0 \\ -\sin\chi & \cos\chi & 0 \\ 0 & 0 & 1 \end{pmatrix} \begin{pmatrix} 1 & 0 & 0 \\ 0 & \cos\theta & \sin\theta \\ 0 & -\sin\theta & \cos\theta \end{pmatrix} \begin{pmatrix} \cos\varphi & \sin\varphi & 0 \\ -\sin\varphi & \cos\varphi & 0 \\ 0 & 0 & 1 \end{pmatrix} \\
&= \begin{pmatrix} \begin{matrix} -\cos\theta\sin\varphi\sin\chi \\ +\cos\varphi\cos\chi \end{matrix} & \begin{matrix} \cos\theta\cos\varphi\sin\chi \\ +\sin\varphi\cos\chi \end{matrix} & \sin\theta\sin\varphi \\ \begin{matrix} -\cos\theta\sin\varphi\cos\chi \\ -\cos\varphi\sin\chi \end{matrix} & \begin{matrix} \cos\theta\cos\varphi\cos\chi \\ -\sin\varphi\sin\chi \end{matrix} & -\sin\theta\cos\varphi \\ \sin\theta\sin\chi & \sin\theta\cos\chi & \cos\theta \end{pmatrix}
\end{aligned}
\tag{1.7}
$$

As a consequence, the products of inertia vanish, leaving only the diagonal elements, called the *principle* or *main moments of inertia*. To unambiguously assign these to the actual axes, the moments of inertia are sorted according to their values and given the subscripts a, b, and c, the smallest principle moment of inertia being I_a,
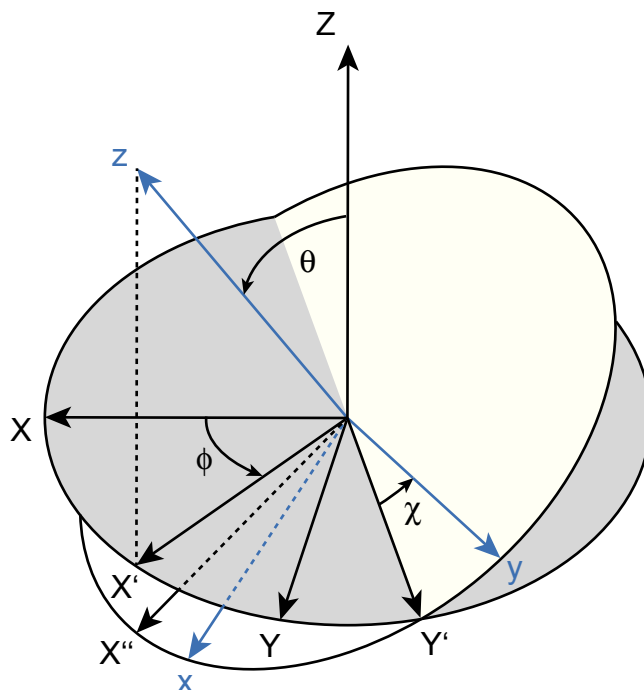
Figure 1.1: Definition of the Eulerian angles ϕ, θ and χ according to [27]. The initial orientation of the coordinate system is X,Y,Z, the final orientation (x,y,z) is given in blue. Please note that the vectors of the axes X'' and x are partially concealed by the grey plane.

Table 1.1: Types of rotors along with their symmetry requirements

type of rotor	definition	example	symmetry requirement
asymmetric	$I_a < I_b < I_c$	indole	no C_n with $n > 2$
linear	$I_a = 0$, $I_b = I_c$	HCl	C_∞
prolate symmetrical	$I_a < I_b = I_c$	BrCH$_3$	C_n with $n \geq 3$ or S_4
oblate symmetrical	$I_a = I_b < I_c$	benzene	$-"-$
spherical	$I_a = I_b = I_c$	SF$_6$	several C_n with $n \geq 2$

the largest I_c.

$$I_a \leq I_b \leq I_c \tag{1.8}$$

This allows a classification of the molecules to certain types of rotors facilitating the theoretical treatment, as selection rules stay the same within a class of rotors. Table 1.1 summarizes the possible rotors along with their symmetry requirements and given examples.

In terms of classical mechanics the overall energy of a system is given by its Hamilton function H, which is the sum of kinetic (T) and potential energy (V). The fact,

that the potential energy of a body rotating in field-free space is zero, entails that the total energy is equal to the kinetic energy.

$$H_{rot} = T_{rot} + V_{rot} = T_{rot} \tag{1.9}$$

The expression for T in its *principle axes system* (*PAS*, the coordinate system, in which $\widetilde{\mathbf{I}}$ is diagonal) is

$$T_{rot} = \frac{1}{2} \vec{\omega}^T \widetilde{\mathbf{I}} \vec{\omega} \tag{1.10}$$
$$= \frac{1}{2} \left(I_a \omega_a^2 + I_b \omega_b^2 + I_c \omega_c^2 \right)$$

After inserting the components of the angular momentum $P_\alpha = I_\alpha \omega_\alpha$ it turns into

$$T_{rot} = \left(\frac{P_a^2}{2I_a} + \frac{P_b^2}{2I_b} + \frac{P_c^2}{2I_c} \right) \tag{1.11}$$

This classical expression can be transformed into the analogue quantum mechanical one according to the correspondence principle. The angular momentum P is substituted by the appropriate operator $\widehat{\mathbf{J}} = -i\hbar \left(\mathbf{R} \times \nabla \right)$, being proportional to the cross product of the nuclei's coordinates $\mathbf{R}$ and the nabla operator ∇. Hence, equation 1.9 becomes

$$\widehat{\mathbf{H}}_{rot} = \frac{\widehat{\mathbf{J}}_a^2}{2I_a} + \frac{\widehat{\mathbf{J}}_b^2}{2I_b} + \frac{\widehat{\mathbf{J}}_c^2}{2I_c} \tag{1.12}$$

Introduction of the rotational constants A, B, and C, corresponding to the inertial axes a, b, and c , allows for a choice of unit according to the method applied and system investigated. For our purposes it is suited best to state the relative position of lines in a spectrum in Hertz. Hence, the rotational constants are given as

$$A = \frac{h}{8\pi^2 I_a} \qquad B = \frac{h}{8\pi^2 I_b} \qquad C = \frac{h}{8\pi^2 I_c} \tag{1.13}$$

and the final form of the expression for the energy becomes

$$\widehat{\mathbf{H}}_{rot} = \frac{4\pi^2}{h} \left(A\widehat{\mathbf{J}}_a^2 + B\widehat{\mathbf{J}}_b^2 + C\widehat{\mathbf{J}}_c^2 \right) \tag{1.14}$$

The commutator rules given in equation 1.15, state that any component of $\widehat{\mathbf{J}}$ commutes with the square of the angular momentum $\widehat{\mathbf{J}}^2$. The same applies for components defined in different coordinate systems (space-fixed and molecule-fixed), but they do not commute within one coordinate system. From the rules regarding $\widehat{\mathbf{H}}_{rot}$

it is evident, that the quantum number for rotations J and the projection of $\widehat{\mathbf{J}}$ onto the space-fixed coordinates, giving rise to the quantum number M, are always well defined. However, the same does not hold for the last equation of 1.15: $\widehat{\mathbf{J}}_z$ does only commute with the energy of the rotation, if I_x equals I_y. This does not apply for the majority of systems as these belong to the asymmetric rotor class. The next section will deal with asymmetric rotors in more detail.

$$
\begin{aligned}
[\widehat{\mathbf{J}}^2, \widehat{\mathbf{J}}_i] &= 0 \\
[\widehat{\mathbf{J}}^2, \widehat{\mathbf{J}}_\alpha] &= 0 \\
[\widehat{\mathbf{J}}_\alpha, \widehat{\mathbf{J}}_i] &= 0 \\
[\widehat{\mathbf{J}}_i, \widehat{\mathbf{J}}_j] &= ie_{ijk}\hbar\widehat{\mathbf{J}}_k \\
[\widehat{\mathbf{J}}_\alpha, \widehat{\mathbf{J}}_\beta] &= -ie_{\alpha\beta\gamma}\hbar\widehat{\mathbf{J}}_\gamma \\
[\widehat{\mathbf{H}}_{rot}, \widehat{\mathbf{J}}^2] &= 0 \\
[\widehat{\mathbf{H}}_{rot}, \widehat{\mathbf{J}}_Z] &= 0 \\
[\widehat{\mathbf{H}}_{rot}, \widehat{\mathbf{J}}_z] &= i\hbar\left(\frac{1}{2I_x} - \frac{1}{2I_y}\right)\left(\widehat{\mathbf{J}}_x\widehat{\mathbf{J}}_y - \widehat{\mathbf{J}}_y\widehat{\mathbf{J}}_x\right)
\end{aligned}
\tag{1.15}
$$

The indices i, j, and k refer to a space-fixed coordinate system, α, β, and γ to a molecule-fixed one and the permutation symbol e_{ijk} is defined as:

cyclic permutation	$e_{ijk} = e_{kij} = e_{jki}$
anticyclic permutation	$e_{kji} = e_{jik} = e_{ikj}$
all other permutations	0

1.1.1 The Asymmetric Rotor

All systems discussed in this work belong to the class of asymmetric rotors, having three different rotational constants. The last line in equation 1.15 illustrates that $\widehat{\mathbf{H}}_{rot}$ does not commute with $\widehat{\mathbf{J}}_z$ in the given case: The Hamilton matrix, although still diagonal in J as $[\widehat{\mathbf{J}}^2, \widehat{\mathbf{H}}_{rot}] = 0$, is not diagonal in K. The quantum number K defines the orientation of $\widehat{\mathbf{J}}$ onto the *molecule-fixed* coordinate system. In this regard it is analogue to M in the space fixed coordinate system. Thus, the Hamilton matrix consists of a set of blocks of differing J, each one of the dimension $(2J+1)\times(2J+1)$. These submatrices can be solved algebraically only for very low values of J. To find a suitable description, pseudo quantum numbers have been introduced like K_a and K_c by Mulliken [4] and the derived quantity $\tau = K_a - K_c$ [25]. The nomenclature of K_a and K_c is based on the description of the asymmetric rotor using the limiting

Table 1.2: Mapping of the internal axes x, y, z onto the main inertial axes system a, b, c

	I^R	I^L	II^R	II^L	III^R	III^L
x	b	c	c	a	a	b
y	c	b	a	c	b	a
z	a	a	b	b	c	c

cases of the symmetrical rotors (prolate and oblate). If the value of I_b draws close to I_a, the asymmetric rotor approaches the oblate symmetrical top and c becomes the symmetry axis of the molecule. Mulliken characterized this case by $K = K_c$. If, on the other hand, I_b approaches I_c, a prolate symmetrical top is given and the matrix is diagonal again. K becomes K_a is this case, respectively. As the near-symmetry axis of the molecule depends on the limiting case the rotor is closest to, a closer look should be taken at the assignment of the internal axes.

For mapping the arbitrarily oriented internal axes x, y, z onto the main inertial axes a, b, c there are $3! = 6$ possible associations as shown in Table 1.2. Each association can be either right- or lefthanded, displayed by the appropriate superscript R or L. None of these mappings actually changes the eigenvalues of the Hamiltonian, but the right choice reduces the computing effort needed: If, for instance, the asymmetric top resembles a prolate symmetrical one, assignment I is best as the z axis corresponds to the a-axis and the off-diagonal elements get as small as possible. For nearly oblate symmetrical rotors III is favourable, and for utterly asymmetric rotors II is to be chosen as in this case the elements on the diagonal approach zero. The right- and lefthanded form within one of the representations lead to the same Hamiltonian.

The actual asymmetry of a rotor is conveniently described by the parameter κ introduced by Ray [1].

$$\kappa = \frac{2B - A - C}{A - C} \tag{1.16}$$

Its value varies between -1, corresponding to the prolate symmetrical rotor, and 1 for the oblate symmetrical one. The most asymmetric rotor exhibits a value of $\kappa = 0$. Another parameter of asymmetry is δ, defined as [25]:

$$\delta = (\kappa + 1)/2 = (b - c)/(a - c) \tag{1.17}$$

The wave functions needed to describe the asymmetric rotor can be derived from

symmetrical top functions, as pointed out by Dennison: "[...] every asymmetric-top wave function $A_{J\tau M}$ can be expressed as a linear combination of symmetrical-top functions"[24].

$$A_{J\tau M} = \sum_{K,\gamma} a_{K\gamma}^{JM\tau} S_{JKM\gamma} \tag{1.18}$$

The functions $S_{JKM\gamma}$ must be defined starting from the symmetrical top wave

Table 1.3: Character table of the point group D_∞

D_∞	E	∞C_n^z	∞C_2
Σ_1 (odd J)	1	1	1
Σ_2 (even J)	1	1	-1
Π	2	$2\,cos2\pi/n$	0
Δ	2	$2\,cos4\pi/n$	0
Φ	2	$2\,cos6\pi/n$	0
$\vdots$	$\vdots$	$\vdots$	$\vdots$

functions $\psi_{JKM}(\theta,\phi,\chi)$, which may be written as [24]:

$$\psi_{JKM}(\theta,\phi,\chi) = \Theta_{JKM}(\theta)e^{iK\phi}e^{iM\chi} \tag{1.19}$$

These wave functions ψ_{JKM} belong to the continuous symmetry group D_∞ shown in Table 1.3: Each of the infinite number of representations corresponds to a value of K. Except for $K = 0$, corresponding to Σ_1 and Σ_2, all representations are doubly degenerate due to $\pm K$. The task now is to transform ψ_{JKM} in such a way, that it is always defined under the symmetry classification of the asymmetric rotor Hamiltonian, which is D_2 (cf. Table 1.4). According to Van Vleck [28, 29], the

Table 1.4: Character table of the point group D_2

D_2	E	C_2^x	C_2^y	C_2^z		
A	1	1	1	1		x^2, y^2, z^2
B_x	1	1	-1	-1	z, R_z	xy
B_y	1	-1	1	-1	y, R_y	xz
B_z	1	-1	-1	1	x, R_x	yz

slightly modified wave function $\psi_{JKM}^\times$ is introduced with β being the larger of the

two quantities K and M, removing an irregularity of sign.

$$\psi^\times_{JKM} = (-1)^\beta \, \psi_{JKM} \tag{1.20}$$

Furthermore, the functions

$$S_{JKM\gamma} = \frac{1}{\sqrt{2}} \left(\psi^\times_{JKM} + (-1)^\gamma \, \psi^\times_{J-KM} \right) \qquad \text{for } K \neq 0 \tag{1.21}$$

$$S_{J0M\gamma} = S_{J0M0} = \psi_{J0M} \qquad\qquad\qquad \text{for } K = 0 \tag{1.22}$$

are defined. The parameter γ can take the values 0 and 1 and is set to 0 for $K = 0$ as these functions are no linear combinations. The result of this definition is that the functions $S_{JKM\gamma}$ are now characterized by the representations A, B_x, B_y, and B_z of the point group D_2. Although these representations are defined relative to the arbitrarily oriented axes x, y, z, correlating them with main inertial axes is easy, as illustrated in Table 1.5, adapted from Reference [25]. As pointed out in

Table 1.5: Symmetry classification of the submatrices in $D_2(x,y,z)$ and corresponding species in mapping I^R (cf. Table 1.2)

Sub-matrix	K	γ	$J+\gamma$ J even	J odd	Species representation (x,y,z) J even	J odd	$(a,b,c)I^R$ J even	J odd
E^+	even	even	even	odd	A	B_z	$A\,(ee)$	$B_a\,(eo)$
E^-	even	odd	odd	even	B_z	A	$B_a\,(eo)$	$A\,(ee)$
O^+	odd	even	even	odd	B_y	B_x	$B_c\,(oe)$	$B_b\,(oe)$
O^-	odd	odd	odd	even	B_x	B_y	$B_b\,(oo)$	$B_c\,(oe)$

the beginning of this section, the Hamilton matrix for the asymmetric rotor is not diagonal in K. In a representation based on the functions $\psi^\times_{JKM}$ we end up with J submatrices of the dimension of $(2J+1)^2$. By choosing the $S_{JKM\gamma}$ as functions, the Hamilton matrix $\mathbf{H}$ can be further factorized into four submatrices

$$\mathbf{U}_J^{-1}\mathbf{H}\mathbf{U}_J = \mathbf{E}^+ + \mathbf{E}^- + \mathbf{O}^+ + \mathbf{O}^- \tag{1.23}$$

using the *Wang matrix* U_J [28].

$$\mathbf{U}_J = \mathbf{U}_J^{-1} = \frac{1}{\sqrt{2}} \begin{pmatrix} \ddots & & & & & & \cdot^{\cdot^{\cdot}} \\ & -1 & 0 & 0 & 0 & 1 & \\ & 0 & -1 & 0 & 1 & 0 & \\ & 0 & 0 & \sqrt{2} & 0 & 0 & \\ & 0 & 1 & 0 & 1 & 0 & \\ & 1 & 0 & 0 & 0 & 1 & \\ \cdot^{\cdot^{\cdot}} & & & & & & \ddots \end{pmatrix} \tag{1.24}$$

Each submatrix is approximately of the order of $J/2 \times J/2$. The symbols for the submatrices refer to the even- or oddness of the values of K and γ: E (O) denotes that K is even (odd) and $+$ (-) refers to γ equal 0 (1). For symmetrical rotors all energy levels for $K > 0$ are twofold degenerate, resulting in $(J+1)$ energy levels. This degeneracy is lifted for $\kappa \neq \pm 1$ as shown in Figure 1.2. The more κ deviates from the limiting cases of the symmetrical tops, the larger the *k-splitting* becomes.

Selection Rules

The selection rules regarding J are the same as the ones for symmetrical tops: J can change by -1, 0, and $+1$, giving rise to the well-known P, Q, and R branches. As for the pseudo quantum number K_a and K_c refer to Table 1.6. A transition is allowed, if the product of the irreducible representations Γ of all wave functions involved in the excitation and the transition dipole moment $\vec{\mu}$ contains the totally symmetric representation (A) of the point group.

$$\Gamma^{initial} \otimes \Gamma(\vec{\mu}) \otimes \Gamma^{end} \supseteq A \tag{1.25}$$

The representations of the initial and final state are given in Table 1.5. The representation of the transition dipole moment depends on its orientation within the molecule. Basically, it can have components along all three internal axes a, b, c. These components transform like a rotation around the given axis. In assignment I^R the a-axis corresponds to the z-axis. According to the character table of D_2, the representation for a rotation around this axis is B_z, corresponding to B_a in the chosen axes mapping. Thus a-type transitions can connect two states whose symmetry product is also B_a like A and B_a, and B_b and B_c.
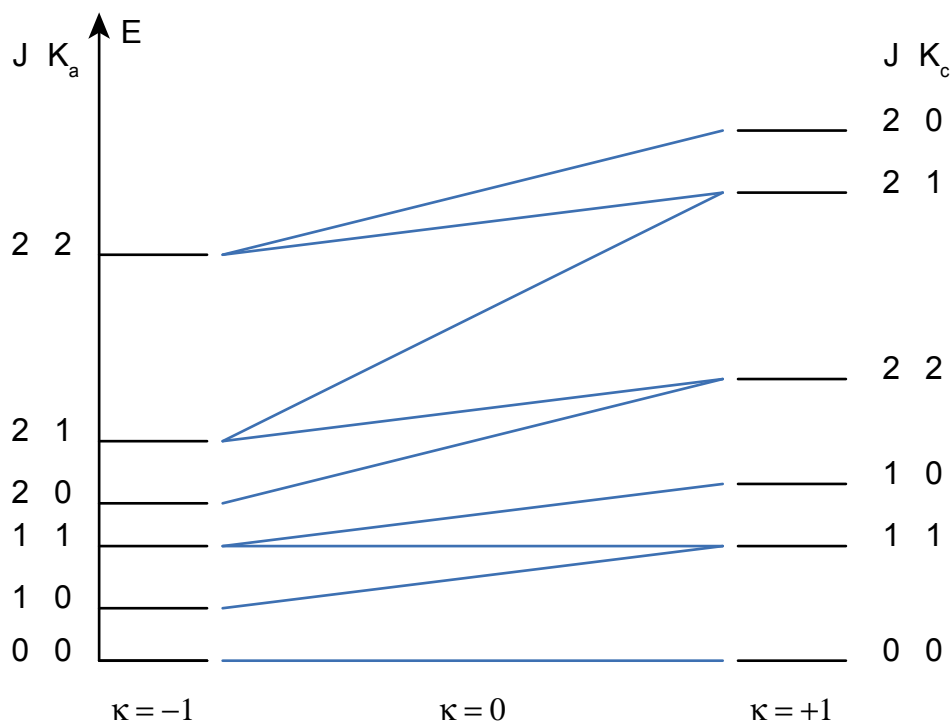
Figure 1.2: Schematic correlation of the rotational energies for asymmetric rotors. The black bars at the side denote the energy levels of the symmetric cases depending on the quantum numbers J and K: prolate symmetrical on the left, oblate symmetrical on the right. The subscripts for K denote which pseudo-quantum number has major influence near the respective limiting case. Note that the energy of the oblate symmetrical rotor decreases for higher values of K, while for prolate symmetrical tops it is *vice versa*.

1.2   Internal Rotation

As stated in the beginning of this chapter, treating a molecule as a rigid frame is often a good approximation as long as no internal motion is present. But as soon as a part of the molecule has a finite barrier for internal rotation, an inversion, or a puckering motion, additional spectroscopical features appear, demanding an appropriate treatment. For rotationally resolved spectroscopy these features are the appearance of torsional sublevels, each exhibiting a distinct set of rotational constants. For further reading beyond this section refer to the detailed description of internal rotation by Herschbach [30], Lin and Swalen [31], and the corresponding chapter by Gordy & Cook [21].

Before we can start to set up the Hamiltonian, we have to choose a coordinate system capable of dealing with internal rotation. One possibility would be to retain the main inertial axes system used so far and define an additional axis running through the

Table 1.6: Selection rules for rotational transitions in asymmetric rotors

a-type	$\vec{\mu}_a \neq 0$	$A \leftrightarrow B_a$	$B_b \leftrightarrow B_c$	$\Delta K_a =$	$0, \pm 2, \pm 4, \ldots$
		$ee \leftrightarrow eo$	$oo \leftrightarrow oe$	$\Delta K_c =$	$\pm 1, \pm 3, \pm 5, \ldots$
b-type	$\vec{\mu}_b \neq 0$	$A \leftrightarrow B_b$	$B_a \leftrightarrow B_c$	$\Delta K_a =$	$\pm 1, \pm 3, \pm 5, \ldots$
		$ee \leftrightarrow oo$	$eo \leftrightarrow oe$	$\Delta K_c =$	$\pm 1, \pm 3, \pm 5, \ldots$
c-type	$\vec{\mu}_c \neq 0$	$A \leftrightarrow B_c$	$B_a \leftrightarrow B_b$	$\Delta K_a =$	$\pm 1, \pm 3, \pm 5, \ldots$
		$ee \leftrightarrow oe$	$eo \leftrightarrow oo$	$\Delta K_c =$	$0, \pm 2, \pm 4, \ldots$

bond the internal rotor is moving around. Wilson [32] and Crawford [33] elaborated this model and called it the *principle axis method, PAM*, which requires at least one group featuring cylindrical symmetry. This group is called *top*, attached to the other group called *frame*, which may be asymmetric or symmetric like the top. The interactions between the rotation of the whole molecule and the torsion are treated via perturbation theory.

The other approach, called *internal axis method, IAM*, was presented by Nielsen [34] and Dennison *et al.* [35, 36]: one axis corresponds to the internal axis of torsion, while the others may be chosen randomly according to the molecule. Both descriptions yield the same results and have a field of systems where they work best: while the PAM method is more widely applicable, the IAM has the advantage of a smaller coupling between rotational and torsional motion.

The following explanations are based on the PAM formalism as here the inertial tensor $\widetilde{\mathbf{I}}$ is diagonal, which facilitates the comparison to the rigid rotor.

The kinetic energy of a molecular rotor exhibiting internal rotation is given as

$$T = \frac{1}{2} \sum_{g=a,b,c} I_g \omega_g^2 + \frac{1}{2} I_\phi \omega_\phi^2 + I_\phi \omega_\phi \sum_{g=a,b,c} \lambda_g \omega_g \tag{1.26}$$

Comparison to equation 1.10 shows, that the first part of this expression is just the kinetic energy of the rigid rotor. The second part describes the internal rotation: ϕ is the torsional angle and I_ϕ the moment of inertia of the top rotating with the angular velocity ω_ϕ. The last term gives the coupling term between external and internal rotation. The λ_g are the direction cosines between the main inertial axes and the torsional axis.

Now we define two types of angular momenta [30]: $\widehat{\mathbf{J}}_g$ are the components of the total angular momentum along the principle axes a, b, c. They consist of a part that depends on the geometry of the molecule ($I_g \omega_g$) and the internal angular momentum

times the direction cosine λ_g.

$$\widehat{\mathbf{J}}_g = \frac{\partial T}{\partial \omega_g} = I_g \omega_g + \lambda_g I_\phi \omega_\phi \tag{1.27}$$

$$\widehat{p} = \frac{\partial T}{\partial \omega_\phi} = I_\phi \omega_\phi + I_\phi \sum_g \lambda_g \omega_g \tag{1.28}$$

The total angular momentum of the internal top, represented by the operator $\widehat{p}$ $(= i\hbar \partial/\partial \phi)$, only depends on the geometry of the top itself and is independent of I_g. The commutator rules regarding $\widehat{\mathbf{J}}_g$ stay the same as stated in equation 1.15 and $\widehat{p}$ and $\widehat{\mathbf{J}}_g$ commute. Having defined $\widehat{p}$ and $\widehat{\mathbf{J}}_g$, the equation for the kinetic energy may be rewritten as

$$2T - \sum_g \frac{\widehat{\mathbf{J}}_g^2}{I_g} = r I_\phi \omega_\phi^2 \qquad \text{with} \qquad r = 1 - \sum_g \frac{\lambda_g I_\phi}{I_g} \tag{1.29}$$

The product of I_ϕ and the reducing factor r is called the *reduced moment of inertia* for internal rotation. Introducing the relative angular momentum $\widehat{p} - \mathfrak{P}$ with

$$\mathfrak{P} = \sum_g \widehat{\mathbf{J}}_g \rho_g \qquad \text{and} \quad \rho_g = (\lambda_g I_\phi)/I_g \tag{1.30}$$

allows the Hamiltonian to be expressed as

$$\widehat{\mathbf{H}} = \widehat{\mathbf{H}}_{rot} + F\left(p - \mathfrak{P}\right)^2 + V\left(\phi\right) \tag{1.31}$$

F $(= \hbar/(8\pi^2 r I_\phi))$ is the *reduced torsional constant* for internal rotation and V_ϕ the potential energy function. The Hamiltonian can easily be decomposed into the sum of the rotational $\widehat{\mathbf{H}}_R$, torsional $\widehat{\mathbf{H}}_T$ and coupling part $\widehat{\mathbf{H}}_{RT}$. One has to be careful to note that $\widehat{\mathbf{H}}_R \neq \widehat{\mathbf{H}}_{rot}$: As shown in equation 1.32 the internal motion gives rise to the term $F\mathfrak{P}^2$. This however provides no qualitative change, as it is a quadratic expression in $\widehat{\mathbf{J}}_g$. Since $\widehat{\mathbf{H}}_R$ does not depend on the torsional angle ϕ and $\widehat{\mathbf{H}}_T$ is independent of the rotational quantum number J, torsional and rotational motion could be separated, if it were not for the expression $-2F\mathfrak{P}p$. However, if the barrier for internal rotation is high enough the term $\widehat{\mathbf{H}}_{TR}$ can be treated simply as a perturbation.

$$\begin{aligned} \widehat{\mathbf{H}}_R &= \widehat{\mathbf{H}}_{rot} + F\mathfrak{P}^2 \\ \widehat{\mathbf{H}}_T &= Fp^2 + V\left(\phi\right) \\ \widehat{\mathbf{H}}_{TR} &= -2F\mathfrak{P}p \end{aligned} \tag{1.32}$$

In order to describe the barriers for internal rotation suitable potential functions are needed. While the top rotates relative to the frame, the torsional angle ϕ changes from 0 to 2π. During this rotation the potential energy changes depending on the number of minima N. For methyl rotors like in ethane there are three equivalent minima, while for example ethene has two minima and CH_3–NO_2 six. Obviously, the potential function has to be periodic in ϕ, repeating itself N times before the starting position is reached again. A Fourier series expansion

$$V(\phi) = a_0 + \sum_{k=1}^{\infty} a_k \cos\left(kN\phi\right) \tag{1.33}$$

with $a_0 = -\sum_{k=1}^{\infty} a_k$ satisfies this requirement. The potential function for a barrier with N-fold symmetry is given by the sum in equation 1.34, with V_N being the respective barrier height.

$$V(\phi) = \frac{V_N}{2}\left(1 - \cos(N\phi)\right) + \frac{V_{2N}}{2}\left(1 - \cos(2N\phi)\right) + \cdots \tag{1.34}$$

In the further course of this section we will only consider the threefold barrier needed for the description of a methyl rotor. Inserting 3 for N in the Fourier series yields

$$V(\phi) = \frac{V_3}{2}\left(1 - \cos(3\phi)\right) + \frac{V_6}{2}\left(1 - \cos(6\phi)\right) + \cdots \tag{1.35}$$

from which only the first expansion is kept, as higher order contributions are not relevant in the cases treated here.

$$V(\phi) = \frac{V_3}{2}\left(1 - \cos(3\phi)\right) \tag{1.36}$$

To achieve deeper insight in the consequences of the barrier for the quantum mechanical treatment the two limiting cases for the barriers are discussed: V_3 could either get very large or very small. In case of V_3 getting very small, the molecule approaches the *free rotor limit* and the energy for internal rotation given by $E = Fm^2$ with m being an integer value. The free rotor states are all doubly degenerate except those for $m = 0$. This degeneracy originates in the two possible directions of internal rotation. The other case is a very large V_3. This would result in small torsional oscillations in the minimum of the potential well, being threefold degenerate as there are three equivalent minima. The respective wave function $\psi(\phi)$ has the same form as the harmonic wave equation. Hence, the frequency ν of the oscillation can be

computed from the barrier height and the reduced moment for internal rotation.

$$\nu = \frac{3}{2\pi}\sqrt{\frac{V_3}{2I_r}} \qquad (1.37)$$

Lowering the barrier height from infinity to a finite value leads to a tunneling motion from one minimum to the other. Hence, the threefold degenerate torsional levels split into a non-degenerate level A and a doubly degenerate level E. The designation of the sublevels is based on the behaviour of wave functions as the symmetry operators of the point group C_3 (cf. Table 1.7) act on them. The wave function of an A level resembles a harmonic vibration in the minimum of the potential well and is periodic in $2\pi/3$, while the wave function of E states is more like a free rotation, periodic in 2π, attributed to the tunneling from one minimum to the other. The wave functions themselves can be obtained by solving the Mathieu equations [37]. The solutions have the general appearance of $\psi_{tor}(v\sigma)$, with v being the principle torsion quantum number and $\sigma = 0, \pm 1$ being the index to distinguish the sublevels: A corresponds to $\sigma = 0$, E to $\sigma = \pm 1$. A suitable basis for the internal rotor
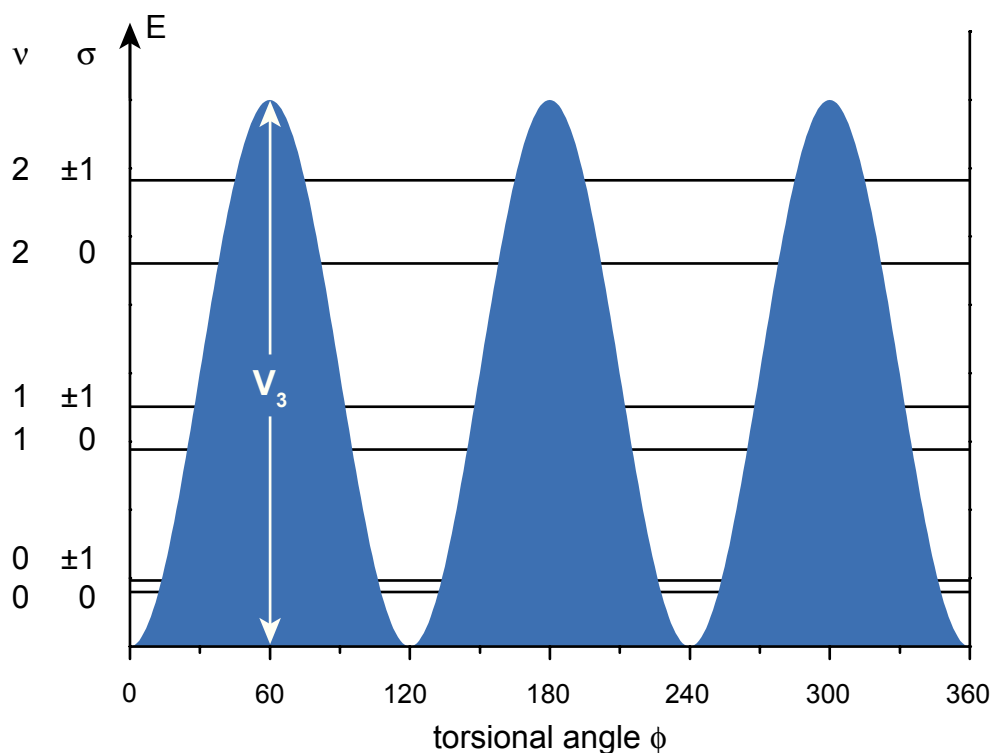

Figure 1.3: Vibrational sublevel for $v = 0$ to $v = 2$ in a V_3 potential.

Hamiltonian can be constructed from the rotor wave functions ψ_{rot}, treated in the

Table 1.7: Character table of the point group C_3

C_3	E	C_3	C_3^2
A	1	1	1
$E\Big\{\quad E$	1	$e^{i2\pi/3}$	$e^{-i2\pi/3}$
E	1	$e^{-i2\pi/3}$	$e^{i2\pi/3}$

section about asymmetric rotors, and the torsional wave functions ψ_{tor}.

$$\psi_{tor} = \sum_{k=-\infty}^{\infty} A_k^{(\nu)} e^{i(Nk+\sigma)\phi} \tag{1.38}$$

In this basis the parts $\widehat{\mathbf{H}}_R$ and $\widehat{\mathbf{H}}_T$ are diagonal, but the coupling Hamiltonian $\widehat{\mathbf{H}}_{TR}$ introduces off-diagonal elements, preventing diagonalization. In order to solve the problem, Van Vleck elaborated the following method [29, 38]: First, the Hamiltonian $\widehat{\mathbf{H}}$ is grouped into blocks of different values of v. These blocks, which represent the rotational submatrices, are connected by off-diagonal elements originating from the coupling Hamiltonian $\widehat{\mathbf{H}}_{TR}$. To reduce the off-diagonal elements the *Van Vleck transformation* is applied, folding the off-diagonal elements back into the v-blocks. After the transformation is carried out, the coupling elements are so small, that they can be neglected. Comparison of the energy spacings between rotational level E_R on the one hand and torsional level E_T on the other hand shows that for reasonable high barriers the latter is much larger. Hence, it is save to approximate $E_{R'T'} - E_{R''T''} \simeq E_{T'} - E_{T''}$, leading to the *effective rotational Hamiltonian* $\widehat{\mathbf{H}}_{v\sigma}$ [31, 39]:

$$\begin{aligned}
\widehat{\mathbf{H}}_{\nu\sigma} &= \widehat{\mathbf{H}}_{rot} + F \sum_{n=1}^{\infty} W_{\nu\sigma}^{(n)} \mathfrak{P}^n \\
&= A\widehat{\mathbf{J}}_a^2 + B\widehat{\mathbf{J}}_b^2 + C\widehat{\mathbf{J}}_c^2 + F \sum_{n=1}^{\infty} W_{\nu\sigma}^{(n)} (\widehat{\mathbf{J}}_a \rho_a + \widehat{\mathbf{J}}_b \rho_b + \widehat{\mathbf{J}}_c \rho_c)^n
\end{aligned} \tag{1.39}$$

The perturbation coefficients are given as

$$\begin{aligned}
W_{\nu\sigma}^{(0)} &= \frac{E_{\nu\sigma}}{F} \\
W_{\nu\sigma}^{(1)} &= -2\langle \nu, \sigma | \widehat{p} | \nu, \sigma \rangle \tag{1.40} \\
W_{\nu\sigma}^{(2)} &= 1 + 4F \sum_{\nu'} \frac{|\langle \nu, \sigma | \widehat{p} | \nu, \sigma \rangle|^2}{\Delta_{\nu\nu'}} \tag{1.41}
\end{aligned}$$

with $\Delta_{\nu\nu'} = E_{\nu\sigma} - E_{\nu'\sigma}$.

The first perturbation coefficient $W_{\nu\sigma}^{(0)}$ is the energy of the torsion. Higher order

coefficients ($n > 2$) can be computed from known coefficients via the relationship

$$\frac{W_{\nu\sigma}^{(n+2)}}{W_{\nu\sigma}^{(n)}} \approx \frac{-(2\pi/3)^2}{(n+1)(n+2)} \qquad \text{for } n > 0 \tag{1.42}$$

All perturbation coefficients decrease in size with increasing barrier except for $W_{\nu\sigma}^{(0)}$, as it is constant. For an infinitely high barrier they become zero and the Hamiltonian $\widehat{\mathbf{H}}_{\nu\sigma}$ is equal to the expression for a rigid rotor. Furthermore, the coefficients depend on the torsional state [30]:

$$\begin{aligned}
W_{\nu 0}^{(n)} &= 0 \qquad\qquad \text{for } n \text{ odd} \\
W_{\nu 1}^{(n)} &= (-1)^n W_{\nu -1}^{(n)} \\
W_{\nu 0}^{(n)} &\simeq -2W_{\nu 1}^{(n)} \qquad \text{for } n > 0 \text{ and even}
\end{aligned} \tag{1.43}$$

As shown above, all odd perturbation coefficients for A level are zero. If fourth and higher order perturbation coefficients are discarded, the Hamiltonian for the A level becomes

$$\widehat{\mathbf{H}}_{\nu 0} = A_{\nu,0}\widehat{\mathbf{J}}_a^2 + B_{\nu,0}\widehat{\mathbf{J}}_b^2 + C_{\nu,0}\widehat{\mathbf{J}}_c^2 \tag{1.44}$$

with the effective rotational constants

$$\begin{aligned}
A_{\nu\sigma} &= A + W_{\nu\sigma}^{(2)} F \rho_a^2 \\
B_{\nu\sigma} &= B + W_{\nu\sigma}^{(2)} F \rho_b^2 \\
C_{\nu\sigma} &= C + W_{\nu\sigma}^{(2)} F \rho_c^2
\end{aligned} \tag{1.45}$$

which incorporate the second order perturbation contribution. Neglecting terms of n higher than two like for the A level, the Hamiltonian for the E level becomes with $D_g = F W_{\nu,1}^{(1)} \rho_g$.

$$\widehat{\mathbf{H}}_{\nu,\pm 1} = A_{\nu,\pm 1}\widehat{\mathbf{J}}_a^2 + B_{\nu,\pm 1}\widehat{\mathbf{J}}_b^2 + C_{\nu,\pm 1}\widehat{\mathbf{J}}_c^2 + D_a\widehat{\mathbf{J}}_a + D_b\widehat{\mathbf{J}}_b + D_c\widehat{\mathbf{J}}_c \tag{1.46}$$

The observed splitting between A and E levels originates from the fact that the perturbation coefficients in equation 1.43 differ in magnitude and sign for different values of σ. The selection rule for σ is $\Delta\sigma = 0$: As the methyl top has cylindrical symmetry, torsional motion does not affect the transition dipole moment ($\partial\mu/\partial\phi$).

1.3   Line Intensities

The intensity of transitions within rotationally resolved fluorescence spectra depend-son a variety of factors like the line strength factors, the Franck-Condon overlap, the thermal population of the ground state and the statistical weights of the nuclear spins. The number of molecules that can be excited from a quantum state depends on the probability of the excitation as well as on the population in this state. For thermodynamically equilibrated systems the occupation is given by the *Maxwell-Boltzmann distribution*. All investigations presented in this thesis were performed under *molecular beam* conditions. This means that the sample, seeded in a carrier gas, is expanded through a small orifice into high vacuum. Of course molecules are not thermally equilibrated under this conditions, and the distribution function has to be modified to match the system. Chapter 3.2, concerning the experimental setup, provides a detailed discussion of this phenomenon. In this section the line strength factors will be considered exclusively. For a thorough treatment of the statistical weights refer to [40].

The *line strength* S^{nm} of a transition corresponds to the square of the transition probability W_{nm} between the initial state n and the final state m.

$$S^{nm} = |W_{nm}|^2 = \sum_{M',M''} |\langle m, M' | \hat{\vec{\mu}} | n, M'' \rangle|^2 \tag{1.47}$$

The parameters M account for the degeneracy of the respective state in the quantum number M and $\hat{\vec{\mu}}$ is the transition dipole moment operator. Considering the Born-Oppenheimer approximation[1], S^{nm} can be treated separately for rotational, vibrational and electronic excitation. Making use of the asymmetric wave functions defined in equation 1.18, equation 1.47 yields for the rotational part [41]:

$$S^{nm} = \sum_{F=X,Y,Z} \sum_{M',M''} |\langle A\left(J', \tau', M'\right) | \hat{\vec{\mu}}_F | A\left(J'', \tau'', M''\right) \rangle|^2 \tag{1.48}$$

The additional sum extends over the three spatial directions of the space-fixed coordinate system. In the absence of an external field X, Y and Z are equivalent, so the treatment can be reduced to one axis, which in our case is the Z axis.

$$S^{nm} = 3 \sum_{M',M''} |\langle A\left(J', \tau', M'\right) | \hat{\vec{\mu}}_Z | A\left(J'', \tau'', M''\right) \rangle|^2 \tag{1.49}$$

---

[1]cf. Chapter 2, page 31ff.

So far, the transition dipole moment is defined with respect to the space-fixed coordinates. Excitation requires the light to interact with the transition dipole moment, rotating with the frame of the molecule. Use of the rotation matrix $\mathbf{\Phi}$ (cf. equation 1.6) relates the two axes systems and the matrix element becomes:

$$\langle A\left(J',\tau',M'\right)|\mathbf{\Phi}\hat{\vec{\mu}}_Z|A\left(J'',\tau'',M''\right)\rangle = \sum_{\alpha=a,b,c} \langle A\left(J',\tau',M'\right)|\hat{\vec{\mu}}_\alpha|A\left(J'',\tau'',M''\right)\rangle$$

$$(1.50)$$

The total line strength factor S^{nm} is composed of the appropriate factors for every internal axis given as squared cosine of the angle between the transition dipole moment and the axis α.

$$S^{nm} = S_a^{nm} + S_b^{nm} + S_c^{nm} = cos^2 \sphericalangle(\mu,a) + cos^2 \sphericalangle(\mu,b) + cos^2 \sphericalangle(\mu,c) \qquad (1.51)$$

This discussion is restricted to the rotational part of the total wave function. For the contributions of the electronic and vibrational part see Chapter 2.

1.4 Axis Reorientation

The energy of a rotational transition is defined by a set of quantum numbers and the rotational constants as shown in equation 1.14 on page 9. Each set of rotational constants belongs to three principle axes which are fixed in the molecule for a given geometry. According to the Born-Oppenheimer approximation, the electronic excitation of a molecule usually results in a change of the geometry in consequence of the altered occupation of the molecular orbitals. If the symmetry of the system is low enough (below C_{2v}) these geometry changes may result in a reorientation of the main inertial axis system [42]. This effect is called *axis reorientation* or *axis switching*, and its consequences were first described in detail by Hougen and Watson [42]. Regarding rotationally resolved electronic spectroscopy, Held *et al.* published another fundamental approach to describe this effect [43]. An example of the impact of axis reorientation on the intensities of vibrationally resolved spectroscopy is given by Mebel *et al.* [44]. The following summary is, unless cited differently, based on the publications by Hougen and Watson [42], and Held *et al.* [43].

If a molecules exhibits axis reorientation the orientation of the main inertial axes does not coincide for the ground and electronically excited state. As two axis systems have to be considered, these have to be interconverted into each other by means of

a rotational matrix analogue to the Eularian angles on page 7.

Starting from a coordinate system fixed in space, the geometry is rotated by a matrix $\mathbf{S}^{-1}$ either into the principle axis system of the electronic state A or B [42].

$$\mathbf{S}^{-1}(\chi_A, \theta_A, \phi_A) \cdot (x_{iA} + d_{iA}) = \mathbf{S}^{-1}(\chi_B, \theta_B, \phi_B) \cdot (x_{iB} + d_{iB}) \tag{1.52}$$
$$x_{iA} + d_{iA} = \mathbf{S}(\chi_A, \theta_A, \phi_A) \cdot \mathbf{S}^{-1}(\chi_B, \theta_B, \phi_B) \cdot (x_{iB} + d_{iB})$$
$$= \mathbf{T} \cdot (x_{iB} + d_{iB})$$

Here x_{iA} are the equilibrated internal coordinates of the atom i in the respective electronic state A, and d_{iA} the distortions induced by vibrations. Combination of the matrices for both states yields the matrix $\mathbf{T}$. In zero-order approximation only the changes of the equilibrium geometry are taken into account, and instantaneous geometry changes induced by vibrations are neglected. Hence, axis reorientation occurs if the reorientation matrix $\mathbf{T}$ differs from the unit matrix [42]. Applying an unitary transformation to $\mathbf{T}$ according to Wigner [3] yields the matrix $\mathfrak{D}^{(1)}$.

$$\mathfrak{D}^{(1)}(\chi_A, \theta_A, \phi_A) = \mathbf{U} \cdot \mathbf{S}(\chi_A, \theta_A, \phi_A) \cdot \mathbf{U}^{-1}$$
$$= \mathbf{U} \cdot \mathbf{T} \cdot \mathbf{U}^{-1} \cdot \mathbf{U} \cdot \mathbf{S}(\chi_A, \theta_A, \phi_A) \cdot \mathbf{U}^{-1} \tag{1.53}$$
$$= \mathfrak{D}^{(1)}(\mathbf{d}_{iB}) \cdot \mathfrak{D}^{(1)}(\chi_B, \theta_B, \phi_B)$$

Apart from the normalization constant $((2J+1)/8\pi^2)^{1/2}$ the elements of $\mathfrak{D}^{(1)} = \mathfrak{D}_{KM}^{(1)}$ are the rotational wave functions of the symmetrical top for $J = 1$ [42]. The wave functions for higher values of J can be computed according to the following equation.

$$\mathfrak{D}_{KM}^{(J)}(\chi_A, \theta_A, \phi_A) = \sum_{K'} \mathfrak{D}_{KK'}^{(J)}(\chi_T, \theta_T, \phi_T) \cdot \mathfrak{D}_{K'M}^{(J)}(\chi_B, \theta_B, \phi_B) \tag{1.54}$$

The asymmetric rotor basis function in the excited state $|J'K_a'K_c'\rangle$, which are constructed from symmetrical top wave functions $|JK\rangle$ (cf. Section 1.1.1 on page 10ff.) are rotated by the switching matrix $\mathfrak{D}_K^{(J)}$.

$$|J'K_a'K_c'\rangle = \sum_{K'} c_{\text{J'K'}} \sum \mathfrak{D}_K^{(J)}(\chi_T, \theta_T, \phi_T)|JK\rangle \tag{1.55}$$

Therefore, the asymmetric rotor hamiltonian is diagonalized for each state in its respective axis system. This means that for every value of J a $(2J + 1) \times (2J + 1)$ rotation matrix has to be evaluated, using the method of Hougen and Watson [42]. A less expensive way to compute the matrix elements was given by Held *et al.* [43]. They rotatate the Hamiltonian into a common coordinate system by means of a 3×3

matrix and diagonalize the resulting matrix afterwards. For planar molecules with
the internal c-axis perpendicular to the aromatic plane this results in:

$$
\begin{aligned}
\widehat{\mathbf{H}}'_{rot} &= \mathbf{U}\widehat{\mathbf{H}}_{rot}\mathbf{U}^{-1} \\
&= \mathbf{U}(A\widehat{\mathbf{J}}_a^2 + B\widehat{\mathbf{J}}_b^2 + C\widehat{\mathbf{J}}_c^2)\mathbf{U}^{-1} \\
&= A\widehat{\mathbf{J}}_a^2 + B\widehat{\mathbf{J}}_b^2 + C\widehat{\mathbf{J}}_c^2 + D(\widehat{\mathbf{J}}_a\widehat{\mathbf{J}}_b + \widehat{\mathbf{J}}_b\widehat{\mathbf{J}}_a)
\end{aligned}
\tag{1.56}
$$

$\widehat{\mathbf{H}}'_{rot}$ is the nondiagonal Hamiltonian rotated into the new axis system. Because
of the off-diagonal elements $D(\widehat{\mathbf{J}}_a\widehat{\mathbf{J}}_b + \widehat{\mathbf{J}}_b\widehat{\mathbf{J}}_a)$ the wave functions of both electronic
states can no longer be labeled by the same designations based on the group D_2.
As a result it is not possible to assign all rotational transitions within a spectrum
uniquely as a, b, or c-type transitions. Furthermore, intensity is shifted between
transitions of different type. So the effect of axis reorientation is a breakdown of the
intensity rules derived for systems where only the equilibrium configuration has to
be considered [42].

The axis reorientation angle can be computed for any planar molecule using Carte-
sian coordinates in the principal axis system of each state:

$$
tan(\theta_T) = \frac{\sum_i m_i(a'_i b''_i - b'_i a''_i)}{\sum_i m_i(a'_i a''_i + b'_i b''_i)}
\tag{1.57}
$$

Here, the doubly primed coordinates a''_i and b''_i refer to the coordinates of the ith
atom in the principal axis system in the electronic ground state, the singly primed
coordinates to the respective excited state coordinates and m_i is the atomic mass of
the ith atom in the molecule.

1.5   Line Widths and Profiles

Excitation from one quantum state to another has a certain energy, corresponding
to the energy difference between both levels. The resulting line in a spectrum, how-
ever, is not monochromatic, but exhibits a broadening around the center frequency.
There are several reasons for line broadening in gas phase experiments and the re-
sulting line shape depends on the broadening mechanisms being of consequence in
the actual experiment [45]: The limited lifetime in the excited state gives rise to the
natural linewidth. Elastic collisions between molecules can shift the internal energies
of a radiating collision partner and in this way shift the emitted frequency. Inelastic
collisions lead to faster depopulation of the excited state resulting in an additional

lifetime broadening. Both effects are summarized as *collisional broadening* and the latter is sometimes referred to as *pressure broadening*. Movement of the sample parallel to the incident radiation results in a respective *Doppler broadening*. *Saturation broadening* is caused by high laser intensities saturating a transition between two states, while *transit-time broadening* occurs if the interaction time between the sample and the exciting radiation (the flight time of the molecule through the laser focus) is very short compared to the lifetime of the excited state. Hence, it only arises in molecular beam experiments when a sample with long excited state lifetime ($\tau \geq ms$) crosses a laser beam at right angles, or if the laser focus is small.

The presented experiments were performed on molecules with excited state lifetimes in the nanosecond regime using comparatively low radiation intensity under molecular beam conditions. Therefore collisional, saturation and transit-time broadening can be neglected and only the Doppler broadening and the natural linewidth contribute to the resulting line profile. For a more detailed introduction to line broadening mechanisms refer to "*Laser Spectroscopy*" by Demtröder [45].

1.5.1   Natural Linewidth

The time a molecule spends in its excited state is limited and there is a variety of deactivating processes that finally lead to the ground state. Electronic excitation to a singlet state may lead to *fluorescence*, a radiative deactivation under spontaneous emission of a photon. Radiationless decay includes isoenergetic transitions to vibrationally excited levels of the electronic ground state or a lower lying excited singlet state (*internal conversion*) and *intersystem crossing* to levels belonging to a state of different multiplicity. Which one of these mechanisms is most important and thus determines the lifetime of a molecule depends on its composition and vibronic structure. The probability of every molecule i belonging to an ensemble to spontaneously emit a photon within a period Δt is the same and does not depend on external influences. Hence, the spectral line shape is governed by a homogeneous broadening function. The intensity distribution can be derived by regarding the excited system classically as a damped harmonic oscillator [45]: During the emission of a photon the electronic transition dipole moment oscillates, damped by the radiative loss of energy. Making the reasonable assumption that the damping constant γ is usually much smaller than the emitted frequency ($\nu_0 \gg \gamma$), the oscillating dipole moment is given as

$$\mu = \mu_0 \cdot e^{-(\gamma/2)t} cos(2\pi\nu_0 t) \tag{1.58}$$

Fourier transformation and normalization of this expression yields the *Lorentzian profile* $L(\nu)$.

$$L(\nu) = \frac{\gamma}{4\pi^2(\nu - \nu_0)^2 + (\gamma/2)^2} \tag{1.59}$$

Its *full width at half maximum* (*FWHM*) equals the damping constant γ divided by 2π. The mean lifetime τ is $1/\gamma$.

Another motivation can be achieved employing Heisenberg's uncertainty principle regarding time and energy. It is obvious that short excited state lifetimes (small Δt) induce a large ΔE. This is equivalent to a broad frequency distribution.

$$\Delta t \cdot \Delta E \geq \hbar \tag{1.60}$$

The connection between the excited state lifetime τ ($\widehat{=}\Delta t$) and the full width at half maximum $\Delta \nu$ is given as

$$\Delta E = h \cdot \Delta \nu \geq \frac{\hbar}{\tau} \Rightarrow \Delta \nu \geq \frac{1}{2\pi\tau} \tag{1.61}$$

1.5.2 Doppler Width

The Doppler width results from the shift of frequency $\Delta \nu$ molecules experience when they move parallel to the propagation direction of the incident radiation. The corresponding energy shift is a consequence of the respective component of velocity and has either to be added or subtracted, depending on the direction of travel. To reduce the Doppler width the velocity parallel to the detector and excitation source has to be confined like in a molecular beam machine presented in Chapter 3.2.

Contrary to the natural linewidth, the chance to emit a photon with the specific frequency ν is not the same for all molecules within the ensemble but depends on the inhomogeneous velocity and therefore leads to inhomogeneous broadening [45]. The one-dimensional velocity distribution of a thermally equilibrated gas is described by the Maxwell-Boltzmann distribution.

$$f(\nu)d\nu = \sqrt{\frac{m}{2\pi kT}} \cdot e^{-\frac{m\nu^2}{2kT}} d\nu \tag{1.62}$$

The resulting line profile is a Gauss function

$$G_\nu = \frac{2}{\delta\nu}\sqrt{\frac{\ln 2}{\pi}} \cdot e^{-4\ln 2\left(\frac{\nu - \nu_0}{\delta\nu}\right)^2} \tag{1.63}$$

with the respective FWHM

$$\delta\nu = \frac{\nu}{c}\sqrt{\frac{8kT\,ln\,2}{m}} \tag{1.64}$$

The experimentally observed intensity profile exhibits contributions from both the natural linewidth and Doppler broadening. Accordingly, a Gauss and a Lorentzian function have to be convoluted to describe the overall profile. The resulting function is called *Voigt profile*.

$$V(\nu) = \int_{-\infty}^{\infty} G(\nu') \cdot L(\nu - \nu')d\nu' \tag{1.65}$$
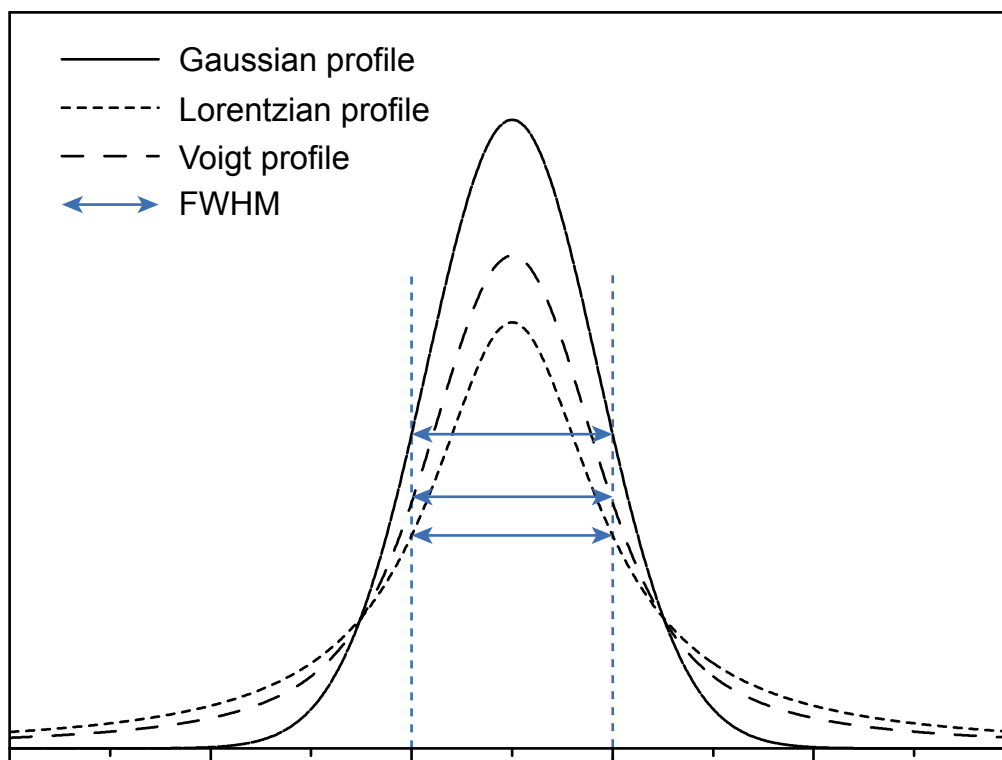
All three functions are depicted in Figure 1.4

Figure 1.4: Line profiles of a Gaussian and a Lorentzian distribution as well a Voigt profile. All distributions are normalized to the same FWHM.

1.6   Nomenclature of the ^1L_a and ^1L_b States

This thesis is concerned with the interplay of the two lowest excited singlet states of indole and several of its derivatives. As they differ substantially in their excited

state properties and may change their energetic ordering, it is not sufficient to label them just S_1 and S_2. Platt introduced a convenient nomenclature for cata-condensed hydrocarbons based on the free electron orbital method [5]. Cata-condensed hydrocarbons are described by the formula $C_{4n+2}H_{2n+4}$ and each carbon atom belongs to a maximum of two rings. Two examples, naphthalene and phenylanthracene, are shown in Figure 1.5. Based on postulate, that "the classification of π-orbitals in
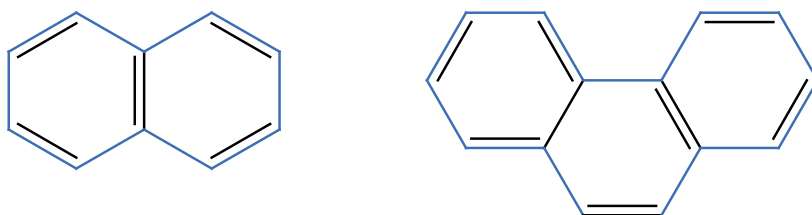

Figure 1.5: Naphthalene and phenylanthracene. The perimeter around which the electrons can move is drawn in blue.

cata-condensed systems [is] like that of the orbitals of a free electron traveling in a one-dimensional loop of constant potential around the perimeter", the energy of the electron is equal to a particle in a one-dimensional box [5].

$$E = \frac{q^2 \cdot h^2}{2m_e l^2} \tag{1.66}$$

The length of the box l is the perimeter of the hydrocarbon along which the electrons may travel and q is the *ring quantum number*. The energy level are quadratically spaced and doubly degenerate, except for the lowest orbital, as electrons with a finite velocity may travel clockwise and counter-clockwise along the perimeter l.

Each of the $4n+2$ C-atoms contributes one π electron. Hence, the highest occupied shell has the quantum number n and is designated as f. This is regardless of the actual value of n. The first unoccupied shell is g, the second occupied shell h, and so on. The *total ring quantum number* Q, which is the same as the total angular momentum, describes the actual states and is gained by adding and subtracting the quantum number q algebraically. States designed $A, B, C, \cdots$ correspond to $Q = 1, 2, 3, \cdots$. Higher values of Q like $2n, 2n+1$ and $2n+2$ are given the characters K, L and M. If an electron is excited from an $f(q = n)$ to an $g(q = n+1)$-shell, the resulting states are described as linear combinations: $Q = n \pm (n + 1)$. Thus two doubly degenerate $B(Q = 1)$ and $L(Q = 2n + 1)$ states result. Furthermore, both

Figure 1.6: Shells according to Platt [5]
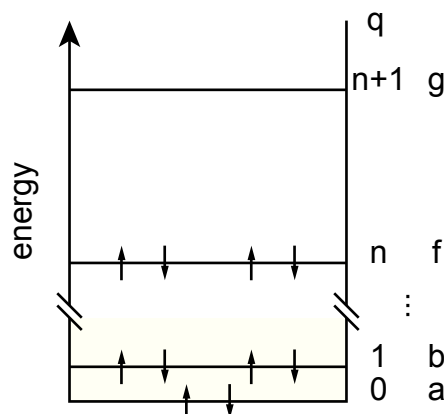
sets are present as singlet and as triplet states.

Except for highly symmetrical molecules like benzene, the degeneracy of the states is lifted. The resulting sublevels are denoted a and b, depending on the orientation of the nodal planes within the molecule. For the ^1L_a state, the nodal planes are situated in such a manner, that the electron density is located at the **a**toms, while the effective charges go to the **b**onds for the ^1L_b state. This is illustrated in Figure 1.7. According to the third of Hund's rules, the L states are energetically always lower than the B states.

Compared to naphthalene 2 CH groups are replaced by a NH group in indole. So if only the π-electrons are regarded, indole and naphthalene are isoelectronic (10 π electrons). This is the reason why this nomenclature was adapted to indole by Weber [17]. The different excited state properties of ^1L_a and ^1L_b are presented in the beginning of Chapter 6 on page 75.
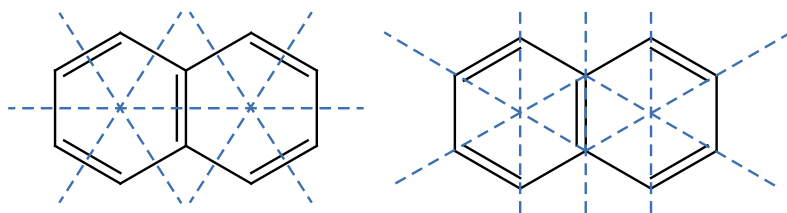

Figure 1.7: Nodal planes (blue dashed line) for the L_a (left) and L_b (right) of naphthalene.

2. Born-Oppenheimer, Franck-Condon and Beyond

The *Born-Oppenheimer* approximation is a fundamental concept for visualizing molecular quantum mechanical objects [46, 47]. It is based on the much smaller mass of the electrons compared to those of the atoms[1]. Hence, the electrons can adapt instantaneously to the movement of the nuclei in a molecule and their motions can be separated. The outcome are *potential energy surfaces* (PES), for each electronic state on which the nuclei move. The Born-Oppenheimer approximation is accurate for diatomic molecules in most cases as well as in polyatomic molecules in the electronic ground state [48]. Thus, the approximation was assumed to be generally applicable except for some very special cases. Modern experiments focusing on the excited states of polyatomic molecules, however, contradict this paradigma. In the spotlight of research most of all *conical intersections* (CI) and their influence on photophysics are regarded as a very interesting field of research [49–54]. Here, potential energy surfaces cross and constitute effective funnels for the energy towards lower PESs [55]. This is accompanied by a very fast change of geometry which essentially contradicts the Born-Oppenheimer approximation as now the movement of nuclei and electrons happens on a comparable time scale. In HRLIF experiments, events on a nanosecond timescale are the fastest phenomena which still allow a thorough interpretation. Thus, the time horizon is not capable to monitor events in a conical intersection which take place within several tens to hundreds of femtoseconds. Nevertheless our experiments can unambiguously trace back the influence of these funnels on the steady state spectra. Another important factor are vibronic couplings between electronic states. Depending on the energetic gap between the coupling states the Condon approximation and sometimes also the Born-Oppenheimer approximation may no longer be applicable. In the following

---

[1]The ratio of masses for an electron and a proton $m_e/m_p = 5.446\,170\,2178(22) \cdot 10^{-4}$. *2010 CODATA recommended values*: proton-electron mass ratio. National Institute of Standards and Technology. Retrieved 2012-01-01.

section first of all the Born-Oppenheimer approximation and the Condon principle are revisited before their violations detected in *high resolution laser induced fluorescence* (HRLIF) experiments are discussed. These range from small influences that can be tackled by perturbation theory to cases where the approximations break down completely. The following excerpts are mainly based on the works by Jensen [56], Cederbaum [48] and Yarkony [57].

2.1 The Born-Oppenheimer Approximation

We start with the non-relativistic total Hamiltonian $\widehat{\mathbf{H}}_{tot}$ in a space-fixed coordinate system. Our model system consists of n electrons i and N nuclei a with the appropriate mass M_a and nuclear charge Z_a. The distance between two particles is denoted as r or (R if it refers to nuclear coordinates exclusively). The nabla operator ∇ can act both on the electrons i and the nuclei a.

$$\widehat{\mathbf{H}}_{tot} = -\sum_{i=1}^{n} \frac{\hbar^2}{2m} \nabla_i^2 - \sum_{a=1}^{N} \frac{\hbar^2}{2M_a} \nabla_a^2 - \sum_{i=1}^{n} \sum_{a=1}^{N} \frac{Z_a e^2}{r_{ia}} \tag{2.1}$$
$$+ \sum_{i=1}^{n} \sum_{j>i}^{n} \frac{e^2}{r_{ij}} + \sum_{a=1}^{N} \sum_{b>a}^{N} \frac{Z_a Z_b e^2}{R_{ab}}$$

Keeping the order, equation 2.1 can be abbreviated as stated in the next equation. Here the kinetic energy operators are denoted as $\widehat{\mathbf{T}}$, the potential energy operator as $\widehat{\mathbf{V}}$.

$$\widehat{\mathbf{H}}_{tot} = \widehat{\mathbf{T}}_e + \widehat{\mathbf{T}}_n + \widehat{\mathbf{V}}_{en} + \widehat{\mathbf{V}}_{ee} + \widehat{\mathbf{V}}_{nn} \tag{2.2}$$

The next step involves transformation to a molecule-fixed coordinate system with its origin at the origin of mass of the nuclei $\mathbf{S}$ ($\widehat{=} \sum_a M_a \cdot \mathbf{R}_a = \mathbf{0}$). This introduces a new term to the total Hamiltonian called *mass polarization* $\widehat{\mathbf{H}}_{mp}$. Here M is the total mass of the molecule, taking both nuclei and electrons into account.

$$\widehat{\mathbf{H}}_{mp} = -\frac{\hbar^2}{2M} \sum_{i,j} \nabla_i \cdot \nabla_j \tag{2.3}$$

It arises as it is not possible to separate the center of mass movement rigorously from internal motion in a system containing more than two particles [56]. Freezing the nuclear geometry, which is equal to setting $\widehat{\mathbf{T}}_n$ to zero, leaves us with the the *electronic Hamiltonian* $\widehat{\mathbf{H}}_e$. This is an operator in electronic space that depends on

the nuclear geometry ($\mathbf{R}$) only parametrically through equation 2.5.

$$\widehat{\mathbf{H}}_e = \widehat{\mathbf{T}}_e + \widehat{\mathbf{V}}_{en} + \widehat{\mathbf{V}}_{ee} + \widehat{\mathbf{V}}_{nn} + \widehat{\mathbf{H}}_{mp} \qquad (2.4)$$

The orthonormal set of eigenfunctions $\phi_i(\mathbf{r}, \mathbf{R})$ to the electronic Hamiltonian forms a complete basis in the electronic space at every value of $\mathbf{R}$. In order to describe the overall system the wave function $\psi_{tot}(\mathbf{r}, \mathbf{R})$ is expanded in the electronic eigenfunctions of $\widehat{\mathbf{H}}_e$. Please note that the index i now refers to eigenfunctions of $\widehat{\mathbf{H}}_e$.

$$\psi_{tot}(\mathbf{r}, \mathbf{R}) = \sum_i^\infty \chi_i(\mathbf{R}) \phi_i(\mathbf{r}, \mathbf{R}) \qquad (2.5)$$

This expansion is known as the *adiabatic approximation* with the expansion coefficients being functions of the nuclear coordinates [47]. It is exact as long as the expansion is complete. Inserting the ansatz for $\psi_{tot}(\mathbf{r}, \mathbf{R})$ into the expression for the total Hamiltonian, multiplying from the left by $\langle \phi_j |$, and integrating over the electron coordinates results in [48] :

$$[\widehat{T}_n + V_j(\mathbf{R})]\chi_i(\mathbf{R}) - \sum_i \Lambda_{ji} \chi_i(\mathbf{R}) = E_{tot} \chi_j(\mathbf{R}) \qquad (2.6)$$

On the left hand side, the nuclear kinetic energy operator and the eigenvalue of $|\phi_j\rangle$ $V_j(\mathbf{R})$ can be seen. The latter constitutes the potential in which the nuclei move in the electronic state j. The matrix $\boldsymbol{\Lambda}$ contains terms that couple the different electronic states: the first and the second order *non-adiabatic coupling elements* (with regard to the power of ∇) as well as the mass polarization Hamiltonian.

$$\Lambda_{ji} = \frac{1}{2M} \left[2\langle \phi_j | \nabla_a | \phi_i \rangle (\nabla_a \chi_i) + \langle \phi_j | \nabla_a^2 | \phi_i \rangle + \langle \phi_j | \mathbf{H}_{mp} | \phi_i \rangle \right] \qquad (2.7)$$

If the mass polarization term is neglected, which is a good approximation for large polyatomic molecules, $\boldsymbol{\Lambda}$ depends on operators in the $\mathbf{R}$-space only. Defining the *non-adiabatic derivative couplings* $\mathbf{F}_{ji}$ as

$$\mathbf{F}_{ji}(\mathbf{R}) = \langle \phi_j | \nabla_a | \phi_i \rangle \qquad (2.8)$$

and the *scalar couplings* G_{ji} as

$$G_{ji}(\mathbf{R}) = \langle \phi_j | \nabla_a^2 | \phi_i \rangle \qquad (2.9)$$

the matrix elements Λ_{ji} can be phrased as

$$\Lambda_{ji} = \frac{1}{2M}[2\mathbf{F}_{ji} \cdot \nabla_a + G_{ji}] \tag{2.10}$$

The derivative couplings themselves are vectors in nuclear space. At this point we take a closer look at the *adiabatic approximation*. Here the total wave function is restricted to one electronic surface. In doing so all coupling elements between different electronic states are neglected and only terms with $j = i$ survive. If the wave function $\psi(\mathbf{r}, \mathbf{R})$ is real, the derivative coupling $\langle \phi_j | \nabla_a | \phi_j \rangle$ vanishes [48]. Thus, Λ_{jj} equals $1/2M \langle \phi_j | \nabla_a^2 | \phi_j \rangle$. If the wave function is chosen to be complex, $\mathbf{F}$ is not zero and thus plays a role in the so-called *complex adiabatic approximation*. Completely neglecting Λ_{jj} is called the *Born-Oppenheimer approximation* [56]. Furthermore, the degrees of freedom regarding the atoms can be described separately, which means that vibrational and rotational degrees of freedom can be treated independently.

2.2   The Franck-Condon Principle

Based on the Born-Oppenheimer approximation the Franck-Condon principle explains the intensities of vibrational lines in an electronic spectrum by introduction of an additional approximation [58, 59]. Starting with the transition probability W_{nm} the transition dipole moment vector $\hat{\vec{\mu}}$ (TDM) is expressed as a sum of the different contributions. The TDM operators for the nuclear (N) and electronic (e) parts for a molecule consisting of j electrons and i nuclei a with the nuclear charge Z_a are defined as:

$$\hat{\vec{\mu}}_N(\mathbf{R}) \quad = \sum_i e \cdot Z_a \mathbf{R}_i \tag{2.11}$$

$$\hat{\vec{\mu}}_e(\mathbf{r}, \mathbf{R}) = \sum_j e \cdot \mathbf{r}_j \tag{2.12}$$

$\mathbf{R}_i$ and $\mathbf{r}_j$ are the position vectors of the particles and e is the elementary charge.

$$
\begin{aligned}
W_{nm} &= \langle \chi'_m \phi'_m | \hat{\vec{\mu}}(\mathbf{r}, \mathbf{R}) | \chi''_n \phi''_n \rangle \\
&= \langle \chi'_m \phi'_m | \hat{\vec{\mu}}_e(\mathbf{r}, \mathbf{R}) + \hat{\vec{\mu}}_N(\mathbf{R}) | \chi''_n \phi''_n \rangle \\
&= \langle \chi'_m \phi'_m | \hat{\vec{\mu}}_e(\mathbf{r}, \mathbf{R}) | \chi''_n \phi''_n \rangle + \langle \chi'_m \phi'_m | \hat{\vec{\mu}}_N(\mathbf{R}) | \chi''_n \phi''_n \rangle \\
&= \underbrace{\langle \chi'_m | \chi''_n \rangle}_{FC\ Integral} \underbrace{\langle \phi'_m | \hat{\vec{\mu}}_e(\mathbf{r}, \mathbf{R_0}) | \phi''_n \rangle}_{Orbital\ Part} + \underbrace{\langle \phi'_m | \phi''_n \rangle}_{=0} \cdot \langle \chi'_m | \hat{\vec{\mu}}_N(\mathbf{R}) | \chi''_n \rangle
\end{aligned}
\tag{2.13}
$$

The third integral in the last line equals zero as both electronic wave functions $|\phi'_m\rangle$ and $|\phi''_n\rangle$ are eigenfunctions of the same Hamiltonian and thus orthonormal. The vibrational wave functions χ in the Franck-Condon (FC) integral on the other hand are eigenfunctions to different vibrational Hamiltonians (one for each electronic state). Therefore, the strength of an electronic transition is proportional to the overlap of the vibrational wave functions of the two states concerned. The last line introduces the approximation: the electronic integral does not depend on the displacements of the nuclei. So the value at the equilibrium position is taken as a constant known as the *Condon approximation*.

2.3   Vibronic Coupling

If the Condon approximation is violated, the electronic transition dipole moment depends on the instantaneous geometry of the molecule. This dependency can be approximated by expanding $\mu_{mn} = \langle \phi_m | \hat{\vec{\mu}}_e | \phi_n \rangle$ in a Taylor series about the equilibrium position at $\mathbf{R}_0$. The displacements are achieved by the $3N - 6$ normal coordinates Q_i of the molecule. Retaining only the first two terms of the expansion yields the following equation for the transition probability W_{nm} [60].

$$W_{nm} = \langle \chi'_m | \chi''_n \rangle \cdot \mu_{mn}(R_0) + \sum_i \left(\frac{\partial \mu_{mn}}{\partial Q_i} \right)_{R_0} \langle \chi'_m | Q_i | \chi''_n \rangle \tag{2.14}$$

The partial first derivatives in the sum are fully written out:

$$\left(\frac{\partial \mu_{mn}}{\partial Q_i} \right)_{R_0} = \left(\langle \frac{\partial \phi_m}{\partial Q_i} | \hat{\vec{\mu}}_e | \phi_n \rangle + \langle \phi_m | \frac{\partial \hat{\vec{\mu}}_e}{\partial Q_i} | \phi_n \rangle + \langle \phi_m | \hat{\vec{\mu}}_e | \frac{\partial \phi_n}{\partial Q_i} \rangle \right)_{R_0} \tag{2.15}$$

The partial derivative of the transition dipole moment vector is very small and hence set to zero. The derivatives regarding the wave functions can be treated using a perturbation theory ansatz [60]:

$$\left(\frac{\partial \phi_n}{\partial Q_i} \right)_{R_0} = \sum_{p \neq n} \left(\frac{\langle \phi_p | \partial \widehat{\mathbf{H}} / \partial Q_i | \phi_n \rangle}{E_p - E_n} \right)_{R_0} \phi_p \tag{2.16}$$

As the above equation illustrates, electronic states mix through vibronic interactions [60]. The size of this perturbing matrix element depends very much on the respective electronic states, so that a large denominator (the energetic difference of the two states) can be overcompensated, if the states couple extensively. This

coupling mechanism is called *Herzberg-Teller coupling* (*HT*). For the molecules with no symmetry (point group C_1) the Herzberg-Teller and the Franck-Condon part do not exclude each other as for higher symmetries like e.g. in the case of benzene [61]. So both FC and HT contribute to the intensity of a vibronic spectrum and the overall transition probability can be expressed by inserting equation 2.15 into equation 2.14:

$$W_{nm}^{HT} = \langle \chi_m' | \chi_n'' \rangle \cdot \mu_{mn}(R_0) + \sum_p \sum_i \left(\langle \phi_m | \hat{\vec{\mu}}_e | \phi_p \rangle \langle \phi_p | \frac{\partial}{\partial Q_i} | \phi_n \rangle \right. \tag{2.17}$$

$$\left. - \langle \phi_m | \frac{\partial}{\partial Q_i} | \phi_p \rangle \langle \phi_p | \hat{\vec{\mu}}_e | \phi_n \rangle \right)_{R_0} \langle \chi_m' | Q_i | \chi_n'' \rangle$$

This stealing of intensity additionally causes the perturbed state to gain orbital character of the perturbing state. In the Herzberg-Teller coupling scheme the Condon approximation is abandoned. If the perturbing states are very close, which means separated by not more than two quanta of a coupling mode, the Born-Oppenheimer approximation starts to fail as well and the adiabatic approximation has to be abandoned [60]. As a result a large number of vibrational modes of the perturbing state influence the perturbed state [62]. For a thorough treatment refer to [62], [63], and [60].

2.4 Conical Intersection

As all couplings are scaled by the inverse of the total mass M (cf. equation 2.10) it is tempting to assume it to play a minor role. At this point it is helpful to express the derivative couplings as follows for $i \neq j$:

$$\mathbf{F}_{ji}(\mathbf{R}) = \frac{\langle \phi_j(\mathbf{r}, \mathbf{R}) | (\nabla \mathbf{H}_e) | \phi_i(\mathbf{r}, \mathbf{R}) \rangle}{V_i(\mathbf{R}) - V_j(\mathbf{R})} \tag{2.18}$$

Excluding the numerator from discussion it is clear that the denominator becomes very small if the electronic surfaces i and j intersect one another. As pointed out by Yarkony these intersections leading to non-adiabatic processes are rather ubiquitous than seldom [64]. A conical intersection is defined by the linear lifting of the degeneracy when the molecule moves away from the intersection. The two-dimensional subspace in which this linear dependence can be observed is called the *branching space* [65]. Orthogonal to the branching space lies the *seam space* which connects conical intersections between two states. There are several types of conical intersections: they can be symmetry-required or accidently symmetry-allowed, and the following remarks concentrate on conical intersections of two electronic states with
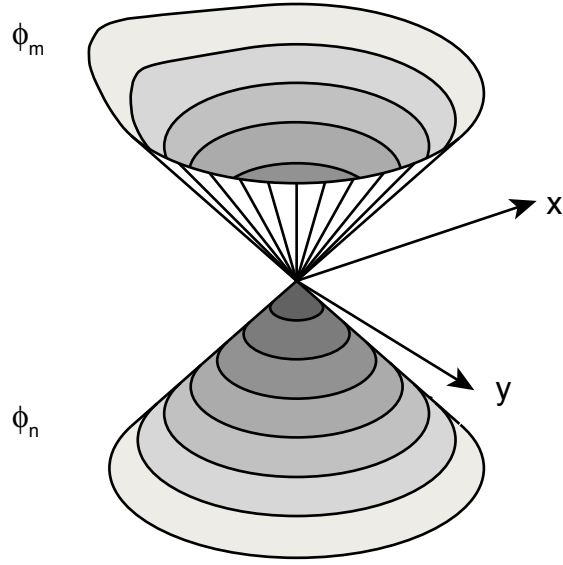
Figure 2.1: Conical intersection between to states ϕ_m and ϕ_n in the branching space spanned by the intersection adapted coordinates $\mathbf{x}$ and $\mathbf{y}$.

the same symmetry. For a more in-depth general treatment see [57].

A Hamiltonian $\widehat{\mathbf{W}}(\mathbf{R})$ for two coupling states can be written as [57]:

$$\widehat{\mathbf{W}}(\mathbf{R}) = \begin{pmatrix} \widehat{\mathbf{H}}^e_{1,1}(\mathbf{R}) & \widehat{\mathbf{H}}^e_{1,2}(\mathbf{R}) \\ \widehat{\mathbf{H}}^e_{2,1}(\mathbf{R}) & \widehat{\mathbf{H}}^e_{2,2}(\mathbf{R}) \end{pmatrix} \tag{2.19}$$

$$= \begin{pmatrix} \frac{\widehat{\mathbf{H}}^e_{1,1}(\mathbf{R})+\widehat{\mathbf{H}}^e_{2,2}(\mathbf{R})}{2} & 0 \\ 0 & \frac{\widehat{\mathbf{H}}^e_{1,1}(\mathbf{R})+\widehat{\mathbf{H}}^e_{2,2}(\mathbf{R})}{2} \end{pmatrix} + \begin{pmatrix} -D(\mathbf{R}) & W(\mathbf{R}) \\ W(\mathbf{R}) & D(\mathbf{R}) \end{pmatrix}$$

with $D(\mathbf{R}) = [-\widehat{\mathbf{H}}^e_{1,1}(\mathbf{R}) + \widehat{\mathbf{H}}^e_{2,2}(\mathbf{R})]/2$ and $W(\mathbf{R}) = \widehat{\mathbf{H}}^e_{1,2}(\mathbf{R})$. From the eigenvalues $V_\pm(\mathbf{R})$ of $\widehat{\mathbf{W}}(\mathbf{R})$

$$V_\pm(\mathbf{R}) = \frac{\widehat{\mathbf{H}}^e_{1,1}(\mathbf{R}) + \widehat{\mathbf{H}}^e_{2,2}(\mathbf{R})}{2} \pm \sqrt{D^2(\mathbf{R}) + W^2(\mathbf{R})} \tag{2.20}$$

it is apparent that both $D(\mathbf{R}_x)$ and $W(\mathbf{R}_x)$ have to be zero at the intersection $(\mathbf{R}_x)$ for the two states to have equal energy. For the intersection to be conical $\nabla D(\mathbf{R}_x) \equiv \mathbf{g}(\mathbf{R}_x)$ and $\nabla W(\mathbf{R}_x) \equiv \mathbf{h}(\mathbf{R}_x)$ have to be unequal zero. Based on these derivatives *intersection adapted coordinates* were introduced [66]: In this cartesian coordinate system $\mathbf{x}$ and $\mathbf{y}$ are unit vectors along the gradients $\mathbf{g}$ and $\mathbf{h}$.

$$\mathbf{x} = \frac{\mathbf{g}(\mathbf{R}_x)}{\|\mathbf{g}(\mathbf{R}_x)\|} \qquad \mathbf{y} = \frac{\mathbf{h}(\mathbf{R}_x)}{\|\mathbf{h}(\mathbf{R}_x)\|} \tag{2.21}$$

Only if displayed in these coordinates, a conical intersection forms a double cone as shown in Figure 2.1.

3. Experimental Setup

The rotationally resolved investigations of electronically excited states requires a special experimental setup. The exciting laser source has to generate tunable light in the UV regime with a line width lower than that of the rovibronic transitions. The requirements concerning the environment, in which the sample is present during the measuring process, demand as little perturbing interactions with other molecules as possible. These conditions can be achieved by using a frequency doubled continuous wave (cw) dye laser in combination with a molecular beam. In a molecular beam the sample is expanded, either neat or seeded in a carrier gas, through a small nozzle into high vacuum. Along with a separation of the molecules in the beam, collisions in the post nozzle region effectively cool the internal degrees of freedom, leading to rotational temperatures of a few tenths of a Kelvin up to 10 K. Therefore, the recorded density of lines is reduced significantely. This reduction opens the possibility of investigating even relatively large molecules as the rotational constants are proportional to the inverse of the mass of a molecule. The experimental setup is divided into two parts, presented in the following sections:

- the laser laboratory

- the molecular beam machine together with the data acquisition.

3.1   The Laser System

The present laser system consists of an Ar^+ laser pumping a ring dye laser system. The emitted light in the visible regime is coupled into an external doubling cavity for second harmonic generation. The resulting UV beam is guided to the molecular beam machine, where the experiment takes place. Determination of the absolute frequency is accomplished by comparison of a simultaneously recorded iodine absorption spectrum to tabulated lines [67]. Relative frequency shifts are eliminated

by linearization of the raw spectra with the help of a reference etalon spectrum with
known free spectral range.

3.1.1   The Optical Table

The laser apparatus is located on a table especially designed to meet the require-
ments of HRLIF spectroscopy. As stated before, the line width of the generated
UV radiation has to be as narrow as possible, to prevent additional broadening of
the rotational transitions. To ensure this, the laser system has to be isolated from
external perturbations as much as possible. One of the main tasks is to decou-
ple the laser from vibrations: these originate from the building itself, the vacuum
pumps and sound waves. To reduce the transmitted vibrations from the pumps,
the laser apparatus and the molecular beam machine are situated in adjacent rooms
and thus spatially separated. The remaining vibrations are damped by the *optical
table*. Several layers of materials shield the laser passively: The foundation of the
table consists of a block made of polystyrene foam plates. On top of it is a sand
bath, in which a 10 cm thick slab made of ferro-concrete is placed. To protect the
table from organic solvents, which may harm the polystyrene foam, the construction
is enveloped in 2 mm thick PVC foil. On top of this construction a 44 mm thick
multiple layer ply board is tightly fixed to the concrete slab. Around this table a
2.05 m high steel rack has been erected, equipped with a transparent acrylic glass
ceiling and PVC stripes hanging at the sides. Thus, the optical table is protected
from sound waves and dust. Additionally, a multi-stage air filter system constantly
removes dust particles down to a size of less than 1 μm from the ambient air before
flowing it in a laminar stream on the table.

3.1.2   The Pump Laser

During the course of the presented investigations a Millenia X Nd:YAG laser from
Spectra-Physics and in a later stage of the project a Coherent Innova Sabre argon
ion laser were used as optical laser pumps. Nd:YAG lasers are based on a yttrium
aluminium garnet (YAG) host lattice doped with triply ionized neodymium, serving
as the active laser medium [68]. On average 0.6 to 0.8% of the Y^{3+} ions are replaced
by Nd^{3+}. The main laser line generates radiation of 1064 nm. Frequency doubling
yields visible light of 532 nm at maximum output power of 10 W in the case of the
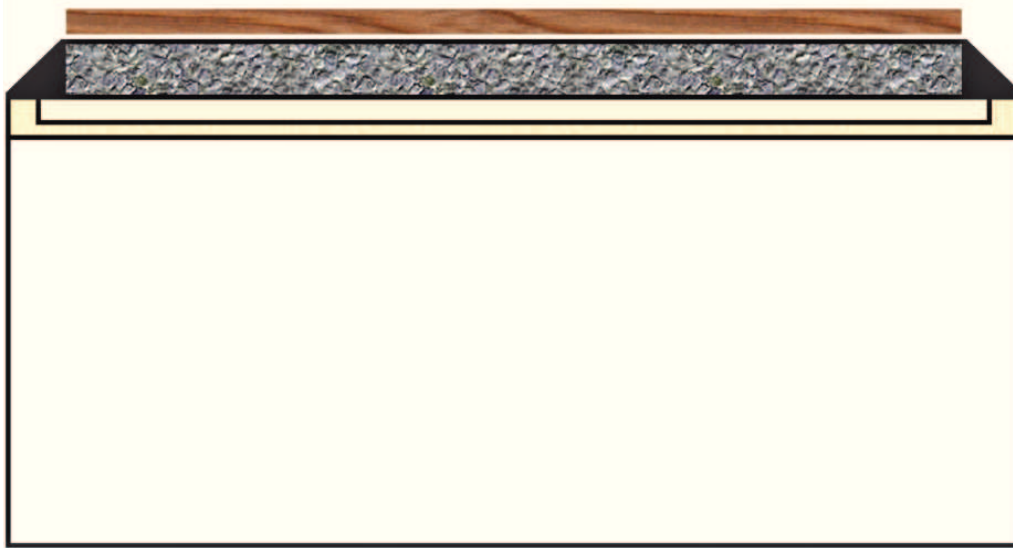
Figure 3.1: Schematic view of the different layers of the optical table.

present laser[1]. During the course of this thesis it was replaced by an argon ion laser. For this laser, the optical pumping process requires an electric discharge in the laser tube [69]: Argon is transfered to excited states of the ion Ar^+, leading to lasing on several lines extending from UV to IR. For our experiments the line at 514.5 nm was used excusively, matching the strong absorption band of both laser dyes used, Rhodamine 6G and Rhodamine 110.

3.1.3 The Ring Dye Laser System

Tuneability in the visible range is granted by dye lasers, using solutions of organic dyes as active medium. With appropriate optical components like filters and etalons, the line width of the emitted light can be reduced, but single longitudinal mode operation requires a special design of the cavity. In linear cavities, the spatial structure of a mode is determined by the length of the cavity and the wavelength of the selected mode. This results in areas of the active medium where population inversion is present, but cannot contribute to the mode as it has a node at this position. Another mode with a slightly different frequency may use this population inversion and starts to oscillate in the cavity itself, giving rise to severe instabilities of the emitted radiation. Ring lasers on the other hand allow the nodal structure of a mode to travel through the cavity, granting access to the whole extent of the dye jet, thus permitting single mode operation. A schematical overview of the Matisse
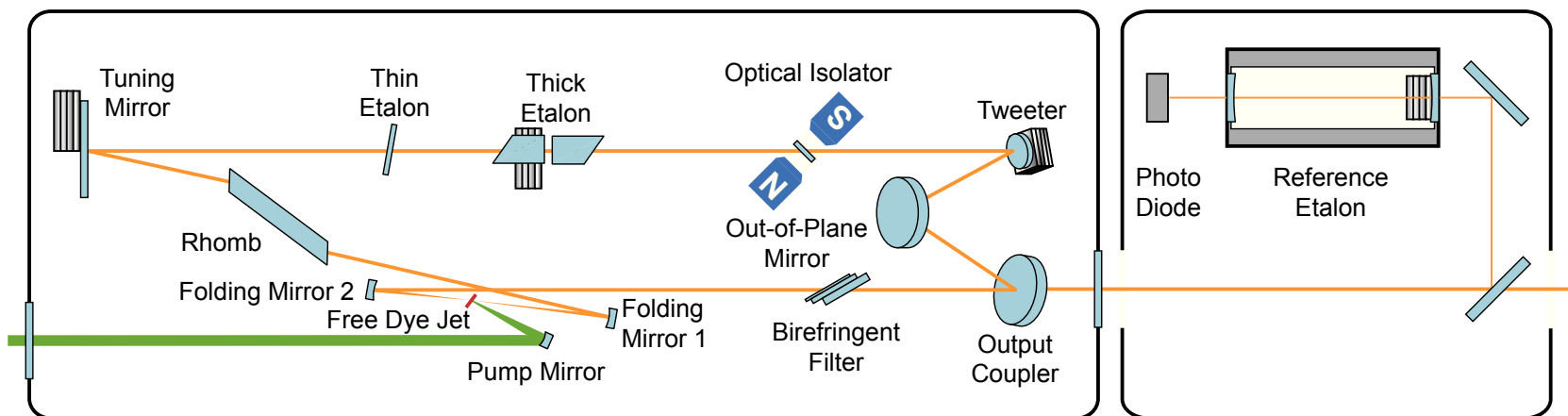
Figure 3.2: Schematic view overview on the Matisse DS dye laser [70]. The laser is excited by a continous wave pumplaser and the standing wave in the resonator propagates counterclockwise. A part of the light is coupled into an external reference etalon for mode-locking.

DS laser, used for the experiments, is given in Figure 3.2.

The drawback of ring lasers is the wave being able to travel in both directions: clockwise and counterclockwise. To ensure propagation in a single direction, an *optical isolator* has to be employed. The isolator of the Matisse includes a *Faraday rotator* as well as a mirror rotated by 13° out of plane of the remaining optics [70]. The Faraday rotator consists of a terbium gallium garnet plate exhibiting a high Verdet constant, exposed to a constant magnetic field. The polarization of the incoming laser light changes depending on its direction with respect to the applied magnetic field. In the desired direction its influence is compensated by the out-of-plane mirror to keep the favored plane of polarization. The polarization of the light running in the unwanted direction, which is clockwise, is tilted twice by the same amount and therefore experiences losses at all Brewster surfaces.

The monochromatic radiation of the pump laser excites the laser dye molecules to the vibrationally excited S_1 state. From here on collisions with solvent molecules deactivate the dye molecule within several ps to the vibrationless S_1 state. The majority of the molecules reaches the electronic ground state by a spontaneous or induced emission of a photon, the latter contributing to the laser process. A small fraction however passes over to the triplet state. Although this process is forbidden by spin selection rules, causing a much smaller transition probability than for fluorescence, the long excited state lifetimes of the triplet molecules lead to accumulation. In the end this leads to a quenching of the lasing process. To circumvent this problem, a rapidly flowing *free dye jet* is used. Applying up to 20 bars of pressure, the dye streams through a Sapphire nozzle and forms a laminar jet. The short interaction time between the laser field and the individual dye molecule thus prevents an accumulation in the triplet state. The dye pump reservoir contains about 4 litres in total, allowing molecules in the triplet state to reach the ground state before they are excited again. Collisions of the dye and the solvent within the jet lead to a homogeneous broadening of the emitted laser light. In Figure 3.3 the emitted wavelength range of rhodamine 6G in ethylene glycol is shown, spanning approximately 60 nm.

For the following discussion about the line width of laser beams, two terms are of importance and should be defined first: the *free spectral range* (FSR) and the *finesse* $\mathcal{F}$ [45]. During a scan the transmission spectra of all optical elements used in the dye laser repeat themselves periodically. The free spectral range is the range of frequency

---

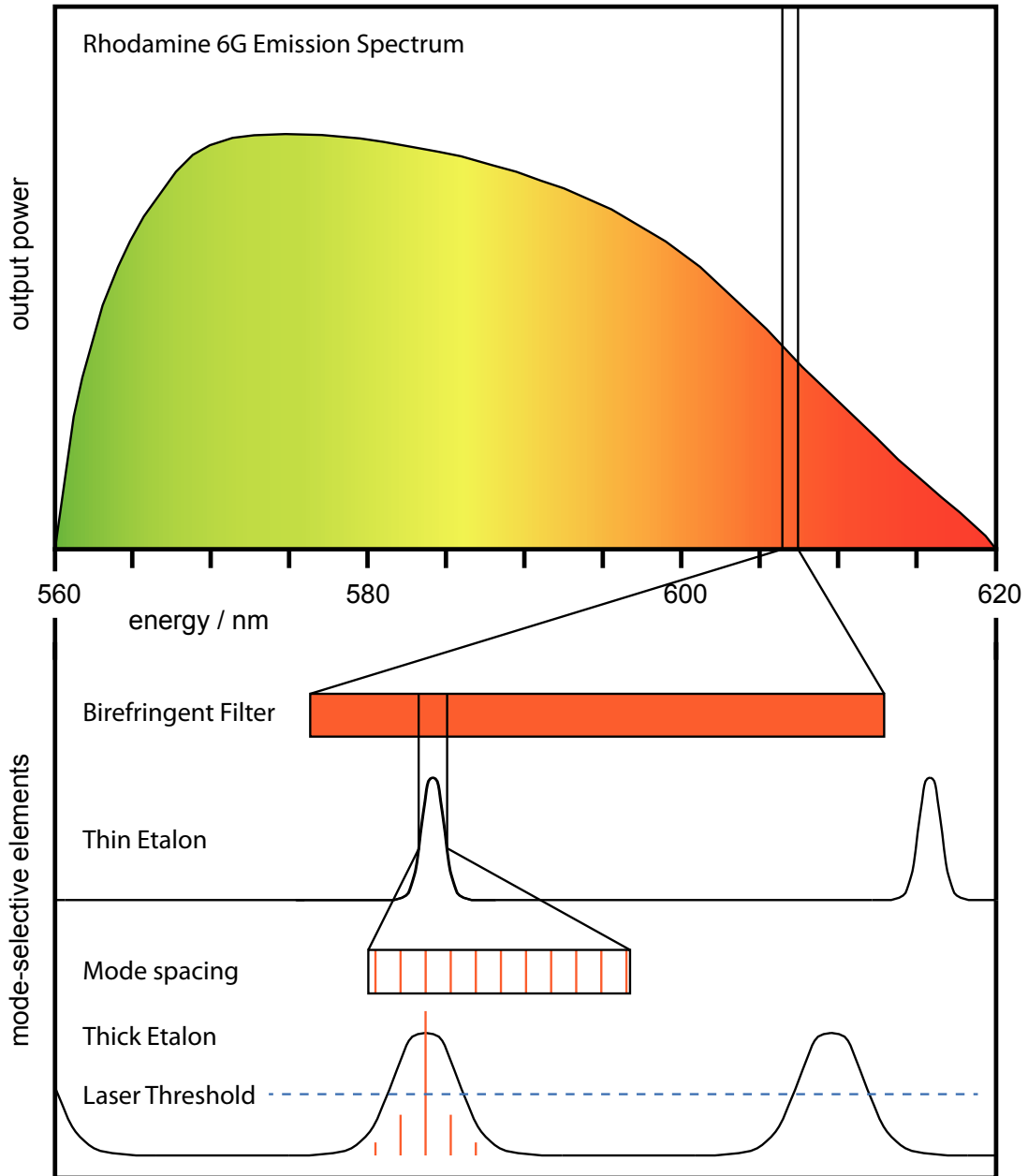[1]for details about frequency doubling refer to Section 3.1.5 on page 47

Figure 3.3: Laser dye emission curve of Rhodamine 6G in Ethylenglycol. In the lower traces the influence of the mode selective elements of the Sirah Matisse DS on the line width of the emitted laser light is shown [70]. For further details refer to the description given in the text.

$\delta\nu_{\text{FSR}}$ between the maxima of two consecutive transmission peaks. The finesse is connected with the free spectral range via the full width at the half maximum (FWHM) of the peaks (see Figure 3.4).

$$\mathcal{F} = \frac{\delta\nu_{\text{FSR}}}{\delta\nu_{\text{FWHM}}} \tag{3.1}$$

To select a single mode several optical elements are required. The Matisse uses three components of different finesse and free spectral range to reduce the emission to just one mode. These components will be presented in the next paragraphs. Additionally, their influence is visualized in Figure 3.3. A rough frequency preselection is obtained
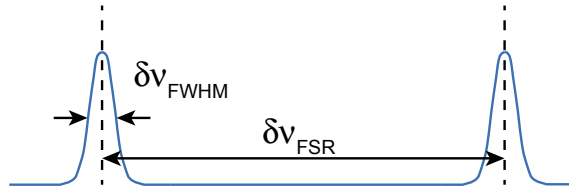

Figure 3.4: Frequency intervals determining the Finesse $\mathcal{F}$.

by a *birefringent filter*. It consists of a birefringent crystal situated between two polarizing filters. The irradiating light is polarized by the first filter and passes the crystal. Unless the polarization of the light is exactly parallel or perpendicular to the optical axis, it is influenced by two different refraction indices caused by the anisotropic polarisability of the crystal. This introduces a phase shift $\Delta\varphi$ depending on the wavelength λ, the optical pathlength through the crystal δ and its ordinary and extraordinary refraction indices (n_o and n_e) [71]:

$$\Delta\varphi = \frac{2\pi}{\lambda}\,\delta \cdot |n_o - n_e| \tag{3.2}$$

The transmission of the second polarizing filter is a function of the wavelength

$$T(\lambda) = T_0\,cos^2(\Delta\varphi) \tag{3.3}$$

with a free spectral range of $\delta\nu_{\text{FSR}} = c/(n_o - n_e)d$. Connecting n filters in series, each being twice as thick as the preceding, the resulting finesse is approximately 2^{n+1}. The birefringent filter used consists of three crystals, whose thickness ratios are 1:3:15, and narrows the frequency range in which lasing is possible to several hundred GHz [70]. Polarizing filters are not needed as all optical components in the resonator, except for the mirrors, are mounted in *Brewster angle*. Light of the

unfavoured polarization experiences large losses and hence is suppressed. The modes of the laser are 165 MHz apart, so further frequency confinement is indispensable. Two *etalons* with a free spectral range of 250 GHz and 20 GHz, respectively, are employed. An etalon consists of two parallel, highly reflective surfaces situated at a distance d [71]. The intensity of the transmitted light I_t is given by the *Airy-function*.

$$I_t = \frac{I_i}{1 + \mathrm{F} \cdot sin^2(\delta/2)} \tag{3.4}$$

I_t depends on the optical pathlength δ between the two surfaces, the intensity of the incoming light I_i and the reflectivity r of the surfaces, which are all summarized in the *coefficient of finesse F*, a term that should not to be confused with the finesse $\mathcal{F}$.

$$F = \left(\frac{2r}{1 - r^2} \right)^2 \tag{3.5}$$

To change the transmitted wavelength, the optical pathlength δ and hence d have to be altered. This is either done by adjusting the air-gap between two Littrow-prisms (thick etalon) or by tilting the angle of the etalon to the incident radiation (thin etalon). The resulting external linewidth is specified to lie below 20 MHz, broadened mainly by fluctuations in the cavity length. These are caused by vibrations, fluctuations in the dye jet and air turbulences. To stabilize the laser and reduce the internal linewidth to a maximum of 250 kHz, the laser is locked to a highly stable reference etalon. Disturbances inside the cavity are damped by the tweeter which is mounted on a fast acting piezo. To generate the appropriate error signal the laser monitors the spectrum of the reference etalon as every change in the laser wavelength corresponds to a variation in the transmitted intensity. Scanning of the laser is done by changing the optical path length of the cavity with the help of the tuning mirror which is mounted on a slow acting piezo. The maximum scan range spans around 40 GHz.

3.1.4   Determination of the Relative and Absolute Frequency

In rotationally resolved spectroscopy, geometrical data are derived from the analysis of line positions in a spectrum. Hence the validity of these data depends critically on the accuracy of the spectrum. As the velocity of the tuning mirror is not perfectly constant, recorded lines are shifted depending on the instantaneous velocity of the

mirror. To eliminate these shifts, part of the emitted light is coupled into a Fabry-Perot interferometer during the scan. Special attention was set on the design of this interferometer: Due to the very small thermal expansion coefficient $< 1 \cdot 10^{-7}$ K^{-1} the ceramic compound Zerodur$^{\circledR}$ was chosen to fix the distance between the the two mirrors. Multiple dielectric coatings on the concave inner surface of the mirrors with a resulting coefficient of reflectivity r above 0.995 lead to a theoretical finesse of more than 600. Slight misalignments of the incoming beam, however, result in an actually realized value of around 200. Sealed in vacuum, changes of the refraction index of the air due to temperature and/or moisture fluctuations become irrelevant. Highly accurate determination of the FSR was achieved by comparison to microwave data of indole: A HRLIF spectrum of the electronic origin was recorded and transitions assigned to quantum numbers. The difference between two transitions having the upper rotational state in common only depends on the ground state. These values are known from microwave experiments [72] and therefore the FSR could be precisely determined to be 149.9434(56) MHz. The recorded emission spectra is used to linearize the raw spectra by means of a cubic spline interpolating between adjacent maxima and thus yielding the desired spectrum.

The rough position of the laser is set with the birefringent filter of the dye laser. This, however, is by no means accurate enough. The determination of the absolute frequency requires the comparison to an external standard, like a reference etalon. In this setup a simultaneously recorded absorption spectrum of iodine is used. Kept at 1 mbar to avoid collisional broadening, the spectrum covers a range of more than 5000 cm^{-1}. Cross correlation of the recorded spectrum with a digitalized version of tabulated lines [67] grants an accuracy of 0.1 wavenumber for the absolute position of the spectrum.

3.1.5 Frequency Doubling

If the intensity of light interacting with matter becomes large enough, the optical properties of the medium start to depend on the irradiated light intensity [71]. This can be traced back on the inability of the outer electrons of the material to linearly follow the alternating $\mathbf{E}$-field of light, if its amplitude becomes too large. Therefore, the linear expression for the polarization $\mathbf{P} = \epsilon_0 \chi \mathbf{E}$ has to be extended to

$$P = \epsilon_0 \sum_{i=1}^{\infty} \chi_i E_i \tag{3.6}$$

with the vacuum permittivity ϵ_0 and the susceptibility χ, represented in a power series as well:

$$\chi = \chi_1 + \chi_2 E + \chi_3 E^2 + \dots \tag{3.7}$$

The susceptibilities of higher order terms ($i > 1$) are significantly smaller than χ_1. Hence, they can be neglected unless the field strength gets very large. To motivate second harmonic generation the series of **P** is truncated after the quadratic term and the alternating field $E = E_0 cos\omega t$ is introduced. Equation 3.6 becomes then

$$\begin{aligned} P &= \epsilon_0 \chi_1 E_0 \cos \omega t + \epsilon_0 \chi_2 E_0^2 \cos^2 \omega t \\ &= \epsilon_0 \chi_1 E_0 \cos \omega t + \frac{\epsilon_0 \chi_2 E_0^2}{2} \left(1 + \cos 2\omega t\right) \end{aligned} \tag{3.8}$$

The first part is the normal polarization, which is responsible for the propagation of the light with the initial frequency. The second line of equation 3.8 makes use of double angle identity for $cos^2\omega t$. As can be seen, a term depending on twice the frequency ω appears, representing *second harmonic generation*. Effective frequency conversion can only be obtained if destructive interference between the two waves (ω and 2ω) in the matter can be prevented. To ensure this, the refraction indices for the fundamental and frequency-doubled wave have to coincide.[2] If the fundamental beam propagates through a birefringent crystal as an ordinary beam, the second harmonic is generated as an extraordinary beam. Plotting the refraction indices of birefringent materials versus the angle between the optical axis and the polarization of the light, yields a sphere for the ordinary ray and an ellipsoid for the extraordinary one. To match the refraction indices the crystal is tilted to the angle at which the sphere and the ellipsoid intersect, called *phase matching angle*. Effective frequency conversion is done using crystals made of, for instance, β-barium borate (BBO) or potassium dihydrogen phosphate (KDP). The output power of the generated harmonic P_{harm} is proportional to the square of input power of the fundamental laser P_{fund} times the conversion coefficient c [73].

$$P_{harm} = c \cdot P_{fund}^2 \tag{3.9}$$

The coefficient depends on the characteristics of the laser beam and the crystal. Pulsed laser systems provide enough energy per shot for the wave mixing process to

---

[2]Another possibility is to reduce the crystal's thickness to the *coherence length*. The maximum thickness of such a crystal is around ten times the wavelength of the fundamental and hence impractical small compared to crystals used for phase matching, which can be well up to 10 mm thick [71].

be efficient. For continuous wave applications on the other hand, external doubling cavities locked to the wavelength of the fundamental are necessary to build up the required energy density. The doubling cavity used in the present setup is a delta concept cavity (WaveTrain, Spectra-Physics) [74]. It is based on a Delta-cavity, schematically shown in Figure 3.5. The incoming light is coupled into the
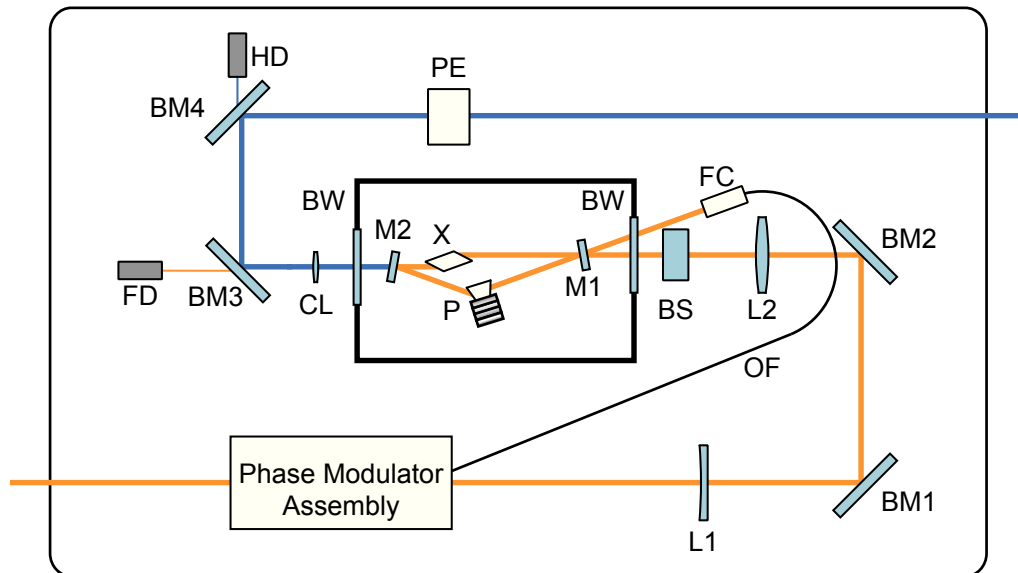

Figure 3.5: Schematic overview on the WaveTrain external frequency doubling unit by SpectraPhysics [74].

actual cavity via the two bending mirrors BM1 and BM2. To adjust the diameter and divergence of the fundamental, the beam passes two lenses (L1 and L2). Fine positioning is done with the help of the beam shifter (BS). Frequency conversion takes place in the cavity defined by the two mirrors M1 and M2, the nonlinear crystal X and the prism P. To minimize perturbations the cavity is housed in a sealable block with Brewster windows (BW) for the incoming and outgoing radiation. During a scan of the laser the optical length of this cavity has to be stabilized to the changing wavelength of the fundamental. This can be achieved by moving the prism mounted on a piezo-crystal. To generate the error signal for the piezo, the *Pound-Drewer* method is applied [75].

In the phase modulator assembly sidebands (± 80 MHz) are added to the spectrum of the incoming light. The modulation frequency of 80 MHz is chosen to guarantee complete reflection of the sidebands at M1 as those are well outside the resonator passband [74]. The reflected beam interferes with the light leaking from the cavity which is in antiphase to the reflected light. Thus, the cancellation of the two waves strongly depends on their respective frequency near the resonance [75]. The light is

coupled (fiber coupler, FC) into an optical fiber and guided to the phase modulator assembly. A subsequent comparison of the phase-dependent demodulation to the frequency-fixed position of the sidebands yields the desired antisymmetric frequency discriminator curve needed to lock the cavity.

The harmonic beam leaves the cavity through mirror M2 and is deflected by BM3 and BM4 to the output direction. The dichroitic coatings of those two bending mirrors prevent further propagation of the fundamental, leaking from the cavity. Two detectors monitor the power of the fundamental (FD) and the harmonic (HD). A cylindrical lens (CL) and two prisms (prism expander, PE) reduce the astigmatism of the UV light and assure a circular beam profile.

3.2 The Molecular Beam Apparatus

3.2.1 Fundamental Principles

Molecular beams create the environment of choice for HRLIF experiments: an isolated sample in the gas phase is prepared, intermolecular interactions are reduced to a minimum and low internal temperatures of several Kelvin are achieved. Proceedings from the *Rarefied Gas Dynamics* symposia, review articles and essay collections provide an excellent introduction to beam methods and their applications from which a summary will be presented hereafter [76–79].

Basically, the sample, either neat or seeded in a carrier gas, is expanded from a reservoir through a small orifice or nozzle into a region of lower pressure. What kind of expansion is formed depends on the pressure in the reservoir P_0, the backing pressure in the vacuum chamber P_b and γ, being the heat capacity ratio C_p/C_v [80]: If the ratio of P_0 and P_b is smaller than the critical value $G = ((\gamma + 1)/2)^{\gamma/(\gamma-1)}$, a *subsonic* expansion is present, which lacks the advantage of effective cooling. If on the other hand the value is met, the expansion will flow with sonic speed at the exit of the nozzle. In this case the *free path length* is much smaller than the diameter D of the nozzle and a large number of collisions result. These effectively cool the translational degrees of freedom in the mixture. Thus, a cold translational bath is created, cooling the internal degrees of freedom in the post nozzle region. How effectively a given vibration or rotation is cooled depends on how well its coupling to the bath; cooling is therefore driven more by kinetics than thermodynamics: The extent of excited state depopulation depends on the actual processes occurring during the collisions in the beam and is specific for a species under given conditions. Further-
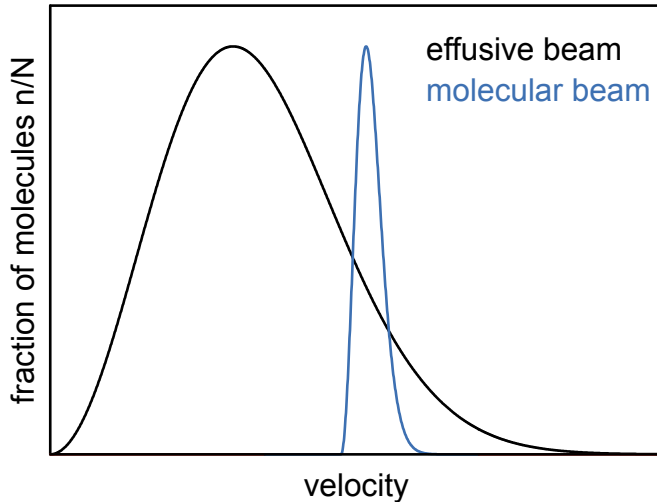
Figure 3.6: Comparison of the thermal distributions present in effusive and molecular beams. The latter is considerably narrowed and shifted by the stream velocity.

more, the temperatures parallel and perpendicular to the beam have to be described separately in the collisionless regime. As Edwards and Cheng pointed out, $T_\perp$ cannot be described by a simple gaussian distribution [81]: Collisions in streamwise direction cause a tail in the distribution. Adding up over two weighted gaussians is a better way to reproduce the experimental results. Analysis of the temperature in the beam incorporates therefore the two temperatures model formulated by Wu and Levy [82]:

$$n(T_1, T_2, w_T) = e^{-E/kT_1} + w_T e^{-E/kT_2} \tag{3.10}$$

Under beam conditions the velocity distribution is shifted to higher velocities and strongly narrowed, as can be seen in Figure 3.6. Instead of a Maxwell-Boltzmann distribution like present in an effusive beam, we observe a distribution based on the temperature in the beam $T_\parallel$ superimposed on the stream velocity v_s in this direction [83, 84].

A frequently used velocity distribution model treats the velocities which are parallel ($v_\parallel$) and perpendicular ($v_\perp$) to the stream, separately. Assuming ellipsoidal drifting it is formulated as [80]:

$$f(v) = n \cdot \left(\frac{m}{2\pi k T_\parallel}\right)^{\frac{1}{2}} \left(\frac{m}{2\pi k T_\perp}\right) \cdot exp\left\{ -\frac{m}{2kT_\parallel}(v_\parallel - v_s)^2 - \frac{m}{2kT_\perp}v_\perp^2\right\} \tag{3.11}$$

For an ideal gas the temperature T and pressure P in the isentropic expansion can

be connected to the local Mach number M [80].

$$\frac{T}{T_0} = \left(\frac{P}{P_0}\right)^{\frac{\gamma-1}{\gamma}} = \left(1 + \frac{\gamma-1}{2}M^2\right)^{-1} \tag{3.12}$$

T_0 is the temperature in the reservoir and M is the ratio of the stream velocity and the local speed of sound, which is given as $a = \sqrt{\gamma RT/m}$. If skimmers are used to collimate a supersonic expansion, it is called a *molecular beam*, if no skimmers are used, the term *free jet* is employed. As the molecules move away from the nozzle, the density of gas decreases and the further flow of energy to the bath is disrupted. A transition from a continuum flow to a free molecular flow ensues. In this collision-free region the molecule remains frozen in its non-equilibrated quantum state and can be examined without interactions to the coolant. For several reasons this scheme only work for supersonic expansions. One of them is that the pressure at the exit of the nozzle is equal to P_0/G and therefore in this case independent of P_b. The so-called *underexpanded* jet continues to expand, cools down and thus reaches higher Mach numbers.[3] The essential point is, that information about the backing pressure propagates with the speed of sound. Molecules in the beam do not sense P_b (they move in the *zone of silence*) until their velocity drops below $M = 1$ and shock surfaces are formed. Here the meanwhile overexpanded beam is compressed and entails large temperature and pressure gradients.

3.2.2 The Apparatus

In Figure 3.7 a cut view on the molecular beam apparatus is shown. The expansion takes place in the chamber on the left (1) and the molecular beam propagates to the right ($1 \rightarrow 5 \rightarrow 6$). Previous to the expansion the sample is located in the reservoir of the sample holder (2). To create a sufficient vapour pressure the device can be heated up to 220°C. The nozzle diameter itself can be varied between 80 and 500 μm in order to tune the composition of the samples in the beam: Smaller diameters imply a higher fraction of three- or four-body collisions in the nozzle which promote the formation of molecular clusters. Independently selectable heating resistors allow keeping the nozzle at a slightly higher temperature than the sample holder to prevent condensation inside the nozzle. The carrier gas argon is fed into the

---

[3]An increase in the Mach number does not mean that the stream velocity actually increases very much. As M is proportional to $1/\sqrt{T}$, a reduction of the temperature results in an increasing M, even if v_s stays constant.
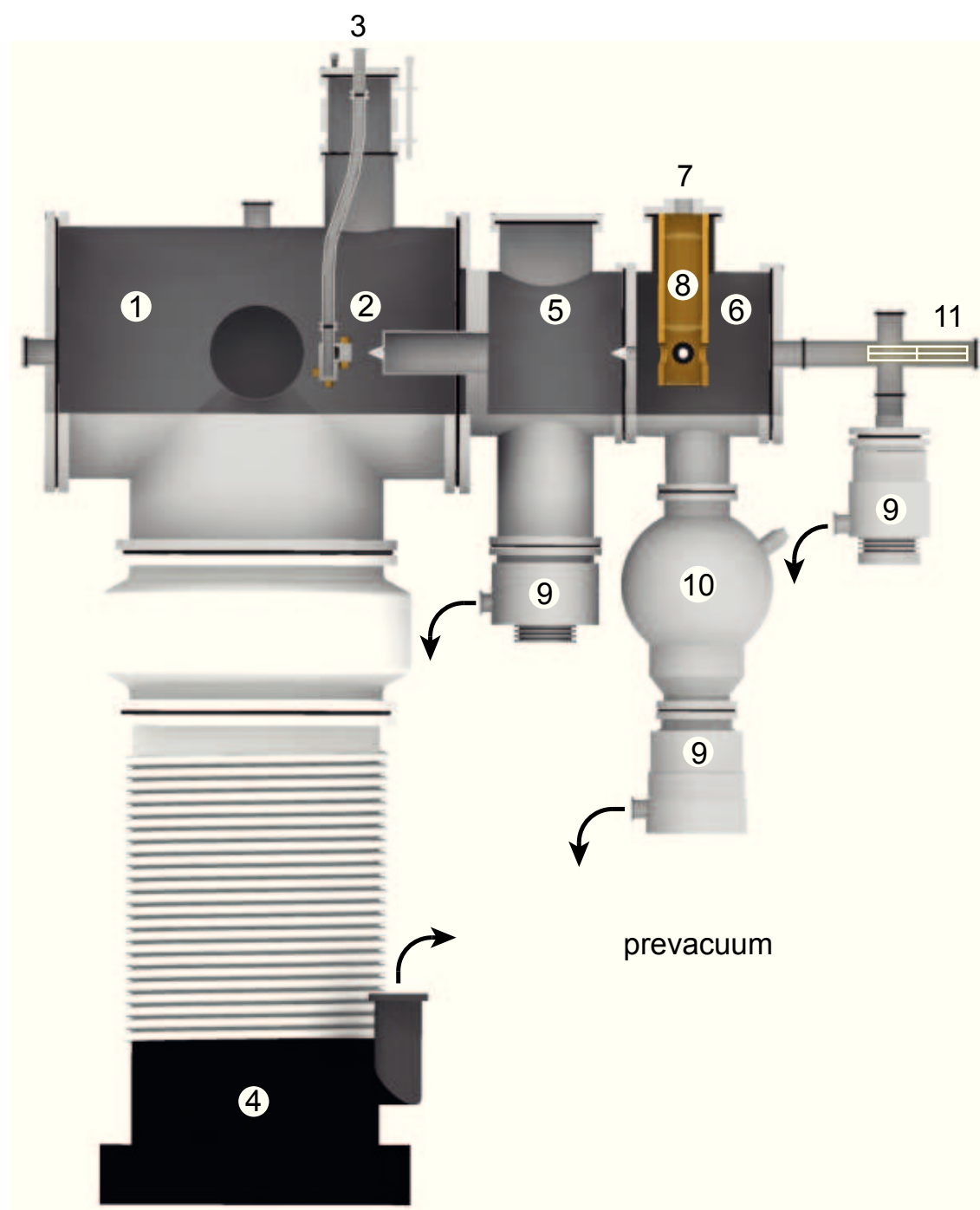
Figure 3.7: Cut view on the molecular beam apparatus: (1) expansion chamber, (2) sample holder and nozzle, (3) noble gas supply, (4) oil diffusion pump, (5) buffer chamber, (6) measurement chamber, (7) position of the photomultiplier, (8) imaging optics, (9) turbo molecular pumps, (10) baffle for liquid N_2 and (11) quadrupole mass spectrometer.

machine at position (3), connected with the sample holder via a flexible corrugated tube. Furthermore, this allows an insertion of the sample without the need to ventilate the whole machine. 20 mm behind the nozzle, the jet hits the first skimmer. A skimmer is a hollow cone with an orifice at the top. The edge is sharpened to prevent molecules from scattering back into the beam. Having a orifice of 1 mm, the vast majority of the gas ballast arises in this chamber. To maintain the required backing pressure, an oil diffusion pump with a pumping capacity of 8000 l/s is employed (4). The prevacuum of all high vacuum pumps is connected to avoid damaging of the skimmers while the apparatus is ventilated. Three roots blower pumps ($\approx$ 83.3 l/s each) maintain the prevacuum, each one preceded by one rotary pump ($\approx$ 18.1 l/s). During the experiment all pressures are constantly surveyed by a combination of different vacuum gauges. After passing the first skimmer the beam propagates through the buffer chamber (5) to the second skimmer, situated 150 mm behind the first one with an orifice of 3 mm. This combination of skimmers reduces the Doppler contribution arising from the velocity perpendicular to the beam to 18 MHz. The excitation of the sample and the detection of the fluorescence takes place in the third chamber (6). Here the UV-light crosses the molecular beam at a right angle. The actual position is depicted by the white dot. The emitted fluorescence light is collected and imaged onto a photomultiplier at position (7) by a combination of two lenses and a mirror situated in a nickelplated brass tube (8). For more details refer to the next paragraph and Figure 3.8. To ensure the generation of the molecular beam, there has to be a pressure gradient in its propagation direction. Three turbo molecular pumps (360 l/s) (9) and a baffle containing liquid nitrogen (10) reduce the pressure by one order of magnitude in each consecutive chamber. For an optimal alignment of the molecular beam the nozzle has to be centered in front of the first skimmer. This is done by means of two step motors (not shown in the figure) which shift the position parallel to the skimmer. To track the position the mass channel of Argon is monitored with a quadrupole mass spectrometer from Hiden Analytical (11).

The imaging optics consist of two lenses and a mirror (cf. Figure 3.8). One plano-convex lens and the spherical mirror (focal length 50 mm each) collect the emitted light and generate a parallel beam. Focused by a second plano-convex mirror ($f = 100$ mm) the light falls on the cathode of the photomultiplier and is registered. The amplified signal is converted by a photon counter card in the measurement computer. At the same time, the iodine absorption spectrum, the spectrum of the reference etalon and the UV power are recorded via an AD converter card. Data acquisition

and processing is done with the program KHiDaq by Marcel Böhm [85] and Jochen Küpper [86].
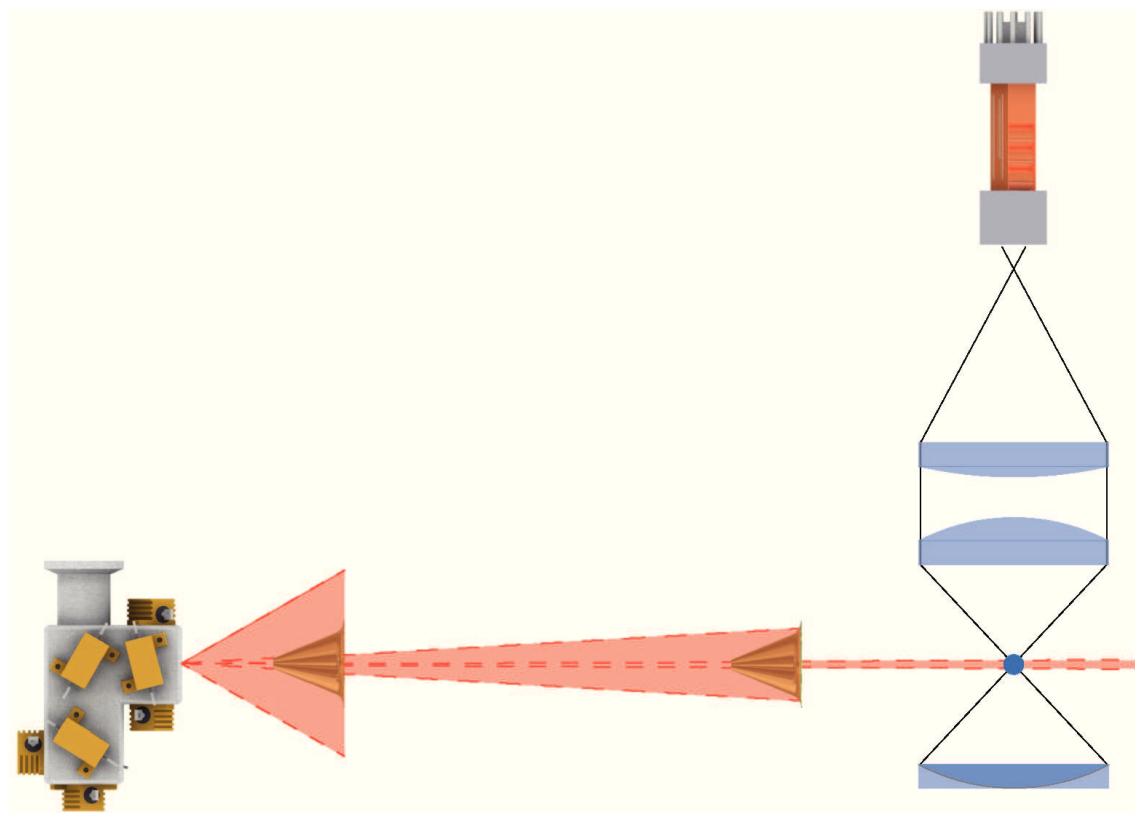

Figure 3.8: View on the molecular beam and the imaging optics. The doubly skimmed molecular beam (light red) is hit by the UV beam at a right angle (blue dot) and a part of the emitted fluorescence light is imaged onto a photomultiplier tube.

4. Interpretation of Rovibronic Spectra

The interpretation of rotationally resolved laser induced fluorescence spectra poses a challenge due to the high-dimensional nature of the optimization problem: even the simplest case of only one contributing component, which can be treated as a rigid rotor, requires 14 parameters to describe the spectrum as a whole.[1] These parameters are the rotational constants A, B and C for the electronic ground and excited state respectively, the orientation of the transition dipole moment vector $\vec{\mu}$ via the polar angles ϕ and θ, the relative origin ν referred to the arbitrary starting point of the spectrum, the rotational temperature of the sample molecule in the beam, described by two temperatures T_1 and T_2 and their weighting factor w_T and contributions of the Doppler and Lorentz profile to the broadened lines. The classical method to interpret a spectrum is to manually optimize the parameters in an iterative manner: starting from an initial set of values, quantum numbers and transitions are assigned to lines of the spectrum. Based on this assignment the initial values are refined, and successively more and more lines can be labeled until satisfying agreement between the experimental and theoretical spectrum is obtained. There are nevertheless some serious disadvantages of this procedure:

- The system is based on finding patterns in the spectrum by eye, so it depends strongly on the experience of the researcher.

- The initial set of values has to be as reliable as possible to make an assignment feasible.

- Every iteration of the parameter set has to be done by hand.

- There have to be single lines in a spectrum corresponding to only one transi-

---

[1]The following listing assumes the minimal set of parameter needed by the program *ga*, which is used in our work group. Using different temperature or line shape models for instance may alter the number of parameters.

tion, so that quantum numbers can be assigned.

Despite being a very time-consuming way of interpretation the first two items can be tackled with experience, precise quantum mechanical calculations and complementary experimental methods like microwave spectroscopy. The increasing density of lines in a spectrum however may render a classical interpretation impossible. To illustrate this fact, the spectra of the electronic origin of indole and the B conformer of melatonin are compared, the former being the smallest, the latter being the largest system investigated[2]. In the upper part of Figure 4.1 the overall fit of the electronic origin of indole is shown. The lower trace shows an enlarged view on a part of the P-branch. Although some transitions overlap, the majority of lines can be assigned to only one set of quantum numbers. If we move to larger systems, the moments of inertia get larger and consequently the rotational constants smaller[3]: Lines start to overlap more and isolated transitions become scarce. A striking example is given in the lower part of Figure 4.1. The upper trace shows the whole spectrum of melatonin B, taken from the best fit of an evolutionary strategy fit, which is described in detail later in this chapter. The simulated stick spectrum of the P-branch in the middle trace impressively illustrates the large density of lines in the spectrum: What seems to be a single line in the spectrum is revealed by the analysis to be a superposition of a few hundred lines [4]. The Q-branch in the lowest trace contains even several hundred lines. Without a doubt, spectra of this type overexert a classical analysis. A very elegant method to face this problem are *evolutinary algorithms*.

4.1   Evolutionary Algorithms

By publishing his famous discourse "*On the Origin of Species*" in 1859 Charles Darwin laid the foundation for the theory of evolution [88]. Natural processes like *selection*, *mutation* and *heredity* influence the development and distinction of species and lead to a better adaptation to the surrounding world. This could either be dominated by natural factors like the climate and available food sources or by artificial ones like a breeder´s wanting. Since the early 1960´s these principles of evolution were made use of in the field of optimization problems. Independently of each

---

[2]For the theoretical results concerning indole refer to Chapter 6, the experimental results were published by Küpper *et al.* [87]. The high resolution spectra of melatonin are discussed in Chapter 14

[3]cf. Chapter 1.1

[4]Only those transitions were taken into account whose intensity is at least 10% of the most intense transition in the band.
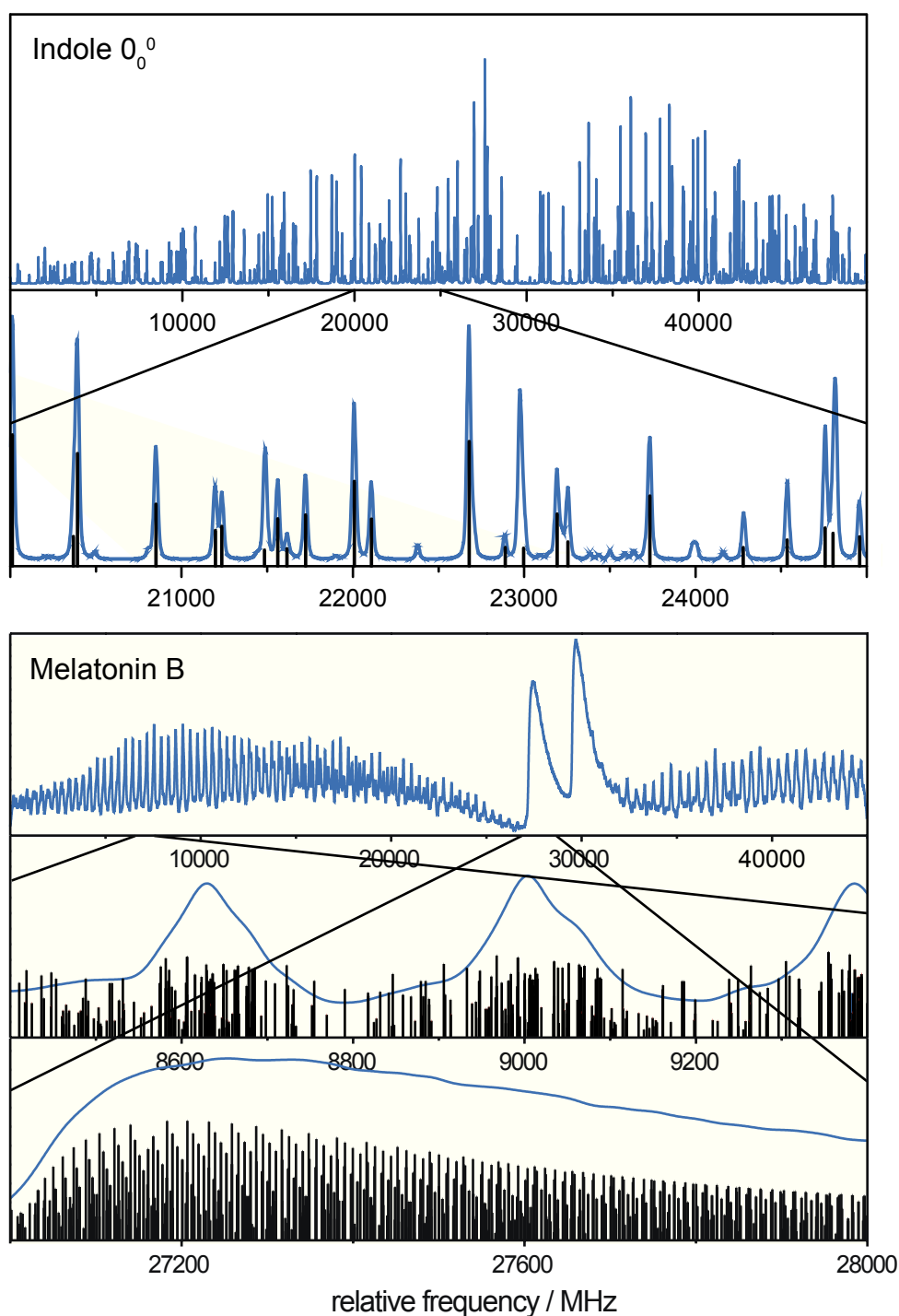
Figure 4.1: Best fit of the electronic origin of indole and the B conformer of melatonin. The lower traces show enlarged portions of the fit together with the appropriate stick spectra. Only those transition are displayed in the stick spectra, whose intensity is at least 10% of the most intense transition in the band.

other several approaches emerged, summarized by the generic term *evolutionary al-gorithms* [89]: *evolutionary programming* was developed in the group of Lawrence J. Fogel in San Diego [90, 91], *genetic algorithms* in Ann Arbor under the direction of John H. Holland [92, 93] and *evolutionary strategies* by Rechenberg and Schwefel at the TU Berlin [94, 95]. The latest method called *genetic programming* was presented in the early 1990´s by Koza [96, 97]. Several treatises offer insight into this interesting field and the different approaches [89, 98–103]. The books by Eiben and Smith [103], Weicker [100] and Pohlheim [102] give a comprehensive overview even on new developments of all evolutionary algorithms while Schöneburg, Heinzmann and Fedderson concentrate on the basics of genetic algorithms and evolutionary strategies including extensive references to biological evolution [98].

Implementation of evolutionary algorithms in the analysis of rotationally resolved laser induced fluorescence spectra was first presented by Hageman *et al.* in 2000 [104].[5] Ever since this ansatz is further being extended and developed in the groups of W. Leo Meerts in Nijmegen and Michael Schmitt in Düsseldorf [105, 106]. This adaptation made it possible for the first time to investigate large and complex systems, some of whom will be discussed in this thesis.[6] In the program package *ga* genetic algorithms (*GA*) and evolutionary strategies (*ES*) are implemented, both of them are discussed in detail in the next section.

4.2   Basic Principles

Both genetic algorithms and evolutionary strategies imitate processes of natural selection and adapt them to optimization problems. Referring to high resolution fluorescence spectroscopy the experimental spectrum plays the role the surroundings do in natural evolution: the individuals have to adapt to it to be successful. These individuals, also called *chromosomes*, are data strings containing all the relevant information of one possible solution. In genetic algorithms they are encoded as binary numbers while evolutionary strategies use real numbers. Every parameter, or *gene*, has a global range of values it can be varied within. Hence it is, in principle, no longer necessary to know the exact initial value of a given parameter although it accelerates the optimization routine. During the *initialization* a starting generation

---

[5]Another available program is for example *JetBeam95* by David Plusquellique: *http://www.nist.gov/pml/div682/grp01/jb95.cfm*.

[6]The complicity of a spectrum depends on a lot of parameters and cannot be reduced to size alone. Internal motion, overlapping spectral features from different conformers/isotopes and coupling to other electronic states are additional reasons despite the smaller spacing between rotational lines for increasing complicity.

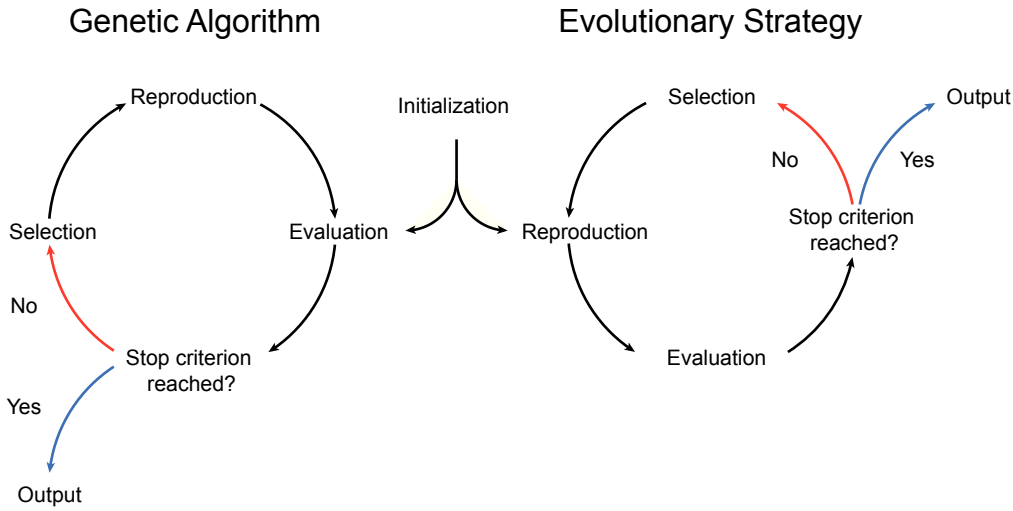$g = 0$ containing μ individuals is generated.

Figure 4.2: Basic optimization cycle of genetic algorithms and evolutionary strategies.

In the case of the genetic algorithms the Hamilton operator is solved for every individual and the obtained spectra are compared to the experimental one. Evaluation of the individuals is in general done in the program *ga* by the *fitness function F_{fg}*. It is defined as a weighted cross-correlation, normalized on the weighted autocorrelations of both the experimental f and fitted spectrum g.

$$F_{fg} = \frac{\sum_{i,j}^{N} f_i W_{ij} g_j}{\sqrt{\sum_{i,j}^{N} f_i W_{ij} f_j} \sqrt{\sum_{i,j}^{N} g_i W_{ij} g_j}} = \frac{(\mathbf{f}, \mathbf{g})}{\|\mathbf{f}\| \cdot \|\mathbf{g}\|} \tag{4.1}$$

The indices i and j include all N points of the spectra. The matrix elements W_{ij} belong to the weighting matrix $\mathbf{W}$, penalizing too large shifts of the spectra f and g with respect to each other, and hence accelerate the algorithm. Writing down the two spectra in vector notation $\mathbf{f} = (f_1, f_2, \cdots, f_N)^T$ and $\mathbf{g} = (g_1, g_2, \cdots, g_N)$ yields the last part of equation 4.1 using the definition of the inner product $(\mathbf{f}, \mathbf{g}) = \mathbf{f}^T \mathbf{W} \mathbf{g}$. Afterwards the individuals are ranked according to their fitness function. During the following creation of a new generation this value determines the probability of an individual to bequest its information (genes) to the next generation. This is done by *sexual recombination* of two members of the parent generation: genes are exchanged and thus the new generation created. There are several methods of crossover, some of them depicted in Figure 4.3. Cutting the data strings at N random positions and merging them together result in two offsprings and is called *N-point crossover*, while it is decided for each parameter separately to which offspring it is assigned in the
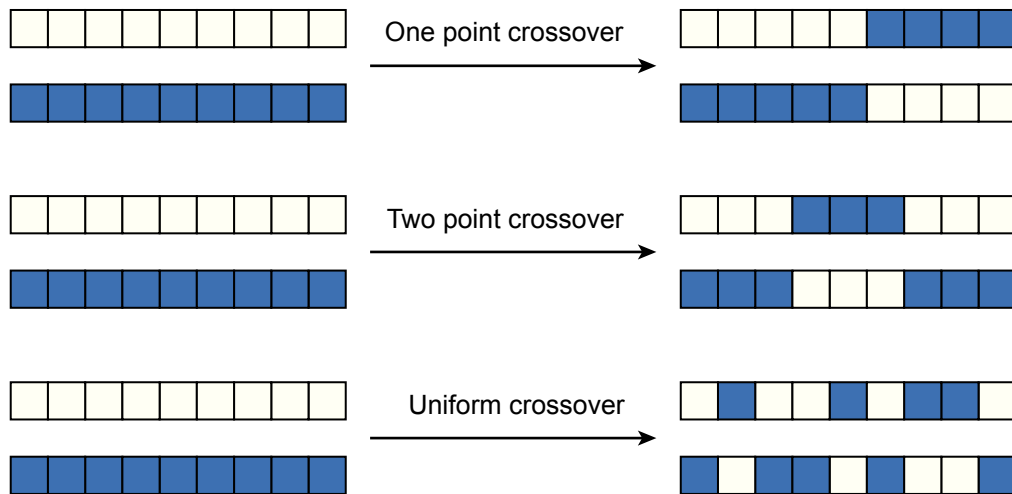
case of *uniform crossover.*

Figure 4.3: Methods of sexual recombination

As sexual recombination only recombines genes, the quantity of values for a parameter is restricted to the population number μ. To explore new areas of the hyper surface and circumvent premature convergence in local minima, a small numbers of *mutations* are carried out. These change the value of a parameter randomly within the global boundaries. The best solutions are often protected from mutations by *elitism.*

The principle setup of evolutionary strategies differs in several key points from genetic algorithms. One of them is the sequence of processes as shown in Figure 4.2: the evaluation of the individuals is preceded by the reproduction. The mechanisms for creation and selection vary from one strategy to the other: $(\mu + \lambda)$-ES create λ offsprings from μ parents, diversify them solely by mutations and finally select the μ best individuals from the pool of both groups. While an individual with sufficient good fitness function may survive forever according to this model, (μ, λ)-ES only consider the offsprings during the selection. Additional models include, for instance, sexual recombination, varying evolutionary pressure and parallel evolving subpopulations.

The analysis of all rotationally resolved spectra presented in this work was done using exclusively evolutionary strategies. The latest and most successful strategy is the *CMA-ES* by Hansen and Ostenmeier [107, 108]. This evolutionary strategy uses a covariance matrix to adapt the distribution of the individuals to the multi-dimensional search space (Covariance Matrix Adaptation). It was designed to work reliably even on rugged search landscape, exhibiting sharp ridges, noise and local

minima and tackle ill-conditioned and non-separable problems. The following section shines a light on the different mechanisms of the CMA-ES and is mainly based on "*The CMA Evolution Strategy: A Tutorial* " by Nikolaus Hansen [109].

4.3 The CMA Evolutionary Strategy

A n-dimensional normal distribution $\mathcal{N}(\mathbf{m}, \mathbf{C})$ of λ points is uniquely defined by its distribution mean $\mathbf{m}$ ($\mathbf{m} \in \mathbb{R}^n$) and its covariance matrix $\mathbf{C}$ ($\mathbf{C} \in \mathbb{R}^{n,n}$). The mean specifies the center of the distribution and is computed from the position vectors $\mathbf{x}$ of the individuals i in the search space ($\mathbf{m} = \sum_{i=1}^{\lambda} \mathbf{x}_i$); so it is analogue to the center of mass of a molecule. The covariance matrix describes the shape of the distribution. Diagonalizing $\mathbf{C}$ yields a hyper ellipsoid, which can be viewed as a surface of equal distribution density. The main axes of the ellipsoid correspond to the eigenvectors of the covariance matrix, its shape is governed by the eigenvalues. Regarding $\mathbf{C}$ as the inverse Hessian of a quadratic convex object function leads to a rescaling of the ellipsoid into a sphere [109]. As a spherical normal distribution has the largest possible entropy and thus can sample the search space most effectively [94], it is the goal of the covariance matrix to approximate the inverse Hessian [109]. Put another way, the covariance matrix tries to shape the distribution in such a way, that it perfectly follows the contour lines of the object function. An equivalent expression for the normal distribution would be

$$\mathcal{N}(\mathbf{m}, \mathbf{C}) \sim \mathbf{m} + \mathcal{N}(\mathbf{0}, \mathbf{C}) \tag{4.2}$$

Instead of expressing $\mathcal{N}$ in dependency of $\mathbf{m}$, the mean is added to a normal distribution with zero mean. Both parts of the equation have the same normal distribution as indicated by the symbol $\sim$. The actual step size of a population, meaning the size of the normal distribution´s ellipsoid is defined by the standard variance σ. Based on an evaluated generation g, the following expression is used to create the next generation.

$$\mathbf{x}_k^{(g+1)} \sim \mathbf{m}^{(g)} + \sigma(g)\mathcal{N}(\mathbf{0}, \mathbf{C}(g)) \qquad \forall \quad k = 1, \dots, \lambda \tag{4.3}$$

This requires the selection of the μ best solutions from λ individuals of the preceding generation g. Otherwise the new generation is only a reproduction of the foregoing one. How many individuals are chosen depends on the dimensionality of the problem and the size of the total population. On average a quarter of all individuals are

taken into account for computing the new generation. Based on the selection $\mathbf{m}$, $\mathbf{C}$ and σ are updated. Summarizing over the i best of λ solutions $\mathbf{x}_{i:\lambda}$ gives the new distribution mean $\mathbf{m}^{(g+1)}$. The weighting factor w_i favors solutions according to their fitness function: hence the best individuals have the greatest impact.

$$\mathbf{m}^{(g+1)} = \sum_{i=1}^{\mu} w_i \mathbf{x}_{i:\lambda}^{(g+1)} \tag{4.4}$$

Shifting the distribution mean moves the normal distribution $\mathcal{N}(\mathbf{m}, \mathbf{C})$ further in the direction of the hyper surface's minimum.

The covariance matrix $\mathbf{C}$ has to be estimated from scratch in the beginning of the optimization and is improved consecutively as generations move on. One possibility to guess $\mathbf{C}$ is shown in equation 4.5.

$$\mathbf{C}_{\lambda}^{(g+1)} = \frac{1}{\lambda} \sum_{i=1}^{\lambda} \left(\mathbf{x}_i^{(g+1)} - \mathbf{m}^{(g)} \right) \left(\mathbf{x}_i^{(g+1)} - \mathbf{m}^{(g)} \right)^T \tag{4.5}$$

Without selection mechanisms this equation yields the covariance matrix of the preceding generation g. Implementation of the weighting factors w_i leads to the next equation, depending only on the μ best solutions.

$$\mathbf{C}_{\mu}^{(g+1)} = \sum_{i=1}^{\mu} w_i \left(\mathbf{x}_{i:\lambda}^{(g+1)} - \mathbf{m}^{(g)} \right) \left(\mathbf{x}_{i:\lambda}^{(g+1)} - \mathbf{m}^{(g)} \right)^T \tag{4.6}$$

Equation 4.6 is only able to make a reliable guess of $\mathbf{C}$, if λ is large. The drawback is, that large populations slow the algorithm down significantly. To solve the problem, not only the last generation is regarded, but implicate all forgoing ones, whose influence decays exponentially. The learning rate c_μ ($0 < c_\mu \leq 1$) determines the influence of the so called *backward time horizon*. On the average it influences the generation of a new matrix by 63%.

$$\mathbf{C}^{(g+1)} = (1 - c_\mu)\mathbf{C}^g + c_\mu \frac{1}{\sigma^{(g)2}} \mathbf{C}_{\mu}^{(g+1)} \tag{4.7}$$

Introduction of $\mathbf{y}_i^{(g+1)} = (\mathbf{x}_i^{(g+1)} - \mathbf{m}^{(g)})/\sigma^{(g)}$ and examination of one coordinate i in equation 4.5 tells us something about the time evolution of $\mathbf{m}$ with respect to this coordinate: it can be viewed as consecutive steps along this coordinate. As $\mathbf{y}\mathbf{y}^T = -\mathbf{y}(-\mathbf{y})^T$ the sign of each step is irrelevant from the mathematical point of view. The evolutionary path $\mathbf{p}_C^{(g+1)}$ solves this problem by summing up over

successive steps and thus creating a dependency on earlier optimization steps.

$$\mathbf{p}_c^{(g+1)} = (1 - c_c)\mathbf{p}_c^{(g)} + \sqrt{c_c(2 - c_c)\mu_{\text{eff}}} \cdot \frac{\mathbf{m}^{(g+1)} - \mathbf{m}^{(g)}}{\sigma(g)} \tag{4.8}$$

c_c is the learning rate of the evolutionary path, $\sqrt{c_c(2 - c_c)\mu_{\text{eff}}}$ is a normalization constant and μ_{eff} defined as $(\sum_{i=1}^{\mu} w_i^2)^{-1}$. The final equation for computing the covariance matrix of the following generation $(g + 1)$ is composed of equation 4.7 and 4.8.

$$\begin{aligned} \mathbf{C}^{(g+1)} &= (1 - c_c - c_\mu)\mathbf{C}^{(g)} + c_c\mathbf{p}_c^{(g+1)}\mathbf{p}_c^{(g+1)T} \\ &+ c_\mu \sum_{i=1}^{\mu} w_i \, \mathbf{y}_{i:\lambda}^{(g+1)}(\mathbf{y}_{i:\lambda}^{(g+1)})^T \end{aligned} \tag{4.9}$$

The covariance matrix influences solely the shape of the ellipsoid and not its extension. The step size σ corresponding to the size of the ellipsoid is updated via an evolutionary path as well.

$$\mathbf{p}_\sigma^{(g+1)} = (1 - c_\sigma)\mathbf{p}_\sigma^{(g)} + \sqrt{c_\sigma(2 - c_\sigma)\mu_{\text{eff}}} \cdot \mathbf{C}^{(g)-\frac{1}{2}} \cdot \frac{\mathbf{m}^{(g+1)} - \mathbf{m}^{(g)}}{\sigma(g)} \tag{4.10}$$

Again $\sqrt{c_\sigma(2 - c_\sigma)\mu_{\text{eff}}}$ is a normalization factor and c_σ the respective learning factor. $\mathbf{C}^{(g)-\frac{1}{2}}$ is defined as $\mathbf{B}^{(g)}\mathbf{D}^{(g)-1}\mathbf{B}^{(g)T}$, with $\mathbf{B}^{(g)}$ being an orthonormal basis set of eigenvectors of $\mathbf{C}^{(g)}$, and $\mathbf{D}^{(g)}$ being a diagonal matrix composed of the squared eigenvalues of $\mathbf{C}$. Is the step size chosen optimally the selected individuals are distributed statistically within $\mathcal{N}$. Is this not the case as σ is, for instance, too large, selected solutions concentrate exceedingly near the distribution mean $\mathbf{m}$ and σ is consequently reduced in the next generation.

To illustrate the foregoing section Figure 4.4 depicts an optimization cycle of the algorithm. The task is to find the global minimum which is located in the upper right corner of the search space. The cycle starts in picture 1: Based on the geometrical mean $\mathbf{m}$, depicted in blue, and the covariance matrix $\mathbf{C}$, 35 individuals are created. In the next step these solutions are evaluated and the 15 best of them kept. Updating the shape of the covariance matrix changes the circle into an ellipsoid following the selected individuals. In the third step the size of the ellipsoid, meaning the step-size σ, is updated and finally the geometrical mean is moved in the direction of the estimated minimum. After this step the cycle starts again and the next generation is created, based now on the updated values of $\mathbf{m}^{(g+1)}$, $\mathbf{C}^{(g+1)}$ and $\sigma^{(g+1)}$.

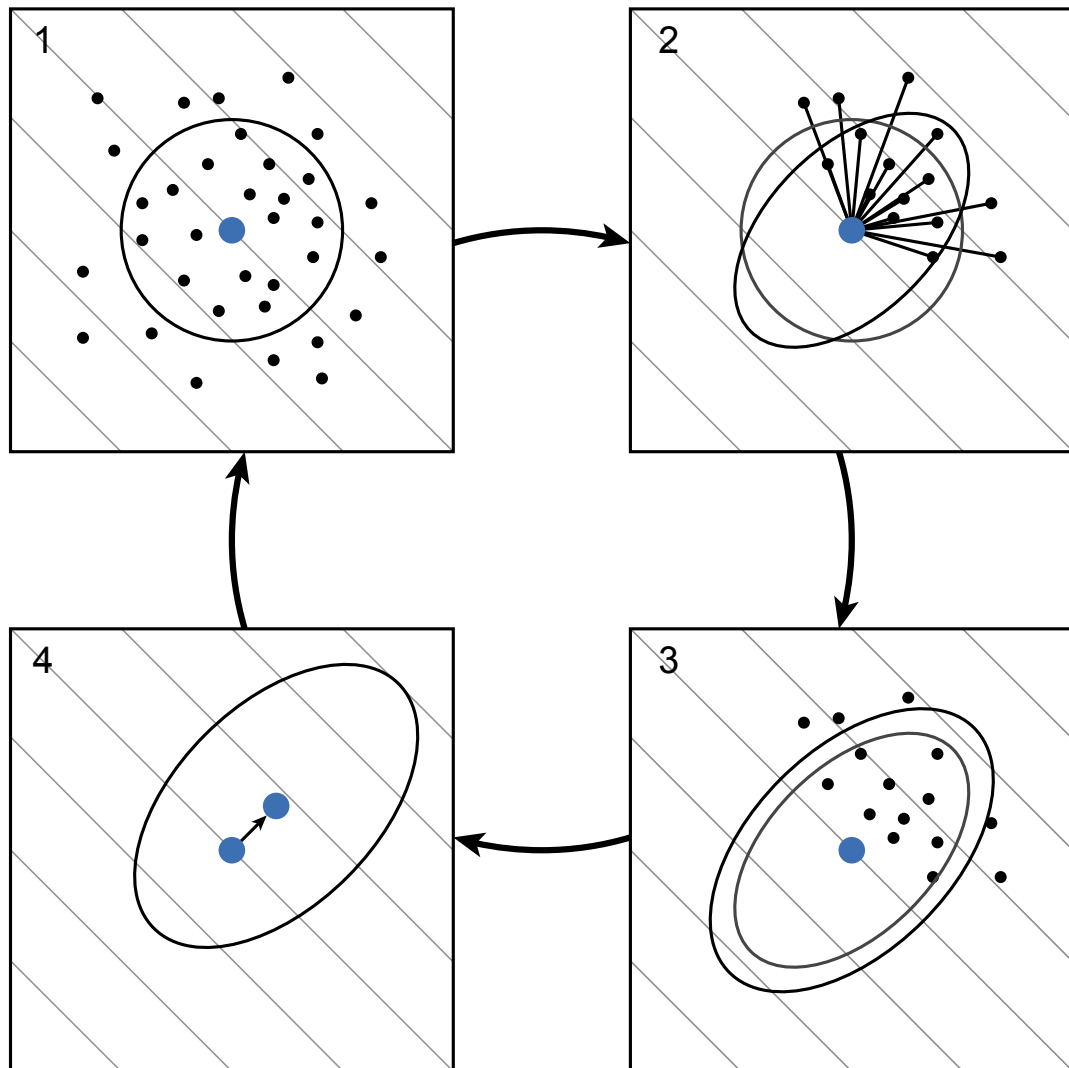Figure 4.4: Optimization cycle of the CMA-ES algorithm on a test surface with the minimum at the upper right corner of the search space [109]. The cycle starts in picture 1 and moves clockwise. After the first generation is created, a certain fraction is selected and consecutively the covariance matrix $\mathbf{C}$ (2), the step-size σ (3) and the geometrical mean $\mathbf{m}$ (4) are updated.

5. Quantum Chemical Calculations

Quantum-mechanical methods aiming for chemical accuracy must account for both dynamic and static correlation effects, i.e. the potential multi-configurational character of electronic states [110]. The distinction between static and dynamic is based on the instantaneous correlation between electrons [56]: Dynamic correlation effects occur between electrons that are spatially close, as they for instance occupy the same orbital. Static correlation on the other hand accounts for interactions between electrons that have less direct contact. The latter is important when the appropriate orbitals are energetically close (near-degeneracy effect).

The correlation methods mainly used in this work are an approximate Coupled Cluster Singles and Doubles method (CC2) [111] and a combination of Density Functional Theory and Multi-Reference Configuration Interaction (DFT/MRCI) [110]. While CC2 is used to optimize the structures of the substances in the various electronic states, excitation energies and electronic properties are calculated based on these structures with DFT/MRCI. The DFT/MRCI method by Grimme and Waletzke is especially designed to yield high accuracy for large systems with over 100 electrons at reasonable computational costs [110]. In the following, we take a look at the general mechanisms of both approaches. The presentation is meant to be rather descriptive than mathematically rigorous. We start, however, with the resolution of the identity, an approximation for 2-electron integrals which is implemented in both programs. Unless cited differently, the following descriptions are based on *Introduction to Computational Chemistry* by F. Jensen [56].

5.1   Resolution of the Identity

A bottleneck in basically all quantum mechanical calculations is the evaluation of four-index two electron integrals $(\alpha\beta|\gamma\delta)$, in particular for the operator $1/r_{12}$ of the interelectronic Coulomb repulsion [112, 113]. The number of such integrals scales

as N^4 with the size N of the basis set. Vahtras *et al.* developed a technique to overcome this bottleneck by introduction of an auxiliary basis set $\{P\}$ for the two electron integrals [113]. This approximation, called the *resolution of the identity*, expands pairs of orbitals $\alpha\beta$ in $\{P\}$:

$$(\alpha\beta|\gamma\delta) = \sum_{PQ} (\alpha\beta|P)V_{PQ}^{-1}(Q|\gamma\delta) \tag{5.1}$$

$(\alpha\beta|P)$ and $V_{PQ} = (P|Q)$ are three-index and two-index two electron integrals. Expressing the four index integrals in such a manner, it is no longer necessary to save them on disk. Thus the requirements are reduced by a factor of around N. Application of the resolution of the identity approximation extends the size of the systems, which can be described by correlation methods, significantly. Hättig and Weigend estimate that for CC2 the limit is pushed back by a factor of 2 to 3 [112].

5.2 Coupled Cluster Methods

The Coupled Cluster approach uses the excitation operator $\mathbf{T}$ to generate excited Slater determinants from a Hartree-Fock determinant. The impact of such an operator on the reference wave function ψ_0 is given in equation 5.2. Here the operator for single excitation $\mathbf{T}_1$ acts on the wave function for the ground state and generates all determinants in which one electron is excited from an occupied orbital i to a virtual orbital a. The respective expansion coefficients t are called *amplitudes* in coupled cluster.

$$\mathbf{T}_1|\psi_0\rangle = \sum_i^{occ} \sum_a^{vir} t_i^a |\psi_i^a\rangle \tag{5.2}$$

In principle, corrections from all possible excitations are considered to generate the coupled cluster wave function ψ_{CC}. Thus, the operator $\mathbf{T}$ is a sum over all excitation operators $\mathbf{T}_n$:

$$\mathbf{T} = \mathbf{T}_1 + \mathbf{T}_2 + \mathbf{T}_3 + \cdots + \mathbf{T}_{N_{\text{elec}}} \tag{5.3}$$

This operator does not act as such on $|\psi_0\rangle$ but as the argument of an exponential function $|\psi_{CC}\rangle = e^{\mathbf{T}}|\psi_0\rangle$, which in turn is expressed as a power series

$$e^{\mathbf{T}} = \mathbf{1} + \mathbf{T} + \frac{1}{2}\mathbf{T}^2 + \frac{1}{6}\mathbf{T}^3 + \cdots = \sum_{k=0}^{\infty} \frac{1}{k!}\mathbf{T}^k \tag{5.4}$$

A specific multiple excitation can be achieved not just by one operator, but by several terms arising in the series expansion. A triply excited state for instance can be generated directly by the operator $\mathbf{T}_3$ or by a combination of single and double excitations ($\mathbf{T}_1^3$ and $\mathbf{T}_1\mathbf{T}_2$). The term $\mathbf{T}_3$, called *connected*, corresponds to three electrons interacting with each other. In the other case, the excitations are *disconnected*: The electron affected by $\mathbf{T}_1$ is not influenced by the pair of electrons excited by $\mathbf{T}_2$, which only interact with each other.

The standard method to evaluate the energy of the coupled cluster wave function

$$\widehat{\mathbf{H}}|\psi_{CC}\rangle = E|\psi_0\rangle \tag{5.5}$$

is to project the Schrödinger equation onto the reference wave function $|\psi_0\rangle$. Therefore equation 5.5 is multiplied from the left by $\langle\psi_0|$ and integrated. As only one and two electron operators are present in the Schrödinger equation, all operators leading to a difference of the excitation level of three or more do not contribute:

$$
\begin{aligned}
E_{CC} &= \langle\psi_0|\widehat{\mathbf{H}}(\mathbf{1} + \mathbf{T}_1 + \mathbf{T}_2 + \frac{1}{2}\mathbf{T}_1^2)|\psi_0\rangle \\
&= \langle\psi_0|\widehat{\mathbf{H}}|\psi_0\rangle + \langle\psi_0|\widehat{\mathbf{H}}|\mathbf{T}_1\psi_0\rangle + \langle\psi_0|\widehat{\mathbf{H}}|\mathbf{T}_2\psi_0\rangle + \langle\psi_0|\widehat{\mathbf{H}}|\frac{1}{2}\mathbf{T}_1^2\psi_0\rangle
\end{aligned}
\tag{5.6}
$$

Projecting the Schrödinger equation on the excited determinants allows for a determination of the corresponding amplitudes. Another possibility is to use a similarity transformation of the Hamiltonian. The operator $e^{-\mathbf{T}}$ acts as a *deexcitation operator* on the bra wave function $\langle\psi|$. Hence, it generates all determinants having a lower excitation level than the reference wave function it acts on. Taking a triply excited wave function $\langle\psi_{mnl}^{efg}|$ as reference yields all singly and doubly excited wave functions as well as the ground state $\langle\psi_0|$. The effect on a singly excited reference is illustrated in the next equation.

$$
\begin{aligned}
0 &= \langle\psi_m^e|e^{-\mathbf{T}}\widehat{\mathbf{H}}e^{\mathbf{T}}|\psi_0\rangle \\
&= \langle\psi_m^e(1 - \mathbf{T}_1)|\widehat{\mathbf{H}}|(1 + \mathbf{T}_1 + (\mathbf{T}_2 + \frac{1}{2}\mathbf{T}_1^2) + (\mathbf{T}_3 + \mathbf{T}_2\mathbf{T}_1 + \frac{1}{6}\mathbf{T}_1^3))\psi_0\rangle
\end{aligned}
\tag{5.7}
$$

Solving the coupled set of equations resulting from 5.7 yields the amplitudes for singly, doubly and triply excited states.

The CC2 Approximation

Expanding equation 5.3 to the number of electrons n is exact but far to expensive
for large organic molecules. Truncation of the expansion yields approximate models
which are called depending on the operators they include: CCSD for instance in-
cludes only single and double excitations. What is very important at this point is,
that although all $\mathbf{T}_n$ with $n > 2$ are neglected, higher excitations can be expressed
via disconnected excitations.

$$e^{\mathbf{T}_1+\mathbf{T}_2} = \underbrace{1 + \mathbf{T}_1 + (\mathbf{T}_2 + \frac{1}{2}\mathbf{T}_1^2)}_{\text{connected and disconnected}} + \underbrace{(\mathbf{T}_2\mathbf{T}_1 + \frac{1}{6}\mathbf{T}_1^3)}_{\text{only disconnected}} + \cdots \qquad (5.8)$$

CC2 is a second-order approximate model based on CCSD [111]. The amplitudes
for double excitation are expressed by equations depending on the single excitation
amplitudes. In this way, the equations for the double excitation cluster amplitudes
are simplified. The resulting energy is expected by the authors to be of the same
quality as MP2, and the computational cost is reduced by a factor of N (number
of basis functions) compared to CCSD. Regarding the excited states, the CC2 re-
sponse function is meant for one-electron perturbations and expected to describe
two-electron perturbations not well [111]. Like CCSD, CC2 is a single-reference
method and hence bound to perform poorly, if the electronic state calculated has a
pronounced multi-configurational character.

We exclusively used CC2 in combination with the resolution of the identity RI-
CC2 [112] which was introduced in Section 5.1. The accuracy achieved provides
a thorough and comprehensible basis when rotationally resolved electronic spectra
are discussed regarding conformers or electronic states. This is shown for instance
for 5-fluoroindole in Chapter 9, where the largest deviation between experiment and
theory regarding the rotational constants lies around 0.1%.

5.3   Density Functional Theory/Multi Reference Con-figuration Interaction

The main motivation that led to a combination of density functional theory (DFT)
and configuration interaction (CI) is the need for a balanced treatment of all corre-
lation effects [110]. As stated before, both have to be considered if high accuracy
is demanded. There are several ways to tackle the problem, like *complete active*

space second order perturbation theory CASPT2 [114], *multireference coupled cluster* MR-CC [115] and *multireference configuration interaction* with single and double excitations MRCI or MRCI-(S)DCI [116]. The drawback is that these *ab initio* methods are computationally very expensive and therefore not applicable to large systems. DFT methods, however, are inexpensive and suitable for dynamic electron correlation. The idea behind DFT/MRCI is to combine DFT with the static correlation from a CI treatment. To account for a potential multi-configurational character of the wave function, a set of configurational state functions is used as a reference space. It can be chosen by the user and may be iteratively improved in subsequent calculations.

Density Functional Theory

The basic approach of *Density Functional Theory* is to express the energy of an atomic or molecular system solely as a functional of the electron density ρ_e. The existence of such a mathematical relation was proven by Hohenberg and Kohn [117] for the electronic ground state, but the correct functional connecting electron density and energy is yet unknown. An ansatz fundamental to many functionals was developed by Kohn and Sham, introducing orbitals to DFT [118]. One common goal of the DFT comunity is to develop improved functionals which match the exact one as much as possible. For an overview and a general introduction to the different approaches refer to the books by Parr and Yang [119] and Jensen [56] as well as the article by Nagy [120].

The program DFT/MRCI uses the BHLYP functional presented by Becke in 1992 [2]. This functional has a special focus on the exchange-correlation energy E_{XC}. The exchange energy E_X is descibed by an equal mixture of Hartree Fock and Becke exchange [121] while the functional by Lee Young and Parr is used for the correlation energy E_C [122]. This method is known as Becke "half-half".

$$
\begin{aligned}
E_{XC} &= E_X + E_C \\
&= \frac{1}{2} E_X^{\text{HF}} + \frac{1}{2} E_X^{\text{Becke}} + E_C^{\text{LYP}}
\end{aligned}
\tag{5.9}
$$

What we get is a determinant for the molecule in the electronic ground state. From this Kohn Sham determinant spin (ω) and space-adapted (w) *configurational states functions* (CSFs) are constructed. These constitute the basis functions for the following configuration interaction optimization.

Configuration Interaction

The *Configuration Interaction* (CI) optimization is based on the variational principle. In general the trial wave function is a linear combination of determinants or configurational state functions (CSF) for the different excitations. Configurational state functions for an excitation are linear combination of all excited Slater determinants leading to the same final occupation. This is illustrated in Figure 5.1.
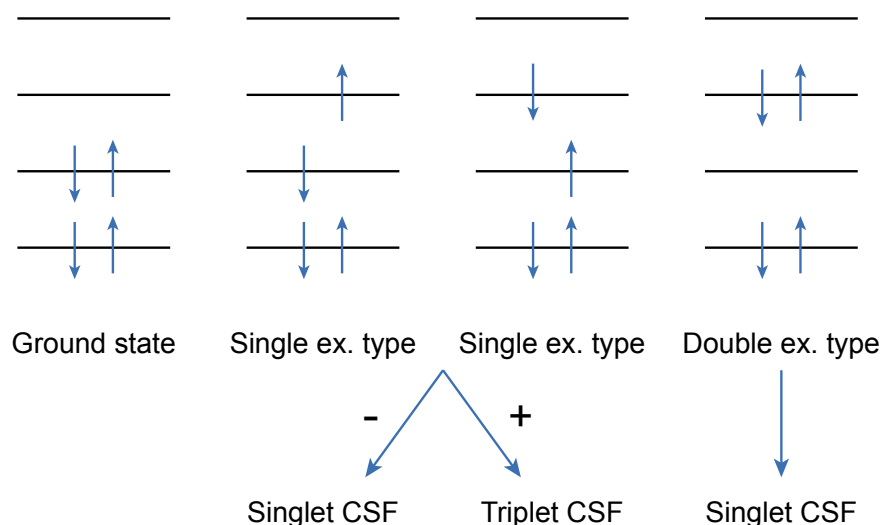

Figure 5.1: Construction of configurational state functions from excited state determinants. The antisymmetric and symmetric linear combination of the two single excitation determinants yields a singlet (-) and a triplet (+) CSF.

A single excitation from the highest occupied molecular orbital to the lowest unoccupied one can affect either the electron with α or with β spin. Hence is the appropriate CSF a linear combination of those two possibilities. The negative sign leads to a singlet, the positive to a triplet. So we get CSFs which can differ in the spin-part ω and/or the space-part w. In general the spin of all excited electrons has to be permuted to yield the needed CSFs. Thus the number of state functions may rise well to hundreds of millions if a large system is to be represented in a reliable base.

Determination of the expansion coefficients of the CSFs is done by demanding that the energy should be a minimum [123]. In principle CI may include all kinds of excitations to the reference space like single (S), double (D), triple (T) and so forth

$$\Psi_{CI} = a_0\Phi_{ground} + \sum_S a_S\Phi_S + \sum_D a_D\Phi_D + \sum_T a_T\Phi_T + \cdots = \sum_{i=0} a_i\Phi_i \quad (5.10)$$

Optimization of the wave function is done with the help of a *Lagrange multiplier L*.

$$L = \langle \Psi_{CI} | \widehat{\mathbf{H}} | \Psi_{CI} \rangle - \lambda(\langle \Psi_{CI} | \Psi_{CI} \rangle - 1) \tag{5.11}$$

The energy is at a minimum, if the derivative with respect to every coefficient a_i equals zero.

$$\frac{\partial L}{\partial a_i} = a_i(E_i - \lambda) + \sum_{j \neq 0} a_j \langle \Phi_i | \widehat{\mathbf{H}} | \Phi_j \rangle = 0 \tag{5.12}$$

The problem is to solve a set of secular equations, one for each coefficient a_i. In matrix notation this is equal to diagonalizing the CI matrix. The eigenvector to each state i gives the coefficients of the determinants or CSFs. The lowest eigenvalue is the ground state, the second lowest the first excited and so on.

$$\begin{pmatrix} H_{00} - E & H_{01} & H_{02} & \cdots & H_{0i} \\ H_{10} & H_{11} - E & H_{12} & \cdots & \vdots \\ H_{20} & H_{21} & H_{22} - E & \cdots & \vdots \\ \vdots & \vdots & \vdots & \ddots & \vdots \\ H_{i0} & \cdots & \cdots & \cdots & H_{ii} - E \end{pmatrix} \begin{pmatrix} a_1 \\ a_2 \\ a_3 \\ \vdots \\ a_i \end{pmatrix} = \begin{pmatrix} 0 \\ 0 \\ 0 \\ \vdots \\ 0 \end{pmatrix} \tag{5.13}$$

Taking a single determinant as reference in a CI procedure attributes a large impact to it. Especially electronically excited states may be described poorly by such an ansatz as they often have a pronounced multi-configurational character.

The DFT/MRCI Approach

To circumvent this problem an initial set of reference determinants is generated in DFT/MRCI before the actual CI starts. An active space, spanning e.g. the five highest occupied and the five lowest unoccupied orbitals based on the Kohn Sham determinant, is constructed and all single and double excitations are taken into account. This initial set and their coefficients are improved during the CI treatment to generate the final wave functions for the different electronic states.

The CI matrix is constructed from the respective CSFs. All elements with the same space-part are computed from the orbital energies of the parent determinant and scaled coulomb and exchange integrals. This is necessary as single DFT calculations, even exclusively for the diagonal elements, would be too expensive. To compensate

this approximation the empiric coefficients p_j and $p[N_0]$ are used. Hence $\widehat{\mathbf{H}}$ is an phenoneological Hamiltonian.

$$\widehat{\mathbf{H}} = \sum_c^{n_{\text{exc}}} F_{cc}^{KS} - \sum_a^{n_{\text{exc}}} F_{aa}^{KS} + \frac{1}{n_{\text{exc}}} \sum_a^{n_{\text{exc}}} \sum_c^{n_{\text{exc}}} p_j(aa|cc) - p[N_0](ac|ac) \tag{5.14}$$

Off-diagonal matrix elements between CSFs with different space-part are additionally scaled by $p_1 e^{-p_2 \Delta E_{ww'}^4}$. Again p_1 and p_2 are empirical coefficients and $E_{ww'}$ is the energy difference of two CSFs.

This additional scaling makes sure, that the dynamic correlation energy is not recovered again by the CI. Due to the damping factor only energetically close CSFs can interact strongly, which corresponds to static correlation. Reduction of the impractical amount of CSF as mentioned before is done by a simple selection procedure: Assuming that highly excited CSFs play a minor role for the computation of the lowest excited states, the *energy gap criterion* δE_{sel} was introduced [110]. Summing up the Kohn-Sham orbital energies of all orbitals that are different with respect to the parent configuration yields an energy difference which corresponds to the energy of the CSF. If this value exceeds a certain threshold, the CSF is discarded.

$$E_{\omega w} - E_{\omega' w'} \approx \sum_c^{n_{\text{exc}}} F_{cc}^{KS} - \sum_a^{n_{\text{exc}}} F_{aa}^{KS} \tag{5.15}$$

The subscripts a and c refer to the annihilation or creation of an electron in an orbital. The error introduced by this approximation is marginal as the matrix element between CSFs with different space part is scaled exponentially with the energy. The dramatic impact of this procedure on the number of configurational state functions to account for was shown for hexahelicene [110]. In this test example the number diminished from 1.2×10^9 to 600.000 with a threshold of 1.0 Hartree. This reduction of relevant CSF can only be done as the dynamic correlation is computed by DFT and only static correlation effects are to be recovered by the CI expansion.

6. Indole

Abstract

The properties of the three lowest singlet electronic states (ground, ^1L_b, and ^1L_a states) of indole (C_8H_7N) have been calculated with second-order approximate coupled-cluster theory (CC2) within the resolution-of-the-identity approximation. Refined electronic energies at the CC2 optimized structures and transition dipole moments were calculated using a density functional theory multi-reference configuration-interaction (DFT/MRCI) approach. Structures, energies, and dipole moments are reported for all three states and compared to experimental values. From the optimized structures and calculated transition dipole moments, we predict that pure ^1L_b bands will have positive signs for both the axis reorientation angle θ_T and the angle θ of the transition dipole moment with respect to the inertial a axis. For ^1L_a bands the signs of both angles will be reversed. Vibronically coupled bands can exhibit opposite signs for θ and θ_T. The absorption and emission spectra of indole are calculated based on the Franck-Condon Herzberg-Teller approximation using numerical transition dipole moment derivatives at the DFT/MRCI level of theory. Implications for the experimentally observed vibronic spectra are discussed. Predictions are made for rotationally resolved spectra of various rovibronic bands. A conical intersection, connecting the ^1L_b and ^1L_a states, which can be accessed to varying extents via different Herzberg-Teller active modes is found approximately 2000 cm^{-1} above the ^1L_b minimum.

6.1 Introduction

As pointed out in the preface the photophysics of tryptophan are governed by its chromophore. Hence a deeper understanding of indole and its photophysics is of great importance. Indole itself consists of a pyrrole and a benzene moiety, sharing the bond between carbon atoms 8 and 9. From the pure rotational spectra, presented by Suenram *et al.* [72], and Caminati and di Bernando [124], the geometry was determined to be planar in the electronic ground state. Upon excitation to the first electronically excited state the plane of symmetry remains [125]. Hence, indole belongs to the point group C_s, exhibiting two irreducable representations: A' and A''.
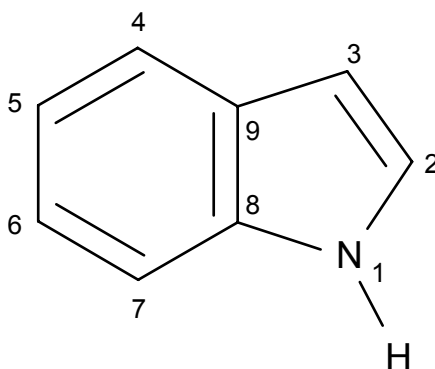

Figure 6.1: Atomic numbering in indole

The first detailed vibrational analysis was presented by Lautié *et al.* [126]. The authors measured Raman and IR spectra of indole and several deuterated isotopologues both in the crystalline and liquid phase. Several experimental and theoretical [127–132] publications followed, but the main focus of attention was set on the electronically excited states and their properties.

Indole exhibits two near degenerate electronically excited singlet states called the ^1L_a and the ^1L_b [5].[1] From early studies it was apparent that the ^1L_b state is lowest in energy in the gas phase and in an apolar surrounding, while perturbations induced by a polar surrounding tend to reverse the energetic ordering [9]. Emission spectra in solution originating from the ^1L_b state exhibit vibrational structure while emission from the ^1L_a is rather broad and lacks distinct features. In order to make full use of this surrounding-dependency for spectroscopic investigations, several questions have to be answered: How large is the onset of the ^1L_a state with respect to the ^1L_b in the unperturbed system? To which extend are both states affected by interactions

---

[1]For a brief explanation of this nomenclature refer to Section 1.6 on page 28.

with solvents, for instance? Do these states couple with each other, and what are the spectroscopical consequences? As we will see in the following paragraphs, over the last decades a large number of studies was performed to answer these questions.

But before we turn to the problem of ^1L_a–^1L_b interaction we will take a look at another subject connected with excited states, that has got a lot of attention lately: effective internal conversion attributable to the influence of a repulsive $^1\pi\sigma^*$ state. From the non-radiative decay rates in the vapor and the vacuum Glasser and Lami deduced the fact that NH-fisson provides a fast non-radiative deactivation pathway for the ^1L_a state in the gas-phase [133]. Sobolewski and Domke found an effective funnel for radiationless transitions from the excited states to the ground state via in-plane NH bond breakage as well, as shown in their extensive *ab initio* investigation of the lowest four singlet states [53]. Later Sobolewski *et al.* reported that the lowest $^1\pi\sigma^*$ state is repulsive in respect of the NH stretching coordinate [134]. From the fact that this state intersects both the ^1L_a and ^1L_b as well as the ground state they concluded an ultrafast internal conversion to the electronic ground state. The mechanism is driven by predissociation in the $^1\pi\pi^*$ state and a conical intersection to the S_0. Dedonder-Lardeux *et al.* [135] contributed the impact of solvation onto the energies of those states. Ground and excited state fluorescence dip infrared spectroscopy (FDIR and FDIRS) on several indole derivatives and their clusters were performed by Dian *et al.* [136]. They found evidences for the $^1\pi\sigma^*$ state in the spectra of the NH stretch vibrations. In some large derivatives (for instance N-acetyl tryptophan amide) the repulsive state is the energetically lowest singlet state, while staying high in energy for indole and being too far away to be reached by IR excitation. Therefore, the two states of importance in apolar surroundings and in the gas phase for in indole are the ^1L_a and the ^1L_b.

As both states belong to the same irreducable representation (A'), they have to be distinguished by their excited state properties. From the absorption spectra of crystalline indole Yamamoto and Tanaka computed the oscillator strength to be 0.024(10) for the ^1L_b and 0.133(112) for the ^1L_a state [137]. In the same publication they stated, the transition dipole moment vectors (TDM) for both states to be situated within the plane of symmetry, to be nearly perpendicular to each other and to form an angle of $\theta = 54°$ (^1L_b) and $-38°$ (^1L_a) with the a-axis, according to the definition of angles in Figure 6.2. In the course of time further knowledge has been gained on the orientation of the TDM. There have been investigations in a stretched polyetylene host [138] and, with increasing rotational resolution, in the vapor [139] and in supersonic jets [87, 125, 140]. Berden *et al.* determined θ to be 38.3(2)° using

an experimental setup similar to the one employed in this thesis [125]. A result, that was confirmed by our group [87]. The permanent electric dipole moments of indole in its ground and electronically excited state were measured by Kang *et al.* [141].

The energetic gap between the ^1L_a and the ^1L_b state can be altered, and the ordering can even be reversed by the influence of polar groups or molecules in the vicinity of indole. This is mainly due to the different excited state dipole moments: Excitation to the ^1L_b state increases the permanent dipole moment only slightly from 2.09 D [124] to 2.3 D [142]. The excited state dipole moment of the ^1L_a state on the other hand was stated to be 5.44 D, corresponding to an increase by a factor of around 2.6 [12]. Therefore, the ^1L_a state is favoured by dipole-dipole interactions and as a consequence shifted more strongly than the ^1L_b state by polar solvents to lower energies.

The excited state geometries along with the Franck-Condon factors were given by Callis *et al.* [143]. Strickland *et al.* [144] reported partial L_a-character of the spectrum 1310 cm^{-1} above the ^1L_b in the vapor, identified by solvent induced shifts, while Lami and Glasser [12] extrapolated the origin of the ^1L_a state to be 1590 ± 90 cm^{-1} above the ^1L_b using a comparable method. Polarized two photon excitation spectra in several polar and apolar solvents were reported by the group of Callis [145, 146]. Bersohn *et al.* investigated indole by means of laser induced fluorescence spectroscopy [147]. They observed a well structured sparse spectrum up until 2200 cm^{-1} above the origin of the ^1L_b state. In order to find the ^1L_a state they measured the lifetimes of 8 bands distributed evenly in the area of interest. Discovering a monotonic decrease of the lifetime they concluded that the ^1L_a state has to lie at higher energies in the gas phase [147]. Single exponential decays for nearly all bands were reported by Bickel *et al.* to be found at energies up to 1000 cm^{-1} above the ^1L_b state, using laser induced fluorescence (LIF) and dispersed fluorescence spectroscopy (DF) [148]. A steep decrease of the ratio between L_b and L_a 1000 cm^{-1} above the ^1L_b state was observed by Cable via polarization-resolved resonant two photon ionization spectroscopy in the vapor [149]. From the occurrence of single sharp minima in the ratio, the ^1L_a state was tentatively assigned to be 1400 cm^{-1} above the ^1L_b. Sammeth *et al.* used polarized one colour two photon fluorescence spectroscopy in the vapor and a jet [150]. From the ratio of absorptivity of circularly polarized light to that for linearized light Ω, they ascertained L_a character 1450 cm^{-1} above the S_1 in accordance with most previous publications, but believed it to be due of vibronic bands. The origin of the ^1L_a state was said to be split between the bands 455 and 480 cm^{-1} above the ^1L_b as those were the first bands in the jet spectra
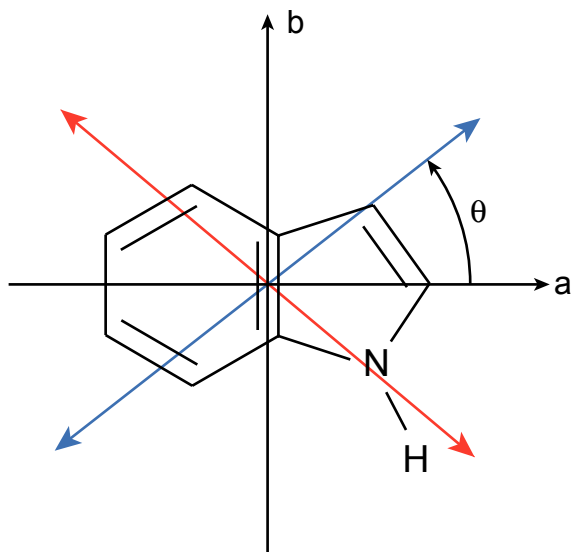
Figure 6.2: Indole in its main inertial axes frame along with the TDM vectors for the lowest two excited singlet states. The TDM vector for ^1L_b state is shown in blue, the one for the ^1L_a in red. The sign of θ is defined to be positive for a counter-clockwise rotation in this orientation of the molecular frame.

showing the appropriate ratio of Ω. However, the authors did not exclude them to be ^1L_b state vibrations coupling to the ^1L_a state, which might be located at higher energies. Intense coupling between S_1 and S_2 was concluded by Nibu *et al.* from a remarkable spectral shift of the vibration at 737 cm^{-1} in the dispersed fluorescence spectrum [151]. While Barstis *et al.* invalidated the theory of a split origin by stating a 1:1 correspondence between excited and ground state vibrations [152], Fender *et al.* published side-selective polarized fluorescence excitation and DF spectra in an argon matrix [153]. The bands at 455 and 480 cm^{-1} were identified to constitute a Fermi doublet involving ν_{28}, a Herzberg Teller-active mode, and a combination of two out-of-plane modes: 39_0^1 and 41_0^1. From the strong red-shift for ^1L_a state bands they assigned the origin to be at $0_0^0(^1L_b) + 1200$ cm^{-1} in the argon matrix and thus around +1400 cm^{-1} in the vapor. They do, however, postulate that the origin is split between several bands.

A conical intersection connecting ^1L_a and ^1L_b states was first proposed by Callis [154] using the semiempirical *intermediate neglect of differential overlap configuration interaction* (INDO/S-CI) method. From the calculated π-orbital density differences he identified the double bond stretch as the primary internal tuning mode for the ^1L_a–^1L_b conical intersection in indole. This work was extended by Slater and Callis who employed CIS and CIS-MP2 treatment for the excited states [155]. They used a 29-dimensional vector of planar internal coordinates connecting the corresponding ^1L_a and ^1L_b minima (the so-called ^1L_a–^1L_b difference vector). Along this path both electronic states show an avoided crossing with an energy gap of about 100 cm^{-1}. Later on, the vibronic spectrum of indole was computed in the Franck-Condon (FC) approximation [143]. The general appearance of the spectrum was well

reproduced, but features that were attributed to Herzberg-Teller (HT) coupling of ^1L_b levels to the ^1L_a state, such as the intensities of the 28^1_0 or 14^1_0 bands, showed considerable deviations from the experiment. Hence, a thorough investigation of the vibrational structure of the excited states of indole requires the inclusion of HT terms. How such calculations may be performed for multidimensional systems within the harmonic approximation including Dushinsky effects has been shown e.g. by Berger *et al.* for benzene and pyrazine [156]. Böhm *et al.* presented an analysis of the vibronic spectrum of tryptamine using Franck-Condon-Herzberg-Teller (FCHT) theory [157]. Theoretical electronic absorption and emission spectra of indole in the gas phase and in solvents were calculated using complete-active-space self-consistent-field (CASSCF) theory and its extension with second order perturbation theory corrections (CASPT2) [158–160].

In summary it can be stated that some of the question could be answered while some still remain open. The crucial point is that it has not been possible yet to unambiguously locate the origin of the ^1L_a state experimentally in the isolated molecule. Although the majority of publications locate it at around 1400 cm^{-1} above the ^1L_b state, a definite answer is still not available. In order to pursue this subject further, 9 vibrational bands of indole up to 1000 cm^{-1} above the electronic origin of the ^1L_b state were recorded with rotational resolution in the group of Pratt in Pittsburgh and our group [87]. The analysis indicates that some bands clearly show L_a character. The question arose if one or another of these bands might be the true ^1L_a origin. But it is also possible, that these bands are ^1L_b bands and gain their oscillator strength (and spectroscopic signature) by vibronic coupling to the ^1L_a state. The fact that this behavior is not monotonic in the energy above the origin of the ^1L_b state - and therefore might be mode-selective - supports (but does not prove) the vibronic coupling argument. Motivated by these experimental findings, we have developed a full *ab initio* description of the photophysics of the three lowest singlet states in indole. Here, we want to address especially the location of the ^1L_a state, the role of Herzberg-Teller coupling [60] in the vibronic spectrum, and the determination of the conical intersection that connects the bound ^1L_a and ^1L_b states.

In the following sections the result of a vibronic analysis of the lowest electronic transitions of indole are presented using HT theory, with density-functional theory multi-reference configuration-interaction (DFT/MRCI) computed derivatives of the transition dipole moment with respect to the normal coordinates. The geometries, energies, dipole moments, transition properties and conical intersections of the low-

est $\pi\pi^*$ states are discussed.

6.2   Computational Methods

Structure optimizations were performed employing Dunning's correlation consistent basis sets of valence triple ζ quality (cc-pVTZ) [161] from the TURBOMOLE library [162]. The equilibrium geometries of the electronic ground and the lowest excited singlet states were optimized at the CC2 level within the resolution-of-the-identity approximation [163–165] using the appropriate triple ζ auxiliary basis sets [166]. Ground state and excited state vibrational frequencies were calculated using numerical derivatives of analytic gradients using the `NumForce` script. Transition dipole moments for the FCHT analysis were calculated using the combined density functional theory multi-reference configuration interaction (DFT/MRCI). Derivatives of the electronic dipole transition moment with respect to normal coordinates were calculated numerically using central finite differences both at the DFT/MRCI and CC2 levels of theory. For more details about RICC2 and DFT/MRCI refer to Chapter 5.

The conical intersection (CI) of the ^1L_a and ^1L_b states has been optimized at the (10,9)-CASSCF level of theory with the 6-311G(d,p) basis set using the Gaussian03 program package [167] with the direct algorithm for location of the lowest energy point on a potential surface crossing published by Bearpark *et al.* [168].

6.3   Results and discussion

6.3.1   Optimized geometries of the ^1L_b and ^1L_a states

Table 6.1 summarizes the ground state heavy-atom structure of indole at the CC2/cc-pVTZ level of theory, and the excited state heavy-atom structures of the ^1L_a and the ^1L_b states as changes of bond lengths with respect to the ground state values. The corresponding atomic numbering is given in Figure 6.1. Cartesian coordinates for all calculated structures are provided in the supplementary material starting on page 267. In Table 6.1, our calculated geometry changes upon electronic excitation are also compared to values from CASSCF optimized structures [158].

While the structures of the S_0 and ^1L_b state could be readily optimized, the ob-

Table 6.1: Ground state geometries and geometry changes of indole upon excitation to the ^1L_b and the ^1L_a states. Distances and their changes are in pm; the full structures are given in the supplementary material starting on page 267. For the numbering scheme refer to Figure 6.1.

	CC2/cc-pVTZ			CASSCF [158]		
	S_0	ΔL_b	ΔL_a	S_0	ΔL_b	ΔL_a
N_1-C_2	138.2	+4.0	-3.6	137.9	+1.4	-0.3
C_2-C_3	137.4	+0.6	+6.3	136.9	+1.5	+10.3
C_3-C_9	143.2	-0.2	-0.9	144.5	-1.8	-3.4
C_4-C_5	138.8	+4.6	+3.9	138.8	+5.8	-1.4
C_5-C_6	141.0	+1.5	-2.8	141.7	+2.4	+1.3
C_6-C_7	138.9	+3.9	+6.6	138.9	+4.5	+7.6
C_7-C_8	139.8	+1.2	-0.6	140.5	+0.7	-1.9
C_8-C_9	142.3	+4.0	-1.2	140.8	+5.5	+2.4
N_1-C_8	137.8	-1.6	+3.6	137.3	-0.5	+1.8
C_4-C_9	140.6	+0.6	+1,9	141.0	+0.9	+6.1

tained minimum-energy ^1L_a structure turned out to be a first order saddle point on the S_1 state potential energy surface from the vibrational analysis. We found one imaginary in-plane mode with main contributions from C_2-N_1 and C_2-C_3 shortening and stretching which lead to the ^1L_b state minimum. All attempts to reoptimize the structure using different coordinate update step sizes led either to the same structure or to the L_b minimum. We conclude that the minimum of the ^1L_a state, if present at all, is very shallow. We will come back to the imaginary in-plane mode and the saddle point in Section 6.3.4.

Comparing with the CASSCF data from Ref. [158], the CC2 optimized excited ^1L_b and ^1L_a states display qualitatively similar structural features. Nevertheless, noticeable disagreement up to few picometers is found when comparing individual bond lengths. The main difference in the structural changes upon electronic excitation between ^1L_b and ^1L_a states can be seen in Figure 6.3. The upper sign gives the direction and magnitude of bond lengths changes for the ^1L_b (in blue), the lower sign for the ^1L_a state (in red). The changes upon excitation to the ^1L_b state are quite symmetric with respect to the quasi plane of symmetry, containing the long (a)-axis of the molecule. The changes upon excitation to the ^1L_a state are much more irregular, with a very large increase in bond length between the C_2 and the C_3 atoms. This coordinate has previously been postulated to be the tuning mode for the $^1L_b/^1L_a$ conical intersection by Callis [154]. L_a changes show an alternating
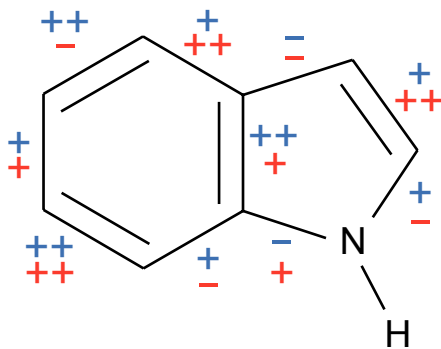
Figure 6.3: Changes of the bond lengths upon electronic excitation. Upper sign (blue) gives the changes upon excitation to the ^1L_b state, lower sign (in red) for excitation to the ^1L_a state.

Table 6.2: Rotational constants of indole in the electronic ground state and their changes upon electronic excitation to L_b and L_a in MHz computed from the CC2 optimized structures using the cc-pVTZ basis set.

| | CC2 | | | | | Exp. [125] | | |
	S_0	^1L_b	^1L_a	Δ^1L_b	Δ^1L_a	S_0	S_1	S_1-S_0
A	3880	3768	3852	-112	-28	3877.8	3743.1	-135
B	1640	1613	1605	-27	-35	1636.0	1618.1	-18
C	1152	1129	1133	-23	-19	1150.9	1130.2	-21

behavior for adjacent bonds, while L_b changes do not.

The rotational constants of the electronic ground state of indole and their changes upon electronic excitation to the ^1L_b and and ^1L_a state from the CC2 calculations are summarized in Table 6.2 and are compared to the experimentally determined changes of the rotational constants [125]. This analysis of the inertial parameters clearly shows, that the lowest electronically excited singlet state is the ^1L_b. None of the hitherto determined rotational constants of vibronic bands within the excited state of indole shows structural L_a character [87, 125].

Inertial axes reorientation upon electronic excitation

The geometry change upon electronic excitation causes a rotation of the inertial axes of the molecule, which can be described for a planar molecule using a single rotational angle θ_T. For indole, the c-axis, which is perpendicular to the aromatic plane, coincides for all three electronic states and θ_T describes the rotation of the a''-axis of the ground state into the a'-axis of the excited state about this axis.

From the *ab initio* optimized structures, the angle of reorientation of the inertial axis system upon electronic excitation θ_T can be determined using the relation for planar molecules given by Hougen and Watson [42], as described in Section 1.4 on

Table 6.3: Calculated vertical and adiabatic (boldface) singlet excitation and emission energies ΔE (cm^{-1}) of indole. All adiabatic excitation energies are zero-point-energy corrected. The zero-point energy correction was obtained at the CC2 level of theory with the cc-pVTZ basis. An asterisk attached to a state label is used to indicate that this state's geometry was optimized for obtaining the energies in the respective row. For vertical transition energies, thus only one of the involved states has an asterisk.

transition	CC2	DFT/MRCI	Experimental
$^1L_b \leftarrow S_0^*$	39269	37210	-
$S_0 \leftarrow {}^1L_b^*$	35109	33030	-
$^1L_b^* \leftarrow S_0^*$	**36496**	**35173**	**35231**
$^1L_a \leftarrow S_0^*$	41385	40179	-
$S_0 \leftarrow {}^1L_a^*$	36287	33885	-
$^1L_a^* \leftarrow S_0^*$	**37324**	**37020**	-
$^1L_a^* \leftarrow {}^1L_b^*$	828	1847	-

page 23. Using the CC2 optimized structures for the ^1L_b and ^1L_a states, we obtained a reorientation angle of +0.9° for the ^1L_b and of -0.6° for the ^1L_a state.

6.3.2   Vertical and adiabatic excitation energies of the ^1L_b and ^1L_a states

Table 6.3 gives the vertical and the adiabatic (boldface entries in the table) excitation (absorption and emission) energies of the ^1L_b and ^1L_a states of indole computed using CC2 and single point DFT/MRCI for the CC2 optimized structures. The transitions given in the table are organized as follows: the first three rows contain transitions with the ^1L_b as final or initial state, the optimized state is marked by an asterisk. The next three rows are the respective values for the ^1L_a transitions. Thus, the first row of numerical entries contains the vertical excitation energy to the ^1L_b, the second row the vertical emission energy from the ^1L_b, and the third row the adiabatic excitation energy of the ^1L_b state.

For the adiabatic excitation energies the zero-point-energy (ZPE) corrections have been calculated from numerical Hessians at the CC2 level of theory for the S_0, ^1L_b and ^1L_a states, respectively. The ZPE-corrected adiabatic DFT/MRCI ^1L_b excitation energy is very close (-58 cm^{-1}) to the experimentally determined one, while CC2 shows larger deviations (+1256 cm^{-1}). The adiabatic energy gap between the ^1L_b and ^1L_a states is calculated to be 828 cm^{-1} using CC2 and to 1847 cm^{-1} at

DFT/MRCI level. In the light of comparison to the experimental ^1L_b excitation energy, the latter should be the more reliable value. This energy gap of 1847 cm^{-1} should be compared to the respective value of 885 cm^{-1} for tryptamine [157], determined at DFT/MRCI level.

We furthermore optimized the lowest triplet state of indole at the CC2 level. This state is known to have ^3L_a configuration and a geometry close to that of the ^1L_a state [160]. A DFT/MRCI single point energy calculation on the CC2 optimized structure of the lowest triplet state yields an ZPE corrected $^3L_a \leftarrow S_0$ excitation energy of 23941 cm^{-1}. This value is in reasonable agreement with the experimental value of 24933 cm^{-1} in an argon matrix [169].

6.3.3 Permanent dipole moments and transition dipole moment orientations of the ^1L_b and ^1L_a states

The orientations of the permanent electric dipole moment in the electronic ground and the excited states and the orientations of the transition dipole moment (TDM) have been calculated using DFT/MRCI for excitation to both, ^1L_b and ^1L_a states, and compared to the experimental values [125, 138, 141, 170]. In Table 6.4 the permanent dipole moments are given in Cartesian components (in Debye, D) with respect to the principal inertial axis system of the S_0 state. The TDM orientations are given as the angle θ between the projection vector of the transition dipole moment on the inertial ab-plane and the a-axis and as the angle ϕ between the TDM and the out-of-plane inertial c-axis:

$$
\begin{aligned}
\mu_a &= \mu \sin\phi \cos\theta \\
\mu_b &= \mu \sin\phi \sin\theta \\
\mu_c &= \mu \cos\phi
\end{aligned}
\tag{6.1}
$$

The values for the permanent ^1L_b state dipole moments are in excellent agreement with the experimental data, both for the absolute value as well as for the components with respect to the inertial axes.

The experimentally determined transition dipole moment orientation ($\theta = +38.3°$ [125]) is clearly that of the ^1L_b state, with very good numerical agreement to the DFT/MRCI values ($\theta = +40°$), while the ^1L_a TDM in-plane angle angle is calculated with the opposite sign ($\theta = -37°$). The experimental value for the TDM orientation of the ^1L_b state is known very accurately from rotationally resolved electronic spec-

Table 6.4: Permanent dipole moment: projections μ_i ($i = a, b$) onto the inertial a and b axes, and absolute values $\mu = |\vec{\mu}|$ in Debye (D). Transition dipole moment: angle θ between the projection of the TDM vector onto the ab-plane and the a-axis, and the angle ϕ between the TDM and the c-axis.

		permanent dipole mom.				transition dipole mom.		
		$|\mu_a|$	$|\mu_b|$	μ		θ		ϕ
S_0		1.38	1.40	1.96	[141]			
^1L_b	exp.	1.56	1.01	1.86	[141]	+38.3	[125]	90
^1L_a		-	-	5.86	[170]	-46	[138]	90
S_0		1.45	1.51	2.09				
^1L_b	DFT/MRCI	1.65	1.11	1.99		+40		90
^1L_a		5.54	1.76	5.82		-37		90
S_0		1.52	1.65	2.24		-		-
^1L_b	CC2	1.85	1.14	2.17		+55		90
^1L_a		5.53	1.33	5.69		-46		90

troscopy [125] and for the permanent ^1L_b dipole moment from Stark experiments in a molecular beam [141], while the transition dipole moment orientation of the ^1L_a state is much less accurately known from linear dichroism measurements on molecules partially oriented in a stretched polyethylene host [138]. Also the permanent dipole moment of the ^1L_a state, determined from Stark absorption spectroscopy of indole doped into a polymethylmethacrylate film, are less accurately known than the respective value for the ^1L_b state.

We summarize the results on the permanent dipole moments and the transition dipole moments of the ^1L_a and the ^1L_b state by stating that both properties are excellently described by the DFT/MRCI method. The numbers from CC2 do not agree with experiment to the very same extent. But the data are quite sufficiently in accord, and nothing essential changes if we deduce the above findings about indole molecular properties solely at the CC2 level of theory.

6.3.4   The conical intersection between ^1L_b and ^1L_a

The geometry of indole at the conical intersection between the ^1L_b and ^1L_a states was optimized at the (10,9)-CASSCF level of theory with the 6-311G(d,p) basis set. According to the CASSCF calculations, the conical intersection is located close to a linearly interpolated path between the ^1L_b and ^1L_a minima, as is the case for tryptamine [157]. Unfortunately, the excitation energies are severely overestimated

by CASSCF treatment due to the neglect of dynamic electron correlation. We therefore also calculated a linearly interpolated path between our CC2 optimized ^1L_b and ^1L_a state geometries. This path is shown in Figure 6.4. The predicted conical intersection in indole at the DFT/MRCI level is located more than 2000 cm^{-1} above the ^1L_b minimum and very close to the ^1L_a minimum. Since our DFT/MRCI path is not the true minimum energy path, this value is only an upper limit for the energy difference. The CI connecting the ^1L_a and ^1L_b states in indole lies significantly higher than the ^1L_b minimum. A perturbative approach for the description of the nonadiabatic coupling between these two states thus can be justified. We calculated how the linear path connecting the ^1L_b and ^1L_a geometries is composed from walks along individual normal modes. Here, many in-plane modes contribute, but the largest coefficient is found for mode 27 (cf. Table 6.5 in Section 6.3.5).

The gradient difference and the derivative coupling vectors, obtained at the (10,9)-CASSCF level of theory with the 6-311G(d,p) basis set, are shown in Figure 6.5. The gradient difference vector represents the tuning coordinate along which the energy difference of the two states connected by the CI is modulated. Together with the derivative coupling vector, which describes the interaction of the two states, it forms the 2D branching space [171].

The main contributions to the tuning vector are located in the pyrrole moiety. A distinct shortening of the bond lengths N_1-C_2 and C_8-C_9 is accompanied by a bond stretching of C_2-C_3. The C_2-C_3 displacement was described to be the main contribution to the tuning mode by Callis [154] on the basis of the differences of π bond orders between ^1L_a and ^1L_b states. The interstate derivative coupling vector, which is shown in the lower trace of Figure 6.5 is mainly located in the benzene moiety and symmetrically distorts the six-ring about bonds C_5-C_6 and C_8-C_9. This vector strongly resembles mode Q_9, along which the gradient of the electronic transition moment is largest (cf. Table 6.6). Mode Q_9 in the excited ^1L_b state is composed of nearly equal contributions of Q_9 and Q_{12} ground state modes (cf. Dushinsky decomposition in Table 6.5), all of which have large TDM derivatives.

For tryptamine the DFT/MRCI calculations predicted a very shallow ^1L_a minimum, so that zero-point motion alone is sufficient to completely couple ^1L_a and ^1L_b levels in the region of the ^1L_a origin [157]. As described in Section 6.3.1 the optimization of the ^1L_a state of indole led to a first order saddle point. Figure 6.6 shows the displacement vectors of the imaginary mode from the normal mode analysis at the
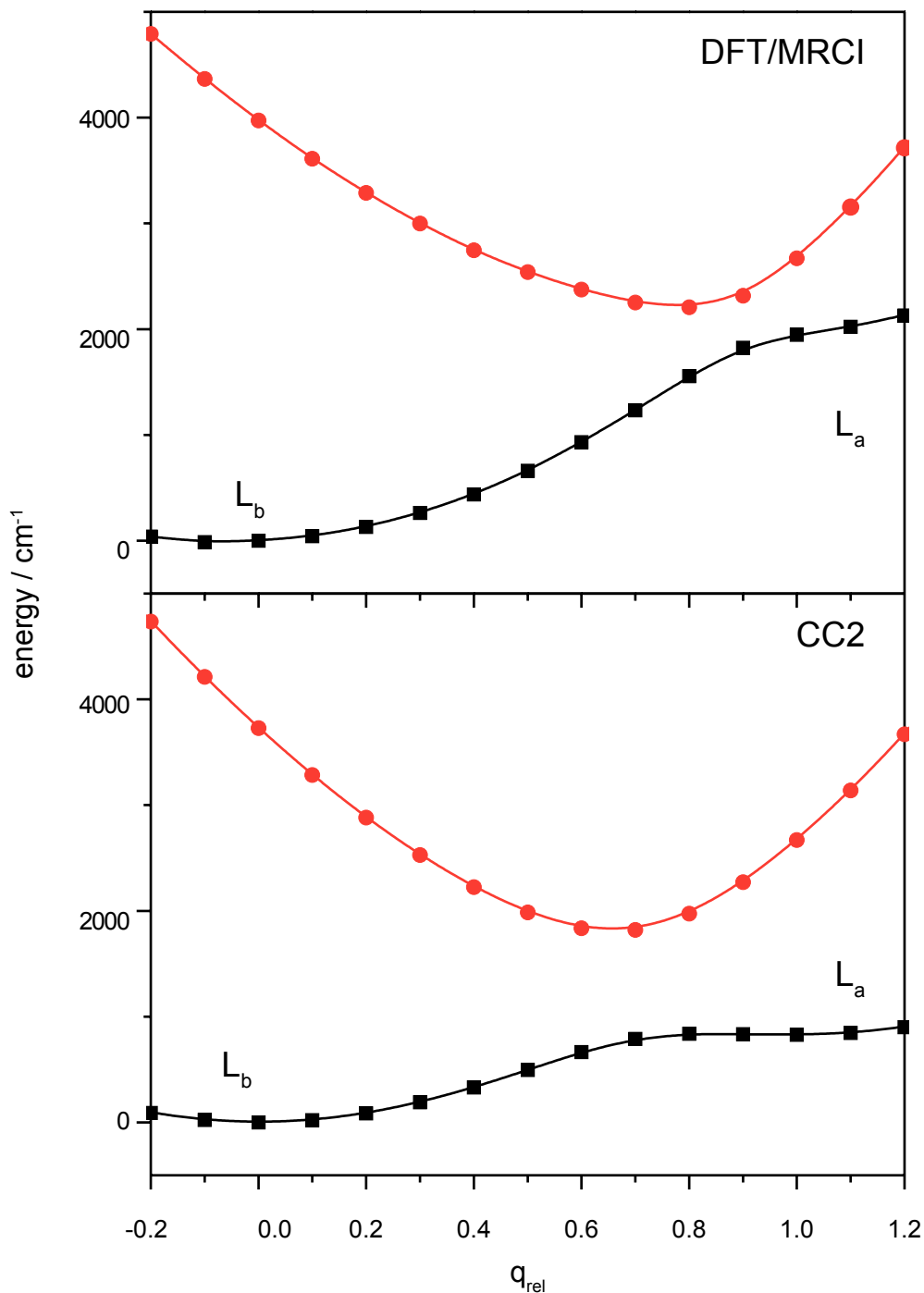
Figure 6.4: One-dimensional cut through the adiabatic multidimensional potential energy surfaces of the S_1 (black squares) and S_2 (red circles) states of indole computed at the DFT/MRCI and CC2 level of theory, along a coordinate connecting the ^1L_b and ^1L_a minima, along which the conical intersection of these two surfaces is located. See the text for further details.
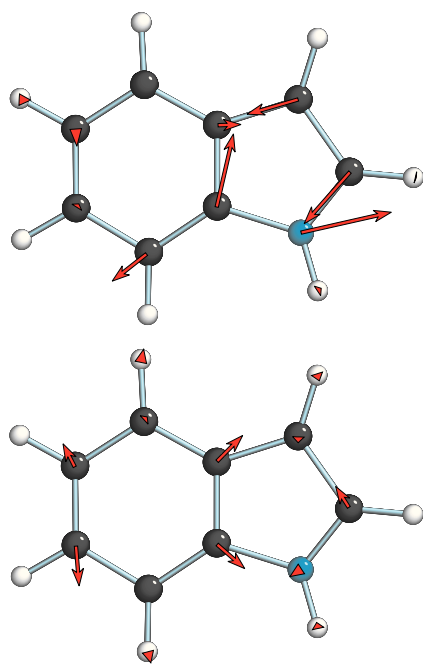
Figure 6.5: Gradient difference (upper trace) and derivative coupling vectors (lower trace) of the optimized point on the CI (computed at the (10,9)-CASSCF level employing 6-311G(d,p) basis sets).

CC2 level at the saddle point geometry. An optimization starting from this geometry displaced along the mode with negative curvature of the PES converged to the ^1L_b geometry. According to Figure 6.4, the ^1L_a state minimum (if existent at all) will be located rather close to the CI. Then, in order to funnel from this ^1L_a structure through the CI into the ^1L_b state, the system needs to overcome only a very shallow barrier, what should be possible already due to zero-point motion. Alternatively, one may suspect that our CC2 optimized ^1L_a geometry is itself a point on the CI if the latter displays an avoided crossing like appearance at the CC2 level of theory. In this case, the imaginary mode from the frequency analysis at the CC2 level should exhibit some similarity with the gradient difference or derivative coupling vectors shown in Figure 6.5. We did, however, not further investigate this aspect.
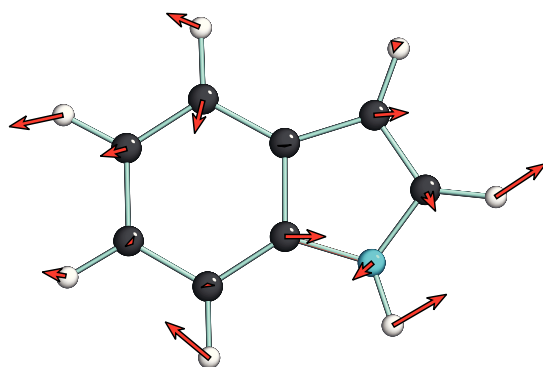

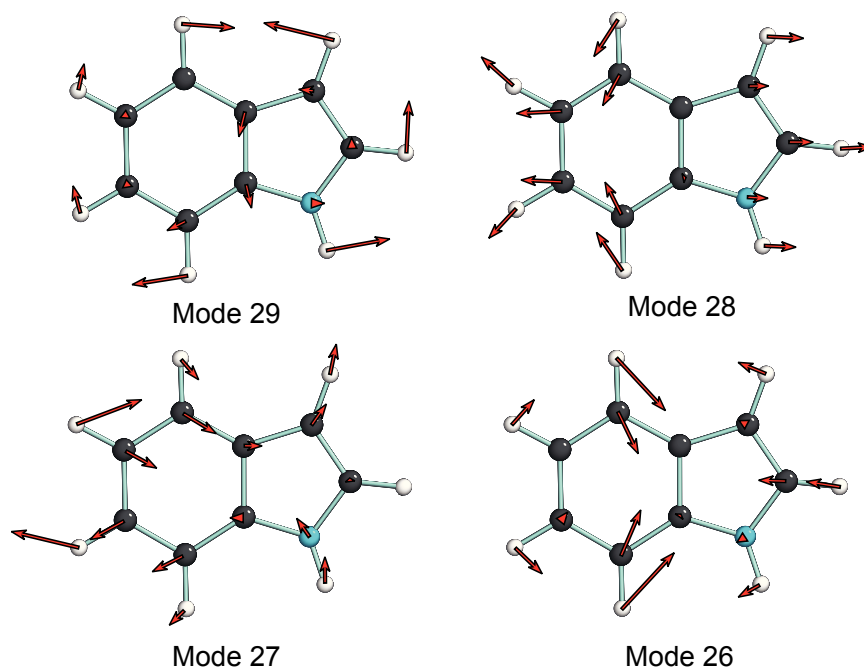Figure 6.6: Displacement vectors of the imaginary normal mode at the lowest first order saddle point of the ^1L_a state.

Figure 6.7: Vibrational in-plane modes Q'_{29} through Q'_{26} of the ^1L_b state.

6.3.5   Franck-Condon-Herzberg-Teller simulation of the ^1L_b vibronic spectrum of indole

Table 6.5 shows the results of a normal mode analysis for the ground and the excited ^1L_b state. For the numbering, the modes are grouped by symmetry and then sorted by descending wavenumbers, first the out-of-plane modes numbered from Q_{42} to Q_{30}, followed by the in-plane modes from Q_{29} to Q_1. The vibrational modes given in Table 6.5 are sorted by ascending frequencies of the calculated S_0 vibrations. Special care must be taken for the ^1L_b state, since the energetic ordering of the modes changes and accordingly the numbering.

The four lowest-wavenumber in-plane (a') modes Q'_{29}–Q'_{26} are depicted in Figure 6.7.

The calculated wavenumbers for both states are compared to the experimental ground state [172] and ^1L_b frequencies [148] in Table 6.5. The last column gives the composition of the excited state mode from the ground state modes. Only elements with a contribution of 0.4 or larger have been taken from the full Dushinsky matrix and have been used to make the assignments of excited state to ground state modes. Based on this Dushinsky matrix we performed the assignments of the ex-

Table 6.5: Calculated vibrational wavenumbers in the ground and electronically excited ^1L_b states in cm^{-1} from CC2 calculations with the cc-pVTZ basis set. The first column gives the mode numbering for the ground state [152], the last column the respective projection of the ^1L_b state modes on the ground state modes according to the Dushinsky matrix; see text for details.

Mode	Sym.	S_0		^1L_b		Dushinsky
		calc.	obs.[2]	calc.	obs.[3]	
Q''_{42}	a"	215	208	170	158	$Q'_{42}(L_b) = 0.97Q''_{42}$
Q''_{41}	a"	242	240	194	183	$Q'_{41}(L_b) = 0.95Q''_{41}$
Q''_{29}	a'	392	400	379	379	$Q'_{29}(L_b) = 0.99Q''_{29}$
Q''_{40}	a"	395	400	438	425	$Q'_{38}(L_b) = 0.58Q''_{40} + 0.44Q''_{33}$
Q''_{39}	a"	423	428	290	278	$Q'_{40}(L_b) = 0.93Q''_{39}$
Q''_{28}	a'	541	544	477	455/480	$Q'_{28}(L_b) = 0.96Q''_{28}$
Q''_{38}	a"	572	575	379	388	$Q'_{39}(L_b) = 0.92Q''_{38}$
Q''_{27}	a'	605	608	563	539	$Q'_{27}(L_b) = 0.96Q''_{27}$
Q''_{37}	a"	612	625	505	500	$Q'_{36}(L_b) = 0.93Q''_{37}$
Q''_{36}	a"	709	715	609		$Q'_{34}(L_b) = 0.54Q''_{36} + 0.47Q''_{31}$
Q''_{35}	a"	740	738	651		$Q'_{32}(L_b) = 0.59Q''_{35} + 0.48Q''_{32}$
Q''_{34}	a"	751	762	568		$Q'_{35}(L_b) = 0.63Q''_{34} + 0.54Q''_{32}$
Q''_{26}	a'	765	761	722	718/720	$Q'_{26}(L_b) = 0.97Q''_{26}$
Q''_{33}	a"	831	800	787		$Q'_{30}(L_b) = 0.80Q''_{33} + 0.39Q''_{35}$
Q''_{32}	a"	836	860	487		$Q'_{37}(L_b) = 0.27Q''_{32} + 0.63Q''_{40}$
Q''_{25}	a'	879	869	858	852	$Q'_{24}(L_b) = 0.91Q''_{25}$
Q''_{24}	a'	899	900	776	784	$Q'_{25}(L_b) = 0.86Q''_{24}$
Q''_{31}	a"	907	930	634		$Q'_{33}(L_b) = 0.75Q''_{31} + 0.40Q''_{32}$
Q''_{30}	a"	935	968	774		$Q'_{31}(L_b) = 0.86Q''_{30}$
Q''_{23}	a'	1025	1015	927	909	$Q'_{23}(L_b) = 0.87Q''_{23}$
Q''_{22}	a'	1079	1068	996		$Q'_{22}(L_b) = 0.62Q''_{22} + 0.44Q''_{23}$
Q''_{21}	a'	1107	1082	1044	1060	$Q'_{21}(L_b) = 0.81Q''_{21}$
Q''_{20}	a'	1138	1122	1086	1086	$Q'_{20}(L_b) = 0.77Q''_{20} + 0.58Q''_{22}$
Q''_{19}	a'	1166	1150	1135	1111	$Q'_{19}(L_b) = 0.89Q''_{19}$
Q''_{18}	a'	1219	1205	1180		$Q'_{18}(L_b) = 0.81Q''_{18}$
Q''_{17}	a'	1259	1245	1224		$Q'_{17}(L_b) = 0.93Q''_{17}$
Q''_{16}	a'	1300	1275	1273		$Q'_{16}(L_b) = 0.91Q''_{16}$
Q''_{15}	a'	1370	1300	1319		$Q'_{15}(L_b) = 0.74Q''_{15} + 0.53Q''_{14}$
Q''_{14}	a'	1409	1348	1357		$Q'_{14}(L_b) = 0.60Q''_{14} + 0.56Q''_{15}$
Q''_{13}	a'	1456	1410	1392		$Q'_{13}(L_b) = 0.54Q''_{13} + 0.47Q''_{12}$
Q''_{12}	a'	1499	1458	1628		$Q'_{12}(L_b) = 0.52Q''_{12} + 0.60Q''_9$
Q''_{11}	a'	1509	1489	1423		$Q'_{11}(L_b) = 0.65Q''_{11} + 0.50Q''_{10}$
Q''_{10}	a'	1536	1510	1432		$Q'_{10}(L_b) = 0.70Q''_{10} + 0.47Q''_{11}$
Q''_9	a'	1606	1578	1628		$Q'_9(L_b) = 0.60Q''_9 + 0.52Q''_{12}$
Q''_8	a'	1655	1617	1555		$Q'_8(L_b) = 0.77Q''_8$
Q''_7	a'	3193	3068	3200		$Q'_7(L_b) = 0.77Q''_7$
Q''_6	a'	3200	3068	3214		$Q'_6(L_b) = 0.84Q''_6$
Q''_5	a'	3212	3068	3226		$Q'_5(L_b) = 0.82Q''_5$
Q''_4	a'	3223	3083	3237		$Q'_4(L_b) = 0.89Q''_4$
Q''_3	a'	3267	3083	3265		$Q'_3(L_b) = 0.85Q''_3$
Q''_2	a'	3285	3140	3303		$Q'_2(L_b) = 0.85Q''_2$
Q''_1	a'	3672	3520	3627		$Q'_1(L_b) = 1.00Q''_1$

cited state vibrations to the respective ground state vibrations. Based on symmetry and normal mode frequencies, the assignments to the experimental frequencies is in general rather straightforward. Since the ordering of the frequencies in the ground and the ^1L_b state is different, for some modes the numbering changes between these two states, i.e., Q'_{25} of the ^1L_b state corresponds to Q''_{24} in the S_0 ground state.

A problem is posed by the close pair of intense transitions at $455/480$ cm^{-1} since no two computed vibrations are sufficiently close to explain both bands. The most probable explanation is a Fermi resonance between the in-plane mode Q'_{28} and the combination of the out-of-plane modes Q'_{39} at 278 cm^{-1} and Q'_{41} at 183 cm^{-1} as already proposed by Barstis et $al.$ [152].

The vibronic spectrum of indole was then simulated within the framework of the perturbative Herzberg-Teller formalism for vibronic coupling. This is discussed in detail in Chapter 2 and the reader is advised to this chapter, if he is not familiar with vibronic coupling. In brief, the wave function is factored in a vibrational part and an electronic part which depends only parametrically on the nuclear coordinates, according to the Born-Oppenheimer approximation. The transition probability W_{mn} from the state m to the final state n depends on the electronic transition dipole moment $\hat{\vec{\mu}}_e$, which is a constant for each electronically excited state (Condon approximation). By expanding $\hat{\vec{\mu}}_e$ in a Taylor series the dependency on the nuclear coordinates $\mathbf{Q}$ can be approximated. The final equation is given as:

$$\vec{W}_{m\chi'',n\chi'} = \vec{\mu}_{mn}(\mathbf{Q}' = \mathbf{0})\langle\chi''_{(m)}|\chi'_{(n)}\rangle + \sum_i \left(\frac{\partial\vec{\mu}_{mn}}{\partial Q'_i}\right)_{\mathbf{Q}'=\mathbf{0}} \langle\chi''_{(m)}|Q'_i|\chi'_{(n)}\rangle \quad (6.2)$$

Please note, that χ is here a vector of the vibrational quantum numbers in the respective electronic state. In the practical calculations, we express the TDM as a function of the final state normal coordinates $\mathbf{Q}'$ and employ the final state equilibrium geometry ($\mathbf{Q}' = \mathbf{0}$) as the reference. The Franck-Condon (FC) integrals $\langle\chi''|\chi'\rangle$ were evaluated using the recursive relations of Doktorov [173]. The integrals $\langle\chi''|Q'_i|\chi'\rangle$ can be calculated from FC integrals via:

$$\langle\chi''|Q'_i|\chi'\rangle = \sqrt{\frac{\hbar}{2\omega_i}}[\sqrt{\chi'_i}\langle\chi''|\chi'_1,\ldots,(\chi'_i-1),\ldots,\chi'_N\rangle$$
$$+ \sqrt{\chi'_i+1}\langle\chi''|\chi'_1,\ldots,(\chi'_i+1),\ldots,\chi'_N\rangle] \quad (6.3)$$

Displacement of the excited state geometry of the state n along normal modes Q'_i mixes so-called crude Born-Oppenheimer wave functions if the coupling between the states is symmetry-allowed and the states are sufficiently close to each other.

Through the displacements, the excited state n may thus gain (or loose) intensity from (or to) perturbing state(s). We calculated the derivatives of the transition moments $\vec{\mu}_{mn}(\mathbf{Q}')$ with respect to the normal modes Q_i' of the ^1L_b state numerically from both DFT/MRCI and CC2 transition dipole moments of the respective state using central finite differences:

$$\left(\frac{\partial \vec{\mu}_{mn}}{\partial Q_i'}\right)_{\mathbf{Q}'=0} = \frac{\vec{\mu}_{mn}\left(\mathbf{0} + \Delta_i \mathbf{1}_i\right) - \vec{\mu}_{mn}\left(\mathbf{0} - \Delta_i \mathbf{1}_i\right)}{2\Delta_i} \tag{6.4}$$

Here, $\mathbf{1}_i$ is a unit vector pointing into the direction of normal mode i. Δ_i is a (scalar) displacement which should be chosen small enough to ensure the applicability of the linear approximation, but large enough to avoid numerical instabilities. In practice, we transform equation 6.4 to dimensionless oscillator coordinates $\mathbf{q} = (\frac{\omega}{\hbar})^{1/2}\mathbf{Q}$ and introduce a common displacement Δ for all normal modes. $\Delta = 0.1$ was used here.

The products $\vec{\mu}_{mn}(\mathbf{Q}' = \mathbf{0})\langle\chi''_{(m)}|\chi'_{(n)}\rangle$ and $\sum_i[(\partial\vec{\mu}_{mn})/(\partial Q_i')]_{\mathbf{Q}'=\mathbf{0}}\langle\chi''_{(m)}|Q_i'|\chi'_{(n)}\rangle$ from equation 6.2, and the moduli of the derivatives $|\partial\vec{\mu}_{mn}/\partial Q_i'|$ according to equation 6.4 are given in Tables 6.6 and 6.7 for each of the modes. Here, the labeling used is the one of the ^1L_b state, taken from the last column of Table 6.5.

Figure 6.8 compares the simulation of the vibronic absorption spectrum of indole using the Franck-Condon approximation (upper trace) and Herzberg-Teller theory (lower trace). Since both the ground and the excited ^1L_b state have a′ symmetry, only a′-symmetric vibrations or even overtones of a″-symmetric vibrations are FC allowed. Clearly, the in-plane mode Q_{28}', which is calculated at 477 cm^{-1} in the excited ^1L_b state (see Table 6.5) gains most of its oscillator strength through vibronic coupling to the ^1L_a state. This can also be seen from the large derivative of the transition dipole moment with respect to mode Q_{28}' in Table 6.6. Also mode 26 (calculated at 722 cm^{-1} for the ^1L_b state) gains intensity from vibronic coupling, although half of its intensity can be ascribed to Franck-Condon activity, as can be inferred from the comparison of a FCHT simulation with the FC simulation in Figure 6.8 and from Table 6.6. The FC factors for the out-of-plane fundamentals are zero, as can be expected for a planar molecule, but these bands gain some intensity via HT coupling. Albeit very weak, it might be possible to detect these bands, since the analysis of the TDM angles shows, that the fundamentals of these bands will have mainly c-type character. The concentration of most of the bands intensity in the Q-branch might make their detection in a rotationally resolved electronic spectrum

Table 6.6: Calculated vibrational frequencies in cm^{-1} for the electronically excited ^1L_b state from CC2 calculations (cc-pVTZ basis set) along with the moduli of the TDM derivatives from the DFT/MRCI calculations in a.u./Å(amu)$^{1/2}$ and the Franck-Condon (FC) contributions $\vec{\mu}_{mn}(\mathbf{Q}' = 0)\langle v''_m|v'_n\rangle$ in cartesian coordinates and moduli.

No.	Sym.	lit.[152]	^1L_b	$|\partial\vec{\mu}/\partial Q'|$	FC_x	FC_y	FC_z	$|FC|$
1	a"	Q'_{42}	170	0.0032	0.0001	-0.0001	0.0000	0.0002
2	a"	Q'_{41}	194	0.0050	0.0000	0.0000	0.0000	0.0000
3	a"	Q'_{40}	290	0.0077	0.0000	0.0000	0.0000	0.0000
4	a'	Q'_{29}	379	0.1892	0.0400	-0.0444	0.0000	0.0598
5	a"	Q'_{39}	379	0.0322	0.0012	-0.0013	0.0000	0.0018
6	a"	Q'_{38}	438	0.0359	0.0000	0.0000	0.0000	0.0000
7	a'	Q'_{28}	477	0.6262	-0.0071	0.0079	0.0000	0.0107
8	a"	Q'_{37}	487	0.0023	0.0000	0.0000	0.0000	0.0000
9	a"	Q'_{36}	505	0.0640	0.0000	0.0000	0.0000	0.0000
10	a'	Q'_{27}	563	0.5097	0.0807	-0.0894	0.0000	0.1205
11	a"	Q'_{35}	568	0.0463	0.0000	0.0000	0.0000	0.0000
12	a"	Q'_{34}	609	0.0536	0.0000	0.0000	0.0000	0.0000
13	a"	Q'_{33}	634	0.0236	0.0000	0.0000	0.0000	0.0000
14	a"	Q'_{32}	651	0.0118	0.0000	0.0000	0.0000	0.0000
15	a'	Q'_{26}	722	0.3087	0.1427	-0.1583	0.0000	0.2131
16	a"	Q'_{31}	774	0.0152	-0.0001	0.0001	0.0000	0.0002
17	a'	Q'_{25}	776	0.5419	0.0129	-0.0143	0.0000	0.0193
18	a"	Q'_{30}	787	0.0009	0.0000	0.0000	0.0000	0.0000
19	a'	Q'_{24}	858	0.2008	0.0343	-0.0380	0.0000	0.0512
20	a'	Q'_{23}	927	0.4174	-0.0514	0.0570	0.0000	0.0767
21	a'	Q'_{22}	996	0.4217	0.1244	-0.1380	0.0000	0.1858
22	a'	Q'_{21}	1045	0.1070	0.0057	-0.0063	0.0000	0.0085
23	a'	Q'_{20}	1086	0.1256	-0.0077	0.0085	0.0000	0.0115
24	a'	Q'_{19}	1135	0.1903	-0.0006	0.0007	0.0000	0.0009
25	a'	Q'_{18}	1180	0.2115	-0.0085	0.0094	0.0000	0.0127
26	a'	Q'_{17}	1224	0.1281	0.0038	-0.0042	0.0000	0.0057
27	a'	Q'_{16}	1273	0.3105	0.0373	-0.0413	0.0000	0.0556
28	a'	Q'_{15}	1320	0.2338	-0.0742	0.0823	0.0000	0.1108
29	a'	Q'_{14}	1357	0.3397	-0.0453	0.0502	0.0000	0.0676
30	a'	Q'_{13}	1392	0.0302	0.0318	-0.0352	0.0000	0.0474
31	a'	Q'_{12}	1423	0.2754	-0.0247	0.0274	0.0000	0.0369
32	a'	Q'_{11}	1432	0.7927	-0.0283	0.0314	0.0000	0.0422
33	a'	Q'_{10}	1465	0.8163	0.0361	-0.0401	0.0000	0.0540
34	a'	Q'_9	1555	1.2050	0.0004	-0.0004	0.0000	0.0005
35	a'	Q'_8	1629	0.6518	-0.0138	0.0153	0.0000	0.0206
36	a'	Q'_7	3200	0.0604	-0.0002	0.0002	0.0000	0.0003
37	a'	Q'_6	3214	0.1704	0.0033	-0.0037	0.0000	0.0050
38	a'	Q'_5	3226	0.1061	-0.0037	0.0041	0.0000	0.0055
39	a'	Q'_4	3237	0.0327	0.0102	-0.0113	0.0000	0.0153
40	a'	Q'_3	3265	0.0481	0.0013	-0.0014	0.0000	0.0019
41	a'	Q'_2	3303	0.0939	0.0071	-0.0079	0.0000	0.0106
42	a'	Q'_1	3627	0.0852	-0.0020	0.0022	0.0000	0.0029

Table 6.7: Calculated vibrational frequencies in cm^{-1} for the electronically excited ^1L_b state from CC2 calculations (cc-pVTZ basis set) along with the Herzberg-Teller (HT) contributions of the normal coordinates in Cartesian components and moduli. Resulting polar angles θ and ϕ of the TDM with the main inertial axes are given for each transition.

| No.	Sym.	lit.[152]	^1L_b	HT_x	HT_y	HT_z	$|HT|$	θ	ϕ
1	a"	Q'_{42}	170	0.0001	-0.0002	-0.0003	0.0003	64	28
2	a"	Q'_{41}	194	0.0000	0.0003	0.0004	0.0005	69	1
3	a"	Q'_{40}	290	0.0001	0.0008	0.0007	0.0010	81	6
4	a'	Q'_{29}	379	0.0326	-0.0682	0.0000	0.0756	65	90
5	a"	Q'_{39}	379	0.0009	-0.0024	0.0032	0.0041	32	19
6	a"	Q'_{38}	438	0.0000	-0.0002	0.0035	0.0035	-5	0
7	a'	Q'_{28}	477	-0.0433	-0.0148	0.0000	0.0458	-40	90
8	a"	Q'_{37}	487	0.0000	0.0001	0.0015	0.0015	40	1
9	a"	Q'_{36}	505	0.0000	0.0000	-0.0023	0.0023	16	0
10	a'	Q'_{27}	563	0.0803	-0.1338	0.0000	0.1560	63	90
11	a"	Q'_{35}	568	-0.0001	-0.0004	0.0047	0.0047	88	1
12	a"	Q'_{34}	609	0.0000	-0.0002	-0.0071	0.0071	48	0
13	a"	Q'_{33}	634	-0.0001	-0.0004	-0.0019	0.0020	63	1
14	a"	Q'_{32}	651	0.0002	0.0009	-0.0019	0.0021	-22	0
15	a'	Q'_{26}	722	0.1147	-0.1815	-0.0001	0.2147	42	90
16	a"	Q'_{31}	774	-0.0068	-0.0322	0.0001	0.0329	-41	8
17	a'	Q'_{25}	776	0.0113	-0.0159	-0.0025	0.0196	-62	90
18	a"	Q'_{30}	787	0.0000	0.0001	-0.0010	0.0010	-36	2
19	a'	Q'_{24}	858	0.0430	-0.0359	0.0000	0.0561	75	90
20	a'	Q'_{23}	927	-0.0729	0.0847	0.0001	0.1117	62	90
21	a'	Q'_{22}	996	0.0871	-0.1322	-0.0001	0.1584	48	90
22	a'	Q'_{21}	1045	0.0087	0.0010	0.0000	0.0088	89	90
23	a'	Q'_{20}	1086	0.0066	0.0034	0.0000	0.0074	34	90
24	a'	Q'_{19}	1135	0.0064	0.0195	0.0001	0.0205	-74	90
25	a'	Q'_{18}	1180	-0.0045	0.0280	0.0000	0.0283	-51	90
26	a'	Q'_{17}	1224	0.0164	-0.0053	0.0000	0.0173	-69	90
27	a'	Q'_{16}	1273	0.0536	-0.0579	0.0000	0.0790	44	90
28	a'	Q'_{15}	1320	-0.0836	0.1033	0.0001	0.1329	50	90
29	a'	Q'_{14}	1357	-0.0571	0.0805	0.0000	0.0987	37	90
30	a'	Q'_{13}	1392	0.0297	-0.0371	0.0000	0.0476	52	90
31	a'	Q'_{12}	1423	-0.0326	0.0091	0.0000	0.0339	66	90
32	a'	Q'_{11}	1432	0.0312	0.0311	0.0000	0.0440	-33	90
33	a'	Q'_{10}	1465	0.0549	-0.0227	0.0000	0.0594	-21	90
34	a'	Q'_9	1555	-0.0611	0.0111	0.0000	0.0620	7	90
35	a'	Q'_8	1629	-0.0191	-0.0053	0.0000	0.0198	-64	90
36	a'	Q'_7	3200	-0.0002	-0.0046	0.0000	0.0046	-14	90
37	a'	Q'_6	3214	0.0153	-0.0010	0.0000	0.0154	4	90
38	a'	Q'_5	3226	-0.0092	0.0003	0.0000	0.0092	4	90
39	a'	Q'_4	3237	0.0081	-0.0113	0.0000	0.0139	58	90
40	a'	Q'_3	3265	0.0007	-0.0051	0.0000	0.0051	76	90
41	a'	Q'_2	3303	0.0048	-0.0142	0.0000	0.0150	70	90
42	a'	Q'_1	3627	-0.0018	-0.0035	0.0000	0.0039	71	90
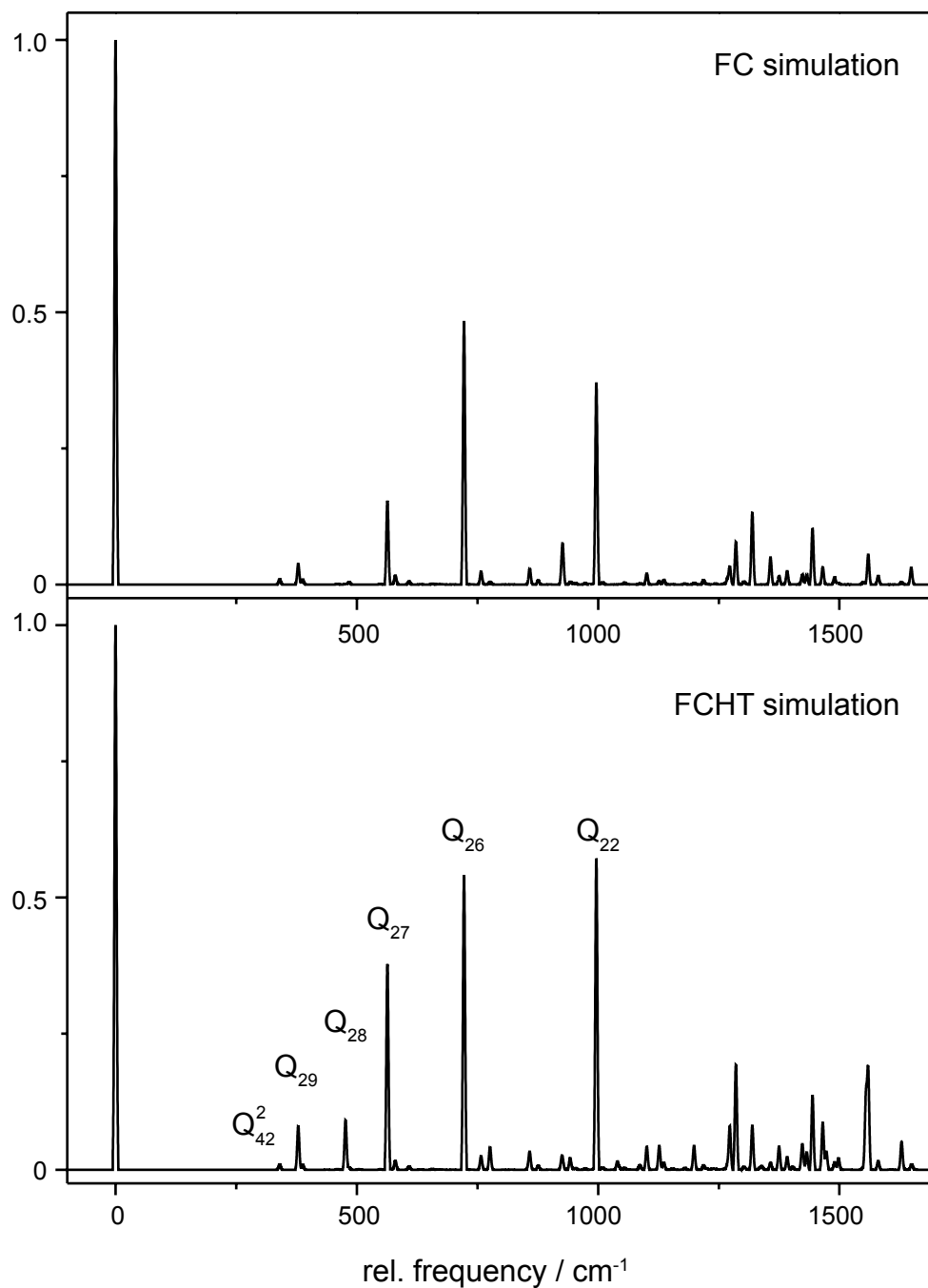
Figure 6.8: Simulation of the first 1800 cm^{-1} of the absorption spectrum of the ^1L_b state using only the FC terms from equation 6.2 (upper trace) and including the Herzberg-Teller terms (lower trace).

possible in the future, utilizing more sensitive detection devices. If these out-of-plane bands gain intensity (and band type) from HT coupling, there must be an electronic state of appropriate symmetry near-by. We propose the repulsive $\pi\sigma^*$ state, which comes from a $5a'' \rightarrow 27a'$ excitation to be the vibronically coupled state, although its oscillator strength is small. The overtones of the out-of-plane vibrations exhibit an angle ϕ of 90 degrees and therefore ab hybrid type for the band shape, as has been observed experimentally [87].

Figure 6.9 compares the computed vibronic spectrum with the experimental (laser induced fluorescence) spectrum [87].

Quite good agreement between the experimental and FCHT simulated absorption intensities is found, keeping in mind, that our model does not account for Fermi resonances and that the intensities of modes Q'_{27} and Q'_{26} should be divided up into two peaks. The intensities toward the blue end of the spectrum are considerably too high (both, for the FC as for the FCHT calculations, but in the latter the effect is more pronounced). This points to a deactivation path which is not considered in the present model. One plausible explanation is a crossing to a repulsive $\pi\sigma^*$ state at higher energies as proposed by Domcke and Sobolewski [53]. Tunneling though the barrier formed by the intersection of $\pi\pi^*$ and $\pi\sigma^*$ state should then decrease the lifetime of high-lying vibronic levels. Experimentally it is found, that the lifetime in the 1000 cm^{-1} region is a factor of three shorter than in the region of the electronic origin [87].

Additionally, we simulated some of the single vibronic level fluorescence (SVLF) emission spectra of indole from the literature in the FCHT approximation. Figure 6.10 shows the simulated and experimental emission spectrum (reconstructed from the emission spectrum [148] and the Franck-Condon factors [143]) observed via excitation of the vibrationless origin 0,0 of the ^1L_b state, the first overtone of mode Q'_{42} at 316 cm^{-1}, mode Q'_{27} at 540 cm^{-1}, and mode Q'_{26} at 718 cm^{-1}.

Also for the emission spectrum the FCHT simulation yields qualitatively better agreement with the experiment, than a pure FC simulation (shown in the respective upper rows of Figure 6.10). Nevertheless, there is still a discrepancy between the experimental and computed intensity of the bands allowed only via vibronic coupling.

Further investigations are on the way, to clarify the reasons of these differences. At least to some part, they may be due the truncation of the Taylor expansion
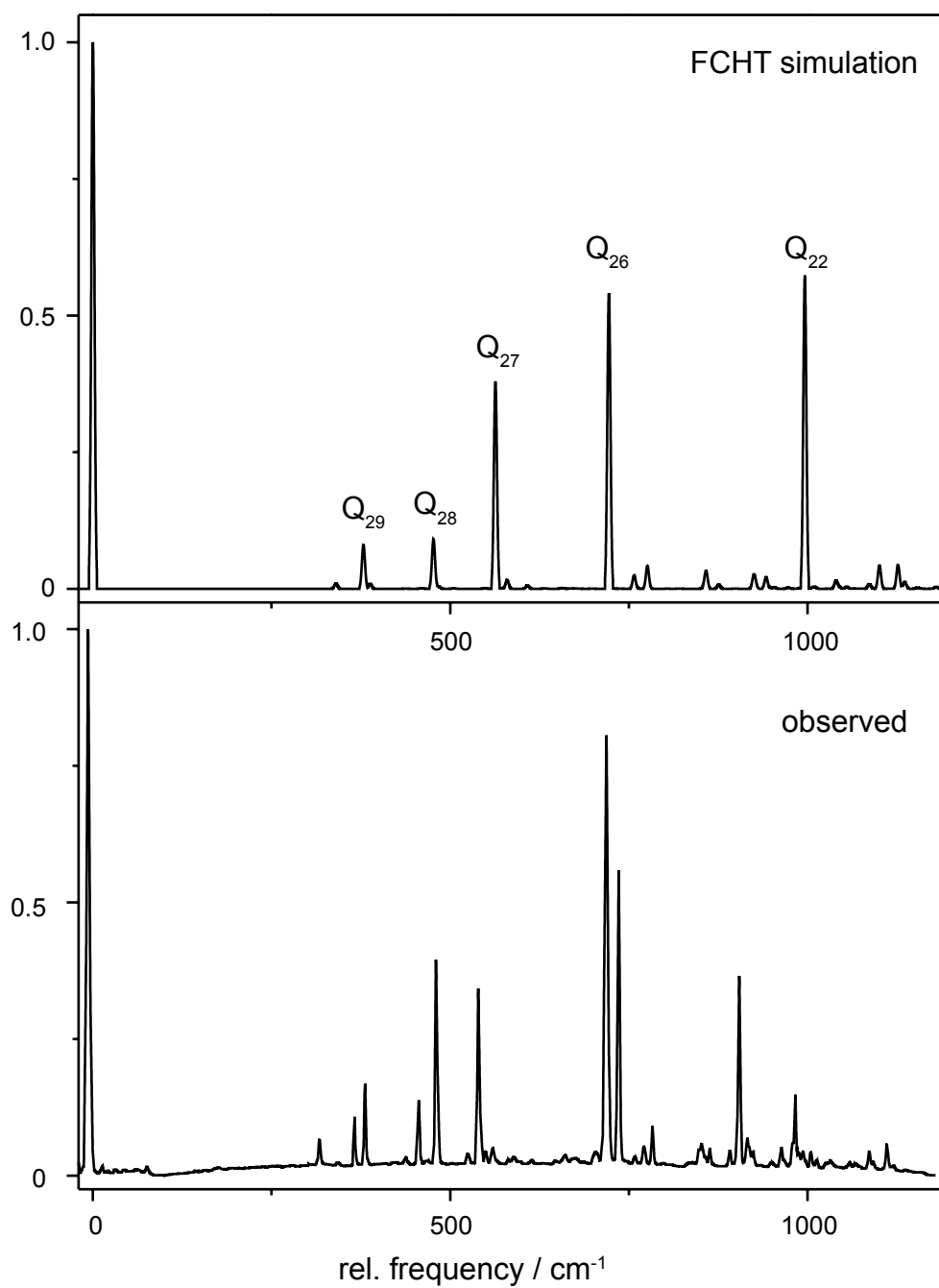
Figure 6.9: Comparison of the simulation of the vibronic spectrum of the ^1L_b state using the FCHT terms from equation 6.2 with the experimental spectrum [87].
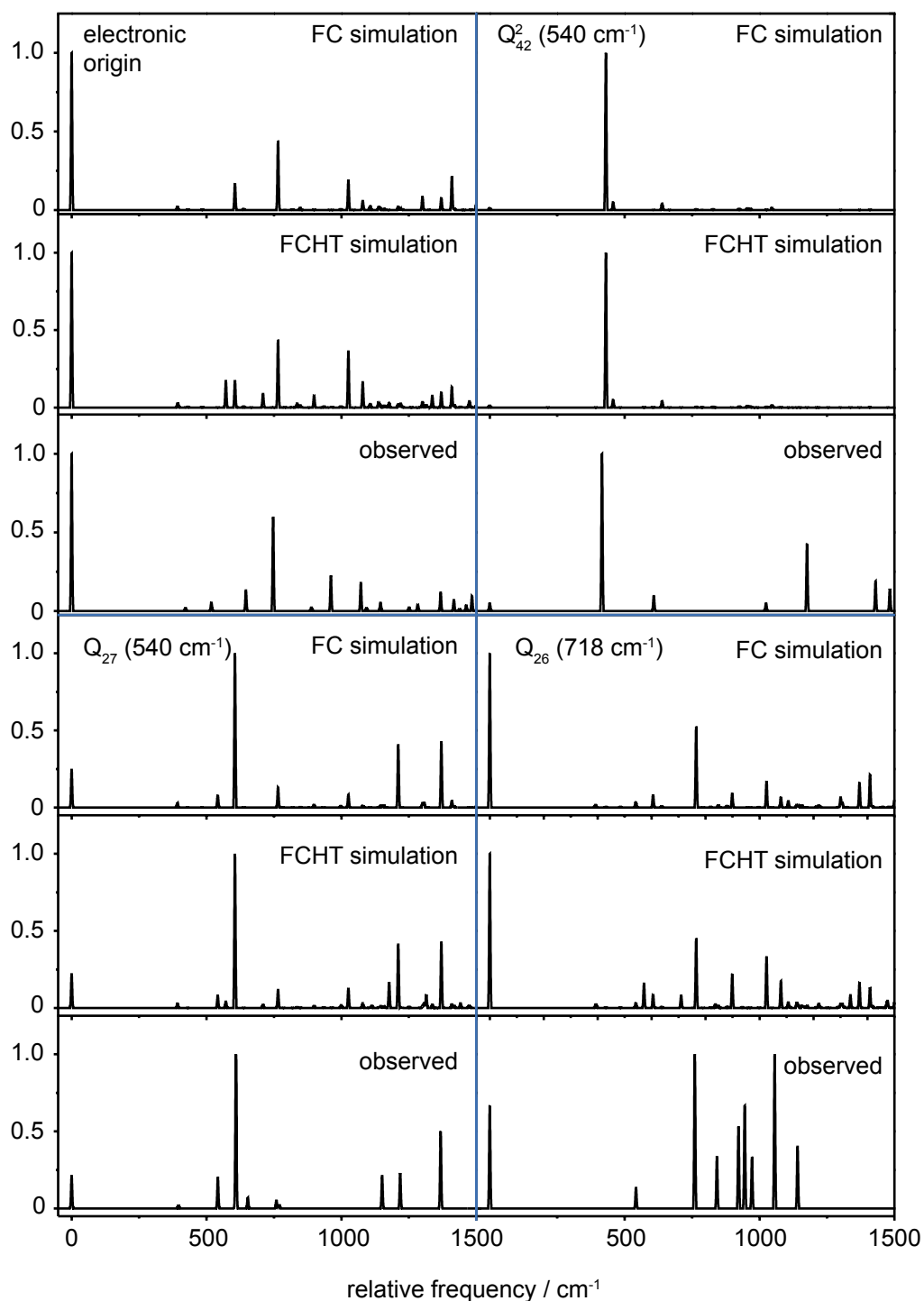
Figure 6.10: Simulation of the fluorescence emission spectrum through the vibronic origin of the ^1L_b state using only the FC terms from equation 6.2 and including the Herzberg-Teller terms. The other traces present emission spectra through the first overtone of mode Q'_{42} at 316 cm^{-1}, mode Q'_{27} at 540 cm^{-1}, and of mode 26 at 718 cm^{-1}.

in equation 6.2 after the linear term. Pointwise calculations of the TDM around the equilibrium position indicate that for some of the modes higher terms of the expansion are needed. Furthermore, anharmonicities should be taken into account in particular for the excited state potential energy surfaces. As the calculations revealed that the ^1L_a state minimum energy structure is located on the adiabatic S_1 state potential energy surface not far away from the ^1L_b minimum, noticeable deviations from harmonic behavior are likely. Anyway, the harmonic approximation is known to perform not overwhelmingly well for low-energy modes of complex molecules. In the extreme case, deficiencies of the perturbation theory methodology for vibronic coupling are involved.

6.4   Conclusions

We have performed *ab initio* optimizations of the geometries of the lowest excited singlet states of indole and computed the electronic transition properties from the ground state to the excited singlet states. The ^1L_a geometry is found to be very close to the conical intersection, connecting the ^1L_a and ^1L_b state. Apparently no noticeable barrier exists between the ^1L_a state and the CI, so that pure ^1L_a states, accessed by a spectroscopic transition, will funnel directly through the CI into the ^1L_b minimum.

From the optimized geometries, the axis reorientation angles upon electronic excitation are computed to +0.9° and -0.6° for excitation to the ^1L_b and ^1L_a states, respectively. The adiabatic excitation energy of the ^1L_b state calculated at the DFT/MRCI level of theory, with inclusion of ZPE correction, of 35173 cm^{-1} is in very good agreement with the experimentally determined value of 35231 cm^{-1}. At the same level of theory the ^1L_a–^1L_b splitting is predicted to be 1847 cm^{-1}. This relatively large gap suggests the application of Herzberg-Teller perturbation theory for the calculation of the vibronic spectrum of indole. In contrast to the case of tryptamine, where a low-lying conical intersection efficiently couples dark vibronic levels of the ^1L_a state to the bright ^1L_b foreground state, the vibronic spectrum of indole is dominated by vibrational activity in the ^1L_b state, with vibronic perturbations of selected vibrational modes. These modes bear some resemblance to the difference vector for passing from the ^1L_b to the ^1L_a geometry. Nevertheless, also coupling to the higher lying B_a and B_b states might contribute to the vibronic coupling. While these states are energetically far away, the larger transition dipole moment can compensate for this. Using DFT/MRCI, we calculated the vertical ex-

citation energy to the B_b state to be 6.08 eV (204 nm) and excitation to the B_a state at 6.53 eV (190 nm). The transition dipole moment vectors make an angle with the inertial a-axis of 18° and 33°, respectively. These values are in fair agreement with the experimental values from Albinsson and Nordén [138]. Within our numerical differentiation scheme for Herzberg-Teller coupling, the configuration interaction wave functions are variationally optimized in a CSF basis for each distorted geometry. The change of the configuration state vector with nuclear geometry may in principle be caused by the whole set of Russel-Saunders states, which are present in the basis. In order to break down the Herzberg-Teller activity into contributions from individual excited states one would need to expand the Herzberg-Teller derivatives in a sum over states. A thorough computation of this type is beyond the scope of the present publication, but will be subject of future work.

To sharpen the description of these results even more, one might say that the HT active modes drive the molecule into the conical intersection, since these modes mark the path along which both states are connected. This might be generalized; whenever there is a conical intersection on a path connecting two energetically nearby bound states, it will be the HT active modes that drive the molecule towards the CI, since it is exactly these modes, which couple the two states electronically.

Gradient difference and interstate coupling vectors for the CI of indole have been computed. While distortions due to the gradient difference vector are located in the pyrrole moiety, the interstate coupling is mediated through benzene like vibrations of Q_9 type. This vibration has the largest gradient of the transition dipole moment and induces therefore most efficiently HT coupling. Thus, this analysis also supports our suggestion that the HT active modes are the driving force for the coupling through the CI.

The preceding conclusions from the theoretical analysis will be used in the following for making some predictions, which we will check and try to verify using high resolution electronic spectroscopy of indole. A detailed description of the experimental results was published in the accompanying paper [87], but for the sake of completeness a short summary will be given at the end of this chapter.

- In the energy range up to about 2000 cm^{-1} the changes of the geometry measured via the rotational constants will indicate exclusively the ^1L_b geometry as final state.

- The axis reorientation angle θ_T for excitation to the vibrationless origin of the ^1L_b state is positive, i.e., it has the same sign as the TDM orientation θ.

Transitions to the vibrationless ^1L_a state are characterized by negative values for both angles, θ and θ_T. Therefore, the angles θ and θ_T have the same sign for pure electronic transitions into both, ^1L_b and ^1L_a, states. Opposite signs of θ and θ_T, which are experimentally observed [87], are a direct indication of vibronic coupling.

- Vibronic transitions in the ^1L_b ladder will show different electronic character depending on the form of the vibrational mode and the resulting vibronic coupling strength. For instance, Q'_{28}, which is calculated at 477 cm^{-1} in the excited ^1L_a character.

- Since the ^1L_a state exhibits no minimum along the path connecting it to the ^1L_b state, there is no observable vibrationless origin of this electronic state in the absorption spectrum.

- Although the FC factors for excitation to the ^1L_b and ^1L_a states are zero for the out-of-plane vibrations of the planar indole molecule, these bands gain some intensity via HT coupling. These bands should exhibit pure c-type character and it should be possible to observe them in a sensitive spectrometer.

- At about 2000 cm^{-1} above the ^1L_b origin a conical section with the ^1L_a state is located, which will alter the appearance of the absorption spectrum in this region considerably, similar to previous experimental observations in tryptamine [157].

6.5   Acknowledgment

6.6   Publication

The contents of this chapter has been published previously in slightly different form as *Vibronic coupling in indole: I. Theoretical description of the ^1L_a–^1L_b interaction*

and the electronic spectrum in *Phys. Chem. Chem. Phys.* (impact factor: 3.57), 2010, **12**, 4968–4979 by Christian Brand, Jochen Küpper, David W. Pratt, W. Leo Meerts, Daniel Krügler, Jörg Tatchen, and Michael Schmitt.

For this publication I did parts of the *ab initio* calculations, was involved in the discussions and prepared parts of the manuscript.

6.7   Further Research

In the accompanying publication by Küpper *et al.* the high resolution spectra of the origin and 12 vibronic bands of indole up to 1000 cm^{-1} above the origin of the ^1L_b were published [87]. Although direct excitation to the ^1L_a state was excluded from the excited state rotational constants, mode-selective vibronic coupling was reported, as predicted by theory. To monitor vibronic coupling between the ^1L_a and the ^1L_b states, information on the absolute sign of the transition dipole moment is needed. The analysis of the relative intensities in the respective spectra yields only the projection of the TDM vector on the inertial a and b-axes and hence no information about the sign. To extract information about the absolute sign of the TDM from the spectra *axis reorientation* was taken into account. For an introduction to axis reorientation refer to Section 1.4 on page 23. Hence, also the absolute sign of θ is accessible. For pure ^1L_b states both signs of both θ and θ_T are positive, while it is *vice versa* for the ^1L_a.

Vibronic coupling was observed for the vibrations 316, 379, 454, 480, 539, 720 and 908, and 968 cm^{-1} above the ^1L_b, while the origin and the bands at 718, 736, and 989 cm^{-1} are pure ^1L_b state transitions. In case of the band being at 907 cm^{-1} a vibronic coupling is not clearly indicated. Very strong effects were observed for the bands at 379, 480 and 539 cm^{-1}, which exhibit different signs for and θ and θ_T as well as an additional lifetime shortening. They are assigned to the modes Q'_{29} (379 cm^{-1}), Q'_{28} (480 cm^{-1}) and Q'_{27} (539 cm^{-1}), which correlate with the results in Table 6.7. The other coupling bands fulfil only one of these conditions. The band at 454 cm^{-1} ($40_0^1 41_0^1$) was ascertained to gain its L_a character in an indirect way via a Fermi resonance to the band at 480 cm^{-1}.

Recently Guissani *et al.* used CASPT2 and CASSCF to calculate the minimum energy path from the ^1L_a to the ^1L_b after UV excitation [174]. While they confirmed our findings concerning a barrierless transition from the ^1L_a to the ^1L_b state via conical intersections, they also found a conical intersection connecting the ^1L_b state

with the ground state at 4.50 eV (36295 cm^{-1}). This CI is characterized by a large out-of-plane distortion and resembles CIs which were found for ethane.

7. Simple Substituents

In the last chapter we took a closer look at the excited state photophysics of indole and discussed mode-selective vibronic coupling between the lowest two excited singlet states. The discussed effects depend on the relative energies of both states concerned which can be influenced in many ways. One possibility is to manipulate the surroundings: Solvent molecules may shift one or both states depending on their dielectricity constant, and even an argon matrix may lead to significant changes. Another possibility is the introduction of substituents. The large variety of potential substituents permits us to study the impact of all kinds of effects on the chromophore. First of all, all substituents exert an influence on the electrons of the frame via *through bond* effects. These are classified depending on whether the π-system (*mesomeric M-effect*) or the σ bond (*inductive I-effect*) is impacted. Larger substituents like an ethyl amino side chain give rise to several conformations which are also able to exert a *through space* effect on the chromophore. These will be introduced in detail later (Chapter 12, page 181). In the beginning we will focus on simple substituents. The term "simple substituents" in this context conveys that all the heavy atoms (everything except the hydrogen atoms) remain in the plane of symmetry and *through space* effects do not occur.

There has been a vast number of studies on substituted indole, most of them dealing with 3-methylindole, as this is the first step from the bare chromophore to the amino acid tryptophan [138, 146, 147, 149, 175–182]. In order to facilitate the following summary on substituted indoles the numbering of the atoms is given in Figure 7.1.

Early extensive studies on the lowest excited singlet states of methyl- and methoxyindole were presented by Eftink *et al.* [175] and Albinsson and Nordén [138]. The latter measured the UV and IR linear dichroism of 8 methyl- and methoxy-derivatives in stretched polyethylene hosts. The transition dipole moment (TDM) orientations of the first four $\pi\pi^*$ states were determined pointing to a conservation of the $^1L_b \leftarrow S_0$ TDM orientation for all substances but 4- and 6-methoxyindole. Flu-
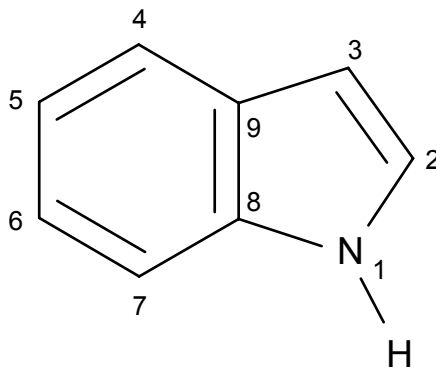
Figure 7.1: Atomic numbering in indole

orescence excitation and anisotropy spectra of all singly substituted methylindoles, 2,3-dimethylindole and several methoxyindoles in propylene glycol glass were presented by Eftink *et al.* and compared to CNDO/S calculations [175]. Their results are qualitatively similar to those of Albinsson and Nordén. Hager *et al.* recorded photoionization spectra of methyl and methoxyindoles and their van-der-Waals clusters [176]. They reported emission from the ^1L_b state for all derivatives in the gas phase, including 1,2,3,4-tetrahydrocarbazole[1]. Yet, experiments with rotationally resolved electronic spectroscopy proved the ^1L_a state to be lowest in energy in the gas phase [183]. Quite closely related to tetrahydrocarbazole is 2,3-dimethylindole. A long lasting debate was held concerning the ordering of the excited singlet states and finally resolved by Short and Callis who could show the ^1L_b state to be lowest in energy in the gas phase [146, 176, 177, 184].

The photophysics of indole and its methyl derivatives were studied very intensively in the group of Callis. Studies in solid argon [177], in solution [146] and in the gas phase [150], were performed with a variety of spectroscopical methods: Fender and Callis determined the origins of both the ^1L_a and the ^1L_b states of some methylindoles in solid argon [177], while Rehms and Callis obtained polarized two-photon fluorescence excitation spectra for indole, 5-methylindole, 3-methylindole and 2,3-dimethylindole in cyclohexane and butanol solutions [146]. Sammeth *et al.* observed a predominant L_a character at several vibrational bands of 3-methylindole on the basis of the two-photon intensity ratios for linear versus circular polarized excitation [179]. Furthermore, Sammeth *et al.* published laser induced fluorescence spectra of 3- and 5-methylindole along with several cluster spectra, assigned the torsional barrier of the methyl group in the ^1L_b state and estimated barriers for the ground and ^1L_a state [180]. A high resolution laser induced fluorescence work on the same

---

[1]In 1,2,3,4-tetrahydrocarbazole position 2 and 3 of the indole chromophore are bridged by an aliphatic butane group.

monomers by Remmers *et al.* provided the respective barriers for the S_0 and ^1L_b as well as the ground and excited state geometry [181].

Another group which is known to be very active in the field of substituted indoles is led by Sulkes. Using laser induced fluorescence mainly they determined the excited state lifetimes of a variety of indole derivatives, ranging from small substituents like fluorine atoms to large biomolecules like N-acetyltryptophan ethyl ester: Huang and Sulkes reported excited state lifetimes of a variety of singly substituted indoles as well as excited state tautomerism in 4-hydroxyindole [185]. The same authors present mass resolved ionization spectra of 2- and 3-methylindole and 5-methoxy-indole and their clusters with several solvents [178]. Arnold and Sulkes suggested that π binding is very potent in lowering the ^1L_a state in contrast to binding at the NH side [182]. They drew this conclusion from laser induced fluorescence spectra of some clusters of methyl- and methoxyindoles. 1,2,3,4-tetrahydrocarbazole and 1,2,3,4-tetrahydro-2-carboline show a lengthening of the excited state lifetime upon complexation with polar solvent molecules attributed to an increase in the L_a/L_b energetic gap, as reported by Teh *et al.* [186]. Sulkes and Borthwick compared the influence of several substituents at position 6 with those at position 4 and 5 [187]. Arnold and Sulkes published the excited state lifetimes of various indoles having carbonyl-containing substituents [188]. They observed a significant shortening of the lifetime for those derivatives in which the carbonyl group is directly attached to the chromophore. This phenomenon is attributed to a charge transfer process.

A charge-transfer-like state was also reported for the lowest excited singlet state of 5-cyanoindole (^1L_a) by Oeltermann *et al.* [189]. Lin *et al.* determined the ionization energies of 3- and 5-methylindole with vibrationally resolved mass analyzed threshold ionization spectroscopy [190] while photodissociation pathways in hydroxy- and methoxy-substituted indoles were investigated by Oliver *et al.* [191]. Barstis *et al.* performed vibrational analyses of 4-, 5,- and 6-fluoroindole in the first electronic excited state, based on 1C-R2PI spectra [192]. Furthermore, ionization energies of some fluoroindoles were reported by Liu *et al.* [193].

Taking into account the literature it becomes obvious that, although methyl- and methoxyindoles have attracted much attention, other substituents did not. An exception forms the great number of publications about excited state lifetimes by the group of Sulkes with no further spectroscopic information given. In the next four chapters 5-cyanoindole, 5-fluoroindole, 5-methoxyindole, and 6-methoxyindole will be discussed in detail. In Chapter 8 the results for 5-cyanoindole are presented. Here, anharmonic corrections to the excited state structure are made use of to allow

for an assignment of the excited state vibrations. Oeltermann *et al.* revealed that the cyano group this position leads to the ^1L_a state being lower in energy than the ^1L_b state [189]. As a cyano groups exerts a large negative mesomeric (-M) effect on the chromophore, the question arises if the same is true for a negative inductive (-I) effect. The results of the investigation of the electronic origin of 5-fluoroindole is presented in the next chapter. 5-Methoxyindole on the other hand donates electron density to the chromophor via a positive mesomeric effect. This engenders a large stabilization of the ^1L_b state compared to indole. The main focus of Chapter 10 is set on the question whether mode-selective coupling between the ^1L_a and ^1L_b states can be observed like in the case of indole. Furthermore, 5-methoxyindole can in principle be present in two different conformers regarding the methoxy group: *syn* and *anti*. To elucidate the different effects of substituents systematically, we choose the methoxy substituent and changed its position at the chromophore from 5 to 6. In Chapter 11 on 6-methoxyindole we take a look on the photophysical consequences of this modification.

8. 5-Cyanoindole

Abstract

The rovibronic spectra of two bands of 5-cyanoindole at 348 and 884 cm^{-1} have been measured and analyzed using a rigid rotor Hamiltonian. A vibrational assignment could be given on the basis of an anharmonic analysis of the vibrational spectrum of 5-cyanoindole making use of the information of the vibrationally averaged rotational constants. Strong vibronic mixing to a higher lying electronically excited state has been found.

8.1   Introduction

The photophysics and photochemistry of indole and substituted indoles is governed by the existence of two electronically excited singlet states, which are labeled ^1L_a and ^1L_b following the nomenclature of Platt for catacondensed aromatics [5]. Depending on the substituent the energy difference between these two states differs largely, in some cases even their energetic order is reversed. Vibronic spectroscopy with rotational resolution provides an elegant approach to the nature of the excited states via determination of the transition dipole moment directions.

For indole it is generally accepted now, that the lowest electronically excited singlet state of indole is a state with L_b character, followed by an L_a like state, approximately 1400 cm^{-1} higher in energy [87, 125, 150, 154, 194, 195]. This has been shown by quantum chemical calculations [154, 195] from the theory side and by two-photon-induced fluorescence anisotropy measurements [194], two-photon excitation spectroscopy [150], linear dichroism measurements on partially oriented indole in stretched polyethylene films [138], and by rotationally resolved spectroscopy of vibronic bands of indole [87, 125].

The introduction of substituents in different positions of the chromophore may change this energetic separation of the two states and sometimes even reverse them. For 5-methoxyindole the ^1L_a state is predicted to lie more than 4000 cm^{-1} above the ^1L_b state, one of the largest gaps in the indole row [196]. For isolated tetrahydrocarbazole, on the other hand, it could be shown that the lowest excited singlet state is the ^1L_a state [183], while for 2,3-dimethylindole the energy order critically depends on the local surrounding of the chromophore. Even a small perturbation like an argon matrix as local surrounding shifts the ^1L_a state below the ^1L_b, with a reversed order in gas phase [146, 177, 184]. In gas phase the spectral position and lifetime of the electronic origin of 5-cyanoindole (5CI) were determined by Huang and Sulkes using time-correlated single photon counting for S_1 levels in supersonic free jet expansions [185]. The rotationally resolved spectrum of the electronic origin was measured and analyzed by Oeltermann *et al.* [189].

In the present publication we show, how the information of vibrationally averaged rotational constants can be utilized for a straightforward assignment of rovibronic spectra.

8.2   Techniques

8.2.1   Experimental procedures

5CI ($\geq 98\%$) was purchased from Activate Scientific and used without further purification. The experimental set up for the rotationally resolved laser induced fluorescence is described in detail in Ref. [197] and Chapter 3. In brief, the laser system consists of a single frequency ring dye laser (Sirah Matisse DS) operated with Rhodamine 6G, pumped with 8 W of the 514 nm line of a Ar$^+$-ion laser (Coherent, Sabre 15 DBW). The dye laser output was coupled into an external folded ring cavity (Spectra Physics Wavetrain) for second harmonic generation. The resulting output power was constant at about 30 mW during the experiment. The molecular beam was formed by co-expanding 5CI, heated to 190°C, and 400 mbar of argon through a 200 μm nozzle into the vacuum chamber. The molecular beam machine consists of three differentially pumped vacuum chambers that are linearly connected by skimmers (1 mm and 3 mm, respectively) in order to reduce the Doppler width. The resulting resolution is 18 MHz (FWHM) in this set-up. In the third chamber, 360 mm downstream of the nozzle, the molecular beam crosses the laser beam at a right angle. The imaging optics setup consists of a concave mirror and two

plano-convex lenses to focus the resulting fluorescence onto a photomultiplier tube, which is mounted perpendicularly to the plane defined by the laser and molecular beam. The signal output was then discriminated and digitized by a photon counter and transmitted to a PC for data recording and processing. The relative frequency was determined with a *quasi* confocal Fabry-Perot interferometer. The absolute frequency was obtained by comparing the recorded spectrum to the tabulated lines in the iodine absorption spectrum [67].

8.2.2 Computational methods

Quantum chemical calculations

Structure optimizations were performed employing Dunning's correlation consistent polarized valence triple zeta (cc-pVTZ) from the TURBOMOLE library [161, 162]. The equilibrium geometries of the electronic ground and the lowest excited singlet states were optimized using the approximate coupled cluster singles and doubles model (CC2) employing the resolution-of-the-identity approximation (RI) [112, 163, 164] including spin-component scaling (SCS) modifications to CC2 [198]. All CC2 calculations were carried out utilizing the TURBOMOLE package, version 6.1 [199]. Vibrational frequencies and zero-point corrections to the adiabatic excitation energies have been obtained from numerical second derivatives using the NumForce script [199]. For more information regarding the quantum chemical calculations refer to Chapter 5

An anharmonic analysis of the vibrational spectrum allows for the determination of vibrational averaging effects due to the individual vibrational motion [200]. Such an anharmonic analysis is implemented in the Gaussian program package [167]. The procedure for the calculation of cubic and of some of the quartic force constants utilizes third derivatives of the potential energy with respect to the normal coordinates. They are calculated for the electronic ground state using numerical derivatives of analytical second derivatives of the MP2 energies using the 6-31G(d,p) basis set. We tried to calculate the same quantities for the excited state vibrational levels using CC2 theory. Since for CC2, only numerical second derivatives are available, numerical instabilities in the calculation of the third derivatives were too large to make the method of any use.

Fits of the rovibronic spectra using evolutionary algorithms

The optimization algorithm employed in the fit of molecular constants to the rotationally resolved electronic spectra is an evolutionary strategy adapting mutations *via* a covariance matrix adaptation (CMA-ES) mechanism. This algorithm was developed by Ostenmeier and Hansen [201, 202]. It belongs, like other search algorithms that are also used in our group (genetic algorithms (GA) [203] and evolutionary strategy employing second generation of derandomized evolutionary strategies (ES-DR2) [204]), to the group of global optimizers that were inspired by natural evolution. For a detailed description of this evolutionary strategy we refer to Refs. [196] and [203] and Chapter 4.

8.3   Results and Discussion

8.3.1   High resolution spectra of several vibronic bands of 5-cyanoindole

Figure 8.1 shows the rotationally resolved spectrum of the electronic origin of 5CI at 33874 cm^{-1}, taken from the publication by Oeltermann *et al.* [189]. The authors simulated the experimental spectrum with a rigid rotor Hamiltonian and almost pure *a*-type selection rules (the transition dipole moment (TDM) angle θ is determined to be 3° equivalent to less than 1% *b*-type for the spectrum). In the course of the present study we refitted this spectra using the CMA-ES strategy, and the values determined for all molecular parameter are well within the boundaries published previously. To facilitate the comparison for the vibrational bands, these values are given in Table 8.1. The enlarged portion detail of the spectrum shows the excellent agreement between experiment and simulation using the parameters from the best fit employing the CMA-ES strategy. The fit of the line shapes to Voigt profiles using a Gaussian (Doppler) contribution of 18 MHz yielded a Lorentzian contribution of 13±1 MHz to the total line width equivalent to an excited state life time of 12±1 ns, in fair agreement with the value from time-resolved spectroscopy of 16.9 ns by Huang and Sulkes [185]. The rovibronic spectra of the 0,0 + 349 and 0,0 + 884 cm^{-1} bands along with the simulations using the best fit parameter, given in Table 8.1 are shown in Figures 8.2 and 8.3. In the fit of the molecular parameters to the experimental spectra, we have set the rotational constants of the ground state to the

Table 8.1: Molecular constants of the electronic origin and of two vibronically excited bands of 5-cyanoindole obtained from the CMA-ES fits of the experimental spectra. Changes of the rotational constants are defined as: $\Delta B_g = B'_g - B''_g$, with B_g as rotational constants with respect to the inertial axes $g = a, b, c$ with primed quantities, defining the excited state and double primed the electronic ground state, respectively. The superscript e refers to the rotational constants at the equilibrium geometry, the superscript 0 to the zero-point vibrational averaged inertial parameters.

	Experiment			Theory		
	Origin[a]	+349	+884	SCS-CC2[c]	MP2(B^e)[d]	MP2(B^0)[d]
A'' / MHz	3370.36(16)	3370.36[b]	3370.36[b]	3364	3364	3346
B'' / MHz	738.00(2)	738.00[b]	738.00[b]	734	734	731
C'' / MHz	605.53(1)	605.53[b]	605.53[b]	602	603	600
$\Delta I''$ / amu Å^2	-0.1385	-0.1385	-0.1385	0.0	0.0	-0.15
A' / MHz	3299.9(16)	3300.3(2)	3295.8(2)	3281	-	-
B' / MHz	730.32(3)	730.33(2)	730.37(1)	725	-	-
C' / MHz	598.16(2)	598.53(1)	598.67(1)	594	-	-
$\Delta I'$ / amu Å^2	-0.2582	-0.7575	-1.1246	0.0	-	-
ΔA / MHz	-70.46(1)	-70.10(1)	-74.64(1)	-83	-	-
ΔB / MHz	-7.68(1)	-7.67(1)	-7.63(1)	-9	-	-
ΔC / MHz	-7.37(1)	-7.40(1)	-7.26(1)	-6	-	-
θ / °	3(3)	32(1)	22(1)	9.4	-	-
ν_0 / cm^{-1}	33874.32(1)	34223.08(1)	34757.89(1)	34811	-	-
$\Delta Lorentz$ / MHz	13(1)	9(1)	13(1)	-	-	-

[a] from Ref. [189]

[b] Held fixed at the values of the electronic origin.

[c] Using the cc-pVTZ basis set.

[d] Using the 6-31G(d,p) basis set.
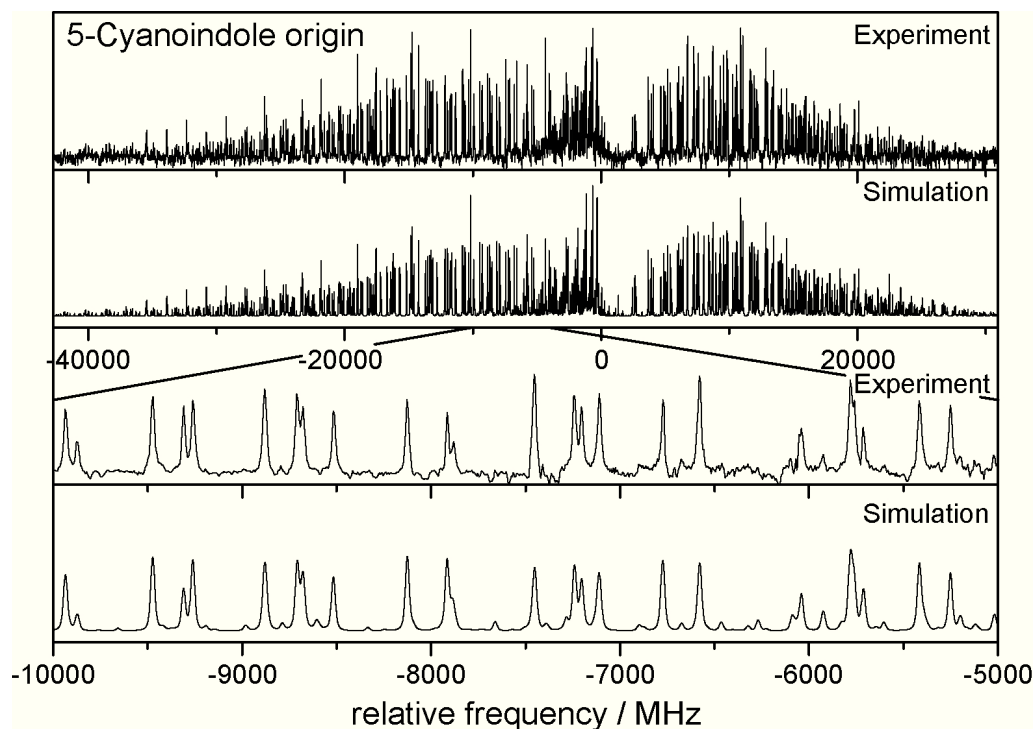
Figure 8.1: Rotationally resolved electronic spectrum of the electronic origin of 5-cyanoindole [189].

values determined from the fit of the electronic origin. This is justified by the fact, that the signal/noise ratio is nearly two orders of magnitude better for the origin band. Both excited vibronic bands exhibit a considerably larger b-type character, than the origin band with TDM angles of 33 and 23°. The life time of the 349 cm^{-1} band increases to 18±2 ns compared to 12 ±1 ns for both the origin and the 884 cm^{-1} band.

8.3.2   Computational Results

Structure and Vibrational Averaging

Commonly, the vibrationally averaged inertial parameters, which are obtained from the experiment are compared to equilibrium values at the potential energy minimum, obtained from quantum chemical calculations. Table 8.1 collects the structural data i.e. rotational constants (A, B, and C) in the electronic ground (double prime) and excited (single prime) states, their changes upon electronic excitation (ΔA, ΔB,
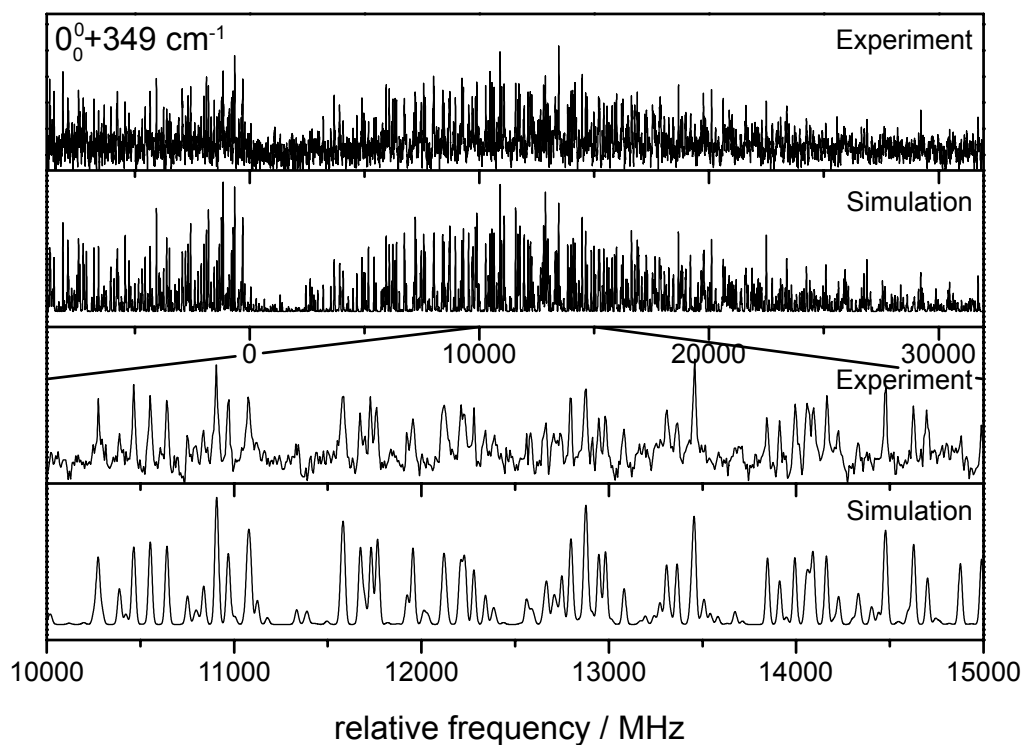
Figure 8.2: Rotationally resolved electronic spectrum of the vibronic band at 0,0 +348 cm^{-1}.

and ΔC), and the respective inertial defects.[1]

The equilibrium structures of the ground and electronically excited states, optimized at the SCS-CC2 and MP2 levels of theory, are planar without imposing symmetry constraints during the optimization. Their *ab initio* calculated inertial defects are therefore exactly zero. The experimental values contain vibrational corrections from the vibrational averaging of the ground and excited state structures. The difference of the experimental and the calculated ΔI values gives 1% as first order approximation to the amount of vibrational averaging contained in the experimental rotational constants.

For the electronic ground state the zero-point vibrationally averaged rotational constants are compiled in Table 8.1. While the inertial defect calculated using the equilibrium inertial parameters is exactly zero as expected for a planar structure, it amounts to -0.15 amu Å^2 for the vibrationally averaged rotational constants, very close to the experimental value of -0.1385 amu Å^2. We thus conclude, that vibrational averaging of the rotational constants is sufficiently well described by the

---

[1] The inertial defect is a measure for the non-planarity of a molecule in a given electronic state, and is defined as: $\Delta I = I_C - I_A - I_B$. For a planar molecule it is close to zero with out-of-plane vibrations generally causing a negative contribution to the inertial defect, and in-plane vibrations often having a small positive contribution [21].
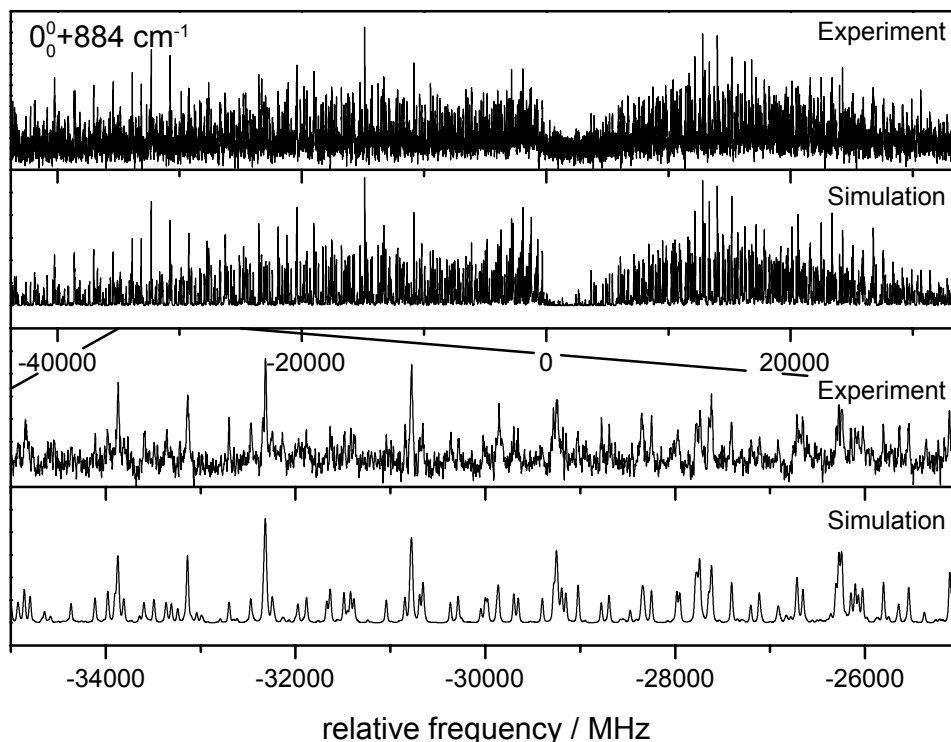
Figure 8.3: Rotationally resolved electronic spectrum of the vibronic band at 0,0 +884 cm^{-1}.

quadratic, cubic and some of the quartic force constants as included in this study. The deviations between the experimental rotational constants and the vibrationally zero-point averaged calculated values amount to less than 1%, thus confirming our first approximation. The complete list of anharmonic and harmonic frequencies, vibrationally averaged rotational constants and inertial defects is given in the online supplementary material (Table 8.3).

An analysis of the electronically excited state vibrations can be performed under the assumption, that the directions and amplitudes of the vibrational displacement vectors are similar in the ground and the electronically excited states. The change of the rotational constants upon vibronic excitation can then be calculated from the sum of the zero-point averaged changes due to pure electronic excitation and to changes due to the individual vibrational excitation. The former are experimentally obtained from the changes of the rotational constants of the vibrationless origin (cf. Table 8.1), the latter from the vibrational anharmonic analysis, compiled in Table 8.2.

The assignment of the 349 cm^{-1} band to vibration 43 (cf. Table 8.3) and of the 884 cm^{-1} band to vibration 28 has been made on the basis of three independent pieces of information. The calculated (anharmonic) vibrational frequencies are uti-

lized in order to narrow down the range of possible modes. Then the vibrationally induces changes of the inertial defects and rotational constants are compared to the experimental value. As these changes are most pronounced for the A' rotational constant, we attribute the main influence to it. In the case of the 349 cm^{-1} band an assignment which is only based on vibrational frequencies could also be made to mode 39 ($\nu_{anharm} = 384$ cm^{-1}) or mode 42 ($\nu_{anharm} = 326$ cm^{-1}) (cf. Table 8.3). Judging from a comparison of the inertial defect, however, mode 39 has to be excluded as $\Delta I'$ increases for this mode, quite in contrast to the experimental finding. Moreover, this vibrations has a relatively large anharmonic correction to the A' rotational constant of +4.6 MHz, which stands in further contradiction to the experimental finding of +0.4 MHz. This slight impact of the vibration on A' is only mirrored by mode 43 ($\Delta A'_{vib} = -0.6$ MHz). For mode 42, the resulting inertial defect matches the experiment, but $\Delta A'_{vib}$ decreases too much (-4.5 MHz).

Mode 28 at 884 cm^{-1} is first assigned on the basis of the anharmonic frequency (869 cm^{-1}). Also, an assignment to mode 24 (902 cm^{-1}) or 29 (855 cm^{-1}) based on the frequency information alone would be possible, but the quite large negative inertial defect of the mode contradicts at least an assignment to mode 24. The preference of mode 28 is based on the significant decrease of the A' rotational constant which is not reproduced by mode 29.

υ_{28} υ_{41} υ_{43}
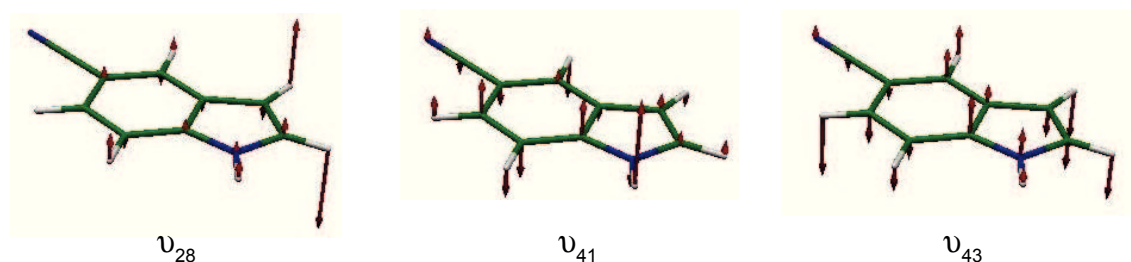
Figure 8.4: Vibrational modes 28, 41, and 43.

The displacement vectors of the modes 28 and 43, which are assigned as being responsible for the 349 cm^{-1} and the 869 cm^{-1} bands are shown in Figure 8.4 together with mode 41. The latter experiences the largest frequency shift of all modes in the anharmonic calculation (+843 cm^{-1}). As can be seen seen, this mode resembles an inversion vibration of the NH bond, which is known to be very anharmonic. Hence, this large anharmonic correction confirms the validity of the anharmonic calculations for the presented analysis.

Table 8.2: Inertial defects of the excited vibronic states $\Delta I'$, vibrational contributions to the rotational constants of the excited vibronic states $\Delta A'_{\text{vib}}$, $\Delta B'_{\text{vib}}$, $\Delta C'_{\text{vib}}$ (defined as $\Delta X_{\text{vib}}(Q_i) = X(Q_i) - X(Q_0)$). Experimental values are extracted from the parameters in Tab. 8.1, calculated values are from an anharmonic analysis of the electronic ground state at the MP2/6-31G(d,p) level of theory; see text for details.

vibration	0^0_0		43^1_0		28^1_0	
	exp.	calc.	exp.	calc.	exp.	calc.
ν / cm^{-1}	-	-	349	338	884	869
$\Delta I'$ / amu Å^2	-0.14	-0.15	-0.76	-0.63	-1.12	-0.38
$\Delta A'_{\text{vib}}$ / MHz	-	-	+0.4	-0.6	-4.1	-2.2
$\Delta B'_{\text{vib}}$ / MHz	-	-	±0.0	±0.0	+0.1	±0.0
$\Delta C'_{\text{vib}}$ / MHz	-	-	+0.4	+0.3	+0.5	±0.0

Transition Dipole Moment Orientation

The direction of the transition dipole moment (TDM) in the molecular frame is an important indicator to the electronic nature of the excited state. For a planar molecule its orientations with respect to the inertial a and b-axes are defined via the angle θ, which is the angle of the transition moment vector with the molecule fixed a-axis:

$$\mu_a = \mu \, \cos\theta \quad \text{and} \quad \mu_b = \mu \, \sin\theta$$

The squares of the projections onto the inertial axes are directly proportional to the experimentally observed contribution to the band type in the electronic absorption spectrum. The SCS-CC2 calculations yield comparably small values of θ for the S_1 state ($9°$) as observed in experiment, while the value obtained for the S_2 state is much larger ($65°$). Thus, the calculations confirm the experimental finding that the TDM orientation of the lowest electronically excited state is mainly directed along the a-axis. The transition to the second excited singlet state is predicted to an ab-hybrid, with predominantly b-type.

In a previous publication we have shown, that the excitations to the S_1 and S_2 states are heavily mixed and the second excited singlet state is accompanied by a considerable charge migration from the indolic NH group to the cyano group [189]. The vibronic bands at 349 and 884 cm^{-1} have a considerably larger transition dipole moment angle θ than the origin band. Since the origin of the next excited singlet state S_2 is expected to be adiabatically more than 3000 cm^{-1} higher in energy [189], the only mechanism which can give rise to such a strong change in the TDM is

Table 8.3: Anharmonic and harmonic vibrational frequencies and vibrationally averaged rotational constants for the individual vibrations.

Mode	ν_{harm}	ν_{anharm}	A/MHz	B/MHz	C/MHz	ΔI/amu Å^2
1	3741	3568	3344.8	730.7	599.8	-0.190
2	3345	3216	3345.2	730.6	599.8	-0.183
3	3327	3198	3345.3	730.6	599.8	-0.181
4	3280	3142	3345.0	730.6	599.8	-0.220
5	3265	3123	3345.2	730.5	599.7	-0.184
6	3258	3133	3345.0	730.6	599.8	-0.192
7	2203	2161	3345.4	729.3	598.9	-0.186
8	1706	1665	3342.6	729.9	599.5	-0.576
9	1648	1602	3342.4	730.1	599.1	0.165
10	1588	1551	3344.2	730.4	599.7	-0.313
11	1550	1513	3343.3	729.9	599.2	-0.122
12	1530	1502	3343.9	730.1	599.7	-0.540
13	1504	1466	3344.1	730.5	599.3	0.269
14	1455	1423	3341.8	730.2	599.3	0.012
15	1384	1359	3345.7	730.5	599.6	-0.064
16	1337	1310	3345.4	730.2	599.5	-0.163
17	1293	1274	3346.3	730.7	599.7	0.004
18	1266	1247	3345.7	730.4	599.5	0.059
19	1185	1168	3345.4	730.8	599.8	-0.063
20	1180	1164	3345.8	730.3	599.5	-0.046
21	1136	1120	3347.1	730.6	599.8	-0.114
22	1113	1088	3346.1	730.8	599.7	0.182
23	966	963	3346.8	730.5	599.6	0.028
24	913	902	3346.1	730.8	599.7	0.069
25	864	999	3344.1	730.6	599.9	-0.416
26	824	943	3347.6	730.5	599.9	-0.359
27	802	806	3346.9	730.5	599.6	-0.010
28	795	869	3344.2	730.7	599.9	-0.382
29	760	855	3345.6	730.6	599.9	-0.347
30	743	746	3346.2	730.5	599.8	-0.195
31	720	751	3344.9	730.6	599.9	-0.423
32	623	620	3345.6	730.9	599.8	0.147
33	591	627	3344.5	730.7	600.0	-0.423
34	562	715	3346.8	730.9	600.1	-0.334
35	542	539	3357.6	730.9	599.9	0.518
36	475	657	3335.9	731.0	600.2	-0.856
37	425	419	3350.8	730.5	599.7	0.096
38	405	621	3345.8	730.5	599.9	-0.523
39	385	384	3351.0	731.0	599.9	0.335
40	384	629	3345.3	730.8	600.2	-0.527
41	347	1190	3350.4	730.4	600.0	-0.430
42	248	326	3341.9	731.2	600.4	-0.637
43	207	338	3345.8	730.7	600.2	-0.633
44	141	140	3372.1	731.5	600.2	1.323
45	98	114	3320.0	731.2	600.5	-1.814

vibronic coupling of these modes to the perturbing S_2 state.

8.4   Conclusions

The vibrational bands at 349 and 884 cm^{-1} above the electronic origin were recorded at rotational resolution and analyzed using an asymmetric rotor Hamiltonian by means of an evolutionary strategy approach. Comparison to anharmonic corrections calculated at the MP2 (6-31G(d,p)) level of theory to the experimentally determined values allowed an assignment of the observed vibrations. This assignment is not only based on the corrected frequencies but accounts for vibrationally induced changes to the excited state geometry as well. Both changes in the rotational constants and the planarity of the molecule are made use of.

The orientation of the TDM vector deviates for both vibrational bands significantly from the value reported for the vibrationless origin [189]. As the change in the TDM orientation is more pronounced for the band at 349 cm^{-1} than for the band at 884 cm^{-1} (+29° compared to +19°), mode-selective coupling to an electronic state lying higher in energy is to be expected. A Herzberg-Teller analysis [60] would be required to explain the observed effects as it has been done before in our group for both indole [195] and tryptamine [157]. The respective analysis is being prepared to answer this question.

8.5   Acknowledgement

8.6   Publication

The rotationally resolved spectra were recorded in collaboration by Olivia Oelter-mann, Martin Wilke, Beatrice Happe, and me. The calculations were done partly by Michael Schmitt and by me. Furthermore, I analyzed the spectra and wrote parts of the paper.

9. 5-Fluoroindole

Abstract

The structure and electronic properties of the electronic ground state and the lowest excited singlet state (S_1) of 5-fluoroindole (5FI) were determined by using rotationally resolved spectroscopy of the vibrationless electronic origin of 5FI. From the parameters of the axis reorientation Hamiltonian, the absolute orientation of the transition dipole moment in the molecular frame was determined and the character of the excited state was identified as L_b.

9.1   Introduction

The electronic properties of the aromatic chromophore indole strongly depend on the nature of the substituents and of the local surrounding. As pointed out in the introduction of the chapter on simple substituents, the two lowest excited singlet states even might change their energetic order, depending on the polarity of the local surrounding. This surrounding can be made up by a matrix, by solvent molecules which form complexes with the chromophore, or flexible substituents, which can interact with the chromophore *via* through-bond or through-space interactions [205–207]. Recently, Oeltermann *et al.* has shown that the introduction of a cyano group, which exerts a strong negative mesomeric (-M) effect in 5-position of the indole ring (5-cyanoindole 5CI), shifts the ^1L_a state below the ^1L_b [189]. In this chapter, we investigate the effect of a purely negative inductive (-I) effect in the 5-position as exerted by a fluorine substituent.

A thorough vibrational and vibronic analysis of the three 4-, 5-, and 6-fluoroindoles has been given by Barstis *et al.* [192] based on jet-cooled one-color resonant two-photon ionization time-of-flight mass spectra (R2PI TOF-MS). Huang and Sulkes

[185] reported the origin frequency using R2PI TOF-MS and the fluorescence life time of 5-fluoroindole from time-correlated single photon counting for S_1 state levels. Their value of 33911 cm^{-1} for ν_0 deviates by 431 cm^{-1} from the value of Barstis *et al.* [192]. In this publication, we find 425 cm^{-1}, supporting the value of Barstis *et al.*.

9.2   Techniques

9.2.1   Experimental procedures

5-Fluoroindole ($\geq$ 98%) was purchased from Activate Scientific and used without further purification. The experimental set-up for the rotationally resolved laser induced fluorescence is described in detail in Chapter 3. In brief, the laser system consists of a single frequency ring dye laser (Sirah Matisse DS) operated with Rhodamine 6G, pumped with 7 W of the 514 nm line of an Ar$^+$-ion laser (Coherent, Sabre 15 DBW). The dye laser output was coupled into an external folded ring cavity (Spectra Physics Wavetrain) for second harmonic generation. The resulting output power was constant at about 15 mW during the experiment. The molecular beam was formed by co-expanding 5FI, heated to 45°C, and 500 mbar of argon through a 200 μm nozzle into the vacuum chamber. The molecular beam machine consists of three differentially pumped vacuum chambers that are linearly connected by skimmers (1 mm and 3 mm, respectively) in order to reduce the Doppler width. The resulting resolution is 18 MHz (FWHM) in this set-up. In the third chamber, 360 mm downstream of the nozzle, the molecular beam crosses the laser beam at a right angle. The imaging optics set-up consists of a concave mirror and two plano-convex lenses to focus the resulting fluorescence onto a photomultiplier tube, which is mounted perpendicularly to the plane defined by the laser and molecular beam. The signal output was then discriminated and digitized by a photon counter and transmitted to a PC for data recording and processing. The relative frequency was determined with a *quasi* confocal Fabry-Perot interferometer. The absolute frequency was obtained by comparing the recorded spectrum to the tabulated lines in the iodine absorption spectrum [67].

9.2.2   Computational methods

Quantum chemical calculations

All calculations were performed with the Turbomole program package [162, 199]. Dunning's correlation consistent polarized valence triple zeta (cc-pVTZ) basis sets from the TURBOMOLE library were used [161]. The equilibrium geometries of the electronic ground and the lowest excited singlet states were optimized using the approximate coupled cluster singles and doubles model (CC2) employing the resolution-of-the-identity approximation (RI) [112, 163, 164]. Spin-component scaling (SCS) modifications to CC2 were also taken into account [198]. Vibrational frequencies and zero-point corrections to the adiabatic excitation energies have been obtained from numerical second derivatives using the NumForce script [199]. Natural population analyses (NPA) [208] have been performed at the CC2 optimized geometries using the wave functions from the CC2 calculations as implemented in the TURBOMOLE package [199]. For more information regarding the computational methods refer to Chapter 5.

Fits of the rovibronic spectra using evolutionary algorithms

We make use of an evolutionary strategy (ES), namely the covariance matrix adaptation ES (CMA-ES) for the fit of the rovibronic spectrum. This algorithm was developed by Ostermeier and Hansen [201, 202]. It belongs, like the other search algorithms that are employed in our group, to the class of global optimizers that were inspired by evolutionary processes. For a detailed description of these evolutionary and genetic strategies for fitting of molecular spectra refer to Chapter 4.

9.3   Results and Discussion

9.3.1   High resolution spectrum of the origin band of 5-fluoroindole

Figure 9.1 shows the rotationally resolved spectrum of the electronic origin of 5FI at 34342 cm^{-1}. The experimental spectrum could be simulated with a rigid rotor Hamiltonian, containing axis reorientation [43, 125] and *ab*-hybrid type selection rules with 27% *a*-type and 73% *b*-type. For molecules with less than C$_{2v}$ symmetry,

the geometry changes upon electronic excitation rotate the inertial axis system. For a planar molecule, this rotation can be described using a single rotational angle θ_T. In 5-fluoroindole, the c-axis is perpendicular to the aromatic plane, and θ_T describes the rotation of the a''-axis of the ground state onto the a'-axis of the excited state about the c-axis. This axis reorientation angle is defined in Figure 9.2. An magnified portion of the spectrum shows the excellent agreement between experiment and simulation using the parameters from the best fit employing the CMA-ES strategy. The fit of the line shapes to Voigt profiles using a Gaussian (Doppler) contribution of 18 MHz yielded a Lorentzian contribution of 13±2 MHz to the total line width, equivalent to an excited state life time of 12±4 ns.
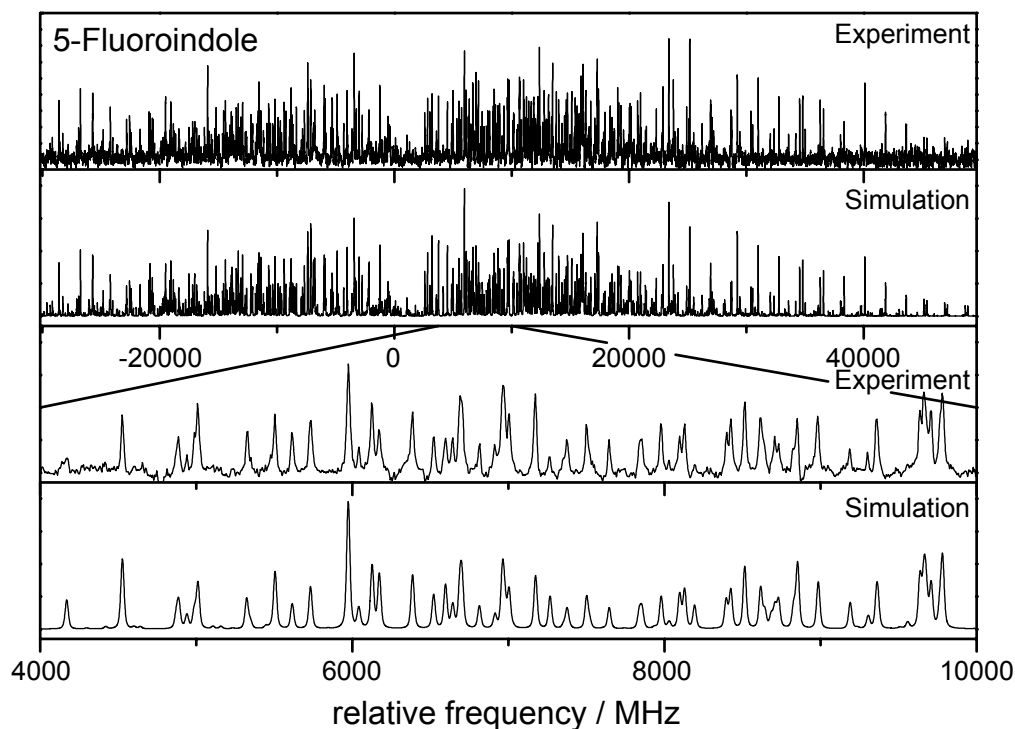
Figure 9.1: Rotationally resolved electronic spectrum of the electronic origin of 5-fluoroindole.

Different thermalization of the JK_AK_c states in a molecular beam requires a description of populations using several temperatures, which take into account the dependence of the rotational cooling from the angular momentum. We used the two temperature model, proposed by Wu and Levy [82] with $n_i = e^{-E_i/kT_1} + we^{-E_i/kT_2}$, were n_i is the population of the ith rovibronic level at energy E_1, k is the Boltzmann constant, T_1 and T_2 are the two temperatures, and w is a weighting factor modelling the contribution from T_2. Best agreement between experimental and simulated spectrum could be obtained with T_1=2.5 K, T_2=4.8 K and w=0.2.

The results of the fit are compiled in Table 9.1. Apart form the rotational constants, which contain the information about the structure of the molecule in both electronic states, the transition dipole moment (TDM) orientation, measured by the angle θ is obtained. Although its sign is undetermined (see Section 9.3.2 below), the axis reorientation Hamiltonian yields the relative signs of θ and θ_T as $\pm$. This means, that if θ is positive also θ_T will be positive and *vice versa*. Using information from the optimized structures for both states from *ab initio* calculations (Section 9.3.2), the absolute sign of θ can be determined.

9.3.2 Computational Results

Table 9.1: CC2/cc-pVTZ calculated molecular parameters of 5-fluoroindole vs. experimental values. Changes of the rotational constants are defined as: $\Delta B_g = B'_g - B''_g$, with B_g as rotational constants with respect to the inertial axes $g = a, b, c$. The *ab initio* calculated constants represent equilibrium values, while the experimental constants are zero-point vibrationally averaged. For details see text.

	CC2/cc-pVTZ	exp.
A''/MHz	3520	3519.57(4)
B''/MHz	1019	1019.79(1)
C''/MHz	790	790.87(1)
$\Delta I''/\text{amu Å}^2$	0.0	-0.1487
A'/MHz	3395	3386.34(3)
B'/MHz	1018	1019.83(1)
C'/MHz	783	784.09(1)
$\Delta I'/\text{amu Å}^2$	0.0	-0.2468
$\Delta A/\text{MHz}$	-125	-133.23(2)
$\Delta B/\text{MHz}$	-1	+0.043(1)
$\Delta C/\text{MHz}$	-7	-6.78(1)
$\theta/°$	± 40	$\pm 59(1)$
$\theta_T/°$	± 0.65	$\pm 0.8(1)$
ν_0/cm^{-1}	35144	34335.89(1)

Table 9.1 collects the structural data, i.e. rotational constants (A, B, and C) in the electronic ground (double prime) and excited (single prime) states, their changes upon electronic excitation (ΔA, ΔB, and ΔC), and the respective inertial defects, which are a measure for the non-planarity of a molecule in a given electronic state, and are defined as: $\Delta I = I_C - I_A - I_B$. For a planar molecule the experimentally determined inertial defect is small and negative. The planar equilibrium structures, calculated at the CC2/cc-pVTZ level of theory both have inertial defects, which are exactly zero, without imposing symmetry constraints in the geometry optimizations.

The experimental value contains vibrational corrections from the vibrational averaging of the ground and excited state structures. The difference of the experimental and the calculated ΔI values gives a first order approximation to the amount of vibrational averaging contained in the experimental rotational constants. We estimate the vibrational contributions to the equilibrium rotational constants to be less than 0.1 % of the value of the respective rotational constant, i.e. a maximum of 3 MHz absolutely.

The genuine CC2 and the SCS-CC2 optimized geometries are almost identical for the lowest excited singlet state of 5FI. Here, CC2 is capable of accurately predicting the geometry parameters of the lowest excited singlet state. In contrast, we found for 5CI [189] that genuine CC2 yields the reverse adiabatic order of the lowest two $\pi\pi^*$ states as compared to SCS-CC2 or SOS-CC2. As a consequence, for that case only the spin-scaled CC2 variants gave rotational constants and TDM orientations in agreement with our experimental high-resolution spectra.

Table 9.2 gives the bond lengths of 5FI in the electronic ground and lowest excited singlet state and their changes, as obtained from the CC2/cc-pVTZ calculations. For atomic numbering cf. Figure 9.2. The bond lengths changes upon electronic excitation are compared to those of 5CI and indole. The lowest electronically excited singlet state in indole was shown to be the ^1L_b state [125, 138, 141, 150, 152, 153, 175], while recently, we could show, that the lowest excited state in 5CI is the ^1L_a state [189]. The bond length changes in 5FI clearly show, that the lowest excited state here is the ^1L_b, like in indole.

The electronic nature of the excited state can also be deduced from the orientation of the transition dipole moment (TDM) in the molecular frame. For a planar molecule the TDM orientation with respect to the inertial a-axis is defined via:

$$\mu_a = \mu \ \cos\theta \tag{9.1}$$

Here, θ is the angle of the transition moment vector with the molecule fixed a-axis. The experimentally observed intensities of a and b-type transitions in the electronic absorption spectrum are directly proportional to the squares of the projections of the TDM onto the inertial a and b axes. One cannot however, distinguish from the relative intensities of a- and b-lines alone between the two orientations (I) and (II) in Figure 9.2, since they have the same projections onto the inertial axes.

Table 9.2: Bond lengths (in pm) of 5FI in the electronic ground and lowest excited singlet state at the CC2/cc-pVTZ level of theory and their changes Δ in pm upon electronic excitation. For atomic numbering cf. Figure 9.2. The bond lengths changes upon excitation to the lowest excited singlet states of 5CI (SCS-CC2/cc-pVTZ) and indole (CC2/cc-pVTZ) are given for comparison.

	S_0	S_1	Δ(5FI)	Δ(5CI)[189]	Δ(indole)[195]
N_1-C_2	137.7	142.2	+4.5	$\pm$0.0	+4.0
C_2-C_3	137.7	138.1	+0.4	+1.9	+0.6
C_3-C_9	142.8	143.1	+0.3	-2.1	-0.2
C_9-C_4	140.6	140.9	+0.3	+1.6	+0.6
C_4-C_5	138.0	142.4	+4.4	+4.8	+4.6
C_5-C_6	140.2	141.2	+1.0	+3.0	+1.5
C_6-C_7	138.9	142.8	+3.9	+3.4	+3.9
C_7-C_8	139.7	141.0	+1.3	+0.6	+1.2
C_8-C_9	142.3	145.5	+3.2	+4.0	+4.0
C_8-N_1	137.7	135.8	-1.9	+0.6	-1.6
N_1-H	100.5	100.9	+0.4	$\pm$0.0	+0.2
C_5-F	135.5	134.2	-1.2	-	-
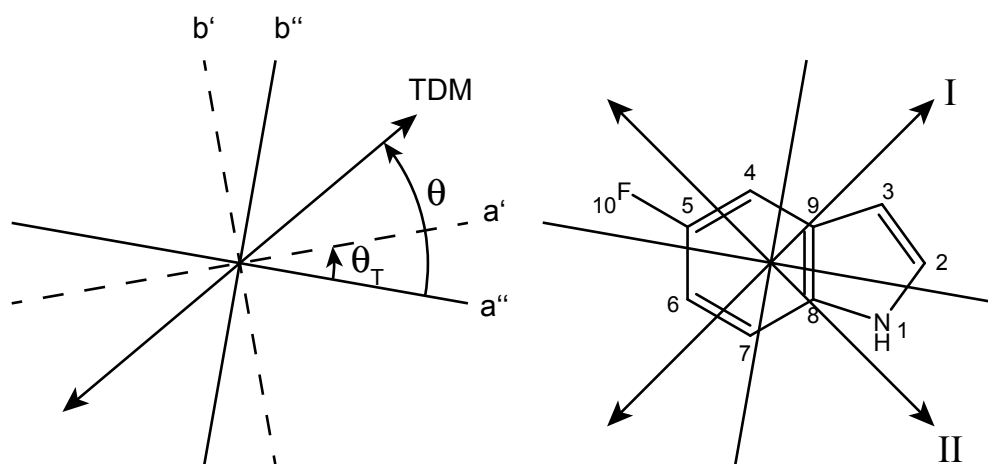
Figure 9.2: a) Definition of the positive direction of the transition dipole moment angle θ and of the axis reorientation angle θ_T. b) Atomic numbering of 5FI and orientation of the inertial axes and the two possible transition dipole moment orientations.

Hougen and Watson [42] gave a relation from which the axis reorientation angle can be computed for any planar molecule using Cartesian coordinates in the principal axis system of each state (cf. Section 1.4):

$$tan(\theta_T) = \frac{\sum_i m_i(a_i' b_i'' - b_i' a_i'')}{\sum_i m_i(a_i' a_i'' + b_i' b_i'')} \tag{9.2}$$

Here, the doubly primed coordinates a_i'' and b_i'' refer to the coordinates of the ith atom in the principal axis system in the electronic ground state, the singly primed coordinates to the respective excited state coordinates and m_i is the atomic mass of the ith atom in the molecule. Using the CC2 optimized structures for the ground and excited states, we obtain an axis reorientation angle of $+0.65°$. We know from the fit of the intensities in the spectrum, that if θ_T is positive, then θ is necessarily positive and *vice versa*. Thus, the determination of the sign of θ_T, which can be determined geometrically provides a direct access to the absolute sign of θ, which cannot be determined directly from the experiment, since the observed intensities depend on the squares of the projections along the inertial axes as described above. The positive direction of the angle θ is defined by a counterclockwise rotation of the inertial a-axis onto the TDM. Therefore, it is the orientation (I) in Figure 9.2, which is observed experimentally. This orientation corresponds to an ^1L_b state in Platt's nomenclature.

Inspection of the leading configurations in the excited state wave functions shows, that the adiabatically lowest state is mainly characterized by LUMO $\leftarrow$ HOMO excitation (coefficient 0.87), to a lesser extent by (LUMO+3) $\leftarrow$ (HOMO-1) (-0.30) and LUMO $\leftarrow$ (HOMO-1) (-0.26), cf. Figure 9.3. The LUMO+3 is the second unoccupied orbital of π symmetry, while LUMO+1 and LUMO+2 are Rydberg like orbitals of σ symmetry, located at the NH group and the fluorine atom, respectively. If one compares the frontier orbitals of 5FI with those of 5CI [189], one sees, that the orbital which is HOMO-1 in 5FI changes to HOMO in 5CI and *vice versa*. The Rydberg orbitals located at the NH group and the fluorine atom in 5FI shift down in energy below the second π^* orbital, while in 5CI, the Rydberg orbitals are situated above the π^* orbitals. Furthermore, the amplitudes at the fluorine substituent are considerably smaller, than those at the cyano substituent.

Recently, we investigated the TDM orientation in 5-cyanoindole (5CI) [189]. In this molecule the TDM is oriented along the a-axis of the molecule and has to be classified as an ^1L_a-type state. As shown above, the orientation of the TDM in the lowest excited singlet state of 5FI makes an angle of 59° with the a-axis. This is
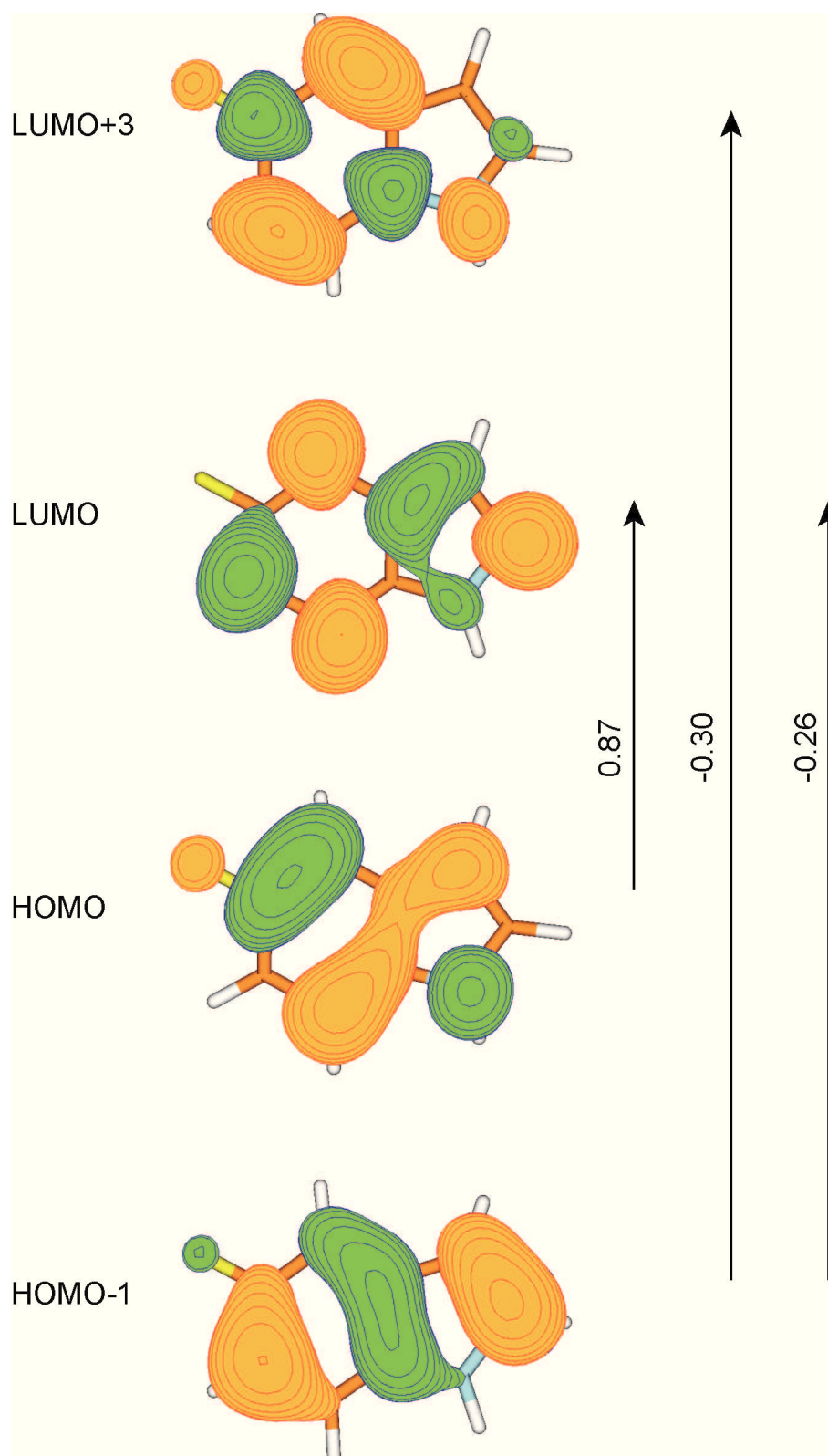
Figure 9.3: Contour plots of the highest occupied and the lowest unoccupied π-type molecular orbitals of 5FI at the optimized S_1 geometry from CC2/cc-pVTZ calculations, isosurface value 0.03. The numbers on the arrows give the coefficient of the excitation regarding excitation to the S_1.

Figure 9.4: Isosurface plots of the density differences $\Delta\rho$ for 5FI and 5CI from the SCS-CC2/cc-pVTZ calculations, isosurface value 0.001. Orange and green show regions of decreased and increased electron density, respectively.
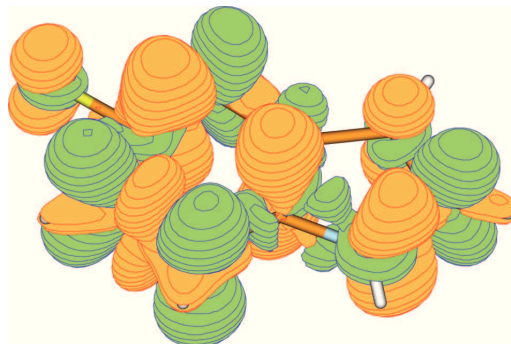
close to the SCS-CC2 calculated value for the S_2-state of 5CI of 65°. This is further evidence, that between 5FI and 5CI the electronic nature of the lowest excited state changes from ^1L_b to ^1L_a. Comparing the structural changes upon excitation, one also finds, that the S_1 geometry of 5FI corresponds to the S_2 geometry of 5CI as calculated at the SCS-CC2 level.

Figure 9.4 compares the density differences between the S_0 and the S_1 states of 5FI and between the S_0 and the S_2 states of 5CI. According to simple chemical ideas, both substituents would be expected to decrease the electron density of the chromophore even in the ground state, the cyano group via -M and the fluoro group via -I effect. But the density differences for excitation to the respective states are considerably different. In both cases a net charge flow from the pyrrole to the benzene ring takes place, like in indole itself [141, 154]. However, this charge migration is considerably larger in 5CI, than in 5FI, in agreement with the fact, that the lowest excitation in 5CI leads to the ^1L_a state.

Averaging the ring charges, obtained from the NBO analysis using the SCS-CC2 wave functions, we find a net charge flow of 0.12 electron charges from the pyrrole ring to the benzene ring upon excitation to the S_1-state of 5FI and of 0.58 e for excitation to the S_2-state of 5CI. The dipole moments of 5CI have been calculated to be 7.1 D and 10.1 D in the S_0 and S_2 states, respectively, while for 5FI we find much smaller values of 3.5 D and 3.7 D for S_0 and S_1, respectively. Most notably, the most of the density differences for the π and the σ orbitals at a given center have different signs for 5FI. Also the importance of electron flow via σ bonds is higher in 5FI than in 5CI. We attribute this to the fact, that the electronic effects of fluorine on the chromophore are purely inductive, while the cyano group exerts mesomeric effects.

Furthermore, the zero-point corrected adiabatic excitation energy (ν_0) of the lowest excited singlet state is given in Table 9.1. The zero-point-energy corrected CC2/cc-

pVTZ calculated value of 35144 cm^{-1} is in fair agreement with the experimental value of 34336 cm^{-1} (0.1 eV deviation).

9.4 Conclusions

The rotational constants of the electronic ground and first excited singlet state of 5FI have been determined for the first time. Very good agreement with the results of quantum chemical calculations at the CC2/cc-pVTZ and SCS-CC2/cc-pVTZ levels is obtained. Contrary to the case of 5CI, already the CC2 level of theory yields the correct ordering of the lowest two excited singlet states and the correct TDM orientation for this state. From the orientation of the TDM in the molecular frame the electronic nature of this excited state could be proven to be similar to the ^1L_b state of indole. Density difference plots for the lowest $\pi\pi^*$ excitation in 5FI and the second $\pi\pi^*$ excitation in 5CI show a considerably different charge flow from the pyrrole moiety to the benzene ring upon excitation.

9.5 Acknowledgement

9.6 Publication

The contents of this chapter has been published previously in slightly different form as *Ground and Electronically Excited Singlet-State Structures of 5-Fluoroindole Deduced from Rotationally Resolved Electronic Spectroscopy and* Ab Initio *Theory* in *ChemPhysChem* (impact factor: 3.412), 2012, **13**, 3134–3138 by Christian Brand, Olivia Oeltermann, Martin Wilke, Jörg Tatchen, and Michael Schmitt.

For this publication the experimental work was done in close collaboration by O. Oeltermann, M. Wilke and me. The respective theoretical calculations were done partly by M. Schmitt and partly by me. Subsequently, I analyzed and interpreted the spectrum and prepared parts of the manuscript.

10. 5-Methoxyindole

Abstract

Rotationally resolved electronic spectra of the vibrationless origin and of eight vibronic bands of 5-methoxyindole (5MOI) have been measured and analyzed using an evolutionary strategy approach. The experimental results are compared to the results of *ab initio* calculations. All vibronic bands can be explained by absorption of a single conformer, which unambiguously has been shown to be the *anti* conformer from its rotational constants and excitation energy. For both *anti* and *syn* conformers, a $^1L_a/^1L_b$ gap larger than 4000 cm^{-1} is calculated, making the vibronic coupling between both states very small, thereby explaining why the spectrum of 5MOI is very different from that of the parent molecule, indole.

10.1 Introduction

As presented in Chapter 6, all bands in the spectrum of indole up to 1000 cm^{-1} above the electronic origin of the ^1L_b belong to this state but are vibronically coupled to the ^1L_a to varying degrees [87, 195]. Owing to a large redshift of its ^1L_b state, 5-methoxyindole (5MOI) has the largest known energetic separation of the ^1L_a and ^1L_b. The energetic gap increases to 3088 cm^{-1} as shown by Martinaud and Kadiri [209] by comparing solvent induced shifts of the UV-absorption in *di-n*-propylether and polyethylene films. Methoxy substituents additionally have an influence on the angle θ_{ab} between the ^1L_a and ^1L_b transition dipole moment vectors, as shown by Eftink *et al.* [175]. This value is nearly 90° for the unsubstituted indole [137]. Albinsson and Nordén determined the angle θ_{ab} between the transition dipole moments of the ^1L_b and the ^1L_a states to be 85° [138].

R2PI spectra of jet-cooled 5MOI have been measured by Hager *et al.* [176] up to
1200 cm^{-1} above the electronic origin. Excited state lifetimes were determined for
various vibronic bands. In a study of Huang *et al.* [178], R2PI spectra of 5MOI
and of 1:1 and 1:2 adducts with water, methanol, and triethylamine were presented.
Florio *et al.* [210] showed by UV-UV holeburning spectroscopy that all bands in the
LIF spectrum of 5MOI arise from a single ground-state level, which they assigned
to the *anti* methoxy conformer (see Figure 10.1). The permanent dipole moment
has been measured by Lami and Glasser [12].
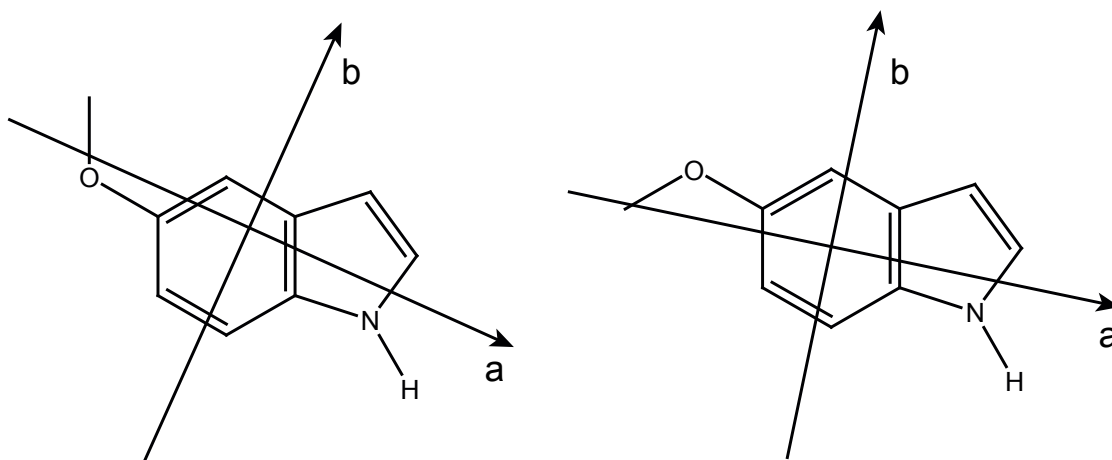
Figure 10.1: Structures and inertial axes of *anti* (left) and *syn* (right) 5MOI.

In this chapter we present the results of an analysis of the electronic origin as well
as of several vibronic bands of 5MOI with rotational resolution. The spectra were
analyzed using an evolutionary strategy (ES) approach and the resulting molecular
parameters were compared to the results of quantum chemical calculations. Our
objective is to contrast the characters of its electronic states with those of the parent
molecule, indole.

10.2   Techniques

10.2.1   Experimental procedures

5-Methoxyindole ($\geq$ 99%) was purchased from Fluka and used without further pu-
rification.

The resonance two-photon ionization (R2PI) spectrum was recorded in the group
of Prof. Weinkauf. The experimental set up for this experiment is described in

detail elsewhere [211]. In brief, the sample molecules were heated to 110 °C to form a suitable partial pressure in a pulsed valve (General Valve) operated at 10 Hz with 4 bar Ar as a carrier gas. The pulsed supersonic beam was skimmed after 30 mm and ionized about 200 mm downstream of the valve in a second vacuum chamber. Ions were accelerated in a two-stage ion source and mass detected in a linear time-of-flight mass spectrometer. The spectra were taken by recording the dependence of the gated ion signal on the laser wavelength. Excitation light was provided by a frequency-doubled pulsed Nd:YAG (Innolas Spitfire 600) pumped dye laser (Lumonics Hyperdye 500) with a 7 ns pulse width.

The experimental set up for the rotationally resolved laser induced fluorescence is described in detail in Chapter 3. In brief, the laser system consists of a single frequency ring dye laser (Sirah Matisse DS) operated with Rhodamine 6G, pumped with 6 W of the 532 nm line of a frequency doubled CW Nd:YAG laser (Spectra). The dye laser output was coupled into an external folded ring cavity (Spectra Physics Wavetrain) for second harmonic generation. The resulting output power was constant at about 25 mW during each experiment. The molecular beam was formed by co-expanding 5MOI, heated to 170°C, and 800 mbar of argon through a 80 μm nozzle into the vacuum chamber. The molecular beam machine consists of three differentially pumped vacuum chambers that are linearly connected by skimmers (1 mm and 3 mm, respectively) in order to reduce the Doppler width. The resulting resolution is 18 MHz (FWHM) in this set-up. In the third chamber, 360 mm downstream of the nozzle, the molecular beam crosses the laser beam at a right angle. The imaging optics setup consists of a concave mirror and two plano-convex lenses to focus the resulting fluorescence onto a photomultiplier tube, which is mounted perpendicularly to the plane defined by the laser and molecular beam. The signal output was then discriminated and digitized by a photon counter and transmitted to a PC for data recording and processing. The relative frequency was determined with a *quasi* confocal Fabry-Perot interferometer. The absolute frequency was obtained by comparing the recorded spectrum to the tabulated lines in the iodine absorption spectrum [67].

10.2.2 Computational methods

Quantum chemical calculations

Structure optimizations were performed employing the valence triple-zeta basis set with polarization functions (d,p) from the TURBOMOLE library [162, 212]. The equilibrium geometries of the electronic ground and the lowest excited singlet states were optimized using the approximate coupled cluster singles and doubles model (CC2) employing the resolution-of-the-identity approximation (RI) [112, 163, 164].

Singlet state energies and wave functions were calculated using the combined density functional theory/multi-reference configuration interaction method (DFT/MRCI) developed by Grimme and Waletzke [110]. Configuration state functions (CSFs) in the MRCI expansion were constructed from Kohn-Sham (KS) orbitals, optimized for the dominant closed shell determinant of the electronic ground state employing the BH-LYP [2, 122] functional. All 56 valence electrons were correlated in the MRCI runs and the eigenvalues and eigenvectors of five singlet states were determined. For more information regarding the computational methods refer to Chapter 5.

10.3 Results and Discussion

10.3.1 R2PI spectrum of 5-methoxyindole

The R2PI spectrum of 5MOI in the region between the electronic origin (0,0) at $33120.53 \ \text{cm}^{-1}$ and $0,0 + 1100 \ \text{cm}^{-1}$ is shown in Figure 10.2. The bands are labeled by their frequencies relative to 0,0; bands marked with a dagger have been investigated using rotationally resolved fluorescence excitation spectroscopy. The R2PI spectrum has been intensity corrected to the pulse energy of the dye laser. Comparing the intensities to those in the LIF spectrum of Florio *et al.* [210] suggests that our intensities are still influenced by saturation effects and/or by different FC factors of the ionization step, not atypical for a R2PI spectrum. Therefore, these intensities cannot be reliably compared to the FCHT analysis performed in Section 10.3.2.
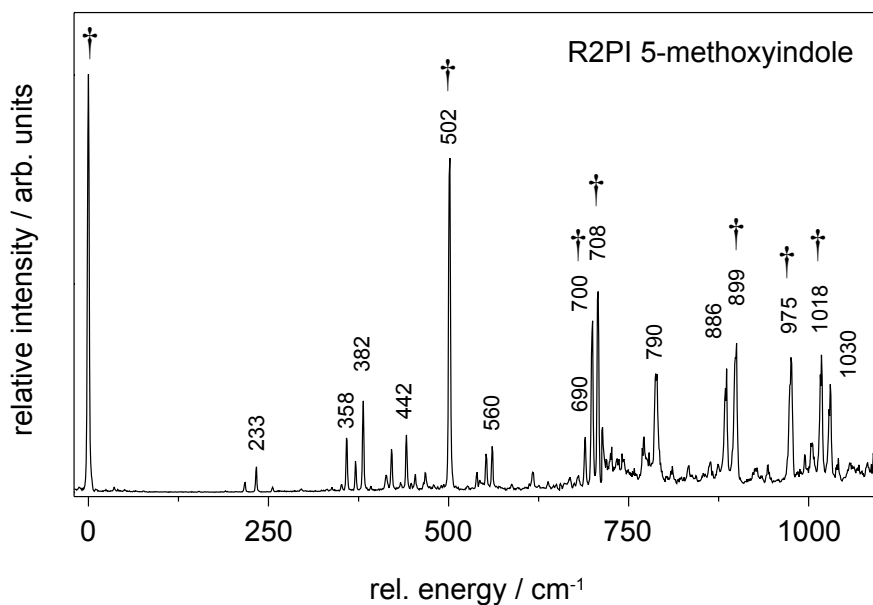
Figure 10.2: R2PI spectrum of 5-methoxyindole. Bands that have been investigated with rotational resolution are marked by a dagger.

10.3.2   Calculated vibrational and vibronic spectra

The *ab initio* calculated fundamental frequencies of the ground and electronically excited ^1L_b state of *anti* 5MOI are compiled in Table 10.1. The 54 vibrational modes are grouped into 37 in-plane (a′) modes and 17 out-of-plane (a″) modes. They are given by ascending wavenumbers in Table 10.1 and are labeled by their symmetry. Q_1 - Q_{37} are the in-plane modes and Q_{38} - Q_{54} are the out-of-plane modes. The ground state vibrational wavenumbers are compared to the results of Raman spectroscopy of a polycrystalline 5MOI sample [213]. For the ground state vibrational wavenumbers, a root mean square deviation (rmsd) of 34 cm^{-1} from the experimental wavenumbers using unscaled computed wavenumbers is found. Scaling the CH and NH stretching vibrations by 0.93 improves the rmsd to 11 cm^{-1}. Assignment of excited state modes to the ground state modes was performed using the elements of the Dushinsky matrix. The largest entries of the complete matrix are given in the last column of Table 10.1. Surprisingly, there is very little mode mixing in 5MOI, compared to indole, where many excited state modes are heavily mixed. As apparent from Table 6.5 on page 91 only 13 of indole's 42 normal coordinates lie mainly on the diagonal. Several modes have changed the energetic position and 16 modes are heavily mixed. Most of the modes in 5MOI retain their identity upon electronic excitation, many of them even retain their energetic position. There are

many entries close to one on the diagonal of the Dushinsky matrix, making the assignment of the ^1L_b modes to the respective ground state modes straightforward.

Using the ^1L_b normal modes Q_i as basis for the nuclear displacements along which the gradients of the electronic transition dipole moment (TDM) are calculated [195], we computed the spectrum of 5MOI in the Franck-Condon (FC) Herzberg-Teller (HT) approximation [60], and compared it to the spectrum computed using the FC approximation, see Figure 10.3. At first sight, no difference in intensities can be seen. Also the band type, which reflects the orientation of the transition dipole moment, is practically the same in the FC and the FCHT approximation. This is very different from the cases of indole and tryptamine [157], where strong vibronic mixing significantly affects both the intensities and the band type of many vibronic bands.
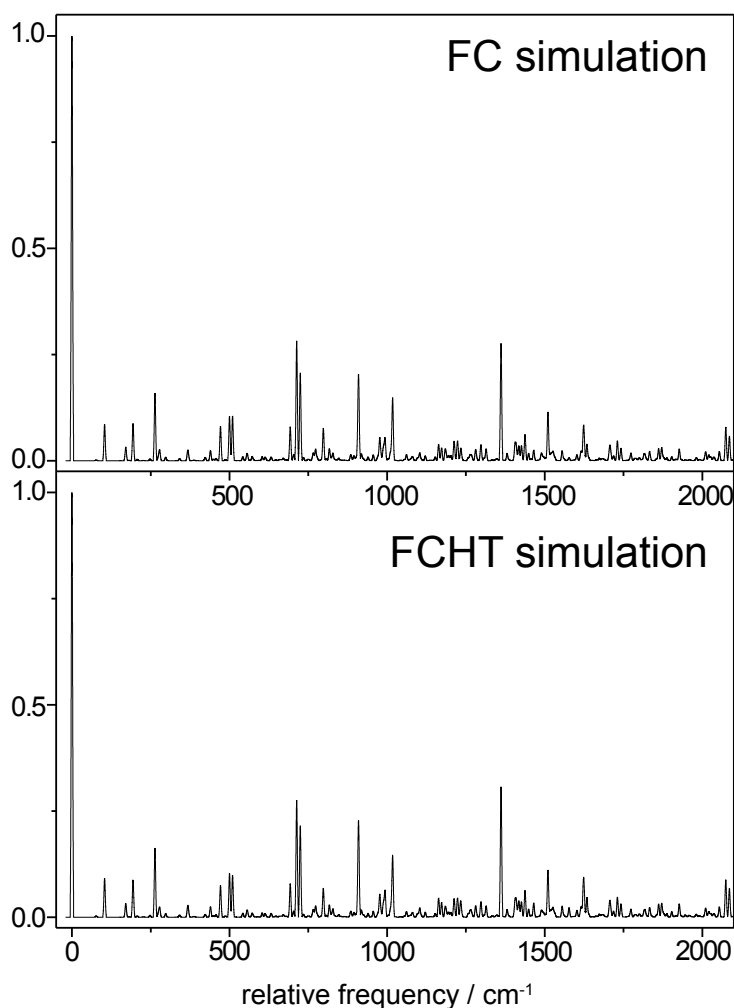
Figure 10.3: Comparison of the FC simulation of the 5MOI spectrum with the FCHT simulation.

Table 10.1: Calculated vibrational wavenumbers in the ground and electronically excited ^1L_b states from CC2 calculations with the cc-pVTZ basis set. The first column gives the mode numbering for the ground state, the last column gives the respective combinations for the ^1L_b state from the Dushinsky analysis; see text for details.

[a]Ground state frequencies from Ref. [213]

[b]Excited state frequencies from this work; wavenumbers of the forbidden a″ vibrations are calculated from the experimental overtones assuming harmonic behavior.

Mode	Sym.	S_0		^1L_b		Dushinsky
		calc.	obs.[a]	calc.	obs.[b]	
Q_{54}	a″	76	-	77		$Q_{54}(L_b) = +0.99Q_{54}(S_0)$
Q_{53}	a″	140	167	104	109	$Q_{53}(L_b) = -0.98Q_{53}(S_0)$
Q_{52}	a″	207	208	171		$Q_{52}(L_b) = +0.87Q_{52}(S_0)$
Q_{37}	a′	220	218	227	233	$Q_{37}(L_b) = +0.82Q_{37}(S_0)$
Q_{51}	a″	271	245	194	191	$Q_{51}(L_b) = +0.73Q_{51}(S_0)$
Q_{50}	a″	352	345	440		$Q_{47}(L_b) = -0.87Q_{50}(S_0)$
Q_{49}	a″	359	-	263		$Q_{50}(L_b) = -0.74Q_{49}(S_0)$
Q_{36}	a′	372	370	370	358	$Q_{36}(L_b) = -0.91Q_{36}(S_0)$
Q_{48}	a″	423	430	278		$Q_{49}(L_b) = -0.67Q_{48}(S_0) + 0.41Q_{50}(S_0)$
Q_{35}	a′	459	458	423	442	$Q_{35}(L_b) = -0.75Q_{35}(S_0)$
Q_{34}	a′	527	525	510	502	$Q_{34}(L_b) = +0.84Q_{34}(S_0)$
Q_{47}	a″	574	513	471		$Q_{46}(L_b) = +0.74Q_{47}(S_0)$
Q_{46}	a″	597	603	554		$Q_{44}(L_b) = -0.63Q_{46}(S_0)$
Q_{33}	a′	608	603	572	560	$Q_{33}(L_b) = -0.91Q_{33}(S_0)$
Q_{45}	a″	678	635	383		$Q_{48}(L_b) = +0.54Q_{45}(S_0) + 0.29Q_{46}(S_0)$
Q_{32}	a′	751	746	713	700	$Q_{32}(L_b) = +0.82Q_{32}(S_0)$
Q_{44}	a″	764	770	724		$Q_{41}(L_b) = -0.79Q_{44}(S_0)$
Q_{43}	a″	789	810	500		$Q_{45}(L_b) = +0.38Q_{43}(S_0) + 0.51Q_{47}(S_0)$
Q_{31}	a′	808	795	798	790	$Q_{31}(L_b) = -0.96Q_{31}(S_0)$
Q_{42}	a″	819	847	631		$Q_{43}(L_b) = +0.78Q_{42}(S_0)$
Q_{30}	a′	906	900	844		$Q_{30}(L_b) = -0.97Q_{30}(S_0)$
Q_{41}	a″	939	932	693		$Q_{42}(L_b) = -0.64Q_{41}(S_0) - 0.51Q_{42}(S_0)$
Q_{29}	a′	954	940	909	899	$Q_{29}(L_b) = +0.87Q_{29}(S_0)$
Q_{28}	a′	1058	1035	994	975	$Q_{28}(L_b) = +0.79Q_{28}(S_0)$
Q_{27}	a′	1090	1070	1017	1016	$Q_{27}(L_b) = -0.85Q_{27}(S_0) + 0.58Q_{28}(S_0)$
Q_{26}	a′	1112	1102	1071		$Q_{26}(L_b) = -0.79Q_{26}(S_0)$

A preliminary assignment of the vibronic bands in the observed spectrum (Fig. 10.2) can be made on the basis of the CC2 calculations (see Table 10.1). Although the chromophore in the ^1L_b state is slightly non-planar, we designate the vibrations as a′ and a″, as if the symmetry were C_s (with the plane of symmetry in the aromatic plane). Nearly all of the observed bands are of a′ symmetry, which would be the only allowed ones in C_s symmetry. The lowest wavenumber band is observed at 218 cm^{-1}. It is assigned as the first overtone of the a″ vibration Q_{53}, calculated at 104 cm^{-1}. This motion can be described as a butterfly vibration of the two rings. The following band at 233 cm^{-1} is assigned to the first totally symmetric a′ vibration Q_{37}, calculated at 227 cm^{-1}. The 358 cm^{-1} band is assigned to vibration Q_{36}. The first overtone of the a″ vibration Q_{51} is observed at 382 cm^{-1}. Vibration

Table 10.2: Calculated vibrational wavenumbers in the ground and electronically excited ^1L_b states from CC2 calculations with the cc-pVTZ basis set, continued from Table 10.1. The first column gives the mode numbering for the ground state, the last column gives the respective combinations for the ^1L_b state from the Dushinsky analysis; see text for details.
[a]Ground state frequencies from Ref. [213]
[b]Excited state frequencies from this work; wavenumbers of the forbidden a″ vibrations are calculated from the experimental overtones assuming harmonic behavior.

Mode	Sym.	S_0		^1L_b		Dushinsky
		calc.	obs.[a]	calc.	obs.[b]	
Q_{40}	a″	1124	1105	926		$Q_{40}(L_b) = +0.76Q_{40}(S_0)$
Q_{25}	a′	1150	1132	1104		$Q_{25}(L_b) = +0.83Q_{25}(S_0)$
Q_{24}	a′	1185	1157	1163		$Q_{24}(L_b) = +0.90Q_{24}(S_0)$
Q_{39}	a″	1186	-	1170		$Q_{39}(L_b) = -0.97Q_{39}(S_0)$
Q_{23}	a′	1231	1200	1213	1212	$Q_{23}(L_b) = +0.94Q_{23}(S_0)$
Q_{22}	a′	1253	1235	1265		$Q_{21}(L_b) = +0.86Q_{22}(S_0)$
Q_{21}	a′	1272	1255	1232		$Q_{22}(L_b) = -0.81Q_{21}(S_0)$
Q_{20}	a′	1319	1290	1298		$Q_{20}(L_b) = +0.83Q_{20}(S_0)$
Q_{19}	a′	1354	1345	1314		$Q_{19}(L_b) = -0.81Q_{19}(S_0)$
Q_{18}	a′	1405	1420	1361	1349	$Q_{18}(L_b) = +0.67Q_{18}(S_0) - 0.54Q_{19}(S_0)$
Q_{17}	a′	1464	1440	1410	1416	$Q_{17}(L_b) = -0.66Q_{17}(S_0) + 0.53Q_{15}(S_0)$
Q_{16}	a′	1487	1452	1416	1457	$Q_{16}(L_b) = +0.79Q_{16}(S_0)$
Q_{15}	a′	1500	1483	1616		$Q_{15}(L_b) = -0.62Q_{15}(S_0) - 0.49Q_{11}(S_0)$
Q_{38}	a″	1503	1470	1504		$Q_{38}(L_b) = -0.98Q_{38}(S_0)$
Q_{14}	a′	1513	1509	1497		$Q_{13}(L_b) = -0.63Q_{14}(S_0) - 0.56Q_{12}(S_0)$
Q_{13}	a′	1536	-	1526		$Q_{11}(L_b) = +0.91Q_{13}(S_0)$
Q_{12}	a′	1544	1580	1465		$Q_{14}(L_b) = +0.69Q_{12}(S_0) - 0.35Q14$
Q_{11}	a′	1612	1624	1510		$Q_{12}(L_b) = +0.74Q_{11}(S_0)$
Q_{10}	a′	1654	-	1577		$Q_{10}(L_b) = -0.85Q_{10}(S_0)$
Q_9	a′	3048	2833	3078		$Q_9(L_b) = -1.00Q_9(S_0)$
Q_8	a′	3125	2911	3171		$Q_8(L_b) = -1.00Q_8(S_0)$
Q_7	a′	3198	2954	3215		$Q_7(L_b) = +1.00Q_7(S_0)$
Q_6	a′	3208	2991	3223		$Q_6(L_b) = +1.00Q_6(S_0)$
Q_5	a′	3232	3028	3245		$Q_5(L_b) = +0.99Q_5(S_0)$
Q_4	a′	3240	3037	3255		$Q_4(L_b) = +0.99Q_4(S_0)$
Q_3	a′	3274	3106	3270		$Q_3(L_b) = +0.93Q_3(S_0)$
Q_2	a′	3294	3125	3303		$Q_2(L_b) = +0.93Q_2(S_0)$
Q_1	a′	3665	3402	3631		$Q_1(L_b) = -1.00Q_1(S_0)$

Q_{35}, calculated at 423 cm^{-1} is observed at 442 cm^{-1}. The vibronic band at 502 cm^{-1} is assigned to Q_{34}, which is calculated at 510 cm^{-1}. This vibration has mainly the character of a C-O-C bending vibration Q_{33}, which will become important in later discussion. Q_{33} is observed at 560 cm^{-1}. If the energetically following band at 700 cm^{-1} is assigned to Q_{32}, there are no other a′ vibrations sufficiently close to explain the 708 cm^{-1} band. We therefore propose a Fermi resonance between Q_{32} and the combination of Q_{50} and Q_{49} (both a″) to be responsible for the pair of bands at 700/708 cm^{-1}. The 790 cm^{-1} band can be assigned to the following a′ vibration Q_{31}, 899 cm^{-1} to Q_{29}, 975 cm^{-1} to Q_{28}, and 1016 cm^{-1} to Q_{27}.

10.3.3 High resolution spectrum of the origin band of 5-methoxyindole

Figure 10.4 shows the rotationally resolved spectrum of the electronic origin of 5MOI along with a simulation, using the best parameters from the CMA-ES fit given in Table 10.3. The spectrum was fit to an asymmetric rotor Hamiltonian with axis reorientation [42, 43] using a derandomized evolutionary strategy [201], presented in Chapter 4. The uncertainties of the parameters are given in parentheses and are obtained as standard deviations by performing a quantum number assigned fit. In this fit those transitions are included that would be used in a typical manual assignment of the spectrum; that is, transitions with an intensity larger than 5% of the maximum intensity and with rotational quantum numbers up to J = 10.
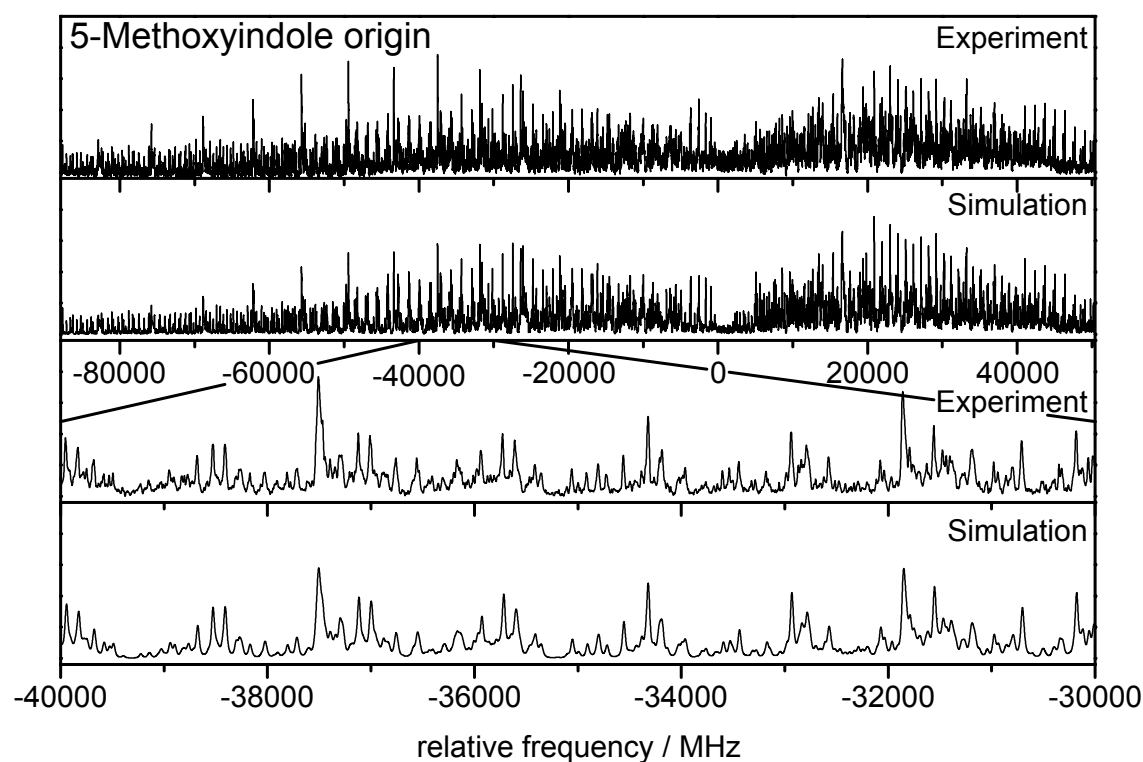
Figure 10.4: Rotationally resolved electronic spectrum of the electronic origin of 5-methoxyindole. The second trace shows the simulation using the best parameters from Table 10.3. The lowest traces show expanded scale portions of the experimental spectrum and the corresponding simulation.

Comparison of the rotational constants to the results of the *ab initio* calculations immediately shows that the observed band is due to absorption of the *anti* conformer, as proposed by Florio *et al.* [210]. Both the structure in the ground state,

Table 10.3: Molecular parameters from the fits to the rotationally resolved electronic spectra of several vibronic bands of 5-methoxyindole.

	Origin	502(red)	502 (blue)	700	708(red)	708(blue)	899 (red)	899 (blue)	1016
A'' / MHz	2851.29(1)	2851.29(1)	2851.29(1)	2851.29(1)	2851.29(1)	2851.29(1)	2851.29(1)	2851.29(1)	2851.29(1)
B'' / MHz	757.72(1)	757.72(1)	757.72(1)	757.72(1)	757.72(1)	757.72(1)	757.72(1)	757.72(1)	757.72(1)
C'' / MHz	601.21(1)	601.21(1)	601.21(1)	601.21(1)	601.21(1)	601.21(1)	601.21(1)	601.21(1)	601.21(1)
$\Delta I''$ / amu Å^2 [a]	-3.59(3)	-3.59(3)	-3.59(3)	-3.59(3)	-3.59(3)	-3.59(3)	-3.59(3)	-3.59(3)	-3.59(3)
ΔA / MHz [b]	-99.32(1)	-96.46(1)	-96.46(1)	-99.38(1)	-98.72(1)	-99.65(1)	-105.14(1)	-99.45(1)	-102.89(1)
ΔB / MHz [b]	+1.26(1)	+0.96(1)	+0.96(1)	+1.05(1)	+0.67(1)	+1.07(1)	+0.97(1)	+0.90(1)	+1.13(1)
ΔC / MHz [b]	-3.63(1)	-3.92(1)	-3.92(1)	-3.61(1)	-3.47(1)	-3.58(1)	-3.50(1)	-3.70(1)	-3.72(1)
$\Delta I'$ / amu Å^2 [a]	-3.73(2)	-3.46(2)	-3.46(2)	-3.98(2)	-4.45(2)	-4.04(2)	-4.44(2)	-4.00(2)	-4.03(2)
θ / °	±58.4(1)	±55.2(1)	±55.2(1)	±62.5(2)	±63.7(2)	±63.9(2)	±64.6(1)	±63.9(1)	±62.3(1)
θ_T / °	±0.40(5)								
ϕ / °	90	90	90	90	90	90	90	90	90
μ_a^2	0.28	0.33	0.33	0.20	0.22	0.19	0.21	0.26	0.30
μ_b^2	0.72	0.67	0.67	0.80	0.78	0.81	0.79	0.74	0.70
μ_c^2	0.00	0.00	0.00	0.00	0.00	0.00	0.00	0.00	0.00
ν_0 / cm^{-1}	33120.53(1)	33622.61(1)	33622.61(1)	33820.55(1)	33829.00(1)	33829.04(1)	34019.05(1)	34019.06(1)	34173.15(1)
$\Delta\nu_0$ / MHz	-	502.08(1)	502.08(1)	700.02(1)	708.47(1)	708.51(1)	898.52(1)	898.53(1)	1016.62(1)
Δ Lorentz / MHz	23.7(2)	16.86(1)	16.86(1)	61.9(2)	29.3(2)	29.3(2)	31.6(3)	31.6(3)	*
$t_{1/2}$ / ns	6.7	9.4	9.4	2.6	5.4	5.4	5.0	5.0	*

[a]The inertial defect ΔI is defined as: $\Delta I = I_c - I_b - I_a$, where the I_g are the moments of inertia with respect to the main inertial axes $g = a, b, c$.
[b]Changes of the rotational constants are defined as: $\Delta B_g = B'_g - B''_g$, with B_g as rotational constants with respect to the inertial axes $g = a, b, c$.

as well as the changes of the structure upon excitation to the ^1L_b state, are well reproduced using CC2 with the cc-pVTZ basis set, see below. The non-zero inertial defect of -3.59 amu Å^2 in the electronic ground state and of -3.73 amu Å^2 in the excited state has its origin in the hydrogen atoms of the methyl group, which are not in the aromatic plane. The CC2/cc-pVTZ calculated inertial defects of the ground and excited state equilibrium structures were determined to be -3.44 amu Å^2 and -3.62 amu Å^2, respectively. The band was found to be an *ab* hybrid, with 72 % *b*- and 28 % *a*-type character. This corresponds to an in-plane angle θ of the transition dipole moment (TDM) with the inertial *a*-axis of 57°. From comparison to the theoretical TDM orientation (see below) and to the results for indole, the sign of θ is determined to be positive. The axis reorientation angle θ_T is determined to be 0.4°. Its sign is determined to be equal to that of the TDM angle θ, in good agreement with the theoretical predictions. The lifetime of the vibrationless origin has been determined from a Lorentz contribution of 23.7 MHz to the Voigt profile to be 6.7 ns.

Geometric parameters of *syn* and *anti* 5MOI in their electronic ground state and lowest two excited singlet states from CC2/cc-pVTZ calculations are given in the supplementary material chapter starting on page 267. Contrary to the case of indole, all excited state structures were identified as minima on the potential energy surface from a normal mode analysis at the level of structure optimization. From the optimized geometries, the rotational constants for both conformers in the three singlet states were determined. They are given in Table 10.4. For comparison, the experimentally determined rotational constants of the origin band also are listed there. Both the ground state values and the changes of the rotational constants upon excitation prove that the observed conformer is *anti* 5MOI.

A geometry change upon electronic excitation might cause a rotation of the inertial axes of the molecule, which can be described for a planar molecule using a single rotational angle θ_T. Since the oxygen of the methoxy group is located in the indole plane and the methyl group is a symmetric (internal) rotor, we can treat 5MOI as a planar molecule. The *c*-axis, which is perpendicular to the aromatic plane, coincides for the ground and excited state and θ_T describes the rotation of the a''-axis of the ground state into the a'-axis of the excited state about the *c*-axis. This effect of axis reorientation on rotationally resolved electronic spectra is described in detail in Section 1.4. Using the CC2 optimized structures for the S_0 and ^1L_b states, we obtained a reorientation angle of +0.2° for the ^1L_b state. A positive angle is defined

Table 10.4: Rotational constants (in MHz) and inertial defects (in amu Å^2) of 5MOI in the electronic ground state and their changes upon electronic excitation to ^1L_b and ^1L_a states, computed from the CC2 optimized structures using the cc-pVTZ basis set.

| | CC2 | | | | | | Exp. | |
| | syn | | | anti | | | | |
	S_0	^1L_b	^1L_a	S_0	^1L_b	^1L_a	S_0	S_1
A	3405	3304	3354	2843	2735	2844	2850.08	2750.85
B	704	703	697	759	760	747	757.41	758.68
C	585	582	579	601	597	594	600.94	597.30
ΔA	-	-101	-51	-	-108	+1	-	-99.23
ΔB	-	-1	-7	-	+1	-12	-	+1.27
ΔC	-	-4	-6	-	-4	-7	-	-3.64
ΔI	-3.36	-3.45	-3.67	-3.44	-3.62	-4.14	-3.59	-3.73

by a clockwise rotation of the ground state inertial axes into the excited state axes according to the orientation given in Figure 10.1.

Table 10.5 gives the calculated energy differences of the *syn* and *anti* conformers of 5MOI at the CC2 and DFT/MRCI levels of theory. The *anti* conformer is by 464 cm^{-1} lower in energy at CC2 level and by 359 cm^{-1} using the DFT/MRCI approach. The relative stabilization energies given in Table 10.5 contain zero-point energy corrections at the CC2/cc-pVTZ level of theory. Depending on the height of the barrier separating the two conformers, it should be possible to observe both conformers in a molecular beam experiment. Nevertheless, in our experiments we were able only to observe the *anti* conformer. We evaluated the barrier to interconversion of the *syn* and *anti* conformer at MP2/6-311G(d,p) level to be 1300 cm^{-1}. This barrier is strongly coupled to the methyl torsional motion in the methoxy group (see below).

Table 10.5 gives the adiabatic and vertical excitation and emission energies of *syn* and *anti* 5MOI, computed at CC2 level with the cc-pVTZ basis and using DFT/MRCI with the BH-LYP functional on the CC2 optimized structures. All adiabatic excitation energies contain zero-point-energy (ZPE) corrections at the CC2 level. The experimentally observed electronic origin of the *anti* conformer at 33120 cm^{-1} is well reproduced at DFT/MRCI level (32946 cm^{-1}). Both for the *syn* and *anti* conformers, a ^1L_a / ^1L_b gap of more than 4000 cm^{-1} is calculated. The origin of the (up to now unobserved) *syn* conformer can be expected to be shifted by approximately 650 cm^{-1} to the red of the *anti* origin.

Additionally, the angles θ between the TDM and the inertial a-axis, obtained at both

Table 10.5: Relative energies of the *syn* and *anti* conformers of 5MOI and excitation and emission energies to and from the ^1L_b and ^1L_a states. All energies are given in reciprocal centimeters, angles in degrees. The adiabatic excitation energies contain zero-point energy corrections at CC2 level

		CC2		DFT/MRCI	
		syn	*anti*	*syn*	*anti*
	Relative energy	464	0	359	0
	$\theta\ (^1L_b{\leftarrow}S_0)$	+66	+66	+68	+67
	$\theta\ (^1L_a{\leftarrow}S_0)$	-16	-16	-21	-22
adiabatic	$^1L_b{\leftarrow}S_0$	32852	33702	32294	32946
adiabatic	$^1L_a{\leftarrow}S_0$	37992	38353	36716	37233
adiabatic	$\Delta(^1L_a\ ^1L_b)$	4915	4651	4197	4287
vertical	$^1L_b{\leftarrow}S_0$	35784	36688	34577	35239
vertical	$^1L_a{\leftarrow}S_0$	41633	42298	39536	40108
vertical	$S_0{\leftarrow}^1L_b$	32595	33276	31423	31887
vertical	$S_0{\leftarrow}^1L_a$	34284	35062	34233	34284

levels of theory, are given in the table. The CC2 values have been calculated from the average of the Cartesian components of left and the right transition moment. For both *syn* and *anti* conformers, a positive angle θ is found for the ^1L_b state and a negative angle for the ^1L_a state. These orientations are similar to the orientation of the ^1L_b TDM orientation in the indole chromophore itself, cf. Figure 10.5. The calculated values of +66 and +67° at CC2 and DFT/MRCI level, respectively, are in good agreement with the experimental value of +58.4° (cf. Table 10.3).

The inertial axis systems of the two conformers are tilted in the *ab* plane with respect to each other by an angle of 13°. Therefore, the orientation of the TDM in the molecular frame is not the same for the *syn* and *anti* conformers, although the numbers in Table 10.5 imply that it is. Projecting the TDM orientation of the ^1L_b state of *anti* 5MOI onto the *pseudo* C_2 axis in indole, we find an angle of +45° compared to +38° for the TDM orientation in indole, while for the *syn* conformer an angle of +55° of the TDM with respect to the *pseudo* C_2 axis in indole is found. The sign of θ is the same as the sign of θ_T.

A closer look at the frontier orbitals that are involved in the two electronic transitions to the ^1L_a and ^1L_b states reveals, that the main contribution to the ^1L_b transition is the excitation from the highest occupied molecular orbital to the lowest unoccupied molecular orbital (LUMO ← HOMO). This is different from the case of indole, where
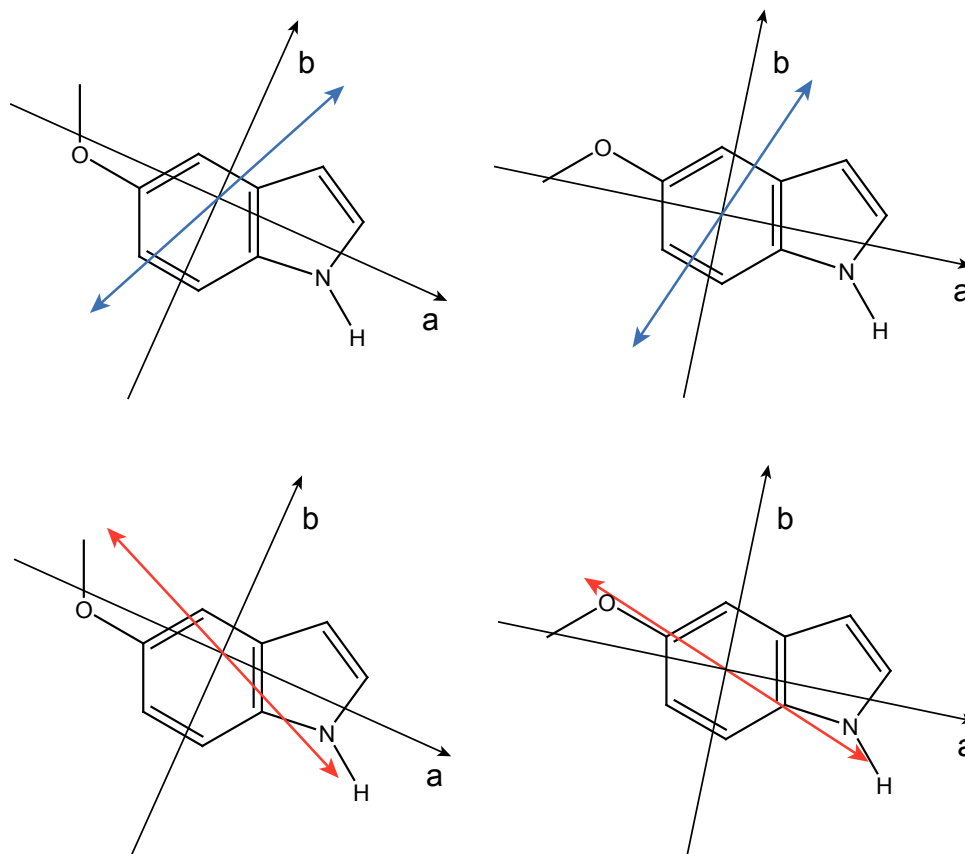
Figure 10.5: TDM orientation of the ^1L_b (upper structures) and ^1L_a (lower structures) states of *anti* (left structures) and *syn* 5MOI (right structures).

this excitation is the signature for ^1L_a excitation. The reason for this apparent change of orbital ordering can be seen in Figure 10.6 from the comparison to the indole frontier orbitals. The methoxy substituent introduces an additional node in the molecular orbital, which was formerly the HOMO-1 in indole, and which now becomes the HOMO in 5MOI. This causes a change in energy ordering between indole and 5MOI for the HOMO and HOMO-1, respectively.

Generally it is believed that excitation to the ^1L_b state in indole arises from a linear combination of LUMO ← (HOMO-1) and (LUMO+1) ← HOMO from analogy to the case of catacondensed aromatics like naphthalene [17, 214], for which the nomenclature of ^1L_a and ^1L_b was introduced by Platt [5]. In systems of lower symmetry than D_{2h}, not only does the meaning of ^1L_a and ^1L_b becomes obscure, but other orbitals might be involved, such as the Rydberg-like orbitals at the indolic NH group or at the methoxy group in 5MOI. At the CC2 level with a cc-pVTZ basis, the Rydberg-like NH orbital in indole becomes energetically the LUMO+1,
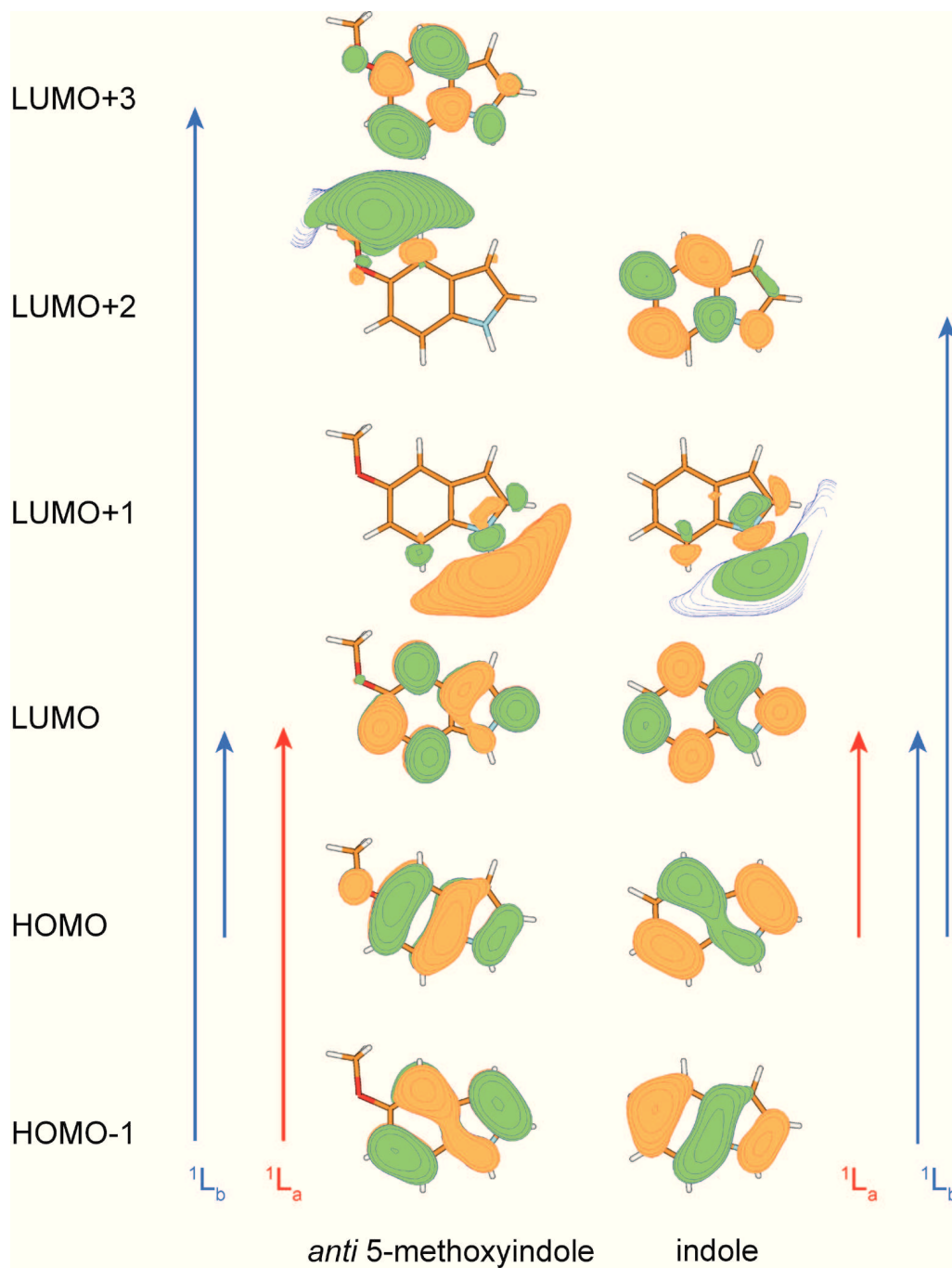
Figure 10.6: Frontier orbitals of *anti* 5-methoxyindole and indole.

so that the transition to the ^1L_b state now involves the LUMO ← (HOMO-1) and (LUMO+2) ← HOMO excitation. Additionally, the Rydberg-like orbital at the methoxy group also lies in the HOMO/LUMO region, so that the ^1L_b state here is comprised of LUMO ← (HOMO-1) and (LUMO+3) ← HOMO excitations.

10.3.4   Rotationally resolved spectra of higher vibronic bands

Figures 10.7 - 10.9 show rotationally resolved electronic spectra of the 0,0 + 502, 700, and 708 cm^{-1} bands of 5MOI. The spectra of the + 899 cm^{-1} and + 1016 cm^{-1} bands are shown in the supplementary material starting on page 267. In all cases the signal-to-noise ratio is not sufficient for a reliable determination of the axis reorientation angle θ_T. This is due to the fact that the intensity variations due to axis reorientation are small.

The 502 cm^{-1} band is composed of two subbands that are separated by 123 MHz. The lowest two traces of Figure 10.7 show the simulations of the individual components. The molecular parameters that were used in the simulations of the spectra have been obtained from ES fits. The ground state parameters have been set equal to the values of the fit of the origin band. The lifetime determined from the Lorentzian contribution to the Voigt profile is 10.4 ns. All molecular parameters obtained in the fit are compiled in Table 10.3. The orientation of the transition dipole moment of both components is the same as that of the origin band.

Changes of the rotational constants upon vibronic excitation of the 700 cm^{-1} band (Figure 10.8) are very similar to those of the 502 cm^{-1} band. Also the transition moment orientation of the band at 700 cm^{-1} is very similar to that of the origin band and the 502 cm^{-1} band. In contrast to the 502 cm^{-1} band, the 700 cm^{-1} band consists of only one component within an uncertainty of about 20 MHz. The lifetime of this band is determined to be 2.4 ns from the Lorentzian contribution to the Voigt profile.

The 708 cm^{-1} band (Figure 10.9) is again split into two components, like the 502 cm^{-1} band, with a splitting of 1026 MHz. Both components exhibit very similar changes of the rotational constants upon electronic excitation. Also the vibronic band at 899 cm^{-1} is a superposition of two vibronic bands, separated by 250 MHz. Both components exhibit quite different changes of the rotational constants upon vibronic excitation and are not as easily detected in a autocorrelation of the exper-
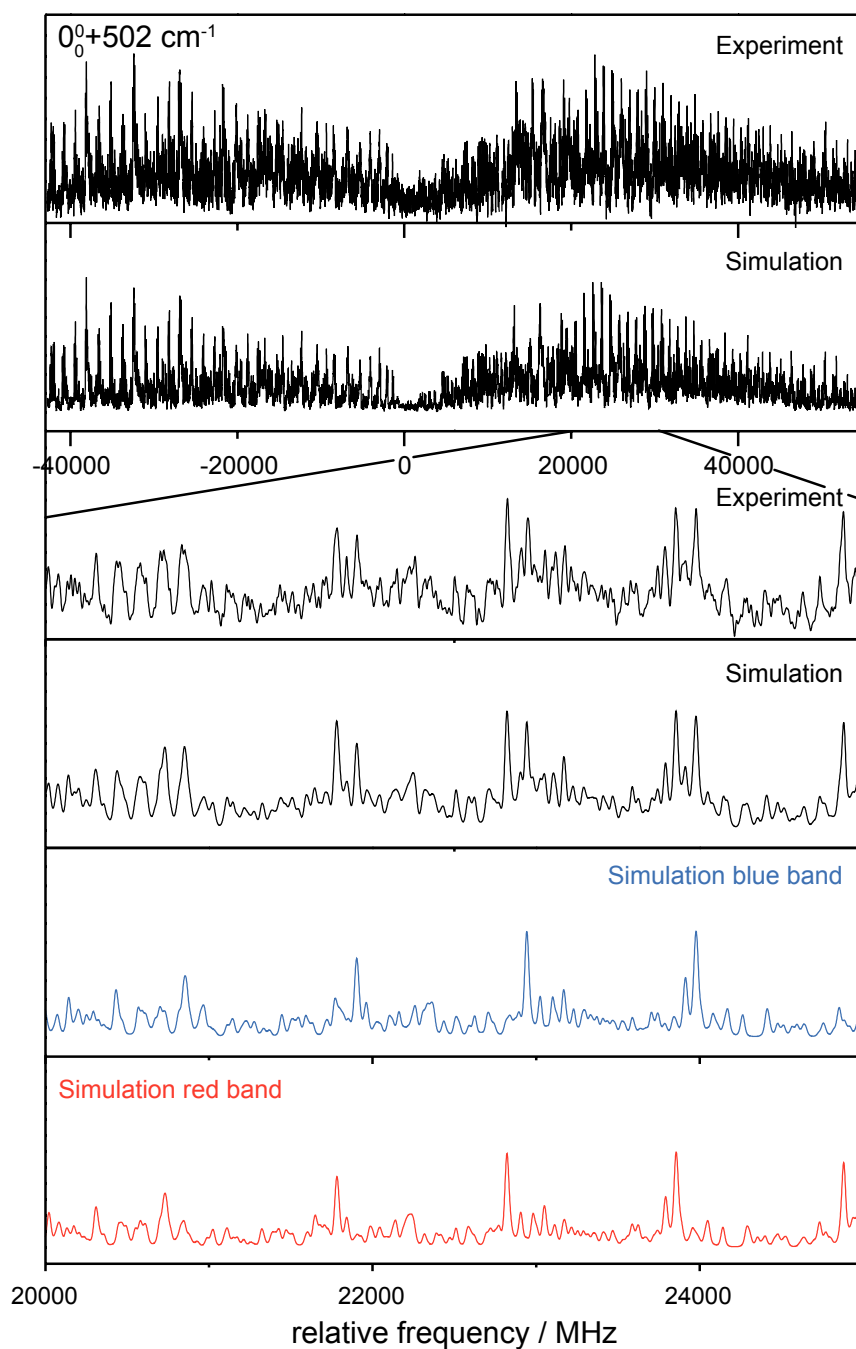
Figure 10.7: Rotationally resolved electronic spectrum of the 502 cm^{-1} band of 5-methoxyindole. The second trace shows the simulation using the best-fit parameters from Table 10.3. The lowest two traces show expanded portions of the experimental spectrum and the simulation.
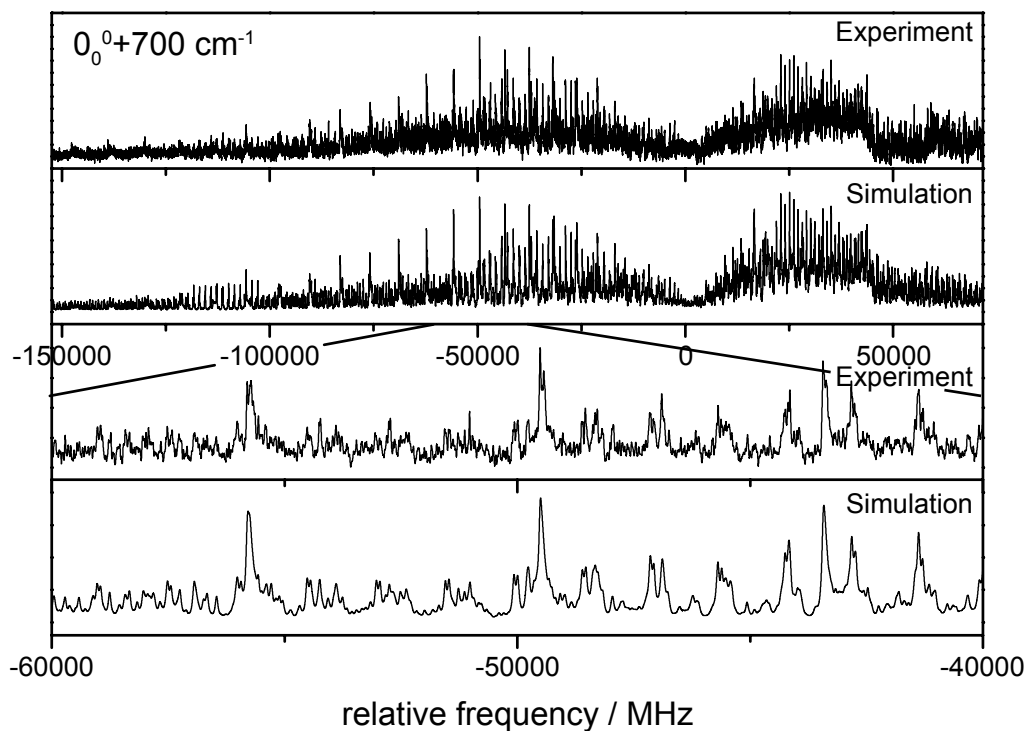
Figure 10.8: Rotationally resolved electronic spectrum of the 700 cm^{-1} band of 5-methoxyindole. The second trace shows the simulation using the best-fit parameters from Table 10.3. The lowest traces show expanded portions of the experimental spectrum and the simulation.

imental spectrum as for the 502 cm^{-1} band.

The highest vibronic band studied here is at 1016 cm^{-1}. Its spectrum is comprised of two subbands, as is the case of the 502 and 899 cm^{-1} bands. Unfortunately, the second component could not be simulated. It is not clear if it is due to another vibronic band, which coincides exactly and exhibits different rotational constants, or if this band is affected by a strong, hitherto unexplained perturbation.

10.3.5   The splitting in the vibronic bands

The reasons for the splitting of selected vibronic bands into two components are not quite clear. Several explanations might apply here. One possibility is a tunneling splitting due to a hindered internal motion. Two internal rotations are possible in 5MOI. The first is the twofold torsion, which interconverts the *anti* and *syn* conformers. Since both minima are different, this motion cannot be responsible for the splitting. The second possible motion is the threefold torsion of the methyl rotor in the methoxy group. The V_3 torsion of a methoxy group about the C-O bond has
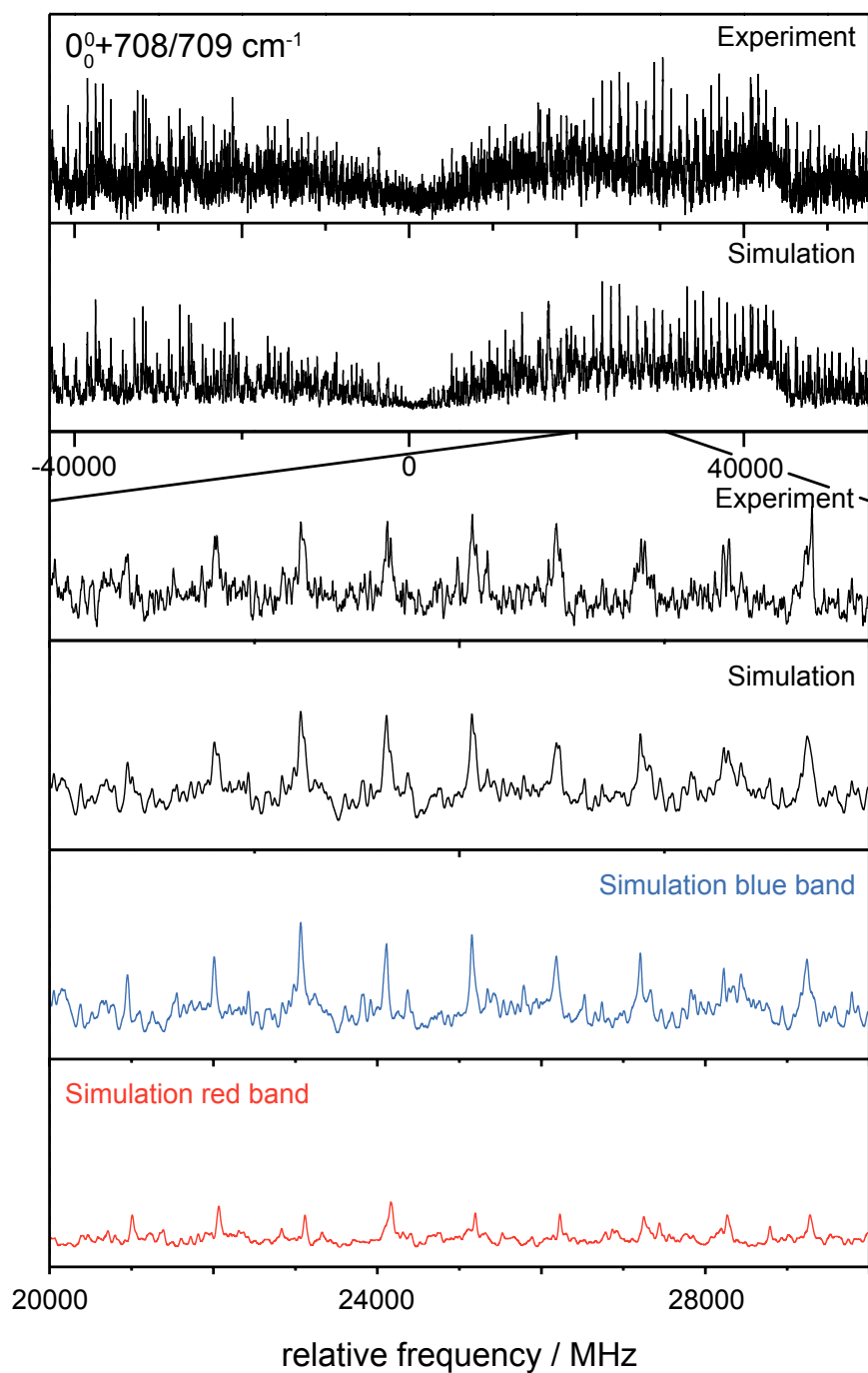
Figure 10.9: Rotationally resolved electronic spectrum of the 708 cm^{-1} band of 5-methoxyindole. The second trace shows the simulation using the best-fit parameters from Table 10.3. The lowest traces show expanded portions of the experimental spectrum and the simulation.

a very high barrier, at least in the electronic ground state. For anisole (methoxy-benzene), a V_3 barrier of 1847 cm^{-1} has been determined from Raman spectroscopy of anisole and anisole-d$_3$ [215]. The ground state tunneling A/E splitting from this barrier would amount to only 0.003 MHz, assuming a torsional constant F of 156 GHz, typical for a methyl group. If the splitting of 123 MHz observed in the 502 cm^{-1} band is a consequence of the threefold torsion of the methoxy group, it must therefore be due to the excited state splitting. Selection rules for the torsional transitions are A↔A and E↔E. The experimentally observed splitting of 123 MHz corresponds to a V_3 barrier in the excited state of 450 cm^{-1}. Since no torsional splitting is observed in the spectrum of the electronic origin, the reason for the large reduction of the barrier cannot be an electronic one alone, but must be caused by a reduction of an effective barrier due to excitation of the torsional vibration in the excited state, or excitation of a band which is at least strongly coupled to the torsion.

To further elucidate this aspect, we calculated the ground state barrier of 5MOI by varying the dihedral angles defining the torsional angle of the methyl group and relaxing all other molecular parameters at each torsional angle. For a torsional angle of zero, the molecule is in its equilibrium position, which before has been determined to be planar. When scanning the torsional angle, the methoxy group becomes non-planar with respect to the indole plane. Thus, the minimum energy path for the methyl (V_3) torsion is strongly coupled to the methoxy (V_2) torsional motion. The effective barrier along this path amounts to 1200 cm^{-1} at MP2/6-311G(d,p) level of theory. At the top of the barrier at -120°, the methoxy group is rotated out of the plane by 45°. At a torsional angle of -60°, the methoxy group has swung back into the indole plane, but is on the *syn* side. Thus, the energy difference of the minima at -180 and -60° gives the energy difference of the *syn* and *anti* conformers at the MP2/6-311G(d,p) level of theory.

Figure 10.10 shows the completely relaxed energy path, along the torsional coordinate (solid line). Additionally, we calculated a relaxed energy path, in which the methoxy group was kept fixed at a coplanar geometry with respect to the indole plane. The result is shown in Figure 10.10 (broken lines). In this case a V_3 barrier of 1500 cm^{-1} is computed. Both potential energy curves (completely relaxed and methoxy group in the indole plane) have maxima at -120°, 0°, and +120°, although the respective geometries are very different (see above). Obviously, the torsional axis changes its orientation during the torsional motion and the torsional constant F is not conserved along this path. Therefore, the usual perturbative approaches

for calculating torsional barriers do not apply and the above estimates for barriers and torsional constants give merely orders of magnitudes.
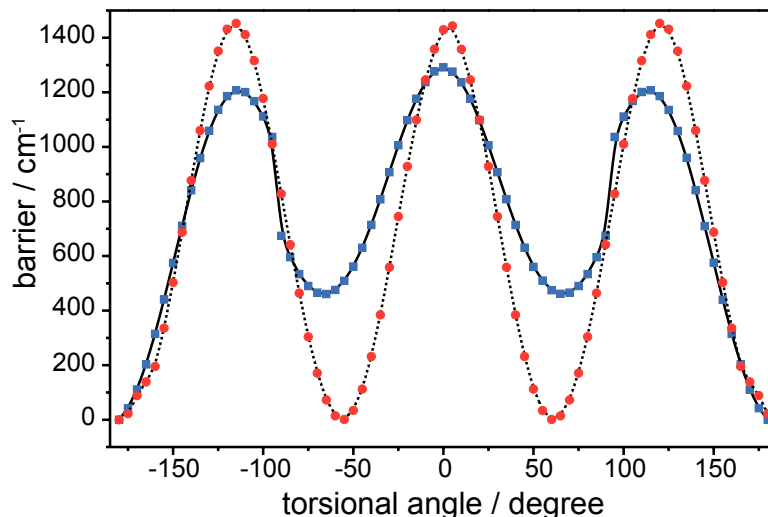
Figure 10.10: MP2/6-311G(d,p) torsional barriers of 5MOI. The full line gives the fully relaxed potential energy along the torsional coordinate α, the broken line the potential energy along α, with the methoxy group held coplanar with the indole ring. For details see text.

A reduction of the V_3 torsional barrier by coupling to other motions can therefore explain the observed splitting. Now, the exact nature of the coupling mode has to be determined. The out-of-plane motion, which gives a large contribution to the relaxed potential energy surface (PES) scan in Figure 10.10, cannot be the sought-after mode, since the respective torsional (V_2) mode is calculated at much lower energy (Q_{54} at 77 cm^{-1}). From the normal mode analysis it can be inferred that in the region of 500 cm^{-1} the only mode, which might be responsible for the coupling to the torsion is the C-O-C in-plane bending of the methoxy group (Q_{34}). We calculated the two-dimensional potential energy surface along the bending and the torsional coordinate at the MP2/6-311G(d,p) level of theory. Figure 10.11 shows the results obtained. The minima are found at a bending angle of 115°, while the saddle points are located at 120°. Thus, it seems very plausible that the splitting of the 502 cm^{-1} band is caused by the methyl torsional motion, whose barrier is lowered by the coupling to the methoxy in-plane bending mode. To test this hypothesis, we fit the spectrum of the 502 cm^{-1} band to a torsion-rotation Hamiltonian for a three-fold torsion using a perturbative approach, as described in Section 1.2 of page 15ff. and the references [21] and [30]. The goodness of this fit to a internal rotation model is even better than for a separate fit of the two components. The details of

Table 10.6: Results of the fit of the vibronic band at 502 cm^{-1} to an Hamiltonian including internal rotation

V_3''/cm^{-1}	1851(50)
F_α''/cm^{-1}	5.088(100)
η''/°	127(2)
ζ''/°	90.8(4)
V_3'/cm^{-1}	452.85(2)
ΔF_α/cm^{-1}	0.019(1)
$\Delta\eta$/°	0(2)
$\Delta\zeta$/°	1.1(6)
Δ EA/MHz	122.4

the fit are given in Table 10.6.
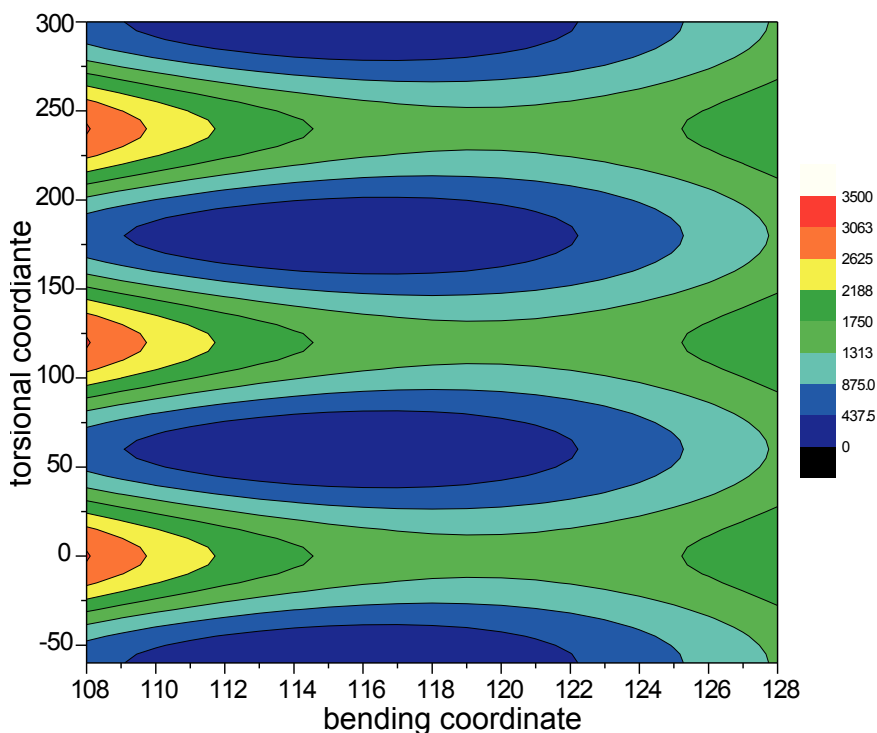
Figure 10.11: MP2/6-311G(d,p) calculated two-dimensional potential energy surface along the methoxy in-plane bending and the methyl torsional coordinates. The values used for color coding are in cm^{-1}.

Another possibility for explaining the observed vibronic splitting might simply be a coincidence of two (different) vibronic bands which are energetically very close. The (harmonic) state density calculated using the ^1L_b frequencies gives a value of less than one state per wavenumber at an excess energy of 500 cm^{-1}. The state density increases to about one state per wavenumber at 700 cm^{-1} and to more than five states per wavenumber above 1000 cm^{-1}. So, it seems unlikely, that a high state

density is responsible for the observed splitting at 502 cm^{-1}.

The 708 cm^{-1} band (Figure 10.9) is split into two components, like the 502 cm^{-1} band, with a splitting of 1026 MHz. If the reason for the splitting is the torsional barrier of the methoxy group, a value of V_3 of 290 cm^{-1} in the electronically excited state would result. On the other hand, we have a state density at 700 cm^{-1}, which already makes it plausible that the splitting is due to a fortuitous coincidence of two vibronic bands. On the basis of the present experimental results it is not possible to distinguish between these two possibilities. Nevertheless, a fit to the model Hamiltonian for internal rotation as for the 502 cm^{-1} band leads to a considerably poorer standard deviation, giving strong indication, that the reason for the appearance of a second band at 708 cm^{-1} is due to the state density here.

The changes of the rotational constants of the two components of the 899 cm^{-1} band are very different, cf. Table 10.3. If the torsional barrier in the excited state is high, as can be assumed from the small splitting of 250 MHz, the rotational constants of the two subbands should be similar, since they are not strongly perturbed. The large difference in the rotational constants in both subbands, makes it very improbable that the reason for the occurrence of two bands at 899 cm^{-1} is a torsional splitting as proposed for the 502 $^{-1}$, and possibly the 708 cm^{-1} bands.

10.4   Conclusions

Rotationally resolved electronic spectra of several vibronic bands in 5MOI have been obtained up to 1000 cm^{-1} in excess energy above the zero-point vibrational level of the first excited singlet state. From the measured values of the ground state rotational constants, it is shown that all observed bands belong to the *anti* conformer of 5MOI. It is also shown that all observed bands have similarly oriented TDMs, consistent with the assignment of the first excited singlet state as the ^1L_b state. In contrast, the parent molecule indole exhibits a TDM which strongly depends on the nature of the excited vibrational mode, owing to vibronic coupling with the ^1L_a state [87, 195].

The reason for this different behavior is the large energy gap between the ^1L_b and the ^1L_a state of more than 4000 cm^{-1} in 5MOI, while this gap is only 1400 cm^{-1} in indole. Also the higher lying B_a and B_b states might contribute to the vibronic coupling owing to their larger oscillator strengths, which can compensate their larger energy gap.

Within the numerical differentiation scheme we adopted for computation of Herzberg-Teller coupling, the CI wave functions are variationally optimized in a CSF basis for each distorted geometry. The change of the configuration state vector with nuclear geometry may in principle be caused by each of the states, which are present in the basis. Breaking down the Herzberg-Teller activity into contributions from individual excited states would require an expansion of the Herzberg-Teller derivatives in sum over states, what is beyond the scope of this study.

A splitting in some of the vibronic bands in the spectrum of 5MOI is analyzed in terms of a torsional splitting due to the threefold rotation of the methoxy group. Although the barrier for this motion is high, both in the ground and the excited state, a lower effective barrier in the excited state is postulated to be caused by excitation of a vibration which is strongly coupled to the torsion. According to our analysis, the 502 cm^{-1} band is due to vibration Q_{34}, which is the C-O-C bending vibration of the methoxy group. It seems plausible that this vibration couples strongly to the torsional motion, giving rise to a saddle point on the two-dimension potential energy surface which lies lower than the transition state on the torsional potential energy curve. The 2D surface along the respective modes in the ground state shows exactly the assumed behavior. The excited state lifetimes of the vibronic bands of 5MOI have been determined to be between 6 and 10 ns, with the exception of the 700 cm^{-1} band, which shows a sharp drop to only 2.4 ns. Thus, this mode seems to be an effective promoter mode for internal conversion to the electronic ground state of 5MOI. A calculation of the DFT/MRCI energies of the S_0 and S_1 potential energy surfaces along mode Q_{32} shows a curve crossing of the two PES. Further work to elucidate this question is under way.

10.5   Acknowledgment

10.6   Publication

The contents of this chapter has been published previously in slightly different form as *Rotationally resolved electronic spectroscopy of 5-methoxyindole* in the *Journal of Chemical Physics* (impact factor: 3.333), 2010, **133**, 024303(1–11) by Christian Brand, Olivia Oeltermann, David W. Pratt, Rainer Weinkauf, W. Leo Meerts, Win van der Zande, Karl Kleinermanns, and Michael Schmitt.

The REMPI spectrum was recorded in the group of R. Weinkauf, the rotationally resolved electronic spectra presented in this publication were recorded by O. Oeltermann and me. The analysis and interpretation of the obtained HRLIF spectra was my responsibility. Furthermore, I made the survey on the literature and wrote parts of the publication.

11. 6-Methoxyindole

Abstract

The structures of *syn* and *anti* 6-methoxyindole have been determined
in the electronic ground and excited states using rotationally resolved
electronic spectroscopy and high level *ab initio* calculations. Second
order coupled cluster theory predicts the lowest excited singlet states to
be heavily mixed and the transition dipole moments to depend strongly
on the geometries. From the analysis of the rovibronic spectra of seven
isotopomers the absolute orientation of the transition dipole moment
within the principle axis frame was determined to be L_b-like for both
conformers.

11.1 Introduction

Control of chemical reactivity through the electronic properties of substituents and
their position in aromatic systems is a routine task in every chemical laboratory.
The prediction of photochemical and photophysical reactivity is a much more de-
manding task. The change of electron density through mesomeric and inductive
effects does not only affect the reactivity of the molecule but also the relative po-
sitions of electronically excited states. Some of these might be repelling and the
position of a crossing (or conical intersection) between them, relative to the exci-
tation energy, strongly influences the photochemical and photophysical behavior.
Thus, a systematic study of the influence of substitution on the relative positions
of excited states is highly desirable. Rotationally resolved spectroscopy of electroni-
cally excited states can be used to label the states via the direction of the transition
dipole moment (TDM) in the inertial frame of the molecule and at the same time
to determine the excited state life times through the line shapes of the individual

rovibronic transitions. The coordinates which drive the excited states into a conical intersection (CI) may be determined by isotopic substitution, which leaves in first order the electronic energy unchanged, but changes the zero-point vibrational energy. Thus, the tunneling probability and as a consequence of this the excited state life is modified, if the states are below the CI.

Recently, we investigated the influence of different substituents at the C5 atom of indole (for atomic numbering cf. Figure 11.1) [189, 196, 216–218]. Depending on whether electrons are donated to or withdrawn from the chromophore, the energetic position of the two lowest excited singlet states can be considerably altered, and even a change of their energetic order is observed. To elucidate the different effects systematically, one could also choose a substituent and change its position at the chromophore, like it was done for instance by Eftink *et al.* [175], and Albinsson and Nordén [138] for methyl- and methoxyindoles. The most peculiar impact regarding the orientation and size of the TDM was observed for solvated 4- and 6-methoxyindole. In contrast to all other derivatives, the TDM vectors for the two lowest excited singlet states are not orthogonal, but make an angle of around 19-40° with respect to each other.

In this publication, we take a closer look at the electronic origin of the *anti* and the *syn* conformers of 6-methoxyindole (6MOI) and compare the experimental results to high level *ab initio* calculations. Furthermore, several deuterated isotopomers are included in this study to clarify the orientation of the TDM vector within the inertial axis frame experimentally. 6-Methoxyindole (6MOI) itself has found only little experimental interest so far. Sulkes and Borthwick measured the excited state lifetimes of both the *syn* and *anti* conformer of 6MOI in a supersonic jet and determined them to be 6.7 and 6.8 ns respectively [187]. From the lifetimes of the vibronic bands they concluded that coupling to the ^1L_a does not take place within 1000 cm^{-1} above the electronic origin. The orientations of the transition dipole moments for several excited singlet states were determined both in a stretched polyethylene host [138] and in glycol glass [175]. Both experiments agree in a significant alteration of the TDM orientation of the ^1L_b state due to a methoxy group at C6 compared to indole. Recently, 5-hydroxyindole has been investigated in our group [216]. From the analysis of the *syn* and the *anti* conformers a significant dependence of the orientation of transition dipole moment on the conformation became apparent. In this context it is very interesting to analyze the possible explanations for the unusual dependency of the TDM on the substituent. Furthermore, 6MOI offers the possibility to investigate both conformers, which was not possible for the related

5-methoxyindole (5MOI) because in this case only the *anti* conformer is present in the jet.
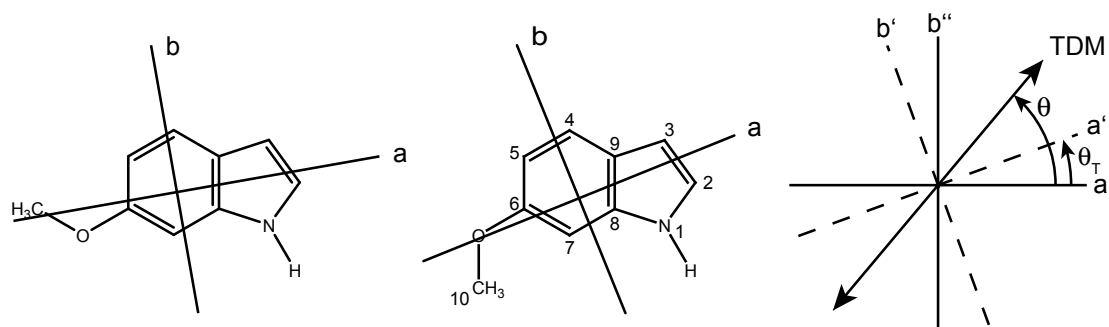
Figure 11.1: Structures of *anti* (left) and *syn* (middle) 6MOI in their respective principle axis frame. The definition of the positive direction of the TDM angle θ and the axis reorientation angle θ_T are shown on the right.

11.2 Techniques

11.2.1 Experimental procedures

6-Methoxyindole ($\geq$ 98%) was purchased from Apollo Scientific and used without further purification. The experimental set-up for the rotationally resolved laser induced fluorescence spectroscopy is described in detail in Chapter 3. In brief, the laser system consists of a single frequency ring dye laser (Sirah Matisse DS) operated with Rhodamine 6G, pumped with 7 W of the 514 nm line of an Ar^+-ion laser (Coherent, Sabre 15 DBW). The dye laser output was coupled into an external folded ring cavity (Spectra Physics Wavetrain) for second harmonic generation. The resulting output power was constant at about 15 mW during the experiment. The molecular beam was formed by co-expanding 6MOI, heated to 194°C, and 650 mbar of argon through a 200 μm nozzle into the vacuum chamber. The molecular beam machine consists of three differentially pumped vacuum chambers that are linearly connected by skimmers (1 mm and 3 mm, respectively) in order to reduce the Doppler width. The resulting resolution is 18 MHz (FWHM) in this set-up. In the third chamber, 360 mm downstream of the nozzle, the molecular beam crosses the laser beam at a right angle. The imaging optics set-up consists of a concave mirror and two plano-convex lenses to focus the resulting fluorescence onto a photomultiplier tube, which is mounted perpendicularly to the plane defined by the laser

and molecular beam. The signal output was then discriminated and digitized by a photon counter and transmitted to a PC for data recording and processing. The relative frequency was determined with a *quasi* confocal Fabry-Perot interferometer. The absolute frequency was obtained by comparing the recorded spectrum to the tabulated lines in the iodine absorption spectrum [67].

11.2.2 Computational methods

Quantum chemical calculations

All calculations were performed with the TURBOMOLE program package [162, 199]. Dunning's correlation consistent polarized valence triple zeta (cc-pVTZ) basis sets from the TURBOMOLE library were used [161]. The equilibrium geometries of the electronic ground and the lowest excited singlet states were optimized using the approximate coupled cluster singles and doubles model (CC2) employing the resolution-of-the-identity approximation (RI) [112, 163, 164]. Spin-component scaling (SCS) modifications to CC2 were taken into account [198].

Fits of the rovibronic spectra using evolutionary algorithms

The search algorithm employed for the fit of the rotationally resolved electronic spectra is an evolutionary strategy (ES) adapting normal mutations via a covariance matrix adaptation (CMA) mechanism. This (CMA-ES) algorithm was developed by Ostermeier and Hansen [201, 202] and is designed especially for optimization on rugged search landscapes that are additionally complicated due to noise, local minima and/or sharp bends. It belongs, like other search algorithms we also use, to the group of global optimizers that were inspired by natural evolution. For a detailed description of these evolutionary strategies refer to refs. [196] and [203] and Chapter 4.

Table 11.1: The CC2- and SCS-CC2-calculated rotational constants of *syn* and *anti* 6MOI calculated in the lowest three singlet states together with the changes upon excitation.

| | | *syn* | | | | | | | | |
| | | CC2 | | | | | SCS-CC2 | | | |
	S_0	S_1	S_2	ΔS_1	ΔS_2	S_0	S_1	S_2	ΔS_1	ΔS_2
A / MHz	2786.9	2679.6	2746.6	-107.3	-40.3	2786.4	2689.5	2735.9	-96.9	-50.5
B / MHz	772.0	774.9	759.2	+2.9	-12.8	768.0	767.0	758.1	-1.0	-9.9
C / MHz	606.9	603.4	597.1	-3.5	-9.8	604.4	599.1	595.8	-5.3	-8.6
θ / °	-	-41	76	-	-	-	-19	85	-	-
θ_T / °	-	±0.00	±0.00	-	-	-	0.10	-0.21	-	-

| | | *anti* | | | | | | | | |
| | | CC2 | | | | | SCS-CC2 | | | |
	S_0	S_1	S_2	ΔS_1	ΔS_2	S_0	S_1	S_2	ΔS_1	ΔS_2
A / MHz	3376.6	3254.3	3337.0	-122.3	-39.2	3373.2	3238.6	3334.0	-134.6	-39.2
B / MHz	710.7	712.3	697.7	+1.6	-13.0	707.8	707.9	696.5	+0.1	-11.3
C / MHz	589.3	586.6	579.2	-2.7	-10.1	587.2	583.1	578.3	-4.1	-8.9
θ / °	-	-39	75	-	-	-	-33	56	-	-
θ_T / °	-	-0.36	0.35	-	-	-	-0.25	0.18	-	-

11.3   Results

11.3.1   Computational Results

The CC2-calculated relative energies along with the adiabatic excitation energies of the first two excited singlet states for the *syn* and *anti* conformer of 6MOI are compiled in Table 11.2. Additionally, the results from the genuine CC2 calculation are shown in Figure 11.2. All energies are corrected for the contribution of zero point vibrations. As can be seen, the energies of both conformers are quite similar in the S_0 and S_1, only in the S_2 state a pronounced difference in the energies of the two conformers is predicted. In the electronic ground state the *anti* conformer is more stable than the *syn* conformer by around 250 cm^{-1}. Both genuine CC2 and SCS-CC2 are in very good agreement regarding this value. In the first excited singlet state both *ab initio* methods agree in diminishing the energetic gap between the conformers. However, they do not agree in the energetic order. While genuine CC2 predicts the *syn* conformer to be more stable by 204 cm^{-1} in the S_1 state, this conformer is shifted slightly to higher energies by the SCS-CC2 calculations. Here the *anti* conformer is more stable by 93 cm^{-1}. In the S_2 state *anti* 6MOI is predicted by both methods to be more stable than the *syn* conformer by 667 and

Table 11.2: Excitation energies and relative energies of the *syn* and *anti* conformer of 6MOI calculated at CC2/cc-pVTZ and SCS-CC2/cc-pVTZ level of theory. All energies are zero-point corrected. Additionally, the oscillator strength f and the permanent dipole moment are given. The contributions of the single-electron excitation refer to the frontier orbitals, shown in Figure 11.3. The HOMO is orbitals 39, and the LUMO is 40.

		S_0		S_1		S_2	
		syn	anti	syn	anti	syn	anti
ν_0 / cm^{-1}	CC2	-	-	34589	34136	38624	37708
ν_0 / cm^{-1}	SCS-CC2	-	-	34508	34337	39239	38125
ΔE (*anti-syn*) / cm^{-1}	CC2	0	+249	+204	0	+667	0
ΔE (*anti-syn*) / cm^{-1}	SCS-CC2	0	+264	0	+93	+850	0
f	CC2 (SCS-CC2)	-	-	0.10 (0.07)	0.13 (0.10)	0.05 (0.03)	0.05 (0.09)
$|\vec{\mu}|$ / D	CC2 (SCS-CC2)	3.08	0.82	4.3 (3.8)	1.9 (1.4)	4.61 (4.8)	2.00 (2.35)
$\theta(\vec{\mu})$ / °	CC2	-85	-72	-83	-69	-56	-33
		-	-	0.84(39→40)	0.89(39→40)	-0.72(39→40)	0.77(38→40)
	CC2	-	-	-0.32(39→44)	0.29(39→44)	0.56(38→40)	-0.48(39→40)
		-	-	-	-	-	0.31(39→44)
contributions		-	-	0.75(39→40)	0.79(39→40)	0.65(39→40)	-0.65(38→40)
	SCS-CC2	-	-	0.40(38→40)	-0.36(39→44)	-0.63(38→40)	0.65(39→40)
		-	-	-	0.35(38→40)	-	-
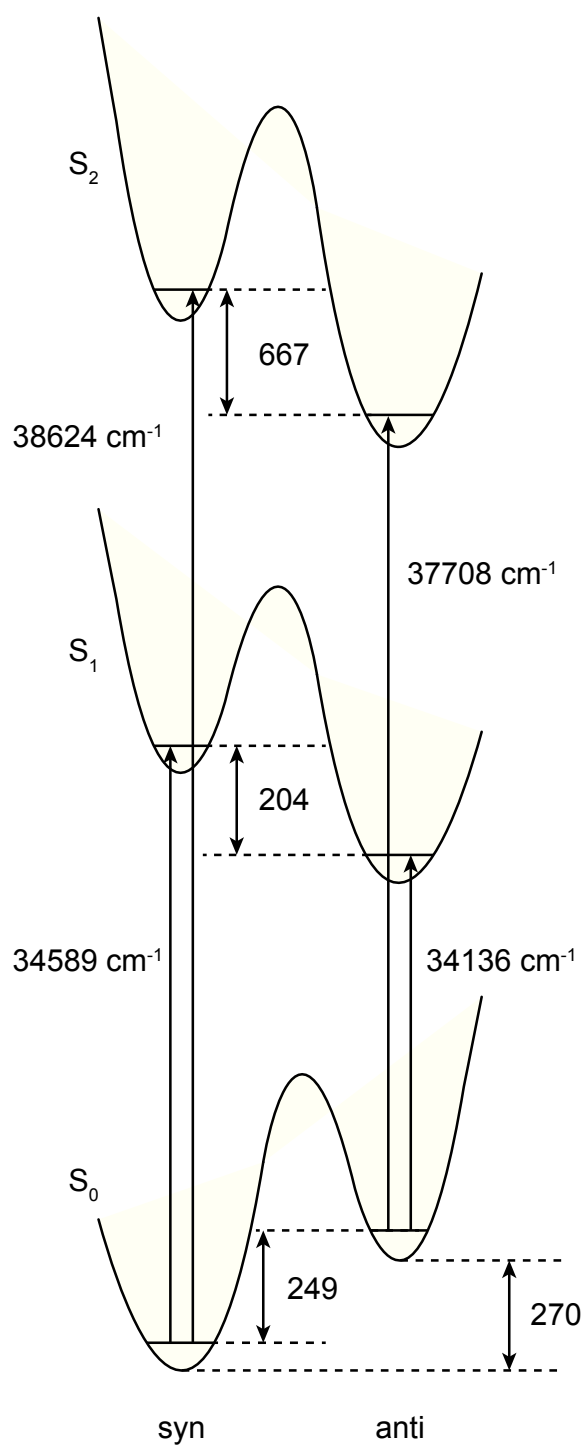
Figure 11.2: Energies of the lowest three singlet states according to the genuine CC2/cc-pVTZ calculations. All energies are corrected for zero point energies. For the results from the SCS-CC2 calculations refer to Table 11.2

850 cm^{-1}, respectively.

Table 11.1 collects the rotational constants A, B and C, in the electronic ground state and their changes upon excitation to the S_1 and S_2 state from the genuine CC2 and SCS-CC2 optimizations. Rotation of the bulky methoxy group about the bond connecting it to the indole chromophore has a pronounced effect on the rotational constants: $A(S_0)$ changes by nearly 600 MHz and $B(S_0)$ by 60 MHz. Therefore, no ambiguities in the assignment of the conformers are to be expected. The changes of the rotational constants upon excitation to S_1 state are similar for both conformers and the same is true for excitation to the S_2. The bond lengths are given in Table 11.3, the Cartesian coordinates of all conformers and states investigated are given in the supplementary material.

Table 11.3: Bond lengths of *syn* and *anti* 6MOI in the electronic ground and lowest excited singlet states from the genuine CC2 calculations utilizing the cc-pVTZ basis set. All angles in degrees, all distances in pm. For atomic numbering refer to Figure 11.1.

	S_0 (*syn*)	S_0 (*anti*)	ΔS_1 (*syn*)	ΔS_1 (*anti*)	ΔL_b (indole)[195]	ΔL_a (indole)[195]
N_1-H_1	100.5	100.5	+0.1	+0.2	+0.2	+0.5
N_1-C_2	138.2	138.2	-2.2	-3.1	+4.0	-3.6
C_2-C_3	137.5	137.4	+3.4	+4.4	+0.6	+6.3
C_3-C_9	143.0	143.2	-2.9	-3.2	-0.2	-0.9
C_9-C_4	140.7	140.1	+2.5	+3.7	+0.6	+1.9
C_4-C_5	138.3	139.1	+4.8	+3.6	+4.6	+3.9
C_5-C_6	141.4	141.2	+0.8	+1.0	+1.5	-2.8
C_6-O	137.0	137.2	-1.4	-1.8	-	-
O-C_{10}	141.9	142.0	+1.1	+1.2	-	-
C_6-C_7	139.2	139.3	+3.8	+3.6	+3.9	+6.6
C_7-C_8	140.2	139.3	+0.8	+1.3	+1.2	-0.6
C_8-C_9	141.9	142.3	+2.6	+0.7	+4.0	-1.2
C_8-N_1	137.5	137.5	+1.8	+2.3	-1.6	+3.6
C_5-C_6-O	115	124	-1	-1	-	-
C_6-O-C_{10}	116	116	+2	+2	-	-
O-C_6-C_7	124	115	-2	-2	-	-

As the orientation of the TDM results from the orbitals involved, it is interesting to take a closer look at these. Taking the energetic order shown in Figure 11.3 as a reference, excitation to the ^1L_a state is in general dominated by HOMO $\rightarrow$ LUMO excitation, while the ^1L_b state involves equal contributions of (HOMO-1) $\rightarrow$ LUMO and HOMO $\rightarrow$ (LUMO+4) (Due to the insertion of Rydberg orbitals in 6MOI, LUMO+4 corresponds to LUMO+1 in the general case) [195, 196]. In Table 11.2 all excitations contributing more than 8% are listed. From the entries it is

apparent that both states have one-electron excitations in common and hence are strongly mixed. According to the genuine CC2 calculations, the major contributions to the S_1 state is HOMO $\rightarrow$ LUMO excitation (71% and 79%) attributed to an ^1L_a-like state, but there are weaker ones (10% and 8%) belonging to an ^1L_b-like state. For the S_2 state the leading contribution depends on the conformer: for the *syn* conformer it is 58% L_a and 32% L_b, and for *anti* it is 69% L_b and 23% L_a. In the SCS-CC2 calculations the state mixing is even more pronounced: In the S_1 state the L_b contributions increase to 16% and 25%, while the S_2 is a 1:1 mixture of L_a and L_b contributions.

The difference in the magnitude of the excited state dipole moment for the S_1 and S_2 state (cf. Table 11.2), another distinguishing characteristic, is much less pronounced than in other indole derivatives, like 5-hydroxyindole [216]. The variation of the permanent dipole magnitude observed for the different conformers of 6MOI can be explained by simple geometric addition of the local dipoles of the NH and the ether group. For the *syn* conformer the angle between the vectors is 40°, while it increases to 165° for *anti* 6MOI. Hence, the local dipole moments of the latter conformer compensate one another partially which leads to a smaller overall dipole moment.

The ambiguity regarding the electronic nature is also mirrored by the excited state structures. The bond lengths of both conformers are compiled in Table 11.3. Comparing the changes upon excitation to the S_1 state to the changes for the ^1L_a and ^1L_b of indole [195], a basic trend is apparent. The changes within the pyrrol ring are closer to those attributed to the ^1L_a state, while the changes within the benzene ring resemble those of the ^1L_b.

11.3.2 High resolution spectra of the *syn* and *anti* conformers of 6-methoxyindole

The high resolution electronic spectrum of the A band at 33716.58 cm^{-1} is shown in Figure 11.4, the corresponding spectrum of the B band at 33948.12 cm^{-1} is shown in Figure 11.5. Our excitation energies of the two conformers are only slightly different from the origin frequencies given by Sulkes and Borthwick [187] (33722 and 33952 cm^{-1}). The assignment of the two observed bands to *syn* and *anti* 6MOI is straightforward: The origins of both conformers are in excellent agreement with the theoretical predictions. In Table 11.4 the molecular parameters taken from the
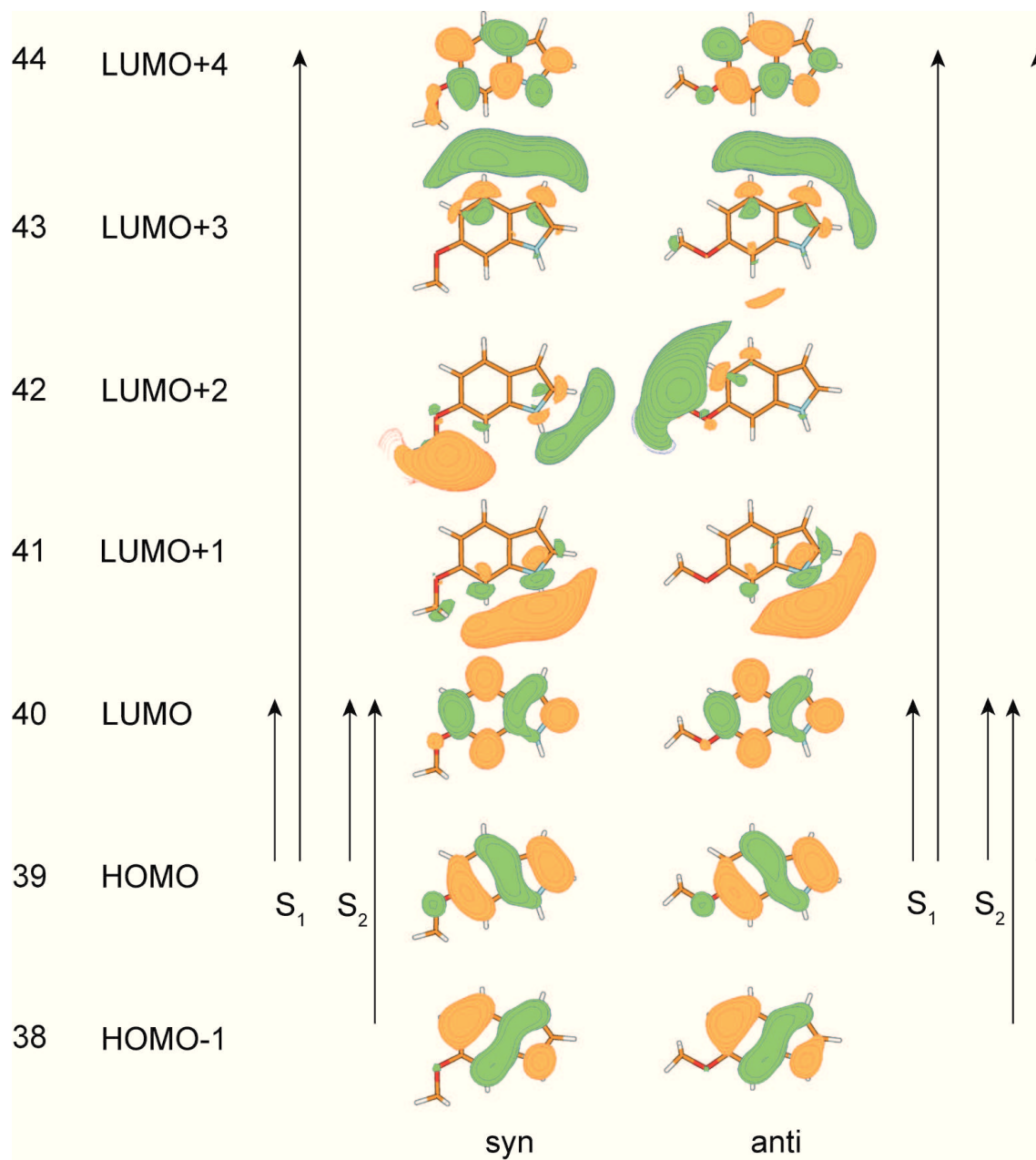
Figure 11.3: Frontier orbitals of 6-methoxyindole and leading contributions according to the genuine CC2 calculations

best fits employing the CMA-ES algorithm of the *anti* conformer are compiled. It contains the rotational constants of the electronic ground (A'', B'', C''), the excited state (A', B', C'), the excited state lifetime τ, and the in-plane orientation of the TDM with respect to the inertial a-axis, described by the angle θ. The respective data for the *syn* conformer are collected in Table 11.5. Based on a comparison of experimental and calculated rotational constants, we assign band A to the *anti* conformer and band B to the *syn* conformer. The predicted rotational constants match the experimental values perfectly for both the S_0 and S_1 state of the *anti* conformer. For the *syn* conformer slight deviations from the experimental values become apparent, but these stay always below 1%. Both spectra were analyzed with a rigid rotor Hamiltonian including axis reorientation within the plane of the chromophore [43]. The band type of both conformers is 68 % a-type and 32 % b-type for the *anti*, and 65 % a-type and 35 % b-type for the *syn* conformer. Hence, the relative orientation of the transition dipole moment (TDM) vector is nearly the same for *anti* 6MOI (34.2°) and *syn* 6MOI (36.2°). As the analysis of the spectra only yields the projection of the TDM vector onto the principle axis, we cannot determine the absolute sign of θ from this information alone. The analysis of isotopomeric spectra and the axis reorientation angle present two possibilities to circumvent this problem, and both of them are made use of in the further analysis.

Close inspection of the experimental bands reveals that each origin is accompanied by a weaker band, which is shifted to higher energies by 4257 MHz (5011 MHz) for the *syn* (*anti*) conformer. Due to contamination of the sample container and tubings with D_2O, we expected these bands to originate from a deuterated form of 6MOI. Assignment of these spectra requires the knowledge of the respective rotational constants, which were computed for all deuterated isotopomers from the *ab initio* structures given in the supplementary material, and are shown in Table 11.6 for the *anti* conformer. The experimentally determined rotational constants of the subband are given in the first line, the difference between theory and experiment in the second line. Perfect agreement is obtained for the isotopomer deuterated at position C_3. This is also the case for the subspectrum accompanying the origin of the *syn* conformer. The facts that both subspectra are shifted by approximately the same energy ($+0.17$ and $+0.14$ cm^{-1}) and have the same relative intensity (20% of the undeuterated origin) support this assignment. Furthermore, we were able to record the spectra of some additional singly and doubly deuterated molecules. All spectra could be assigned unambiguously using the analysis outlined before, and their molecular parameters are compiled in Table 11.4 and 11.5 as well. The
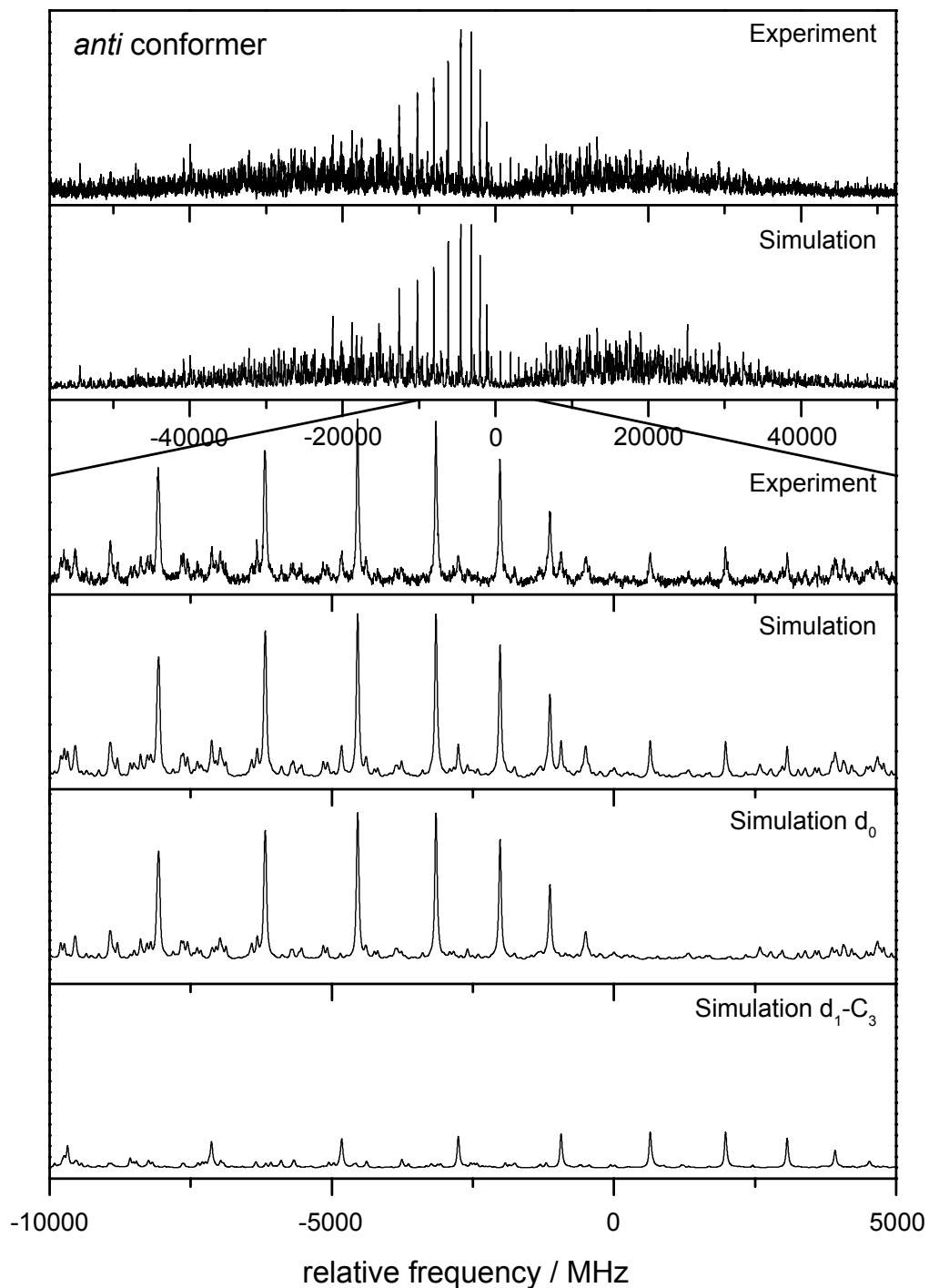
Figure 11.4: Rotationally resolved electronic origin of the *anti* (A) conformer

respective spectra are shown in the online supporting material.

Table 11.4: Experimentally determined molecular parameters of the *anti* conformer along with the deuterated species. Changes of the rotational constants are defined as: $\Delta B_g = B'_g - B''_g$, with B_g as rotational constants with respect to the inertial axes $g = a, b, c$. ν_0 (rel.) is the center frequency of the deuterated band relative to the undeuterated conformer. [a] The excited state lifetime of d_2-N_1C_3 (d_1-C_3) was set equal to the lifetime of the d_1-N_1 (d_0) isotopomer during the fit.

	d_0	[d-N_1]	[d-C_3]	[d_2-N_1C_3]
A'' / MHz	3373.87(3)	3263.9(1)	3299.46(3)	3191.1(1)
B'' / MHz	708.32(1)	703.07(2)	698.27(1)	693.46(2)
C'' / MHz	587.93(1)	580.95(2)	578.72(1)	572.03(2)
$\Delta I''$ / amu Å^2	-3.69	-3.73	-3.66	-3.68
A' / MHz	3248.04(3)	3145.6(1)	3178.04(3)	3077.1(1)
B' / MHz	710.22(1)	704.82(3)	700.32(1)	695.36(3)
C' / MHz	585.35(1)	578.32(2)	576.36(1)	569.67(2)
$\Delta I'$ / amu Å^2	-3.80	-3.82	-3.81	-3.88
ΔA / MHz	-125.83(1)	-118.27(2)	-121.42(1)	-113.98(2)
ΔB / MHz	1.90(1)	1.75(1)	2.05(1)	1.91(1)
ΔC / MHz	-2.58(1)	-2.63(1)	-2.36(1)	-2.37(1)
θ / °	±34.2(1)	±37.2(1)	±33.6(1)	±36.7
θ_T / °	∓0.67(1)	-	-	-
τ / ns	4.3(1)	3.5(1)	[a]	[a]
ν_0 / cm^{-1}	33716.58(1)	33723.66(1)	33716.75(1)	33723.85(1)
ν_0 (rel.) / cm^{-1}	-	+7.08(1)	+0.17(1)	+7.27(1)

11.3.3 Orientation of the transition dipole moment vector

To determine the electronic nature of the first excited singlet states, an analysis of the TDM vector orientation is performed. One method to determine the absolute orientation of the TDM it is the analysis of the axis reorientation angle: Electronic excitation of a molecule with symmetry less than C_{2v} may cause the orientation of the principle axis to deviate from the orientation of the ground state. In planar molecules the reorientation can be described using a single angle θ_T, which describes the rotation of the a''-axis about the c-axis onto the a'-axis in the excited state. Hougen and Watson [42] gave a relation from which the axis reorientation angle can be computed for any planar molecule using Cartesian coordinates in the principal
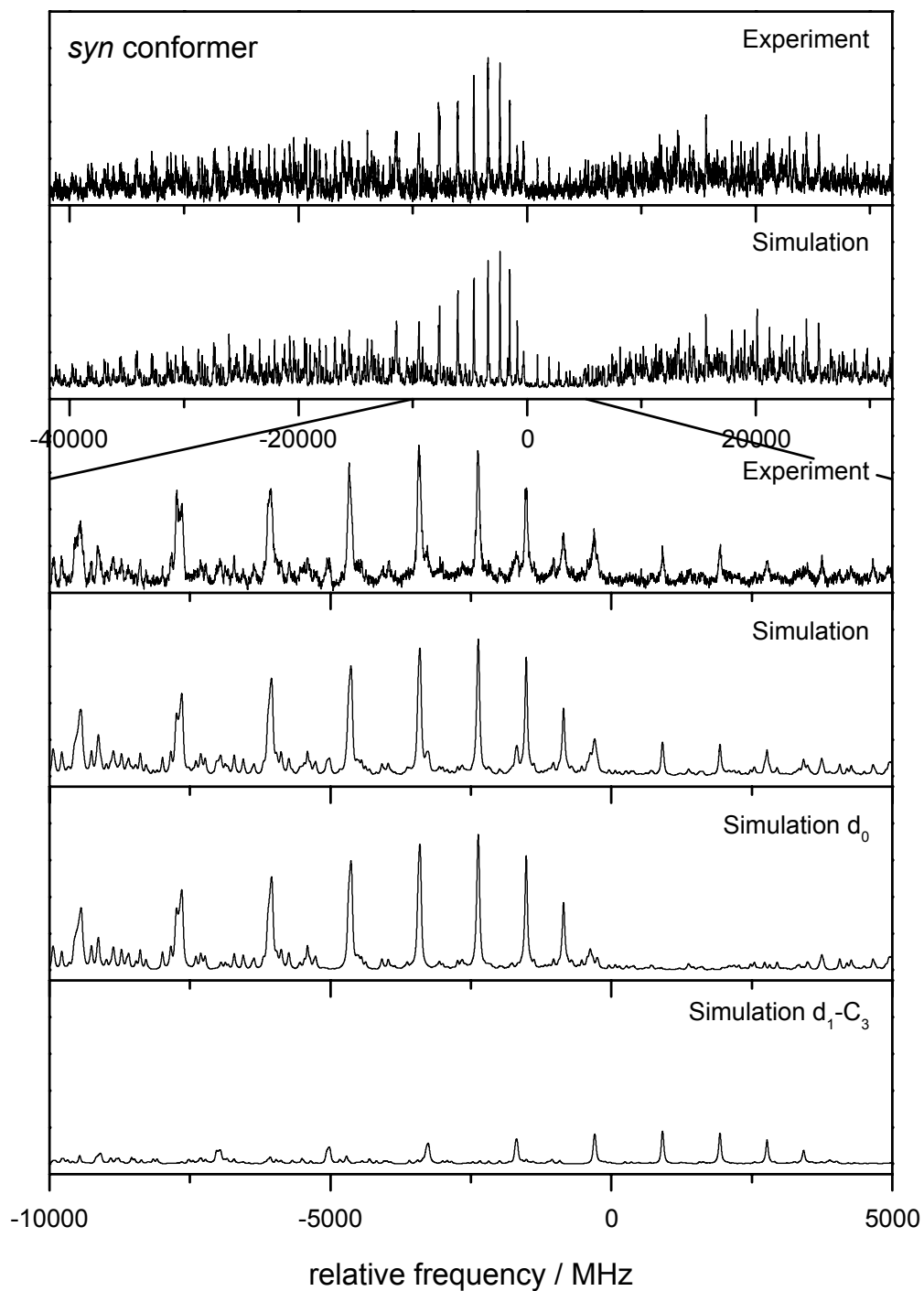
Figure 11.5: Rotationally resolved electronic origin of the *syn* (B) conformer

Table 11.5: Experimentally determined molecular parameters of the *syn* conformer along with the deuterated species. Changes of the rotational constants are defined as: $\Delta B_g = B'_g - B''_g$, with B_g as rotational constants with respect to the inertial axes $g = a, b, c$. ν_0 (rel.) is the center frequency of the deuterated band relative to the undeuterated conformer. [a] The excited state lifetimes of d_1-C_2 and d_2-N_1C_3 were set equal to the lifetime of the d_1-N_1 isotopomer during the fit. The lifetime of d_1-C_3 was set equal to the lifetime of the undeuterated compound.

	d_0	[d-N_1]	[d-C_2]	[d-C_3]	[d_2-N_1C_3]
A'' / MHz	2792.67(3)	2704.0(1)	2769.0(1)	2764.16(3)	2674.9(1)
B'' / MHz	767.59(1)	763.96(3)	749.94(5)	753.72(1)	750.41(3)
C'' / MHz	604.69(1)	598.17(3)	592.71(4)	594.82(1)	588.61(2)
$\Delta I''$ / amu Å^2	-3.59	-3.58	-3.67	-3.71	-3.81
A' / MHz	2698.51(3)	2614.52(1)	2676.1(1)	2671.61(3)	2587.0(1)
B' / MHz	769.43(1)	765.71(4)	751.62(6)	755.69(1)	752.28(4)
C' / MHz	601.43(1)	594.89(4)	589.54(5)	591.77(1)	585.52(3)
$\Delta I'$ / amu Å^2	-3.79	-3.79	-3.90	-3.91	-4.02
ΔA / MHz	-94.16(1)	-89.48(2)	-92.93(2)	-92.55(1)	-87.83(2)
ΔB / MHz	1.84(1)	1.75(1)	1.68(1)	1.97(1)	1.86(1)
ΔC / MHz	-3.26(1)	-3.29(1)	-3.17(1)	-3.05(1)	-3.10(1)
θ / °	±36.2(1)	±38.1(1)	±36.9(1)	±34.7(1)	±36.5(1)
θ_T / °	∓0.06(1)	-	-	-	-
τ / ns	4.5(1)	3.7(1)	a	a	a
ν_0 / cm^{-1}	33948.12(1)	33959.52(1)	33959.18(2)	33948.62(1)	33959.68(1)
ν_0 (rel.) / cm^{-1}	-	+11.40(1)	+11.06(1)	+0.14(1)	+11.56(1)

axis system (PAS) of each state:

$$tan(\theta_T) = \frac{\sum_i m_i(a'_i b''_i - b'_i a''_i)}{\sum_i m_i(a'_i a''_i + b'_i b''_i)} \qquad (11.1)$$

Here, the doubly primed coordinates a''_i and b''_i refer to the coordinates of the ith atom in the principal axis system in the electronic ground state, the singly primed coordinates to the respective excited state coordinates and m_i is the atomic mass of the ith atom in the molecule. For the definition of the sign of θ_T refer to Figure 11.1, which illustrates the influence of a positive angle θ_T on the main inertial axis. From the fit of the high resolution bands we get the relative sign of θ_T with respect to θ for each band, which can be compared to *ab initio* calculations. As the effect of θ_T on a spectrum is a shift of intensity between transitions of different band type, the relative intensities have to be as reliable as possible. Hence, we determined θ_T for each conformer from the electronic origin and set the so determined value as a constant in the subsequent fits of the deuterated species. The reorientation angles computed from the genuine CC2 geometries are -0.36° for the *anti* and 0.00° for the

Table 11.6: Comparison of the experimentally determined rotational constants of the subband accompanying the *anti* conformer to values taken from the CC2/cc-pVTZ calculations. The theoretical values are corrected by the difference between theory and experiment for the undeuterated species (line 2). The resulting deviations from the experimental value are displayed in brackets for each deuterated form.

	A''	B''	C''	A'	B'	C'
experimental	3299.5	698.3	578.7	3178.0	700.3	576.4
Δexp.-theory (d_0)	-2.7	-2.4	-1.4	-6.3	-2.1	-1.2
d_1-N_1	3263.5	703.1	580.9	3145.5	704.8	578.4
Δexp.-theory	(+36.0)	(-4.8)	(-2.2)	(+32.5)	(-4.5)	(-2.0)
d_1-C_2	3364.8	691.0	575.7	3239.7	692.8	573.2
Δexp.-theory	(-65.3)	(+7.3)	(+3.0)	(-61.7)	(+7.5)	(+3.2)
d_1-C_3	3399.2	698.2	578.7	3177.9	700.3	576.4
Δexp.-theory	**(+0.3)**	**(+0.1)**	**(±0.0)**	**(+0.1)**	**(±0.0)**	**(±0.0)**
d_1-C_4	3213.3	708.2	582.8	3091.9	710.1	580.0
Δexp.-theory	(+86.2)	(-9.9)	(-4.1)	(+86.1)	(-9.8)	(-3.6)
d_1-C_5	3298.7	704.3	582.8	3178.9	706.0	580.2
Δexp.-theory	(+0.8)	(-6.0)	(-4.1)	(-0.9)	(-5.7)	(-3.8)
d_1-C_7	3268.2	708	584.4	3146.2	709.9	581.8
Δexp.-theory	(+31.3)	(-9.7)	(-5.7)	(+31.8)	(-9.6)	(-5.4)

syn conformer. The values from the SCS-CC2 calculation are in general agreement. Therefore, we can only make reliable statements regarding the *anti* conformer. The values obtained from the fit of *anti* 6MOI are $\pm 0.67°$ for θ_T, and ∓ 34.2 for θ. This means that if θ_T is positive, θ necessarily must be negative and *vice versa*. Since we know from the *ab initio* calculations that θ_T is negative, θ must be $+34.2°$. In contrast to this, both CC2 methods predict θ_T and θ to have the same relative sign, and θ to be negative. A negative sign of θ is also predicted for *syn* 6MOI. So theory and experiment are contradicting each other regarding the orientation of the TDM vector at this point. In order to get further evidence concerning the absolute orientation of the TDM vector, we carefully analyzed the spectra of several deuterated species.

Exchanging a hydrogen atom by deuterium rotates the PAS towards the heavier deuterium but does not affect the orientation of the electronic transition within the molecule, as it was shown for benzimidazole [219] and 7-azaindole [220, 221]. Thus, the original value of θ is modified by the angle introduced by the H/D exchange. Table 11.7 contains the experimentally determined values for θ and their changes induced by deuteration. These data nicely confirm the assignment of θ to be positive

as we derived experimentally from the reorientation angle. First of all, all deutera-
tions, which rotate the PAS by a negative angle lead to an increase in the relative
value of θ. This increase is more pronounced, if the substituted hydrogen atom is
far away from the axis. Accordingly, the largest rotation is found for *anti* d_1-N_1
6MOI, the smallest for *syn* d_1-C_2 6MOI. Comparing the values determined for the
doubly deuterated isotopomers d_2-N_1C_3 to the shifts of d_1-C_3 and d_1-N_1 illustrates
that the rotations are additive, confirming our assignment.

Table 11.7: Experimentally determined values for θ and their changes $\Delta\theta$ induced
by deuteration for *syn* and *anti* 6MOI.

	syn		*anti*	
	θ	$\Delta\theta$	θ	$\Delta\theta$
d_0	36.2	-	34.2	-
d_1-N_1	38.1	+1.9	37.2	+3.0
d_1-C_2	36.9	+0.7	-	-
d_1-C_3	34.7	-1.5	33.6	-0.6
d_2-N_1C_3	36.5	+0.3	36.7	+2.5

Although the values of $\theta(S_1)$ for both conformers are quite similar, the orientation
within the principle axis system differs. Introduction of a methoxy group at position
6 rotates the PAS of indole by $+10.1°$ (*anti*) or $+22.2°$ (*syn*). Taking this difference
into account, the values for θ would be $+44.3°$ for *anti* 6MOI and $58.4°$ for the *syn*
conformer within the PAS frame of indole, corresponding to a difference of $14.1°$.
Recently, a quite similar difference in the TDM orientation was observed for the
two conformers of 5-hydroxyindole [216]. The experimental results were discussed
to originate either from a hyper conjugative bond between the OH group and a CH
bond or electrostatic interactions induced by the lone pairs of the oxygen. This is
very likely also the case in 6MOI.

11.4   Discussion

Apart from the *ab initio* predicted energy ordering, additional evidence regarding
the question, if the observed state has characteristics of an L_a or L_b state, is the
orientation of the TDM vector. According to the experimental findings the sign
of θ is positive and hence the observed state is L_b-like. The *ab initio* calculations,
however, predict θ to be negative what would be a signature of an ^1L_a state. We
have shown recently that the orientation of the TDM in special cases extremely

depends on the geometry of the electronic states involved [207]. This is also be the case for 6MOI. The contributions to the L_a and the L_b are heavily mixed for both states which is also mirrored by the excited state geometry of the S_1. Slight geometry changes might influence the relative influence of contributions and thus have a pronounced effect on the electronic nature of the respective states. Therefore, we believe that the quite different orientation in the *ab initio* calculation compared to the experiment might be a consequence of vibrational averaging of the equilibrium structure.

From the experimental point of view, the interpretation of the results is less ambiguous. A strong evidence for a positive sign of θ, and hence for the ^1L_b, is the orientation of the TDM vector from the spectra of the deuterated species. In total 7 spectra were analyzed and for all of them θ could be determined with high accuracy. The correct assignment of the spectra to the respective isotopomers is based on the rotational constants and supported by the additivity of the zero point energy shifts and the TDM orientation. Further experimental results pointing towards the S_1 being the ^1L_b, are the excitation energies of the lowest two excited singlet states. In 5-methoxyindole the energetic gap between ^1L_b and ^1L_a increases to 3088 cm^{-1} compared to indole [209]. This is mainly due to a strong redshift of the ^1L_b state, while the ^1L_a is not influenced significantly. As shown in a number of studies the energetic position of the ^1L_a state is not perturbed much by methyl- or methoxy substituents [138, 175] and from linear dicroism measurements it is known that in 6MOI the energetic gap is of the same magnitude. With this in view, it is rather unlikely that changing the position of the methoxy group from 5 to 6 results in a dramatic redshift of the ^1L_a, while the ^1L_b is shifted to the same extent to higher energies. Interestingly, the *ab initio* excitation energies are in good agreement with the experiment, in spite of the other discrepancies.

So in conclusion the electronic nature of the lowest excited singlet state is assigned to be the L_b. This assignment is solely based on experimental evidence while the results of the *ab initio* calculations are not unambiguous.

The excited state lifetimes of both conformers (4.3 and 4.5 ns) are considerably shorter than the corresponding one of indole (17.6(1) ns) [87]. In this context Sobolewski and Domke calculated the reaction path for hydrogen atom detachment from the NH group [53]. The authors explained the short lifetime of the ^1L_a state by the influence of a repulsive $\pi\sigma^*$ state, which leads to an effective radiationless deactivation channel for the excited states. As this mechanism is expected to play a role 5 eV ($\approx$40000 cm^{-1}) above the S_0 in indole, which is more than 6000 cm^{-1}

higher in energy compared to our experiments, this model is rather unlikely to explain our observations. Furthermore, deuteration at the nitrogen atom decreases the excited state lifetime, and hence contradicts a deactivation path promoted by NH-bond elongation. If one takes a closer look at the excited state lifetimes of other methoxyindole derivatives, it becomes apparent that they are below 7 ns [187, 196]. So it seems that the methoxy group itself introduces a channel for radiationless deactivation to indole, which is independent of its position at the chromophore.

11.5   Conclusions

The A and B bands of 6MOI could be shown to belong to two different conformers. They were assigned as the *anti* and *syn* conformer by a combination of rotationally resolved electronic spectroscopy and *ab initio* calculations. It was shown unambiguously from the analysis of the TDM orientation of seven isotopomers and the axis reorientation that the absolute sign of θ is positive. Hence, from the experimental results we assign the electronic nature of the S_1 state to be L_b-like.

The lowest three singlet states have been characterized by genuine CC2 and spin component scaled CC2. While the excited state structures and excitation energies are in good agreement with the experimental results, there is a discrepancy regarding the electronic nature of the excited states. Both CC2 methods predict the S_1 and S_2 state to be strongly mixed of contributions attributed to the ^1L_a and ^1L_b state in indole [195]. According to the calculations the main influence on the S_1 state corresponds an L_a-like state with a negative angle θ for the orientation of the TDM vectors. However, the permanent dipole moments and the oscillator strengths of both excited states are predicted to be nearly equal. Hence, for this molecule a classification of the $\pi\pi^*$ states as being "L_a" or "L_b" in nature is not possible according to the calculations.

The comparison of our gas phase experiments to the condensed phase data of Albinsson and Nordén [138] (stretched polyethylene films) and of Eftink *et al.* [175] (frozen solutions of propylene glycol) is desirable, but at the same time very difficult due to the completely different experimental conditions. Both the transition energy, as the orientation of the transition dipole moment depend critically on the local surrounding, a polar matrix in the case of Eftink *et al.*, a nonpolar matrix in the experiments of Albinsson and Nordén, and the isolated molecule in our case, without intermolecular interactions. Nevertheless, at least the experimental results in the polyethylene film do not stand in severe contrast to the ones published here.

Albinsson and Nordén stated that the angle between the TDM vectors of the ^1L_a and ^1L_b is either 19 or 81°. Considering the orientation of the TDM of the ^1L_a state to be relatively constant, an angle of 81° results in an orientation comparable to our results. The authors chose, however, the smaller of the two possible values in agreement with INDO/S-SDCI calculations published by Eftink *et al.* [175]. Thus, it seems that the excited singlet states of 6MOI pose a problem to quantum chemical calculations in general. This is even more surprising as in 5-methoxyindole these problems do not occur [196].

The considerable shortening of the excited state lifetime compared to the parent molecule indole [87] is proposed to result from the methoxy group itself, introducing a new channel for radiationless deactivation to indole.

Acknowledgement

11.6   Publication

The contents of this chapter has been published in slightly different form as *Position Matters: High Resolution Spectroscopy of 6-Methoxyindole* in the *Journal of Chemical Physics* (impact factor: 3.333), 2013, **138**, 024321(1-9) by Christian Brand, Olivia Oeltermann, Martin Wilke, and Michael Schmitt.

The spectra were recorded by O. Oeltermann, M. Wilke and me, the *ab initio* calculations were done by M. Schmitt and me. I am responsible for the analysis of the data and interpreted them in close collaboration with M. Schmitt. The writing was completely done by me.

12. Flexible Substituents

Going one step further from the simple substituents covered in the preceeding chapters, we arrive now at larger side groups, increasing the complexity of the investigated systems. The introduction of flexible side chains to indole has a number to consequences for its photophysics. First of all, the number of conformers is greatly enhanced. In 5-methoxyindole, for instance, the conformational space encompasses only two possibilites, while this number increases to 54, if additionally an ethyl amino side chain is present like in 5-methoxytryptamine. Although only a small fraction of these possible conformers is actually observed in jet experiments, *ab initio* calculations have to be done for a considerable part of the conformational space to assign the respective structures. As we will see in the chapter on melatonin, the comparison to related structures can reduce the number of important candidates significantely. But the influence of the side chain is not confined to an increase in the number of conformers. Additional to the through bond effects, the side chain may exert an influence on the chromophore via *through space* effects. In this view, the side chain may act as an intramolecular solvent. These considerations may have an effect on the energetic position of electronic states and the couplings between them. Böhm *et al.* showed that the conical intersection connecting the ^1L_a and ^1L_b states, which is 1400 cm^{-1} above the ^1L_b state in indole (cf. Chapter 6), is shifted down to ≈ 400 cm^{-1} above the ^1L_b state in tryptamine [157]. An even more pronounced effect was described by Dian *et al.* for several large indole derivatives [136]. The authors observed a large impact of the permanent dipole moment in the peptide backbone for N-acetyl tryptophan amide (NATA) and N-acetyl tryptophan methyl amide (NATMA) on the chromophore. This leads in some conformers to a switching in the excited states order between the ^1L_a and the ^1L_b, deduced from laser induced fluorescence spectra. Another possibility to manipulate the photophysics is the introduction of a charge to the neutral molecule: Kang *et al.* attributed the short excited state lifetime (380 fs) of protonated tryptophan TrpH$^+$ in an ion trap to electronic mixing of a $\pi\sigma^*$ state to the lowest $\pi\pi^*$ state [222]. The significant

increase in the excited state lifetime upon complexation with two water molecules is believed to result from the shift of the σ^*_{NH} orbital of the side chain to higher energies, as reported by Mercier *et al.* [223]. In summary it can be stated that the energetic position of the excited states and the coupling between them can be influenced to a certain extent by chosing specific substituents and conformers.

Indole is the base frame of a number of biologically active substances. The most important of these is the aromatic amino acid tryptophan. As outlined in the introduction it is the major source of information regarding structure, energy transfer mechanisms and the local surrounding, when the fluorescence of a protein is analyzed. So the monomer was subject to a vast number of studies. For a comprehensive introduction to tryptophan in proteins refer to references [9, 224–228]. Studies in the gas phase proved to be difficult as thermal heating can easily lead to decomposition of the carboxyl group. Pioneering work in this field was done in the group of Levy [229–233]. Combining the techniques of thermospray, thermal desorption and a supersonic expansion Rizzo *et al.* succeeded in recording the first resonant two-photon-ionization (R2PI) spectrum of tryptophan in a molecular jet [229]. In subsequent publications, the features of the vibrationally resolved spectra were assigned to 6 conformers A-F [230, 232]. Recently, an additional conformer G was observed in a molecular jet with cavity ring down spectroscopy by Rouillé *et al.* [234]. Nevertheless, the main focus of attention in the following years was set on conformer A. This was mainly due to unique spectroscopical features within the conformatinal space of tryptophan. It exhibits a pronounced 26 cm^{-1} progression [229], and it has a shorter excited state lifetime and a higher quantum yield for fluorescence than the remainder conformers [233, 234]. Furthermore, an intense red-shifted broad background is observed in the dispersed fluorescence (DF) spectra [232]. The latter was attributed to emisson from the ^1L_a state or an intramolecular exciplex [232, 233]. Snoek *et al.* assigned the structure of conformer A to be characterized by a chain of hydrogen-bonded interactions OH $\rightarrow$ NH$_2$ $\rightarrow$ π based on UV hole-burning and infrared ion dip spectroscopy [235]. Lindinger *et al.* investigated tryptphan in liquid helium droplets and discussed the 26 cm^{-1} progession of the A conformer in terms of a distorted potential energy surface in the excited state [236]. These hypotheses fall in line with the conclusions Dian *et al.* drew from the analysis of large indole derivatives [136].

Sipior and Sulkes discussed the reliability of molecular mechanics calculations for tryptophan [237], and Teh *et al.* contributed LIF and DF spectra of the bare molecule and a number of clusters [238]. The reaction path of hydrogen-transfer-

induced fluorescence quenching including aborted decarboxylation was elaborated by Blancafort *et al.* [239]. A comparative study with different DFT functionals on neutral and cationic tryptophan was presented by Baek *et al.* [240].

Many groups went from the isolated tryptophan to small modell peptides, like the groups of Levy [241, 242], Zwier [243, 244], Gerhards [245, 246] and de Vries [247, 248]. Here, the main focus of attention was set on the conformational space and the influence of the peptide backbone on the photophysics of the chromophore. Time-resolved measurements of protonated dipeptides were performed, for instance, in the groups of Jouvet [249], Schultz [250] and Fuke [251].

Several hormones and neurotransmitters are based on the indole chromophore. These are, for instance, the neurotransmitters tryptamine (3-ethylaminindole), serotonin (5-hydroxytryptamine) and mexamine (5-methoxytryptamine), and the hormones 3-indole acetic acid and melatonin (N-acetyl-5-methoxytryptamine). All of these biologically active substances have been subject to extensive studies in the gas phase. As tryptamine constitutes the scaffold for a number of other neurotransmitters (*vide supra*) and is very closely related to tryptophan, its photophysics have been thoroughly examined [157, 252–261]. The conformational space has been investigated with vibrational and rotational resolution in both the S_0 and S_1 states. In total seven conformers were identified, based on microwave spectroscopy [252], rotational coherence spectroscopy [253], high resolution UV spectroscopy [254], rotationally resolved laser induced fluorescence spectroscopy [255, 256], and resonant ion dip spectroscopy and UV-UV hole burning spectroscopy [257]. Further studies determined the permanent dipole moments of several conformers [258], investigated the energy threshold between different conformers [259, 260] and took a look at the influence of the experimental conditions on the conformational equilibrium [261]. The influence of a conical intersection on the photophysics of tryptamine was illustrated by Böhm *et al.* [157].
The other derivatives based on tryptamine drew considerably less experimental interest: The conformational preferences of serotonin and melatonin and their respective water clusters were subject to several publications by the group of Zwier [210, 262–264], and 5-methoxytryptamine was characterized in a molecular beam by Vu *et al.* [265].

In the next two chapters we take a closer look at tryptamine and melatonin. Although the conformational space of tryptamine has been investigated extensively, the impact of the respective conformation on the photophysics of the chromophore remained mostly unregarded. Hence, in Chapter 13 we look for variations in the

orientation of the transition dipole moment orientation and discuss these in the context of symmetry and intramolecular solvation. The current conformational assignment of melatonin is based on a combination of vibrationally resolved electronic spectroscopy and quantum mechanical calculations. In Chapter 14 the rotationally resolved electronic spectra of the two most intense bands are analyzed and consequently the conformational assignment is refined.

13. Tryptamine

Abstract

A remarkable influence of the orientation of a polar side chain on the direction of the $S_1 \leftarrow S_0$ transition dipole moment of monosubstituted benzenes was previously reported from high-resolution electronic spectroscopy. In search for a more general understanding of this non-Condon behavior, we investigated ethylamino substituted indole and benzene (tryptamine and 2-phenylethylamine) using *ab initio* theory and compared the results to rotationally resolved laser-induced fluorescence measurements. The interaction of the ethylamino side chain with the benzene chromophore can evoke a rotation and a change of ordering of the molecular orbitals involved in the excitation, leading to state mixing and large changes in the orientation of the excited state transition dipole moment. These changes are much less pronounced in tryptamine with the indole chromophore, where a rotation of the transition dipole moment is attributed to Rydberg contributions of the nitrogen atom of the chromophore. For phenylethylamine, a strong dependence of the oscillator strengths of the lowest two singlet states from the conformation of the side chain is found, which makes the use of experimental vibronic intensities for assessment of relative conformer stabilities at least questionable.

13.1 Introduction

The interaction between a flexible polar side chain and a chromophore to which it is connected covalently has found considerable interest over many years, since it mimics the different stabilizations of electronic states by its direct molecular surrounding. Such interactions play an important role in the photophysics of aromatic

chromophores e.g. in native peptides. In some cases it is possible to monitor the influence of the side chain on the conformers by determination of the orientation of the $S_n \leftarrow S_0$ electronic transition dipole moment (TDM) for the different chromophores. In electronic spectroscopy the perturbing light field of the irradiating photon(s) interacts with the wave functions of the electrons in the two electronic states involved in the transition. The TDM is the dipole moment of the oscillating charge density and a measure of electronic charge, that is shifted during the excitation. For a $S_1 \leftarrow S_0$ transition it is defined as

$$\langle \mu_{TDM} \rangle = \int \Psi_{S_1}^* \hat{\vec{\mu}}_e \Psi_{S_0} d\tau_e \tag{13.1}$$

Ψ_{S_1} and Ψ_{S_0} are the wave functions of the corresponding states S_1 and S_0, $\hat{\mu}$ is the electronic dipole operator and the integral runs over the coordinates of all electrons. Changes in the orientation of the TDM with respect to the chromophore describe the modification of the electronic structure, induced by its conformation in at least one electronic state involved. This change in electronic structure is accompanied by a change in reactivity. Knowledge of these mechanisms is indispensable when discussing the photophysics of molecular excited state properties.

A lot of what we know about the interaction between a chromophore and an attached side chain was contributed by the groups and collaborations of Pratt [266–269] and Simons [266–272]. They ascertained the inertial and electronic contributions which are responsible for the rotation of the TDM. Analysis of partly or fully rotationally resolved electronic spectra yields the projection of the TDM onto the principle axis system (PAS) of a molecule. As the conformation changes, the PAS rotates and consequently the orientation of the TDM within this frame changes. This inertial contribution is easy to deal with as soon as the conformation of the molecule is known. Electronic contributions to the orientation of the TDM on the other hand are far more difficult to handle. Hepworth *et al.* analyzed the rotationally resolved fluorescence excitation spectra of 3-hydroxy benzoic acid esters and reported that, within the experimental error, a methyl ester group attached in 3-position to phenol makes a constant electronic contribution to the orientation of the TDM in the molecular frame, independent of its orientation [266]. The influence of the hydroxyl group on the other hand depends much more on its orientation with respect to the ester group. In a following publication the authors report of a small rotation of the TDM in different 3-aminobenzoic acid esters [268].

The location of a polar side chains above the aromatic plane may have a remark-

ably large influence on the orientation of the TDM. The loss of symmetry in some conformers was postulated to be one of the main reasons, resulting in an increase of the number of single-electron excitations, that contribute to the electronic excitation like in 3-phenyl-1-propionic acid [269]. The importance of this interaction was demonstrated by Dickinson *et al.* in a study on n-propyl- and n-butylbenzene [270]. Although these side chains lack polar groups, all *gauche* conformations show a rotation of the TDM. The effect of symmetry reduction alone seems not to turn the balance, since no effect for asymmetric *anti* conformers could be detected. The bottom line of these works is that the loss of symmetry allows the possibility of state mixing, consistent with changes in the orientation of the $S_1 \leftarrow S_0$ TDM. The degree of mixing will depend on the interaction between the ring and the side chain. Dickinson *et al.* could substantiate this interaction researching 2-phenylethyl alcohol and 2-phenylethylamine [271]. They report that the degree of rotation of the TDM in the *gauche* conformer is modulated by the hydrogen-bonding interaction between the terminal hydroxyl or amino hydrogen atom of the side chain and the π-system of the ring. The most thorough theoretical approach to this matter is an *ab initio* work by Kroemer *et al.* [267]. Five singly substituted benzene derivatives were studied, in order to elucidate the interactions which are responsible for the observed rotations of the TDM.

The question arises, if these results also apply for less symmetric chromophores than benzene. Evidence is given by a publication of Hockridge *et al.* [272], who investigated 4-hydroxyphenylethanol: substitution of an OH-group in 4-position greatly reduces the sensitivity of the $\pi^* \leftarrow \pi$ transition to conformational changes. The system we chose to further cast light on this subject is tryptamine (TRA). The conformational space of tryptamine has been the topic of several publications. Park *et al.* found six conformers in low resolution laser-induced fluorescence (LIF) spectra and named them according to the relative intensity A-F [273]. Rotationally resolved laser induced fluorescence spectra were independently presented by Nguyen *et al.* [255] and Schmitt *et al.* [256] and resulted in the unequivocal assignment of the spectra to the seven conformers.

In the current study we present a theoretical analysis of the TDM moment orientations in 2-phenylethylamine (PEA) and in 3-ethylaminoindole (tryptamine=TRA) and make comparison to the results of rotationally resolved electronic spectroscopy.
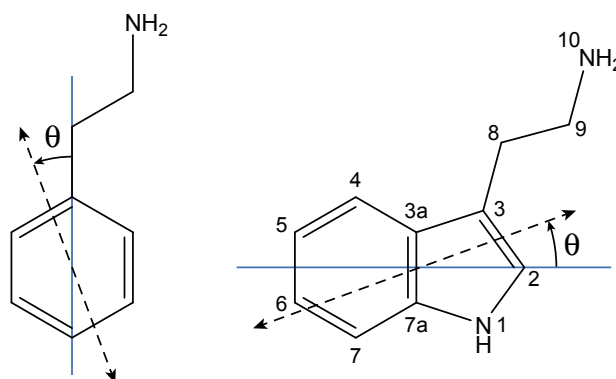
Figure 13.1: Atomic numbering for tryptamine and definition of the polar angle θ (positive sign) for PEA and TRA. The axes which define the angle θ in PEA and TRA are the a-axes of the $Anti(up)$ conformer and of indole, respectively.

13.2 Theoretical Methods and Computational Details

13.2.1 Geometry Optimization

Structure optimizations were performed employing the correlation consistent Polarized Valence Triple Zeta (cc-pVTZ) basis from the TURBOMOLE library [161, 162]. The equilibrium geometry of the electronic ground and excited states were determined using the approximate coupled-cluster singles and doubles model (CC2) in the approximation of the resolution of identity (RI). All optimizations and normal mode analyses were carried out utilizing the TURBOMOLE package, version 5.6 [274].

For the computation of singlet state energies and wave functions, we used the combined density functional theory / multi-reference configuration interaction method by Grimme and Waletzke (DFT/MRCI) [110]. This method was shown to yield excellent electronic spectra of organic molecules at reasonable computational expense. The configuration state functions (CSFs) in the MRCI expansion are built up from Kohn-Sham (KS) orbitals, optimized for the dominant closed shell determinant of the electronic ground state employing the BH-LYP [2, 122] functional. All 62 valence electrons were correlated in the MRCI runs and the eigenvalues and eigenvectors of eight singlet states were determined. The initial set of reference CSFs was generated automatically in a complete active space type procedure (including all single excitations from the five highest occupied molecular orbitals in the KS determinant to the five lowest virtual orbitals) and was then iteratively improved. The MRCI expansion was kept moderate by extensive configuration selection. The

MRCI space was spanned by about 100,000 energy-selected single and double excitations (200,000 singlet CSFs) from approximately 45 reference configurations for PEA and 50 reference configurations for TRA.

13.3 Results and Discussion

13.3.1 Electronic ground state energies and structures

The electronic ground state energies of the five most stable conformers of PEA and of the nine most stable conformers of TRA are calculated using DFT/MRCI on the CC2/cc-pVTZ optimized structures, cf. Tables 13.1. The structures of the conformers investigated in this study are shown in Figures 13.2 and 13.4. The conformational space of PEA was investigated by Dickinson *et al.* using LIF and one- and two-color, mass-selected resonant two-photon ionization (R2PI) spectroscopy [271]. They numbered the theoretically predicted conformers from I to V and could assign conformer II to V to observed spectroscopic features. The five conformers are the *Gauche(in)*, the *Gauche(up)*, the *Gauche(out)*, the *Anti(out)*, and the *Anti(up)* conformer, respectively. In this nomenclature, gauche refers to the gauche orientation of the amino group, and "in", "up", and "out" describe the orientation of the amino lone pair.

The nomenclature for the different TRA conformers, was introduced by Carney *et al.* [257]. Gpy (Gph) designates conformations in which the amino group is in gauche conformation and points to the pyrrole (phenyl) side of the indole chromophore. In all *anti* conformers, the amino group points away from the chromophore. The orientation of the amino group lone pair is described by the identifiers "up", "out" and "in". Although the two "in" conformers of TRA, with the lone pair pointing to the indole ring, have similar ground state energies as the other seven ones, they have never been observed experimentally. For the sake of completeness, the $Gph(in)$ and $Gpy(in)$ conformers of tryptamine and the $Gauche(in)$ conformer of PEA were included in this study. Interestingly, the structure evaluated for the $Gpy(in)$ conformer of TRA deviates strongly from all other tryptamine conformers. The $C_3 - C_8$-bond is rotated by 60° towards the pyrrole ring so that the terminal nitrogen atom of the side chain is located in the plane of the chromophore and a hydrogen-bond is formed between the lone pair and H_{2a} (see Figures 13.1 and 13.4).

Table 13.1: CC2/cc-pVTZ calculated relative stabilities ΔE [kJ/mol] and rotational constants A, B, and C [MHz] of the five most stable 2-phenylethylamine conformers and of the of the nine most stable tryptamine conformers. All calculations include ZPE corrections at the level of the optimization

PEA	Calc.				Exp.[275]		
	ΔE	A	B	C	A	B	C
Anti(out)	0.000	4384	864	773	4396.16	857.41	766.80
Gauche(out)	1.041	3305	1107	972	3313.74	1079.28	959.20
Anti(up)	1.986	4341	862	772	4360.68	855.75	765.33
Gauche(up)	3.206	3270	1093	971	3287.71	1066.35	957.63
Gauche(in)	6.508	3412	1077	916	-	-	-

TRA	Calc.				Exp.[255]		
Gpy(out)	0.000	1733	692	559	1731.02	682.04	551.56
Anti(ph)	1.051	1758	624	481	1767.97	618.39	478.27
Anti(py)	1.738	1764	621	479	1776.28	616.01	478.21
Gph(up)	2.156	1597	755	569	1605.11	737.84	561.51
Anti(up)	2.902	1755	621	479	1761.40	614.75	475.58
Gpy(up)	2.994	1712	691	558	1710.25	682.22	551.10
Gph(out)	4.279	1589	772	567	1590.07	754.94	561.18
Gpy(in)	5.238	2339	576	471	-	-	-
Gph(in)	9.484	1565	759	544	-	-	-

13.3.2   Transition dipole moments

The analysis of rovibronic line intensities in rotationally resolved electronic spectra yields the projection of the transition dipole moment vector onto the principal axes. In flexible molecules with several stable minima on the potential energy surface however, the position and orientation of the principle axis system depends on the actual conformation. In order to compare the orientations of the TDM vector of different conformers independently of the conformation, a reference frame has to be chosen into which all the other coordinate systems have to be rotated. The most obvious choice is the principle axis system of the chromophore itself without the side chain.

To evaluate the experimentally determined transition dipole moments within this coordinate system they have to be converted in cartesian coordinates by using equation 13.2. Here $\mu_\alpha(\alpha = a, b, c)$ are the components of the transition dipole moment vector with respect to the principle axis a, b and c, μ is the magnitude of the transition dipole moment and ϕ and θ are the polar angles of the TDM in the principle axis system (PAS). As no information about the sign of the components can be extracted from the spectra, there are four different orientations which have to be taken into account (2^3 possible permutations of the sign divided by 2, as for instance the combination of only positive and only negative components yields the same vector). However, not all of these possibilities are physically meaningful. Since all excitations of PEA and TRA take place in the (planar) chromophore, all TDM vectors exhibiting an angle ϕ, which deviates much from 90° in the PAS of the chromophore, can be neglected. From the remaining solutions those were chosen which had the smallest deviation to the theoretical predictions.

$$
\begin{aligned}
\mu_x &= \mu \cdot \sin\phi \cdot \cos\theta \\
\mu_y &= \mu \cdot \sin\phi \cdot \sin\theta \\
\mu_z &= \mu \cdot \cos\phi
\end{aligned}
\tag{13.2}
$$

For all 2-phenylethylamine conformers, the reference frame is the Cs symmetric *Anti(up)* conformer. Here, the transition dipole moments of the ^1L_a and ^1L_b states are orthogonal to each other, the one of the ^1L_b oriented parallel to the short-axis (b) of the chromophore [276].

Transition dipole moments of PEA

The results for the orientations and magnitudes of the transition dipole moments from the DFT/MRCI calculations of the five PEA conformers are compiled in Table 13.2. The structures of all conformers are depicted in Figure 13.2 along with the theoretically predicted orientations of the TDM for both states concerned. The ^1L_a TDM is drawn in red and the ^1L_b TDM in blue. The angle θ in Table 13.2 is defined as follows: the side chain is located above the chromophore and rotated to the right. Turning the vector counterclockwise from the a-axis of the C_s symmetric $Anti(up)$ conformer is defined as positive direction.

From the comparison of the orientations and magnitudes of the TDMs several facts are eye-catching: the transition dipole moments of the two lowest electronically excited states are nearly perpendicular to each other in all experimentally ascertained states. In the case of the $Anti(up)$ conformer the relative orientation ($\zeta = \theta(L_b) - \theta(L_a)$) is determined by symmetry to be exactly 90°, but even without symmetry constraint, the minimum value of ζ for the other conformers is 74° for the $Gauche(out)$ conformer. The only conformer, which deviates strongly, is $Gauche(in)$, which has a remarkably small angle ζ of 25°.
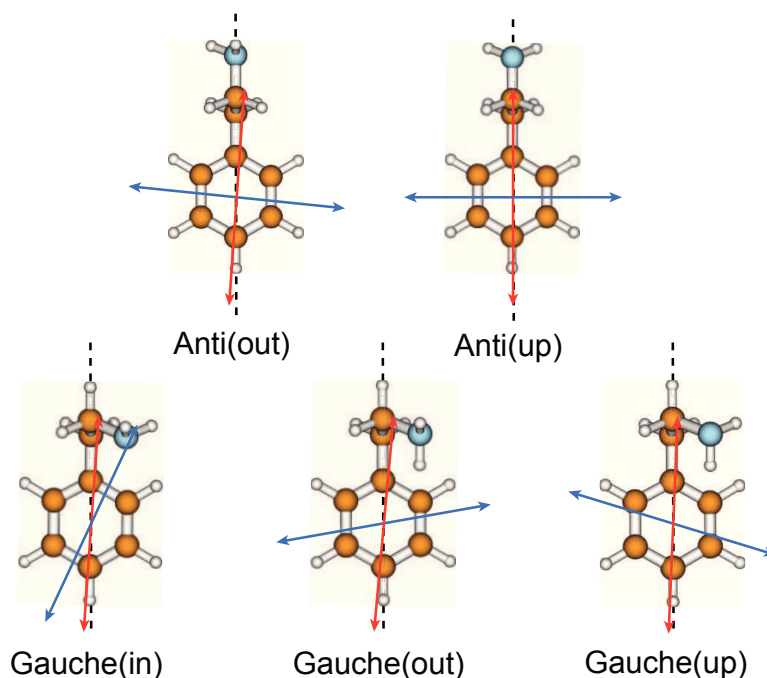
Figure 13.2: DFT/MRCI calculated transition dipole moments of 2-phenylethylamine. The ^1L_a TDM is shown in red, the ^1L_b TDM in blue. For comparison the a-axis of the $Anti(out)$ conformer is also displayed.

Interestingly, the orientation of the ^1L_a TDM is only very slightly affected by the conformation of the side chain. The largest deviation of 20° is observed for the *Gauche(up)* conformer. Comparison to the values published by the Simons group [271] shows that there is reasonable agreement in the theoretical predictions and experimental values. The experimental values for θ in Table 13.2 have been calculated from the experimentally determined projections of the transition dipole moments, given in Ref. [271] according to our definition of the angle θ. Two different values result, since only the projection to to inertial axis is determined from the experiment, and the sign of θ remains undetermined. Adding the angle for rotation of the inertial axis system of the respective conformer into the frame of the *Anti(up)* conformer results in the two different angles, given in Table 13.2.
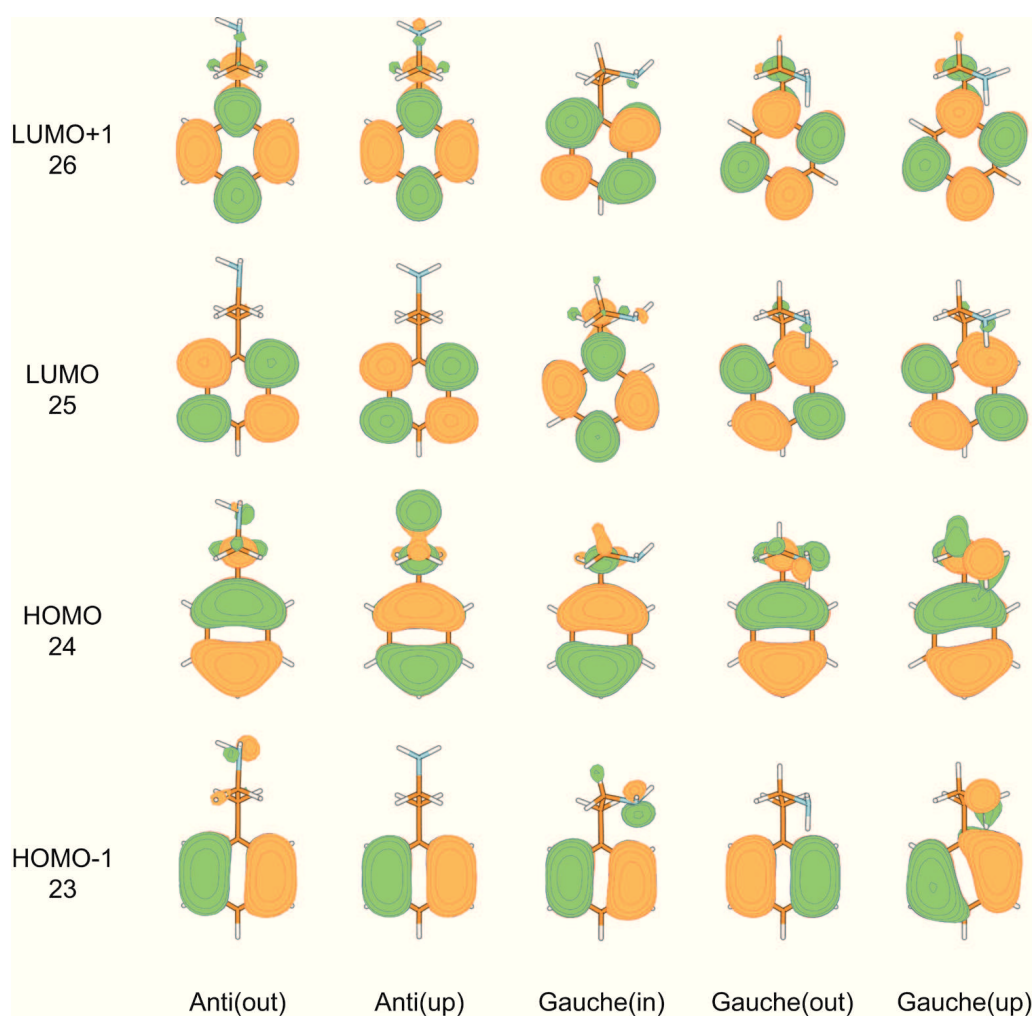
Figure 13.3: Frontier orbitals of the five 2-phenylethylamine conformers.

A closer look at the molecular orbitals and and their contributions to the transitions gives some insight to the factors resulting in dipole moment rotation due to conformational changes. In Figure 13.3 the main contributing frontier orbitals

(HOMO-1 to LUMO+1) are depicted and all excitations including their relative single-electron-contributions are compiled in Table 13.2.

Table 13.2: Leading contributions of single-electron excitations to the electronic transition and oscillator strengths for all conformers of PEA. The contributions of a single-electron excitation equals the square of the coefficient c. The HOMO is orbital 24, the LUMO 25. For a graphical overview over the frontier orbitals refer to Figure 13.3.

conformer	state	c	excitation	osc. strength	θ	θ^{exp}[271]	state
Anti(up)	S_1	0.67703 0.61209	$24 \to 25$ $23 \to 26$	$1.94 \cdot 10^{-3}$	$+90$	$+90$	^1L_b
	S_2	-0.79177 0.54405	$24 \to 26$ $23 \to 25$	$6.47 \cdot 10^{-2}$	± 0		^1L_a
Anti(out)	S_1	0.69962 -0.62435	$24 \to 25$ $23 \to 26$	$6.40 \cdot 10^{-4}$	$+84$	$+90$	^1L_b
	S_2	0.75342 0.61352	$24 \to 26$ $23 \to 25$	$2.07 \cdot 10^{-2}$	-4		^1L_a
Gauche(in)	S_1	-0.64748 0.59123	$24 \to 26$ $23 \to 25$	$1.15 \cdot 10^{-4}$	-25	$-$	^1L_b
	S_2	0.71811 0.55977	$24 \to 25$ $23 \to 26$	$2.76 \cdot 10^{-2}$	-4		^1L_a
Gauche(up)	S_1	0.56142 -0.46683	$24 \to 25$ $23 \to 26$	$9.15 \cdot 10^{-4}$	$+73$	$+84(-56)$	^1L_b
	S_2	0.62670 0.46354	$24 \to 26$ $23 \to 25$	$2.94 \cdot 10^{-2}$	-20		^1L_a
Gauche(out)	S_1	-0.6147 -0.55333	$24 \to 25$ $23 \to 26$	$5.56 \cdot 10^{-4}$	-80	$-88(+46)$	^1L_b
	S_2	0.66821 -0.54093	$24 \to 26$ $23 \to 25$	$2.73 \cdot 10^{-2}$	-5		^1L_a

We start the analysis with the $Anti(up)$-conformer since in this conformer side chain-chromophore-interactions are assumed to play the smallest role within the PEA conformers. The transition to the S_1 state consists of nearly equal contributions of LUMO $\leftarrow$ HOMO and (LUMO+1) $\leftarrow$ (HOMO-1). The TDM makes an angle of 90° with the inertial a-axis. The oscillator strength of the S_1 state is smaller by two orders of magnitude compared to the S_2 (another signature of the ^1L_b state, see Table 13.2). The S_2-state (^1L_a) is governed LUMO $\leftarrow$ (HOMO-1) and (LUMO+1) $\leftarrow$ HOMO. The same behavior can be observed for the $Anti(out)$ conformer with nearly identical coefficients. The $Gauche(up)$ and $Gauche(out)$ conformer show a considerable amount of state mixing of around 30% ($Gauche(up)$) and 20% ($Gauche(out)$)

in both states. The molecular orbitals of these two conformers show a rotation of the nodal structure especially for the unoccupied orbitals; the occupied orbitals are much less affected. An exception is $Gauche(up)$, whose HOMO-1 is rotated significantly towards the side chain due to interactions with the amino group.

The small angle between the TDMs of the $Gauche(in)$ conformer points to a strong change in the electronic excitation compared to the other conformers. Inspection of the frontier orbitals in Figure 13.3 shows, that the LUMO+1 orbital looks very similar to the LUMO of the *anti* conformers, exhibiting a nodal plane along the short axis of the molecule in contrast to all other LUMO+1-orbitals. Both unoccupied orbitals are shifted to higher energies compared to the other conformers. Thus, the large rotation of the ^1L_b TDM for $Gauche(in)$ is a result of the altered ordering of molecular orbitals which in turn is a consequence of the interactions between the lone pair and the aromatic ring, leading to an effective change in the excitation scheme. Moreover, we conclude that the changes of the orientation of the other *gauche* conformers are a result of the rotated electronic symmetry in the unoccupied orbitals, which are due to interactions of the electrons located at the ring and the lone pair of the amino group. The relative orientations of the TDM cannot be used as an argument for the probability of state mixing at least in PEA.

Transition dipole moments of TRA

The orientations of the electronic transition dipole moment of the nine TRA conformers, derived from DFT/MRCI calculations are compiled in Table 13.3 and Figure 13.4. The effect of the side chain positions on the orientations of the transition dipole moment vectors in TRA is much smaller than for PEA. The theoretically predicted values for θ of the ^1L_b state lie between $41°$ and $58°$. Thus, the maximum change of the TDM orientation in TRA is about $17°$ in contrast to $82°$ for PEA. The experimentally determined angles lie between $34°$ and $64°$, so they tend to vary more than predicted. The theoretically predicted values for θ of the ^1L_a state are nearly constant around $44°$. The excitation scheme for TRA is compiled in Table 13.3. It illustrates, that the major contribution to the S_1 excitation is LUMO $\leftarrow$ (HOMO-1) with around 55% for all conformers, while the S_2 is always dominated by a LUMO $\leftarrow$ HOMO-transition. Like in PEA, the ^1L_b state is lowest in energy for all conformers. Additional significant contributions to the excitation are seldom and always occur for the ^1L_b, but quite in contrast to PEA where these additional contributions effectively mix ^1L_a and ^1L_b, this is not the case for TRA: ^1L_a and ^1L_b
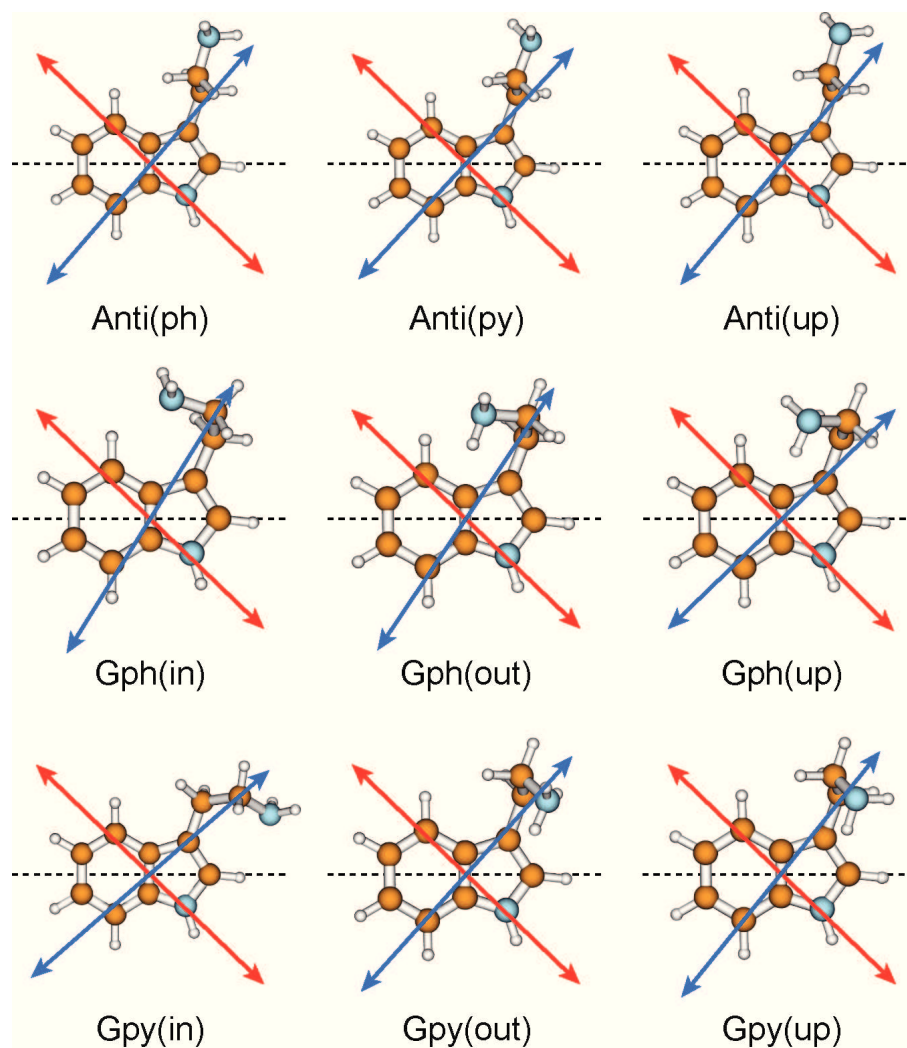
Figure 13.4: DFT/MRCI calculated transition dipole moments of tryptamine together with the a-axis of the chromophore indole. The ^1L_a TDM is shown in red, the ^1L_b TDM in blue.

never have a single-electron-excitation in common that piles up to 5%.

For PEA, the occupied orbitals were nearly unaffected by the conformation and this observation extends to the LUMO in the case of TRA and is more strict: neglecting minor changes of electron density located at the side chain, the HOMO-1, HOMO and LUMO are virtually the same for all conformers. This results in the constant orientation of the TDM for ^1L_a. The higher orbitals differ in ordering and Rydberg-contributions for the different conformers. A rotation of the nodal structure as observed for PEA is not taking place. Comparison of the orbitals involved in the excitation to the ^1L_b and their depicted molecular orbitals reveals, that the symmetry of the π-orbitals located in the chromophore determines which orbitals are involved. The LUMO+1-orbitals of all conformers except $Gph(in)$ and $Gpy(in)$ exhibit identical electron distribution of π-symmetry in the chromophore and differ only by the Rydberg-contributions of the heteroatoms. The orbitals of the two exceptions are shifted higher in energy and become the LUMO+3 and LUMO+2, respectively. So the excitation scheme remains unchanged, as far as only the symmetry of the molecular orbitals in the chromophore is regarded. In a recent publication of our group on 5-methoxyindole we reported exactly the same behavior: unoccupied π orbitals change energetic positions with Rydberg-orbitals, but the (symmetry-adapted) single-electron-excitation scheme stays the same as in indole [196].

For $Gpy(up)$ and $Gph(out)$ both values for θ tend to be significantly larger than the mean value: Interestingly, these two conformers are the only ones exhibiting a large Rydberg-contribution at the nitrogen atom located in the five-membered ring in an orbital that is involved in the excitation.

Permanent dipole moments of PEA and TRA

The calculated permanent dipole moments of the three lowest singlet states of PEA and TRA are given in Table 13.4 along with experimental data from Lopez *et al.* [275] for PEA and of Nguyen *et al.* [258] for TRA.

Good agreement of our data to the experimental values is observed, which ensures us, that DFT/MRCI is well capable of describing both permanent and transition dipole moments.

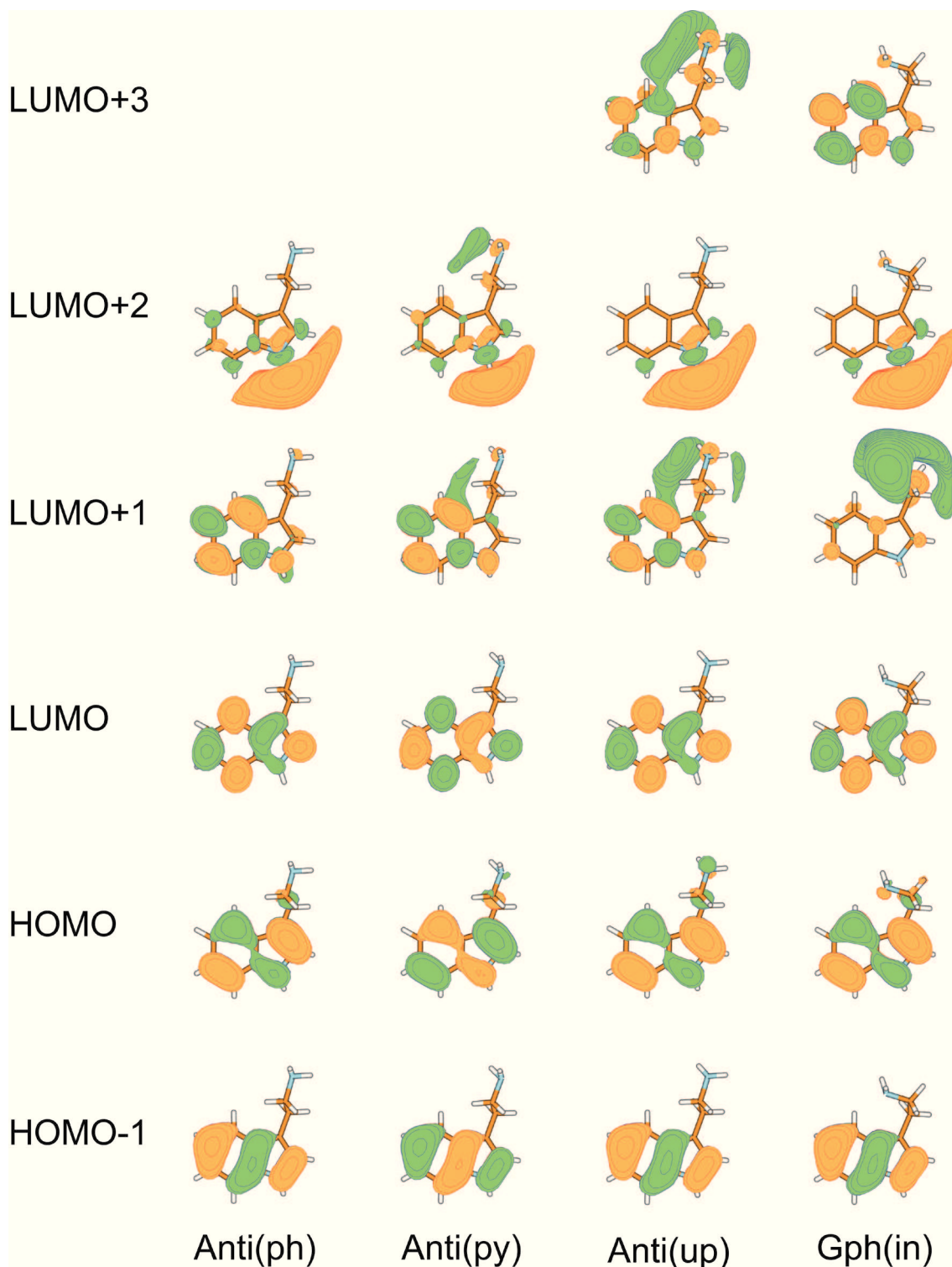The theoretical predictions show, that for TRA excitation to the S_1 has no strong

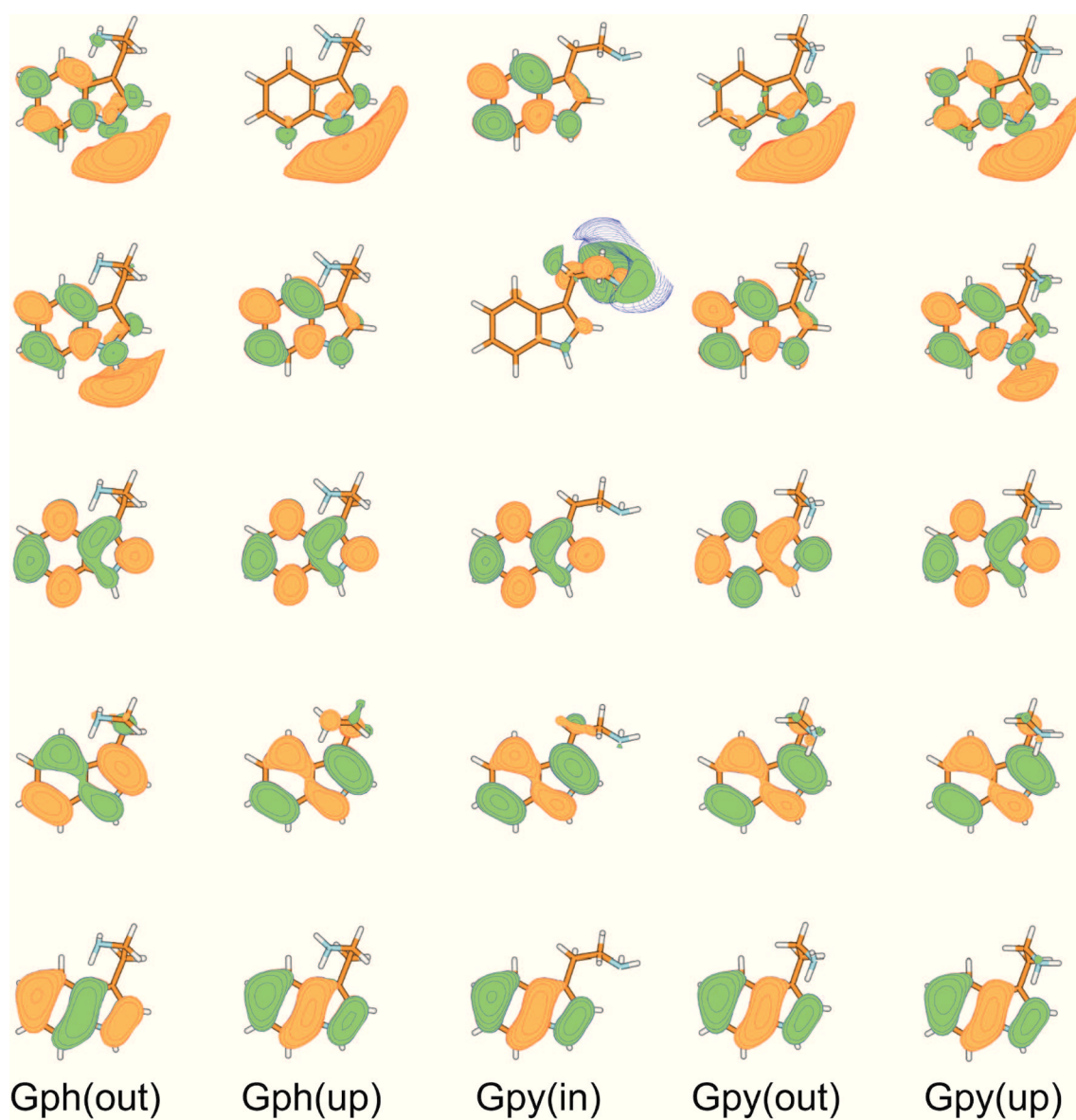Figure 13.5: Frontier orbitals of tryptamine involved in an excitation contributing at least 15%

Figure 13.6: Frontier orbitals of tryptamine involved in an excitation contributing at least 15% - continued

Table 13.3: Leading contributions of single-electron excitations to the electronic transition for all conformers of tryptamine based on DFT/MRCI. The contributions of a single-electron excitation equals the square of the coefficient c. The HOMO is orbital 31, the LUMO 32. For a graphical overview over the frontier orbitals refer to Figure 13.5 and 13.6.

conformer	state	c	exc.	osc. strength	θ	θ^{exp}[255]	state
$Anti(ph)$	S_1	0.74289 0.49637	$30 \to 32$ $31 \to 33$	$1.58 \cdot 10^{-2}$	$+49$	$+37(+61)$	^1L_b
	S_2	-0.90959	$31 \to 32$	$1.02 \cdot 10^{-1}$	-45		^1L_a
$Anti(py)$	S_1	-0.74189 0.50464	$30 \to 32$ $31 \to 33$	$1.73 \cdot 10^{-2}$	$+47$	$+37(+61)$	^1L_b
	S_2	0.91128	$31 \to 32$	$1.05 \cdot 10^{-1}$	-45		^1L_a
$Anti(up)$	S_1	-0.73484 0.44447	$30 \to 32$ $31 \to 33$	$1.33 \cdot 10^{-2}$	$+50$	$+65(+33)$	^1L_a
	S_2	-0.90766	$31 \to 32$	$9.76 \cdot 10^{-2}$	-46		^1L_a
$Gph(out)$	S_1	-0.73856 0.41696	$30 \to 32$ $31 \to 33$	$1.60 \cdot 10^{-2}$	$+56$	$+64(+30)$	^1L_b
	S_2	0.90530	$31 \to 32$	$1.05 \cdot 10^{-1}$	-44		^1L_a
$Gph(up)$	S_1	0.74101 -0.54864	$30 \to 32$ $31 \to 33$	$1.81 \cdot 10^{-2}$	$+44$	$+34(+54)$	^1L_b
	S_2	-0.91353	$31 \to 32$	$1.11 \cdot 10^{-1}$	-45		^1L_a
$Gph(in)$	S_1	0.73834 -0.51843	$30 \to 32$ $31 \to 35$	$1.87 \cdot 10^{-2}$	$+58$	$-$	^1L_b
	S_2	0.89979	$31 \to 32$	$1.09 \cdot 10^{-1}$	-44		^1L_a
$Gpy(out)$	S_1	0.74667 0.53814	$30 \to 32$ $31 \to 33$	$2.00 \cdot 10^{-2}$	$+48$	$+49(+25)$	^1L_b
	S_2	0.91213	$31 \to 32$	$1.03 \cdot 10^{-1}$	-44		^1L_a
$Gpy(up)$	S_1	0.74456 -0.43838	$30 \to 32$ $31 \to 33$	$1.97 \cdot 10^{-2}$	$+51$	$+59(+37)$	^1L_b
	S_2	0.90587	$31 \to 32$	$1.00 \cdot 10^{-1}$	-45		^1L_a
$Gpy(in)$	S_1	-0.73992 0.54851	$30 \to 32$ $31 \to 34$	$1.67 \cdot 10^{-2}$	$+41$	$-$	^1L_b
	S_2	-0.91089	$31 \to 32$	$1.07 \cdot 10^{-1}$	-41		^1L_a

Table 13.4: Permanent dipole moments of the two lowest excited singlet states of PEA and TRA and its polar angle with the a inertial axis of the chromophore. Additionally changes of the angles and magnitudes induced by electronic excitation are given.

	S_0			S_1			S_2			$S_1 - S_0$			$S_2 - S_0$			Exp.[a]	
	θ	ϕ	$|\mu|$	θ	ϕ	$|\mu|$	θ	ϕ	$|\mu|$	$\Delta\theta$	$\Delta\phi$	$\Delta|\mu|$	$\Delta\theta$	$\Delta\phi$	$\Delta|\mu|$	$|\mu|_{S_0}$	$|\mu|_{S_1}$
PEA																	
Anti(up)	0	0	1.20	0	0	1.17	0	+38	1.18	0	0	−0.03	0	38	−0.02	1.36	−
Anti(out)	+90	+51	1.28	+90	+50	1.30	+70	+50	1.37	0	−1	+0.02	−20	−1	+0.09	1.26	−
Gauche(in)	+2	+72	1.83	+2	+70	1.77	−2	+72	2.17	0	−2	−0.06	4	0	+0.34	−	−
Gauche(up)	−130	+18	1.24	−129	+18	1.22	−76	+16	1.00	−1	0	−0.02	54	−2	−0.24	1.36	−
Gauche(out)	−84	+54	1.19	−83	+54	1.20	+80	+50	1.20	−1	0	+0.01		−4	+0.01	1.26	−
TRA																	
Anti(ph)	−40	+71	2.97	−28	+72	3.05	−15	+81	6.34	+12	1	+0.08	+25	10	+3.37	−	−
Anti(py)	−76	+72	1.41	−48	+69	1.24	−14	+84	4.44	+28	−3	−0.17	+57	102	+3.03	−	−
Anti(up)	−48	+63	2.74	−32	+64	2.76	−15	+79	5.88	+16	1	+0.02	+33	16	+3.14	2.6	2.5
Gph(in)	+2	+78	2.32	+12	+79	2.66	+3	+84	5.87	+10	1	+0.34	+1	6	+3.55	−	−
Gph(out)	−42	+75	2.95	−30	+75	2.96	−16	+82	6.12	+12	0	+0.01	+26	7	+3.17	−	−
Gph(up)	−59	+59	2.62	−43	+58	2.53	−17	+78	5.40	+16	−1	−0.09	+42	19	+2.78	2.4	2.2
Gpy(in)	+3	+89	2.34	+11	+89	2.84	+4	+89	6.68	+8	0	+0.50	+1	0	+4.34	−	−
Gpy(out)	−78	+77	1.52	−55	+72	1.26	−16	+84	4.43	+23	−5	−0.26	+62	7	+2.91	1.6	1.4
Gpy(up)	−52	+64	2.87	−39	+63	2.80	−19	+79	5.86	+13	−1	−0.07	+33	15	+2.99	2.7	2.5

[a]The experimental dipole moments for PEA haven been taken from Ref. [275], those of TRA from Ref. [258]

influence on the magnitude of the permanent electric dipole moment, quite in contrast to excitation to the S_2 state. Here, the permanent electric dipole moment is larger by a factor of 2-3, as to be expected for the ^1L_a state in indole derivatives. Nguyen *et al.* observed in their study on TRA that, although the magnitude of the permanent electric dipole moment is not changed much by the excitation to the S_1, the orientation is [258]. As the changes happen to be mainly along the *a*-axis of the conformers, they concluded a shift of electron density from the side chain into the chromophore during the excitation. By using the analysis outlined for the TDM we are now also able to discuss the permanent electric dipole moment with respect to the PAS of the chromophore. The angles of the electric dipole moment with the inertial axes of indole and their changes are given in Table 13.4. Obviously all changes follow a common pattern: the out-of-plane angle ϕ stays nearly the same and θ is always rotated by a positive angle.

Very helpful at this point is a work by Kang *et al.* who presented the electric dipole moments of indole in its ground and electronically excited state [141]. They show that excitation to the S_1 diminishes μ slightly from 1.963 D to 1.856 D and rotates θ by 12.5° in the same direction as we found in TRA. So we believe that the rotation of the excited state dipole moment in all tryptamine conformers is the result of a rotation of the dipole moment in the chromophore and that only little electron migration occurs from the side chain into the ring system as suggested by Nguyen *et al.* [258]. This can be seen best for the *up* conformers where the two dipole moments are perpendicular to each other and the values for $\Delta\theta$ come very close to the experimentally determined one for indole.

13.4   Discussion

Using the above results, we try now to separate the side chain - chromophore interaction into through-space and through bond effects. According to the large differences in the excitation schemes of the various conformers, the through space effect seems to dominate the interaction. Nevertheless, if we compare the excitation scheme of the staggered and eclipsed forms of toluene (Figure 13.7), we find similar effects as observed in the different PEA and TRA conformers. A strong rotation of the orbitals takes place upon symmetry break, resulting in a rotation of the TDM orientation of 60° for the ^1L_b state (0.7[LUMO $\leftarrow$ HOMO]-0.6[(LUMO+1) $\leftarrow$(HOMO-1)]) and of 22° for the ^1L_a state (0.6[LUMO $\leftarrow$ (HOMO-1)]-0.6[(LUMO+1) $\leftarrow$ HOMO]), indicating the importance of symmetry break for the changes of the TDM orientation.

Such a pronounced non-Condon behavior is quite unexpected and can be traced back to the different hyperconjugative interactions in the staggered and eclipsed forms of toluene. Nevertheless, the TDM orientations over 2π along the periodic methyl torsional potential for the ^1L_b state average to $90°$. For PEA such vibrational averaging does not take place, since the potential energy is not symmetrically periodic.
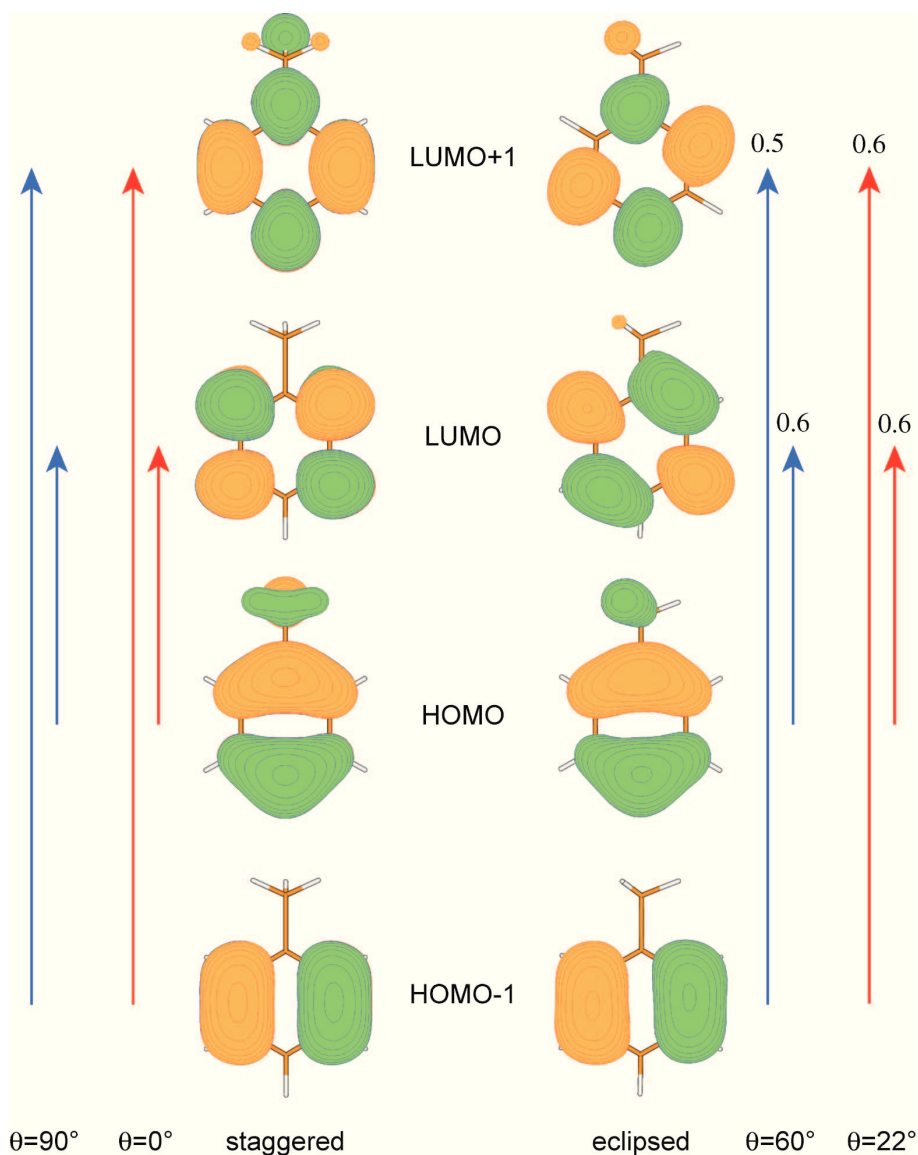
Figure 13.7: Frontier orbitals and excitation scheme of the staggered and eclipsed forms of toluene. The red arrows refer to excitation to the ^1L_a state, the blue arrows for the ^1L_b state. The numbers on top of the arrows give the coefficient of the respective excitation.

If the main interaction between the ethylamino side chain and the chromophore is through-bond mediated, the question arises, why the influence of the side chain orientation on the benzene chromophore is much larger than on the indole chromophore. An explanation of this might be given by the observation, that the ionization po-

tentials of ethylbenzene (8.77 eV [277]) and ethylamine (8.8 eV [278]) are practically identical but very different from that of 3-ethylindole (7.5 eV [279]). This suggests, that ionization (and excitation) in TRA is localized in the chromophore, while it is delocalized between the benzene chromophore and the amino group in PEA. This delocalization causes the large sensitivity of the relative amino orientation with respect to the chromophore in the latter.

13.5   Conclusions

The experimental finding of a large sensitivity of the transition dipole moment for the excitation to the lowest excited singlet state to the conformer structure in phenylethylamine and a much lower sensitivity in ethylaminoindole has been reproduced using DFT/MRCI calculations. The orientation of the TDM of the ^1L_b state in TRA is governed by the chromophore and does hardly change upon geometry changes of the side chain, while its orientation in PEA is governed by the side chain orientation. We trace the large differences in the sensitivity of the TDM orientation on the side chain position back to a delocalized excitation in PEA, while the electronic excitation in TRA is localized in the indole chromophore and experiences only small through space effects from the amino group. The ^1L_a state TDM orientation stays remarkebly constant both in PEA as in TRA. Thus, we have nearly constant angle between the directions of ^1L_a and the ^1L_b transition dipole moment of 90°, while there are large variations in this angle for PEA. For TRA it is immediately obvious, why the ^1L_a state TDM orientation does not depend on the amino group orientation: the main one-electron contribution to the excitation is LUMO $\leftarrow$ HOMO, both of which are independent of the relative amino position. In PEA however, the ^1L_a state state is comprised to nearly equal amounts of (LUMO+1) $\leftarrow$ HOMO and LUMO $\leftarrow$ (HOMO-1). Inspection of the LUMO and LUMO+1 (cf. Figure 13.3) shows, that the rotation of the LUMO is balanced by an oppsite rotation of the LUMO+1.

For the gauche conformers of PEA, ^1L_a and ^1L_b state share up to 30 % of the single electron excitations what reflects a strong mixing of the two states, while in TRA single electron excitations can be assigned to one of the excited states exclusively. Coupling of the two lowest excited states of TRA however, can be induced via Herzberg-Teller coupling through vibrational modes, which resemble the difference vectors of the structures of the two excited states [157]. The smaller ^1L_a / ^1L_b gap in the case of PEA allows the polar amino group in the gauche conformers to stabilize

the polar ^1L_a state so much, that it comes into near degeneracy with the ^1L_b state, thus causing state mixing between them.

13.6   Acknowledgment

13.7   Publication

The contents of this chapter has been published previously in slightly different form as *How and why do transition dipole moment orientations depend on conformer structure?* in the *Journal of Physical Chemistry A* (impact factor: 2.946), 2011, **115**, 9612–9619 by Christian Brand, W. Leo Meerts, and Michael Schmitt.

The quantum mechanical calculations were performed, interpreted and analyzed in close collaboration by M. Schmitt and me. Furthermore, I was involved in all discussions and wrote the major part of this paper.

14. Melatonin

Abstract

Rotationally resolved electronic spectra of the A and B bands of melatonin have been analyzed using an evolutionary strategy approach. From a comparison of the *ab initio* calculated structures of energy selected conformers to the experimental rotational constants, the A band could be shown to be due to a gauche structure of the side chain, while the B band is an anti structure. Both bands show a complicated pattern due to a splitting from the three-fold internal rotation of the methyl rotor in the N-acetyl group of the molecules. From a torsional analysis we additionally were able to determine the barriers of the methyl torsion in both electronic states of melatonin B and give an estimate for the change of the barrier upon electronic excitation in melatonin A. The electronic nature of the lowest excited singlet state could be determined to be ^1L_b (as in the chromophore indole) from comparison to the results of ab initio calculations.

14.1   Introduction

Melatonin (N-acetyl-5-methoxytryptamine) is an animal and plant hormone [280], which regulates physiological processes like the circadian rhythms [281], influences the immune system [282], and acts as free radical scavenger and potent antioxidant [283]. Its physiological action strongly depends on the interaction with specific receptors. Quantitative structure-activity relationship (QSAR) studies have proven, that the crucial motifs for pharmacological activity are the methoxy and the N-acetyl groups, while indole merely serves as scaffold, which determines the distance and relative orientation of these groups. Even the chemically very different naphtha-

lene [284] or tetrahydronaphthalene molecules [285] are good bioisosteric substitutes for indole in melatonin analogues. The exact knowledge of the conformer space of these biologically active serotonin derivatives is crucial for performing and understanding experiments on structure-affinity relationships.

Dian *et al.* [286] studied the infrared-induced conformational isomerization and vibrational relaxation dynamics in melatonin using IR-UV hole-filling spectroscopy and IR-induced population transfer spectroscopy. Using a combination of two-color resonant two-photon ionization (R2PI), laser-induced fluorescence (LIF), resonant ion-dip infrared spectroscopy (RIDIRS), fluorescence-dip infrared spectroscopy (FDIRS), and UV-UV hole-burning spectroscopy, Florio *et al.* [210] investigated the conformational preferences of melatonin in a molecular beam. They identified three major *trans*-amide conformers and two minor *cis*-amide structures. Florio and Zwier [264] studied the influence of water solvation on the conformational space of melatonin. Contrary to the case of tryptamine [256], the conformational richness is not significantly influenced by water complexation. The gas phase He(I) photoelectron spectra of melatonin have been reported by Kubota and Kobayashi [287]. They found, that the interaction of the π orbital of the 5-methoxyindole part of the molecule and the π and the $n_{C=O}$ orbitals of the N-ethylacetamide moiety depend strongly on the conformations.

In the present work, we investigate two major conformers of melatonin by a combination of rotationally resolved electronic spectroscopy and *ab initio* calculations. In molecules of this size, the rotational constants are relatively small, so that the classical line position assignment of the spectra seems to be reaching its limits here. Up to 100 single rovibronic transitions with intensities of more than 10 % of the strongest line can contribute to one feature which is observed as "line" in the experimental rovibronic spectrum. As a result, semi-automated procedures that rely on evolutionary strategies have been used to fit these spectra, thereby testing the applicability of this approach to even larger systems.

14.2 Experimental details

The experiments were performed at the University of Pittsburgh, using an experimental setup that have been described elsewhere [288]. In brief, melatonin was heated to 175-225°C, seeded in 300–500 mbar of argon, and expanded into vacuum. The beam was confined by skimmers, resulting in Doppler-broadening of individual

rotational lines to 20 MHz full-width-at-half-maximum (FWHM) in a differentially pumped vacuum system. The molecular beam was crossed at right angles by UV radiation near 280 nm using an Ar^+ -pumped frequency doubled ring dye laser (FWHM <1 MHz, Spectra Physics 380D). The integrated laser-induced fluorescence was collected using a lens system and detected by a photomultiplier tube. The relative frequency was determined to $\pm$ 0.0005 MHz by comparison to a quasi-confocal Fabry-Perot interferometer and the absolute frequency was determined by simultaneously recording the iodine absorption spectrum and successive comparison to the tabulated transition frequencies [67].

14.3   Computational details

14.3.1   *Ab initio* calculations

Structure optimizations were performed employing the valence triple-zeta basis set with polarization functions (d,p) from the TURBOMOLE library [162, 212]. The equilibrium geometries of the electronic ground and the lowest excited singlet states were optimized using the approximate coupled cluster singles and doubles model (CC2) employing the resolution-of-the-identity approximation (RI) [112, 163, 164].

Singlet state energies and wave functions were calculated using the combined density functional theory/multi-reference configuration interaction (DFT/MRCI) method developed by Grimme and Waletzke [110]. Configuration state functions (CSFs) in the MRCI expansion were constructed from Kohn-Sham (KS) orbitals, optimized for the dominant closed shell determinant of the electronic ground state employing the BH-LYP [2, 122] functional. All 56 valence electrons were correlated in the MRCI runs and the eigenvalues and eigenvectors of five singlet states were determined. The *initial* set of reference configuration state functions was generated automatically in a complete active space type procedure (including all single and double excitations from the five highest occupied molecular orbitals in the KS determinant to the five lowest virtual orbitals) and was then iteratively improved. The MRCI expansion was kept moderate by extensive configuration selection. The selection of the most important CSFs is based on an energy gap criterion as described in Ref. [110]. Only those configurations were taken into account that have an energy below a certain cutoff energy. The energy of a given configuration was estimated from orbital energies within the selection procedure. The cutoff energy was given by the energy of the highest desired root as calculated for the reference space plus a cutoff pa-

rameter $\delta E_{sel} = 1.0 E_{\mathrm{H}}$. The latter choice has been shown to yield nearly converged results [110].

14.3.2   Evolution strategies used for spectra fitting

The rovibronic spectra were fit to a rigid asymmetric rotor Hamiltonian [289] by using a derandomized (DR) evolution strategy (ES) that was developed by Ostenmeier *et al.* [201]. A special implementation, which we employed in the present study, represents the second generation of derandomized ES and is abbreviated as DR2 [204]. It was shown [290] to be a very good alternative to the genetic algorithm based fits we have employed in the past [203]. Evolution strategies like DR2 are optimizers that are inspired by reproduction and natural selection in nature. While classical genetic algorithms aim to find a solution in the parameter space by randomly combining information from a set of trial solutions, the DR2 algorithm can sense in which direction the quality of a fit increases. In the first step, the DR2 algorithm generates trial solutions (offspring) by using a random distribution around some starting point (parent), each consisting of the complete parameter set which is necessary to simulate the spectrum. Offspring with higher fitness than the parent, are kept and used to compute the next generation. The DR2 algorithm makes use of the parameter correlation matrix for successive changes in the parents (mutations). This means that if for some parameter a parent has evolved in the same direction for several generations, resulting in a positive correlation, the most likely solution is assumed to be further in that direction and the next parameter mutation will be larger. Correspondingly, two anticorrelated mutations will lead to a smaller mutation. Compared to classical genetic algorithms, this procedure has been shown to lead to faster convergence of the parameters [290].

14.4   Theoretical Results

14.4.1   Conformer structures and energies

The nomenclature for the melatonin conformers follows the suggestion of Florio *et al.* [210]. In their study, they optimized different melatonin conformers, which have been preselected via OPLS-AA force field calculations, using density functional theory with the Becke-3LYP functional and the 6-31+G*(5d) basis set. The electronic energies of the lowest energy conformers were determined *via* single-point localized

MP2/aug-cc-pVTZ(-f) calculations and corrected for zero-point vibrational contributions using the Becke-3LYP/6-31+G*(5d) vibrational frequencies.

We decided to follow another route for determination of the geometries at the minima of the potential energy surface and the respective energies. Structure optimizations were performed with the approximate coupled cluster singles and doubles model (CC2) within the resolution-of-the-identity approximation (RI) using the cc-pVTZ basis set. This combination of method and basis set has been shown to yield very good results for the structures in the electronic ground and excited singlet states, measured by the differences between the observed rotational constants and the calculated ones. At these geometries, the ground state and excitation energies have been calculated using the DFT/MRCI method from Grimme and Waletzke [110].

Due to the expensive method and the large conformational space, we restricted our search considerably to a subspace that was chosen from experiences on similar systems. Only these starting structures were then subjected to geometry optimization at the CC2/cc-pVTZ level of theory. Melatonin has the following degrees of freedom for internal motions that have to be considered in the generation of the conformers; a threefold rotation about the C_8-C_9 bond, resulting in two different *gauche* and one *anti* conformations, a two-fold rotation about the amide bond (N_{10}-C_{11})), which generates *cis*- or *trans*-amide structures, and a two-fold rotation of the 5-methoxy group, which can lead to *syn* and *anti* conformers, cf. Figure 14.1. From the analysis of the rotationally resolved spectra of 5-methoxyindole [196] and 5-methoxytryptamine [265], we have learned, that all experimentally observed conformers belonged to the *anti* class of conformers for the methoxy group with respect to the indole NH. Therefore, we excluded from the beginning all *syn*-methoxy conformers. Since the *cis*-amide conformers are considerably higher in energy than the respective *trans*-amide structures, they also were not considered as starting structures. Thus, three classes of conformers served as basis of the conformational search, the first is based on the Anti(trans)anti family, the second on the Gpy(trans)anti, and the third on the Gph(trans)anti structures. The remaining degree of freedom is the three-fold rotation about the C_9-N_{10} bond, which leads to conformers that are labeled by the orientation of the amide NH bond with respect to the chromophore as *in*, *out*, and *up*.

For the Anti(trans)anti family the *in*, *out*, and *up* conformers have been used as starting structures, resulting in Anti(trans-out)/anti and Anti(trans-in)/anti minima on the potential energy surface. The *up* structure converged in the course of
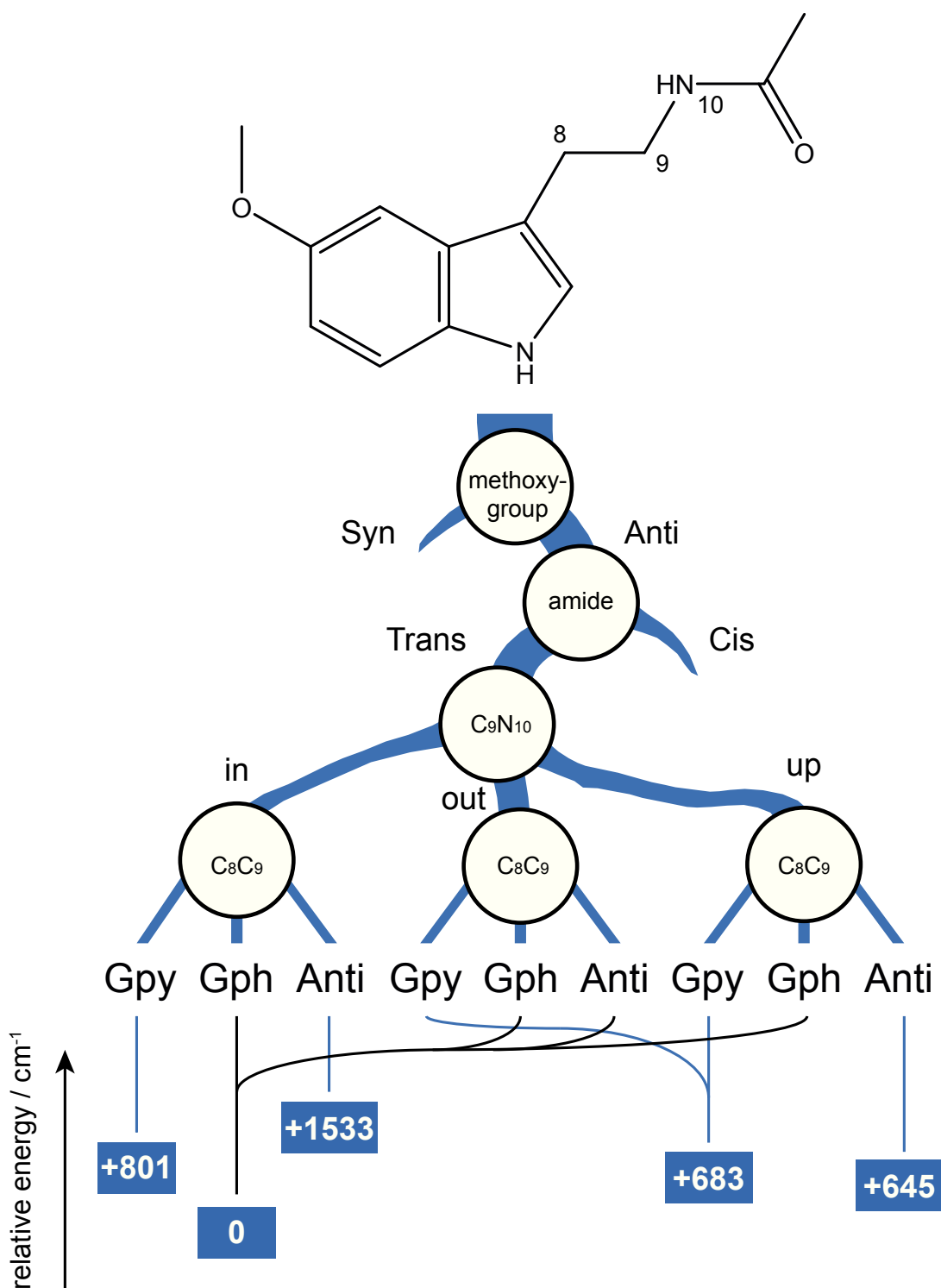
Figure 14.1: Schematic overview of the tree of melatonin conformers. The *syn*-5-methoxy and the *cis*-amide branches have been discarded in this study. In the lower half, it is shown to which minimum the starting structures finally converge. At the bottom, the relative CC2 ground state energies (in cm^{-1}) of the CC2/cc-pVTZ optimized structures are given. For details see text.

the optimization to the Anti(trans-in)/anti minimum. Also, for the two Gauche families, the *up* conformer converged to one of the *in* and *out* conformers. For the Gph conformers, additionally, the *out* conformer relaxed to the *in* structure. Thus, five low energy conformers of melatonin are found in our analysis, keeping in mind, that we did not explore the whole conformational space.

Table 14.1 shows the energies, relative stabilities and rotational constants of the five lowest energy conformers of melatonin, found in our study, calculated for the CC2/cc-pVTZ optimized structures. The most stable conformer was found to be Gph(trans-in)anti, followed by Anti(trans-out)/anti, 645 cm^{-1} above. The energetically following conformer is the analogue of the most stable, but with the side chain pointing in the pyrrole direction Gpy(trans-in)anti, 683 cm-1 above the minimum. In order to check how much the energetics are influenced by basis set superposition error (BSSE) effects of the side chain - chromophore interaction, we optimized the structures of the three most stable conformers with the smaller TZVP basis. The relative energy of the Anti(trans-out)/anti conformer increases, while Gpy(trans-in)anti and Gph(trans-in)anti stay constant relative to each other. Obviously, BSSE effects stabilize both gauche structures equally and will not cause large variations in their relative energies.

The adiabatic excitation energy (CC2/cc-pVTZ) of the Anti(trans-out)/anti conformer is calculated to be 34091 cm^{-1} for Gph(trans-in)anti 33931 cm^{-1}, and for Gpy(trans-in)anti 34317 cm^{-1}. The differences of the excitation energies are considerably larger than the wavenumber difference of the origin bands of conformers A - E in Ref. [210]. In order to quantify the excitation properties, we calculated excitation energies and transition dipole moments using DFT/MRCI at the CC2 optimized structures. This is described in the following section.

14.4.2 Excited singlet states

Using DFT/MRCI at the CC2 optimized geometries, we calculated excitation properties of the four lowest energy conformers, described in the preceding section. Table 14.2 gives the lowest adiabatic singlet excitation energies of the four lowest energy conformers along with the orientations of the transition dipole moments (TDM) in the principal inertial axis system of the conformers (θ and ϕ), and also with respect to the *pseudo*-symmetry axis of the indole chromophore (θ^{ref}, cf. Figure 14.2a), which is independent of the different inertial axis orientations in the different con-

Table 14.1: Relative CC2 ground state energies (in cm^{-1}) of the CC2/cc-pVTZ and CC2/TZVP optimized structures of various melatonin conformers. The energies are measured with respect to the most stable conformer at each level of theory. Rotational constants (in MHz) in both electronic states are for the CC2/cc-pVTZ optimized structures. Adiabatic CC2 excitation energies ν_0 at CC2/cc-pVTZ optimized structures in cm^{-1} without ZPE correction.

Conformer	relative CC2 Energy		S_0			S_1			ν_0
	cc-pVTZ	TZVP	A	B	C	ΔA	ΔB	ΔC	
Gph(trans-in)/anti	0	0	550	497	309	+10	+10	+15	33931
Anti(trans-out)/anti	645	934	630	339	226	+1	+2	+1	34091
Gpy(trans-out)/ anti	683	593	544	505	305	+42	-4	+21	33680
Gpy(trans-in)/anti	801	648	785	310	266	+3	-10	-10	34317
Anti(trans-in)/anti	1533	1925	775	230	181	-4	0	+1	34440

formers. The lowest singlet excitation of all four conformers has its TDM oriented as in the ^1L_b state of indole, with slightly larger angles θ^{ref} than in indole ($+38.3$ °). The positive direction of the angle θ^{ref} is defined in Figure 14.2a.

Table 14.2: Adiabatic DFT/MRCI excitation energies ν_0 of the lowest excited singlet state at CC2/cc-pVTZ optimized structures in cm^{-1} without ZPE correction. θ and ϕ are the polar angles of the TDM in the inertial axis system of the respective conformer, and θ^{ref} is the angle of the TDM with the a-axis (the *pseudo*-symmetry axis) in the indole chromophore, cf. Figure 14.2.

Conformer	ν_0	θ	ϕ	θ^{ref}	f
Gph(trans-in)/anti	34108	16	67	53	0.07
Anti(trans-out)/anti	33797	-22	82	51	0.08
Gpy(trans-out)/anti	33410	-40	65	52	0.07
Gpy(trans-in)/anti	33824	-142	66	46	0.07
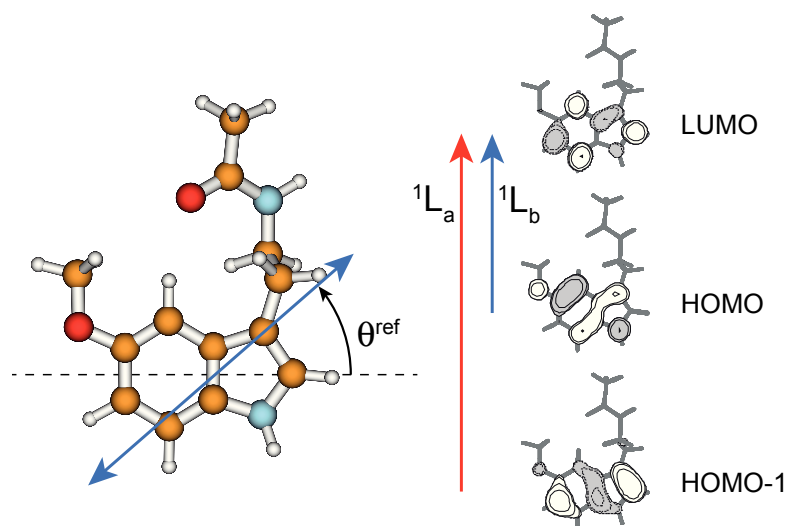
Figure 14.2: Definition of θ^{ref}, the angle between the TDM and the *pseudo*-symmetry axis of the indole chromophore along with the frontier orbitals of the Anti(trans-out)/anti conformer.

The excitation scheme of the lowest singlet excitation is that of a nearly pure LUMO $\leftarrow$ HOMO transition (cf. Figure 14.2b). The excitation to the second singlet state, which is the ^1L_a-state, is mainly of LUMO $\leftarrow$ (HOMO-1) character. These excitation schemes for the ^1L_a and ^1L_b states are different than those of indole. As it was shown in Chapter 10 on 5-methoxyindole, the methoxy substituent introduces an additional node in the molecular orbital, which was formerly the HOMO-1 in indole, and which becomes the HOMO in 5-methoxyindole. This causes a change in energy ordering between indole, 5-methoxyindole and melatonin for the HOMO

and HOMO-1, respectively, and is responsible for the altered excitation scheme of melatonin compared to indole.

The second excited singlet state is the ^1L_a state, about 4000 cm^{-1} above the ^1L_b state for each conformer, with an oscillator strength of about 0.14 (approximately twice that of the ^1L_b state). The permanent dipole moment of this state is calculated to be more than twice that of the ^1L_b state (7.4 vs. 3.5 Debye).

14.5   Experimental results

The rotationally resolved LIF spectrum of melatonin B (referring to the nomenclature of Florio *et al.* [210]) shows a split band with $\Delta\nu$ of 2270 MHz, cf. Figure 14.3. The fit of the spectrum shows that both subbands have very similar rotational constants, both in the ground and in the electronically excited states. The lower frequency component can be fit with a normal rigid rotor Hamiltonian, while the blue component shows slight deviations. We based the analysis of the structure of this conformer on the rotational constants of the red component.

The need for using the automated evolution fitting procedure described above is illustrated in Figure 14.4. Two different regions of the simulated spectrum have been enlarged in the figure in order to highlight the enormous number of rovibronic transitions that contribute to the observable features, which appear as single lines in the spectrum. In the outer wings of the P-branch, up to 100 lines contribute to each feature; in the region of the Q-branch it is a few hundred. A quantum-number based assignment procedure as has been used in the analysis of smaller molecules for decades is thus impossible here.

Comparison to the results of *ab initio* calculations (CC2/cc-pVTZ) prove, that only the rotational constants of the Anti(trans-out)/anti conformer are in agreement with the experimental ones (cf. Figure 14.5). The splitting has to be assigned to a large amplitude motion. Here, we have two possible ones; the three-fold methyl rotation of the 5-methoxy group (high barrier) and the three-fold methyl rotation of the acetyl group (low barrier). N-phenylacetamide for example, has a ground state barrier for the methyl rotation in the acetyl group of less than 30 cm^{-1}, and of 50 cm^{-1} in the electronically excited state with an experimentally observed AE splitting of about 4 cm^{-1} [291]. In melatonin, the acetamide group is separated from the chromophore by two methylene groups. Therefore, we expect the torsional

Figure 14.3: Experimental and simulated spectrum of melatonin B. The lower four traces show expanded views of the experiment, the simulation and the deconvolution into the two torsional subbands. For details see text.
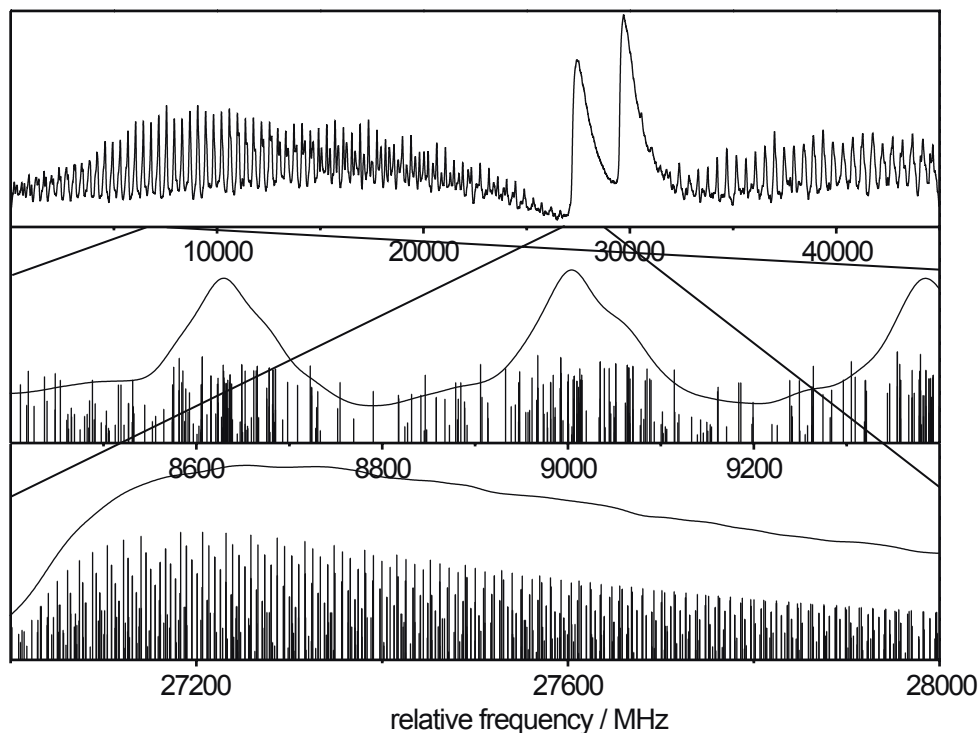
Figure 14.4: Simulated stick spectrum of melatonin B along with the convolution, using the experimental line width. The lower two traces show enlarged regions of the spectra in the P- and in the Q-branch, illustrating the complexity of the spectrum at this resolution.

barrier of the methyl group to be similar in both electronic states, resulting in a much smaller AE splitting. The chemically more similar N-phenethyl-acetamide shows no observable AE splitting of the origin band in the R2PI spectrum [292].

We fit both subbands in the rotational spectrum of melatonin B to an effective rotational Hamiltonian for the torsional state $|v, \sigma\rangle$, which is defined as [21, 30]:

$$H_R^{v\sigma} = \sum_{g=a,b,c} B_g^{v\sigma} P_g^2 + \sum_{g=a,b,c} D_g P_g \qquad (14.1)$$

The quantum numbers, v and σ, are introduced to unambiguously classify the energy levels for the torsional problem. v is the principal torsional quantum number used to classify the torsional states for a single 3-fold potential and the 3 torsional sublevels have to be distinguished by a further quantum number σ. This σ is chosen in such a way that it represents the symmetry of the torsional wave functions and therefore the torsional problem is diagonal in σ. The $B_g^{v\sigma}$ are the torsionally averaged rotational constants for the state $|v, \sigma\rangle$ (terms quadratic in the overall angular momenta P_g)

and the terms linear in angular momentum D_g are defined by

$$D_g = \frac{\lambda_g B_g W_{v\sigma}^{(1)}}{r} \tag{14.2}$$

From the *ab initio* calculated structure of Anti(trans-out)/anti melatonin, we know that the methyl rotor of the acetyl group is parallel to the inertial a-axis and perpendicular to b and c (cf. Figure 14.5). Therefore, only one linear term, namely D_a is needed, while D_b and D_c are zero. λ_g are the direction cosines of the methyl top axis and the main inertial axes (in the case at hand, $\lambda_a = 1$, $\lambda_b = \lambda_c = 0$). $W_{v\sigma}^{(1)}$ the first order perturbation coefficient for the state $|v, \sigma\rangle$, is given by

$$W_{v\sigma}^{(1)} = -2 \langle v\sigma | p | v\sigma \rangle \tag{14.3}$$

and

$$r = 1 - \sum_{g=a,b,c} \frac{\lambda_g^2 I_\alpha}{I_g} \tag{14.4}$$

where I_α is the moment of inertia of the methyl top and I_g are the moments of inertia of the whole molecule with respect to the main inertial axes. The $B_g^{v\sigma}$ are defined by

$$B_g^{v\sigma} = B_g + F W_{v\sigma}^{(2)} \tag{14.5}$$

with second order perturbation coefficients $W_{v\sigma}^{(2)}$ given by

$$W_{v\sigma}^{(2)} = 1 + 4F \sum_{v' \neq v} \frac{|\langle v\sigma | p | v'\sigma \rangle|^2}{E_{v\sigma} - E_{v'\sigma}} \tag{14.6}$$

Thus, the barrier to internal rotation and its change upon electronic excitation can be determined from the values of D_a, from the difference of the torsionally

averaged rotational constants in the E and the A states, and from the subtorsional splitting $\Delta E_{ea} = (E_{\nu'\pm1} - E_{\nu''\pm1}) - (E_{\nu'0} - E_{\nu''0})$. Using a fitting program, which additionally uses the information of higher torsional transitions [293], we made a fit of the barriers in ground and excited state, including the $2e' \leftarrow 1e''$ transition, which we assigned to be the 41 cm^{-1} band in the low resolution R2PI spectrum of Florio *et al.* [210]. According to a harmonic normal mode analysis of Anti(trans-out)/anti melatonin, the lowest energy vibration is the bending vibration of the side chain at 87 cm^{-1}. It seems therefore safe to assign the lowest observed vibronic frequency to the torsional $2e' \leftarrow 1e''$ transition. Fixing the torsional constant F to 5.2 cm^{-1}, we obtained barriers of $V_3(S_0) = 63$ cm^{-1} and $V_3(S_1) = 64$ cm^1. These values are larger than the ground state V$_3$ torsional barrier in acetamide that has been determined to be 25 cm^{-1} by microwave spectroscopy [294]. Also in this molecule, the inertial a-axis is nearly parallel to the internal rotor axis, like in melatonin B.

Since the methyl rotor points away from the bulky indole chromophore, the reason for the higher barrier in melatonin B compared to acetamide cannot be a steric one, but must be electronic. Plusquellic and Pratt [295] have shown, that a correlation exists between the internal rotation barriers of methyl groups attached to a peptide bond and the relative weight of the twoprincipal resonance structures (a purely covalent and an ionic resonance structure) that contribute to the peptide bond. The weight of these resonance structures strongly depends on the nature of the substituents at the peptide bond and their conformations. Thus, the difference of the melatonin B methyl rotor barrier compared to that of acetamide is easily understood.

The rotationally resolved electronic spectrum of the melatonin A band is shown in Figure 14.6. Like the origin band of melatonin B, it is split into two torsional components, which are in this case 3640 MHz (~ 0.12 cm^{-1}) apart. Comparison of the rotational constants of the A subtorsional component, which are given in Table 14.3 to the results of the *ab initio* calculations shows good agreement with the rotational constants of the *Gph(trans-in)anti* conformer. Florio *et al.* [210] assigned the melatonin A band to belong to the *Gpy(trans-in)anti* conformer. Based on the energetics, the rotational constants and their changes upon electronic excitation (cf. Table 14.1), we prefer the assignment of the melatonin A band being due to the *Gph(trans-in)anti* conformer, an alternative assignment, which has not been explicitly excluded by Florio *et al.* [210].
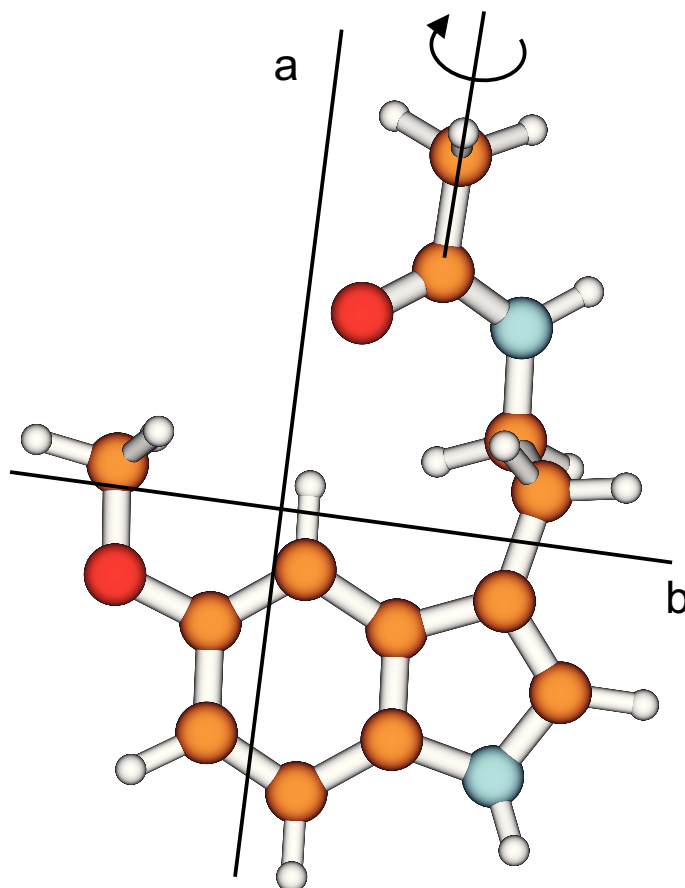
Figure 14.5: Inertial a and b-axes of the Anti(trans-out)/anti conformer of melatonin along with the internal rotor axis of the methyl rotor in the acetyl group. The internal rotor axis is nearly parallel with respect to the inertial a-axis

The center frequency of the melatonin A band is found at 32978.04 cm^{-1}, thus 430 cm^{-1} blue-shifted relative to the origin of melatonin B, which could unambiguously be attributed to the Anti(trans-out)anti conformer. Comparing the DFT/MRCI computed origin frequencies from Table 14.2, one finds the origin of melatonin Gph(trans-in)anti to be blue-shifted by 311 cm^{-1}, while the origins of both Gpy conformers are red-shifted. This is a further indication, that our assignment of melatonin A to the Gph(trans-in)anti conformer is correct.

The torsional analysis in this case is much more difficult than in the case of melatonin B, since the torsional axis makes an angle with all three inertial axes (cf. Figure 14.7). Thus, in addition to the rotational constants for the A and the E subspectra, all three D_g have to be fit for each electronic state. This proved to be impossible for this conformer owing to the enormous line density of overlapping transitions. Using the subtorsional splitting of 3640 MHz and a frequency of 45 cm^{-1} for the $2e' \leftarrow 1e''$ transition of this conformer from Ref. [210], we could estimate the difference of the torsional barriers upon electronic excitation to about 6 cm^{-1} compared to 1 cm^{-1}
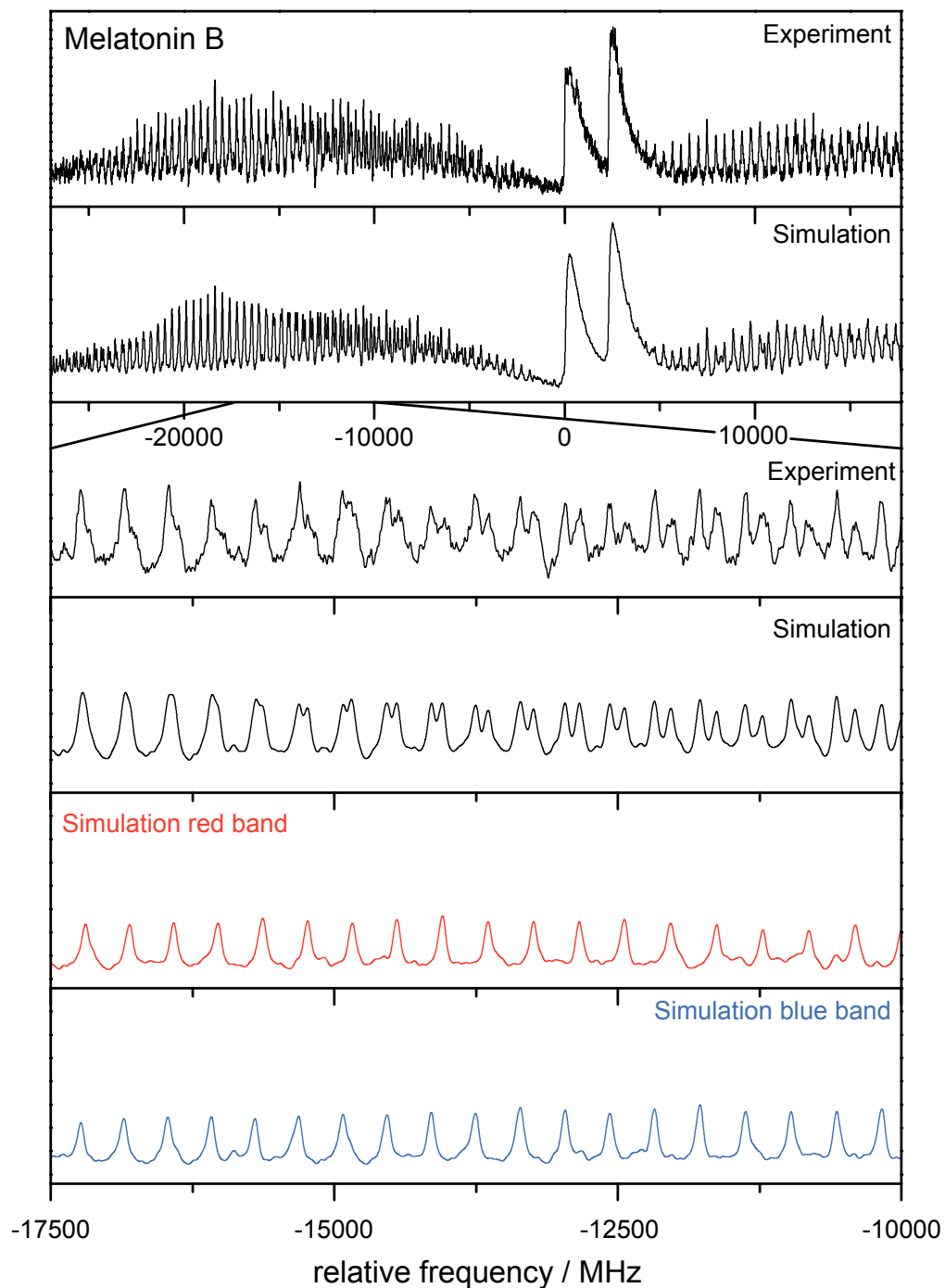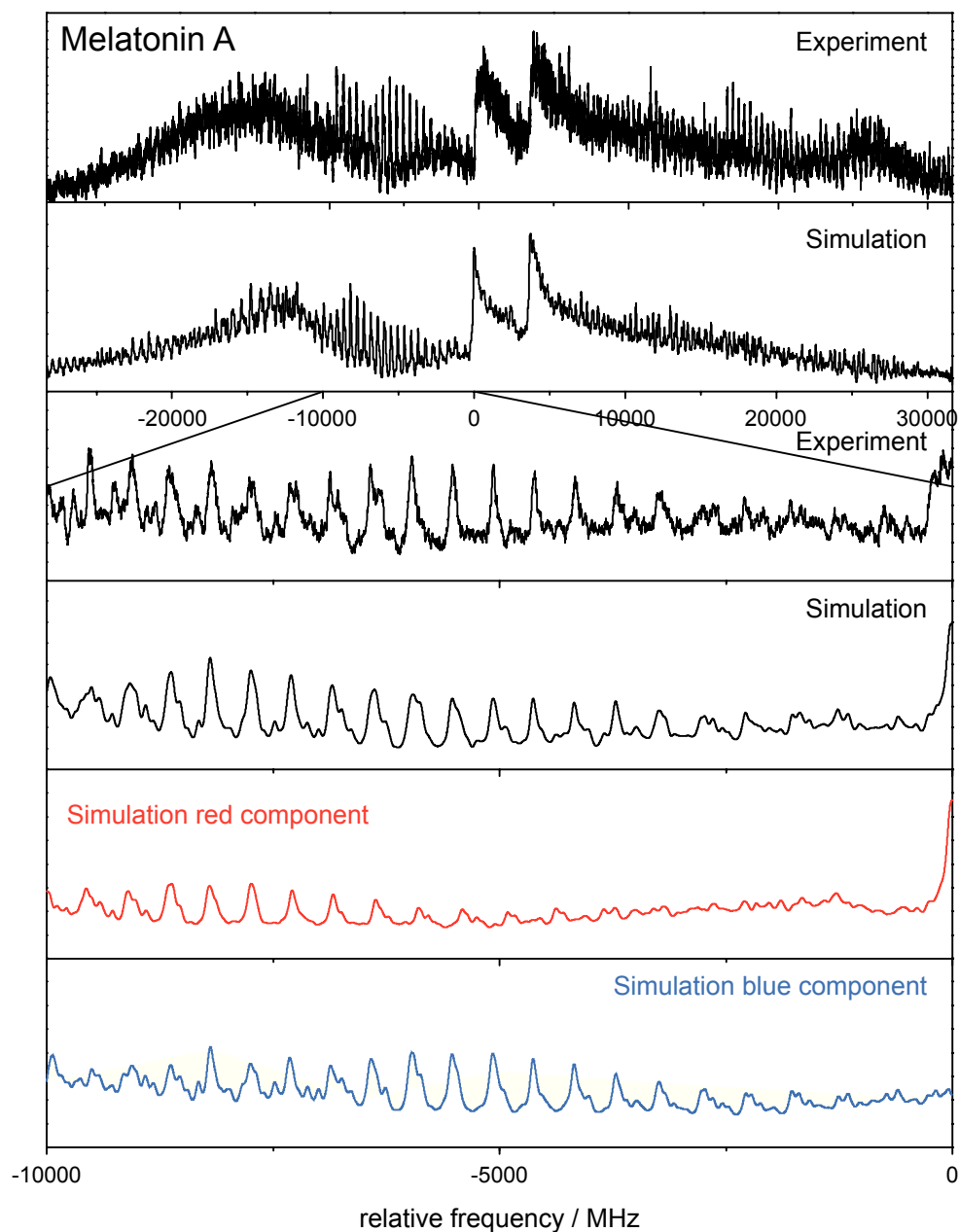
Figure 14.6: Experimental and simulated spectrum of melatonin A. The lower four traces show expanded views of the experiment, the simulation and the deconvolution into the two torsional subbands. For details see text.
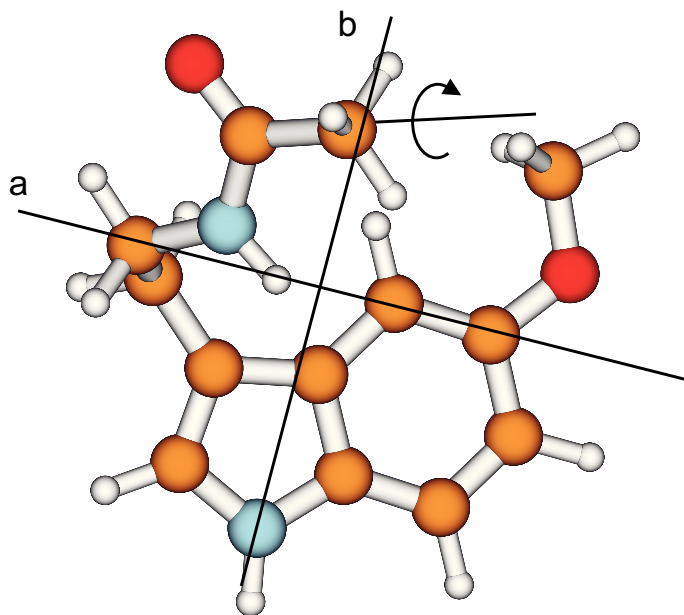
Figure 14.7: Inertial a and b-axes of the Gph(trans-in)/anti conformer of melatonin along with the internal rotor axis of the methyl rotor in the acetyl group. The polar angles of the internal rotor axis with the inertial axes are $\zeta = 40°$ and $\eta = 10°$. Here η is the angle between the projection vector of the 3-fold rotor axis on the ab-plane and the a-axis and ζ the angle between the 3-fold rotor axis and the c-axis.

for melatonin B.

14.6   Conclusions

Comparing the results of *ab initio calculations* with molecular parameters, obtained from the analysis of the rotationally resolved electronic spectra of melatonin A and B, we were able to unambiguously assign a Gauche-phenyl structure to the melatonin A band, and an Anti-structure to melatonin B. The CC2/cc-pVTZ calculated ground state rotational constants of both conformers agree well with the experimentally determined ones. The changes of the rotational constants upon electronic excitation (and thus the excited state structure) are perfectly described by CC2 theory for melatonin B, while the calculated changes of the rotational constants ΔA and ΔC in melatonin A are slightly too large. This points to an overestimate of dispersive interactions at the CC2 level in the excited state of the folded melatonin A, while the linear melatonin B lacks dispersive interactions between side chain and chromophore and hence the geometry change upon electronic excitation is reproduced with higher accuracy for melatonin B. The spectra of both conformers are split by an internal three-fold rotation of the methyl rotor in the acetyl group of the side chain. Since the

Table 14.3: Molecular parameters of the melatonin A and B origin bands obtained from ES-DR2 fits of the experimental spectra. The changes of the rotational constants upon electronic excitation are defined as $\Delta A = A' - A''$ etc. where the doubly primed parameters refer to the electronic ground state and the singly primed to the excited state. The linear angular momentum terms D_a'' and D_a' are defined by equation 14.2. The angles θ and ϕ define the orientation of the transition dipole moment in the principal axis system of the molecule. θ is the angle between the projection vector of the transition dipole moment on the ab-plane, and the a-axis and ϕ the angle between the transition dipole moment and the c-axis. τ is the excited state lifetime, determined from the Lorentz contribution to the Voigt profile of the rovibronic transitions. T_1, T_1, and w_T are the parameters from a two-temperature fit [82] to the relative intensities of the rovibronic transitions: $n(T_1, T_2, w_T) = e^{-E/kT_1} + w_T e^{-E/kT_2}$

	Anti(trans-out)anti		Gph(trans-in)anti	
	A	E	A	E
A''(MHz)	627.62(7)	627.30(7)	541.99(22)	543.93(19)
B''(MHz)	327.50(4)	327.50	487.03(17)	488.90(14)
C'''(MHz)	221.41(4)	221.41	312.26(13)	311.70(12)
D_a''(MHz)	-	338.7(10)	-	-
$\Delta I''$(uA^2)	-65.8(2)	-66.2(2)	-351.9(1)	-341.6(1)
ΔA (MHz)	0.80(3)	0.73(3)	0.62(1)	0.57(2)
ΔB (MHz)	1.12(8)	1.12(7)	8.19(2)	7.53(5)
ΔC (MHz)	0.67(2)	0.76(2)	7.55(3)	6.64(3)
$\Delta I'$ (uA^2)	-66.1(2)	-66.5(2)	-371.9(1)	-358.7(1)
D_a'(MHz)	-	326.8(11)	-	-
θ (degree)	39	39	25	25
ϕ (degree)	88	88	81	81
τ(ns)	3	3	2	2
T_1	9.7	9.7	4.5	4.5
T_2	2.7	2.7	13.4	13.4
w_T	0.34	0.34	0.08	0.08
ν_0(cm^{-1})	32549.19(1)	32549.11(1)	32978.04(1)	32977.92
ΔE_{ea} (MHz)	-2262(3)		-3640(20)	

spacing between the methyl rotor and the chromophore is large, and the side chain bearing the methyl group points away from the chromophore in the Anti-structure, the barriers in both electronic states are virtually the same. This situation changes in the Gauche-conformer. The electronic isolation of methyl top and chromophore is the same as in the Anti-conformer, but due to the close proximity of methyl rotor and chromophore, a through-space interaction may significantly change the barrier height upon electronic excitation.

Independent of the conformer, the lowest electronically excited singlet state has been found to be of ^1L_b character with nearly identical values of the transition dipole moment orientation with respect to the *pseudo*-symmetry axis of the indole chromophore.

Acknowledgments

14.7   Publication

The contents of this chapter has been published previously in slightly different form as *Rotationally resolved electronic spectroscopy of biomolecules in the gas phase. Melatonin* in the *Journal of Molecular Spectroscopy* (impact factor: 1.512), 2011, **268**, 115–122 by John T. Yi, Christian Brand, Miriam Wollenhaupt, David W. Pratt, W. Leo Meerts, and Michael Schmitt. John T. Yi and I contributed equally to this publication.

For this publication the high resolution spectra were recorded by J. T. Yi in the group of D. Pratt in Pittsburgh. The quantum chemical calculations were done by M. Schmitt, M. Wollenhaupt and me. Additional contributions to this study by me were the analysis of the spectra by means of genetic algorithms, discussion of the results with M. Schmitt and W. L. Meerts and preparation of the data for the

manuscript.

15. Summary

This thesis provides a comprehensive survey of the photophysics of indole derivatives. The excited state photophysics of seven model systems were examined in order to illustrate the interplay between the lowest two excited singlet states, namely the ^1L_a and the ^1L_b states. The characterization of the electronic states is based on electronic spectra recorded at rotational resolution. The experimental results are interpreted by comparison to high level quantum chemical calculations, namely approximate coupled cluster (CC2) and multi-reference configuration interaction (DFT/MRCI) theory.

The initial point chosen for a systematical characterization of the electronic properties of indole derivatives is a theoretical study on the chromophore indole itself. It is a generally accepted fact that the S_1 of indole is an ^1L_b-like state. The discussion on the energetic position of the ^1L_a state, however, remained unsolved. According to DFT/MRCI calculations the ^1L_a geometry is located 1847 cm^{-1} above the ^1L_b state. It has been shown to be very close to a conical intersection connecting both states. Apparently no noticeable barrier exists between the ^1L_a state and the conical intersection, so that pure ^1L_a states, accessed by a spectroscopic transition, will funnel directly into the ^1L_b minimum. The influence of the ^1L_a state on the ^1L_b state was studied by means of a perturbative Herzberg-Teller approach to account for vibronic coupling. The results show the vibronic spectrum of indole to be dominated by vibrational activity in the ^1L_b state, with vibronic perturbations of selected vibrational modes. These modes bear some resemblance to the difference vector for passing from the ^1L_b to the ^1L_a geometry.

In subsequent chapters the influence of *through bond* effects on the chromophore was elaborated. Three model substituents with different characteristics were chosen: a fluorine atom, a cyano group, and a methoxy group. The first two withdraw electron density from the chromophore via a negative inductive or mesomeric effect. On the other hand, the methoxy group pushes electron density into the chromophore via

a positive mesomeric effect. In 5-fluoroindole the lowest excited singlet state was confirmed to be the ^1L_b. This is an interesting discovery in respect of the results obtained by Oeltermann *et al* for 5-cyanoindole [189]. For this system the strongly negative mesomeric effect leads to a change in the excited state order of the singlet states, hence the electronic nature of the S_1 is the L_a. For 5-fluoroindole this is not the case. In spite of the large negative inductive effect of the fluorine substituent the energetic order remains the same as for indole.

The chapter on 5-cyanoindole adresses the assignment of rovibronic bands based on anharmonic calculations. Considering anharmonic corrections to the excited state geometries allows for an unambiguous assignment of several vibrational bands. 5-Methoxyindole has one of the largest known energy gaps between the ^1L_b (S_1) and the ^1L_a (S_2). Hence, the question arises to which extent the vibronic coupling described for indole is influenced by the large redshift of the ^1L_b. In order to answer this question several vibronic bands up to 1000 cm^{-1} above the ^1L_b state were analyzed with rotational resolution. For the purpose of reconstructing the vibronic couplings, simulations based on theoretical calculations were performed. Both theory and experiment agree on the fact that vibronic coupling is not present within the first 1000 cm^{-1}. The subbands of the respective spectra are attributed to the influence of the internal rotation of the methoxy group and the increasing density of lines. In the following chapter the position of the methoxy group was altered from position 5 to 6 at the chromophore. This change gives further evidence on the influence of the substituent. Position 6 was chosen as in the literature an atypical orientation of the transition dipole moment (TDM) is reported for this system [138, 175]. Furthermore, quantum chemical calculations performed in the course of this study predict the nature of the S_1 to the the ^1L_a. From the analysis of the spectra of several isotopologues, however, the nature of the lowest excited singlet state could unambiguously assigned to be the L_b. The orientation of the transition dipole moment vector for both conformers was found to fall in line with other ^1L_b-systems. Thus, the hypothesis of an atypical orientation of the transition dipole moment was disproved.

The influence of the conformational space on the photophysical properties of indole was elaborated for tryptamine (3-ethylaminoindole) and compared in detail to 2-phenylethylamine (PEA). In contrast to tryptamine 2-phenylethylamine shows a strong dependency of the TDM orientation on the actual conformation. As a possible reason the assumption of the excitation in PEA to be delocalized between the chromophore and the amino group is discussed, while being localized in the chro-

mophore for tryptamine. The smaller ^1L_a / ^1L_b gap in the case of PEA allows the polar amino group in some conformers to stabilize the polar ^1L_a state so much, that it comes into near degeneracy with the ^1L_b state, thus causing state mixing between them. Hence the polar side chain acts as an intramolecular solvent and thereby greatly influences the excited state photophysics. The study on melatonin concentrates on the spectra of the two most intense conformers present in a molecular beam. From the rotationally resolved spectra the geometries were determined and the conformational assignment for one of the two conformers refined. A splitting observed for the rovibronic bands is attributed to the internal rotation of the acetyl group.

The data obtained from the high resolution analysis of an electronically excited state provides a detailed description of its electronic nature, the couplings to other states, the excited state lifetime and other photophysical properties. In the course of this thesis it becomes evident that these characteristics can be altered significantly by the introduction of an appropriate substituent. Characterizing the influence of a large number of substituents might result in a kind of useful construction kit. This way chromophores with certain photophysical properties can be designed according to the researchers needs. Indole is of special interest as it is the chromophore of the amino acid tryptophan. Hence, non-natural derivatives exhibiting customized excited state properties could be designed to meet the requirements for special applications and thereby greatly enhance our knowledge on proteins.

16. Zusammenfassung

Diese Arbeit stellt eine umfassende Untersuchung der photophysikalischen Eigenschaften von substituierten Indolen dar. Mithilfe der rotationsaufgelösten laserinduzierten Fluoreszenzspektroskopie wurden sieben exemplarisch ausgewählte Modellsysteme untersucht und charakterisiert. Im Zusammenspiel mit Coupled Cluster und Multireferenzkonfigurationswechselwirkungs-Rechnungen gelang es dabei, die grundlegenden Faktoren systematisch zu charakterisieren, welche die photophysikalischen Eigenschaften von Indolderivaten beeinflussen. Das Hauptaugenmerk liegt hierbei auf den Wechselwirkungen zwischen den beiden tiefsten elektronisch angeregten Singulettzuständen ^1L_b und ^1L_a.

Den Ausgangspunkt bildet die Untersuchung des Chromophors Indol. Die elektronische Natur des S_1 Zustands von Indol ist gemeinhin als L_b anerkannt. Die genaue energetische Position des schwingungslosen ^1L_a-Ursprungs allerdings war zur Zeit dieser Arbeit strittig. Laut DFT/MRCI-Rechnungen befindet er sich 1847 cm^{-1} oberhalb des ^1L_b Zustands. Bedingt durch die große Nähe zu einer konischen Durchschneidung, die den S_1 mit dem S_2 Zustand verbindet, führt die spektroskopische Anregung eines puren ^1L_a-Zustands zu einem schnellen nichtstrahlenden Übergang in den ^1L_b-Zustand. Der daraus resultierende Einfluss des ^1L_a auf den ^1L_b konnte mittels störungstheoretischer Herzberg-Teller Analyse in guter Übereinstimmung mit dem Experiment quantifiziert werden. Dabei war zu beobachten, dass Schwingungen, die den ^1L_b in Richtung der konischen Durchschneidung hin auslenken, besonders effektiv an den ^1L_a koppeln.

In den folgenden Kapiteln wird der Einfluss von *Through-Bond*-Effekten auf den Chromophor ausgearbeitet. Dazu wurden drei Modellsubstituenten mit verschiedenen Charakteristika ausgewählt: eine Cyanogruppe und ein Fluorsubstituenten, die dem System Elektronendichte über stark negative mesomere ($-M$) bzw. induktive ($-I$) Effekte entziehen, und eine Methoxygruppe, die dem Chromophor über einen positiven mesomeren ($+M$) Effekt Elektronendichte zur Verfügung stellt.

Bei 5-Fluorindol wurde die elektronische Natur des S_1 als L_b bestätigt. Diese Aus-

sage muss vor dem Hintergrund der experimentellen Befunde über 5-Cyanoindol von Oeltermann *et al.* betrachtet werden [189]. Der stark negative mesomere Effekt der Cyanogruppe führt dort zu einer Umkehr der Reihenfolge der elektronisch angeregten Singulettzustände, sodass der ^1L_a zum tiefsten elektronisch angeregten Singulettzustand wird. Dies gilt jedoch nicht für 5-Fluorindol. Zwar übt der Fluorsubstituent einen starken -I Effekt aus, allerdings reicht dieser Einfluss nicht, um die Reihenfolge von ^1L_b und ^1L_a zu vertauschen.

Im Kapitel über 5-Cyanoindol wird die Zuordnung einiger Schwingungsbanden des ^1L_a Zustands mithilfe von anharmonischen Rechnungen behandelt. Die Berücksichtigung des Einflusses der Schwingungen auf die Struktur im angeregten Zustands erlaubte hier eine eindeutige Zuordung der experimentell beobachteten Banden. 5-Methoxyindol besitzt eine der größten bekannten Energielücken zwischen dem ^1L_b (S_1) und dem ^1L_a (S_2) Zustand. Das Interesse dieser Arbeit gilt nun der Fragestellung, inwieweit die schwingungsabhängigen Kopplungen, wie sie für das Indol beschrieben wurden, durch diese Vergrößerung des energetischen Abstandes beeinflusst werden. Dazu wurden mehrere vibronische Banden bis zu 1000 cm^{-1} oberhalb des ^1L_b rotationsaufgelöst untersucht. Um eventuelle schwingungsinduzierte Wechselwirkungen nachvollziehen zu können, wurden vergleichende Simulationen basierend auf theoretischen Rechnungen durchgeführt. Theorie und Experiment stimmen darin überein, dass vibronische Kopplungen innerhalb der ersten 1000 cm^{-1} oberhalb des ^1L_b nicht auftreten. Die beobachteten Subspektren können auf die interne Rotation der Methoxygruppe und die steigende Schwingungszustandsdichte zurückgeführt werden.

Im darauf folgenden Kapitel werden die Ergebniss der Untersuchung von 6-Methoxyindol vorgestellt. Durch die systematische Änderung der Position des Methoxysubstituenten können neue Erkenntnisse hinsichtlich des Einflusses des Substituenten gewonnen werden. Position 6 wurde gewählt, da in der Literatur für dieses System eine ungewöhnliche Orientierung des Übergangsdipolmoments (ÜDM) für den ^1L_b beschrieben wird [138, 175]. Die im Rahmen dieser Arbeit durchgeführten quantenchemischen Rechnungen sagen zudem den ^1L_a als energetisch tiefsten angeregten Singulettzustand voraus. Durch die Analyse der Spektren von mehreren Isotopomeren konnte die absolute Lage des Übergangsdipolmoments eindeutig bestimmt werden. Daraus ergibt sich sowohl für das *syn*- als auch das *anti*-Konformer, dass die elektronische Natur des S_1 dem L_b entspricht und die Orientierung des ÜDM mit anderen L_b-Systemen vergleichbar ist. Die Hypothese einer atypischen Orientierung wurde somit widerlegt.

Der Einfluss eines umfangreichen Konformerenraums auf die photophysikalischen Eigenschaften des Indolchromophors wurde am Beispiel von Tryptamin (3-Ethylaminoindol) untersucht und mit den Ergebnissen für 2-Phenylethylamin verglichen. Im Vergleich zu Tryptamin ergab sich bei der Untersuchung von Phenylethylamin eine wesentlich höhere Abhängigkeit des ÜDM-Orientierung von der Konformation der Ethylaminseitenkette. Als Grund hierfür wird vermutet, dass die Anregung bei 2-Phenylethylamin, anders als im Tryptamin, über den Chromophor und die Seitenkette delokalisiert ist. Der geringe energetische Unterschied zwischen dem ^1L_a und dem ^1L_b bei 2-Phenylethylamin führt zudem dazu, dass der Einfluss der polaren Aminogruppe bei einigen Konformeren sogar dafür ausreicht, die energetische Lücke zu schließen. Die polare Seitenkette fungiert folglich als intramolekulares Solvens, das ein Koppeln und Mischen der Zustände erleichtert.

In Kapitel 14 schließlich werden die elektronischen Ursprünge der beiden in einem molekularen Strahl intensivsten Konformere von Melatonin behandelt. Frühere Zuordnungen werden durch die in dieser Arbeit bestimmten Strukturen teilweise bestätigt, teilweise jedoch auch widerlegt. Die Aufspaltung der rotationsaufgelösten Spektren wurde auf die interne Rotation der Acetylgruppe der Seitenkette zurückgeführt.

Die dargelegten Ergebnisse veranschaulichen, wie die photophysikalischen Eigenschaften von Indol durch Substituenten in verschiedenen Positionen gezielt beeinflusst werden können. Die vorgestellten Modellsysteme geben hierbei einen Überblick über die Effekte der verschiedenen Substituente. Dieses Wissen ermöglicht es, die Eigenschaften der Chromophore an die Anforderungen des jeweiligen Experiments anzupassen. Indol als Chromophor ist besonders in Hinblick auf nicht-natürliche Tryptophanderivate von Interesse, die aufgrund ihrer modifizierten Absorptions- und Emissionseigenschaften erheblich zum Verständnis der Strukturen von Proteinen beitragen. Die Charakterisierung weiterer Indolderivate könnte folglich die Grundlage für spezielle Tryptophananaloga sein, die unseren Erkenntnisstand über Proteine erheblich erweitern.

Danksagung

und Rüdiger danke ich für die epische Fahrt im Orientexpress.

Ein sehr großes Dankeschön geht an meine Freundin Sandra Knuffinke, die über die Jahre alle kleinen und großen Sorgen und Freuden des Unialltags mit mir geteilt hat und außerdem ein wachsames Auge auf die Orthographie dieser Arbeit hatte. Michael Schmitt, Jörg Tatchen und Katharina Hunger haben diese Dissertation inhaltlich auf Fehler abgeklopft.

Weiterhin bedanke ich mich bei meiner Familie, die mich stets unterstützt und ermutigt hat, und bei allen Freunden, die es mir hoffentlich nicht übel nehmen, dass ich sie in letzter Zeit etwas vernachlässigt habe.

Danke

17. Complete List of Publications

- Christian Brand, Beatrice Happe, Olivia Oeltermann, Martin Wilke, and Michael Schmitt: High Resolution Spectroscopy of Several Rovibronically Excited Bands of 5-Cyanoindole - the Effect of Vibrational Averaging. *J. Mol. Struct.*, http://dx.doi.org/10.1016/j.molstruc.2012.11.049

- Christian Brand, Olivia Oeltermann, Martin Wilke, and Michael Schmitt: Position Matters: High Resolution Spectroscopy of 6-Methoxyindole. *J. Chem. Phys.*, **138**, 024321(1-9), 2013

- Olivia Oeltermann, Christian Brand, Martin Wilke, and Michael Schmitt: Ground and Electronically Excited Singlet State Structures of the syn and anti Rotamers of 5-Hydroxyindole. *J. Phys. Chem. A*, **116**, 7873-7879, 2012

- Christian Brand, Olivia Oeltermann, Martin Wilke, Jörg Tatchen, and Michael Schmitt: Ground and Electronically Excited Singlet-State Structures of 5-Fluoroindole Deduced from Rotationally Resolved Electronic Spectroscopy and ab Initio Theory. *ChemPhysChem*, **13**, 3134-3138, 2012

- Olivia Oeltermann, Christian Brand, Bernd Engels, Jörg Tatchen, and Michael Schmitt: The structure of 5-cyanoindole in the ground and the lowest electronically excited singlet states, deduced from rotationally resolved electronic spectroscopy and ab initio theory. *Phys. Chem. Chem. Phys.*, **14**, 10266-10270, 2012

- John T Yi, Christian Brand, Miriam Wollenhaupt, David W Pratt, W. Leo Meerts, and Michael Schmitt: Rotationally resolved electronic spectroscopy of biomolecules in the gas phase. Melatonin. *J. Mol. Spectros.*, **268**, 115-122, 2011

- Christan Brand, W. Leo Meerts, and Michael Schmitt: How and why do transition dipole moments depend on conformer structure? *J. Phys. Chem. A*, **115**, 9612-9619, 2011

- Olivia Oeltermann, Christian Brand, W. Leo Meerts, Jörg Tatchen, and Michael Schmitt: Rotationally resolved electronic spectroscopy of 2,3-bridged indole derivatives: tetrahydrocarbazole. *J. Mol. Struct.* **933**, 2-8, 2011

- Thi-Bao Chau Vu, Christian Brand, W. Leo Meerts, and Michael Schmitt: Rotationally resolved electronic spectroscopy of 1,4-benzodioxan: The anomeric effect in the ground and electronically excited states. *ChemPhysChem*, **12**, 2035-2041, 2011

- Christian Brand, Olivia Oeltermann, David Pratt, Rainer Weinkauf, W. Leo Meerts, Wim van der Zande, Karl Kleinermanns, and Michael Schmitt: Rotationally resolved electronic spectroscopy of 5-methoxyindole. *J. Chem. Phys.*, **133**, 024303, 2010

- Jochen Küpper, David W. Pratt, W. Leo Meerts, Christian Brand, Jörg Tatchen, and Michael Schmitt: Vibronic coupling in indole: II. Investigation of the $^1L_a - ^1L_b$ interaction using rotationally resolved electronic spectroscopy, *Phys. Chem. Chem. Phys.*. **12**, 4980-4988, 2010

- Christian Brand, Jochen Küpper, David W. Pratt, W. Leo Meerts, Daniel Krügler, Jörg Tatchen, and Michael Schmitt: Vibronic coupling in indole: I. Theoretical description of the $^1L_a - ^1L_b$ interaction and the electronic spectrum, *Phys. Chem. Chem. Phys.*. **12**, 4968-4979, 2010

- Ivo Kalkman, Christian Brand, Thi-Bao Chau Vu, W. Leo Meerts, Yuriy N. Svartsov, Otto Dopfer, Xin Tong, Klaus Müller Dethlefs, Stefan Grimme, and Michael Schmitt: The structure of phenol-Ar_n (n=1, 2) clusters in their S_0 and S_1 states. *J. Chem. Phys.*, **130**, 224303, 2009

- Thi Bao Chau Vu, Ivo Kalkman, W. Leo Meerts, Christian Brand, Yuriy N. Svartsov, Sascha Wiedemann, Rainer Weinkauf, and Michael Schmitt: The conformational landscape of 5-methoxytryptamine studied by rotationally resolved fluorescence spectroscopy and resonant ionization spectroscopy. *Phys. Chem. Chem. Phys.*, **11**, 2433–2440, 2009

Bibliography

[1] B. S. Ray, "Über die Eigenwerte des asymmetrischen Kreisels," *Z. Phys.*, vol. 78, pp. 74–91, 1932.

[2] A. D. Becke, "A new mixing of Hartree-Fock and local density-functional theories," *J. Chem. Phys.*, vol. 98, pp. 1372–1377, 1992.

[3] E. P. Wigner, *Group theory and its application to the quantum mechanics of atomic spectra*, 5th ed. Academic Press, New York, 1968.

[4] R. S. Mulliken, "Species classification and rotational energy level patterns of non-linear triatomic molecules," *Phys. Rev.*, vol. 59, pp. 873–889, 1941.

[5] J. R. Platt, "Classifications of spectra of cata-condensed hydrocarbons," *J. Chem. Phys.*, vol. 17, pp. 484–495, 1949.

[6] M. R. Eftink, "Use of multiple spectroscopic methods to monitor equilibrium unfolding of proteins," *Methods Enzymol.*, vol. 259, pp. 487–512, 1995.

[7] D. Canet, K. Doering, C. M. Dobsen, and Y. Dupont, "High-sensitivity fluorescence anisotropy detection of protein-folding events: Application to α-lactalbumin," *Biophys. J.*, vol. 80, pp. 1996–2003, 2001.

[8] R. M. Ballew, J. Sabelko, and M. Gruebele, "Direct observation of fast protein folding: The initial collapse of apomyoglobin," *Proc. Natl. Acad. Sci. USA*, vol. 11, pp. 5759–5764, 1996.

[9] J. R. Lakowicz, *Principles of Fluorescence Spectroscopy*, 3rd ed. Springer, 2006.

[10] R. Boteva, T. Zlateva, V. Dorovska-Taran, A. J. W. G. Visser, R. Tsanev, and B. Salvato, "Dissociation equilibrium of human recombinant interferon γ," *Biochemistry*, vol. 35, pp. 14 825–14 830, 1996.

[11] M. V. Hershberger, R. Lumry, and R. Verral, "The 3-methylindole/n-butanol

exciplex: Evidence for two exciplex sites in indole compounds," *Photochem. Photobiol.*, vol. 33, pp. 609–617, 1981.

[12] H. Lami and N. Glasser, "Indole's solvatochromism revisited," *J. Chem. Phys.*, vol. 84, pp. 597–604, 1986.

[13] M. Sun and P.-S. Song, "Solvent effects on the fluorescent states of indole derivatives-dipole moments," *Photochem. Photobiol.*, vol. 25, pp. 3–9, 1977.

[14] G. D. Fasman, Ed., *Protein - Volume 1*, 3rd ed., ser. Handbook of Biochemistry and Molecular Biology.   CRC Press, 1976.

[15] M. Noronha, J. C. Lima, P. Lamosa, H. Samtos, C. Maycock, R. Ventura, and A. L. Macanita, "Intramolecular fluorescence quenching of tyrosine by the peptide α-carbonyl group revisited," *J. Phys. Chem. A*, vol. 108, pp. 2155–2166, 2004.

[16] K. Guzow, R. Ganzynkowicz, A. Rzeska, J. Mrozek, M. Szabelski, J. Karolczak, A. Liwo, and W. Wiczk, "Photophysical properties of tyrosine and its simple derivatives studied by time-resolved fluorescence spectroscopy, global analysis, and theoretical calculations," *J. Phys. Chem. B*, vol. 108, pp. 3879–3889, 2004.

[17] G. Weber, "Fluorescence-polarization spectrum and electronic-energy transfer in tyrosine, tryptophan and related compounds," *Biochem. J.*, pp. 335–345, 1960.

[18] J. W. Petrich, M. C. Chang, D. B. McDonald, and G. R. Fleming, "On the origin of nonexponential fluorescence decay in tryptophan and its derivatives," *J. Am. Chem. Soc.*, vol. 105, pp. 3824–3832, 1983.

[19] D. Creed, "The photophysics and photochemistry of the near-UV absorbing amino acids, I: Tryptophan and its simple derivatives," *Photochem. Photobiol.*, vol. 39, pp. 537–562, 1984.

[20] D. M. Rayner and A. G. Szabo, "Time-resolved fluorescence of aqueous tryptophan," *Can. J. Chem.*, vol. 56, pp. 743–745, 1977.

[21] W. Gordy and R. L. Cook, *Microwave Molecular Spectra*, 2nd ed.   Wiley, New York, 1984.

[22] H. W. Kroto, *Molecular Rotation Spectra*, Dover ed.   Dover Publications, New York, 1992.

[23] J. M. Hollas, *High Resolution Spectroscopy*, 1st ed. Butterworths, London, 1982.

[24] D. M. Dennison, "The infrared spectra of polyatomic molecules," *Rev. Mod. Phys.*, vol. 3, pp. 280–345, 1931.

[25] G. W. King, R. M. Hainer, and P. C. Cross, "I. Calculation and symmetry classification of energy levels," *J. Chem. Phys.*, vol. 11, pp. 27–42, 1942.

[26] D. M. Bishop, *Group Theory and Chemistry*, Dover ed. Dover Publications, New York, 1993.

[27] E. B. Wilson, Jr., J. C. Decius, and P. C. Cross, *Molecular Vibrations*, Dover ed. Dover Publications, New York, 1980.

[28] S. C. Wang, "On the asymmetrical top in quantum mechanics," *Phys. Rev.*, vol. 34, pp. 243–252, 1929.

[29] J. H. van Vleck, "On σ-type doubling and electron spin in the spectra of diatomic molecules," *Phys. Rev.*, vol. 33, pp. 467–506, 1929.

[30] D. R. Herschbach, "Calculation of energy levels for internal torsion and over-all rotation. III^*," *J. Chem. Phys.*, vol. 31, pp. 91–108, 1959.

[31] C. C. Lin and J. D. Swalen, "Internal rotation and microwave spectroscopy," *Rev. Mod. Phys.*, vol. 31, pp. 841–891, 1959.

[32] E. B. Wilson, Jr., "The present status of the statistical method of calculating thermodynamic functions," *Chem. Rev.*, vol. 27, pp. 17–38, 1940.

[33] B. L. Crawford, Jr., "The partition functions and energy levels of molecules with internal torsional motions," *J. Chem. Phys.*, vol. 8, pp. 273–281, 1940.

[34] H. H. Nielsen, "The torsion oscillator-rotator in the quantum mechanics," *Phys. Rev.*, vol. 40, pp. 445–456, 1932.

[35] J. S. Koehler and D. M. Dennison, "Hindered rotation in methyl alcohol," *Phys. Rev.*, vol. 57, pp. 1006–1021, 1940.

[36] D. G. Burkhard and D. M. Dennison, "The molecular structure of methyl alcohol," *Phys. Rev.*, vol. 84, pp. 408–417, 1951.

[37] M. Abramowitz, Ed., *Handbook of mathematical functions*, 9th ed. Dover Publications, New York, 1972.

[38] O. M. Jordahl, "The effect of crystalline electric fields on the paramagnetic susceptibility of cupric salts," *Phys. Rev.*, vol. 45, pp. 87–97, 1934.

[39] J. D. Swalen and D. R. Herschbach, "Internal barrier of propylene oxide from the microwave spectrum," *J. Chem. Phys.*, vol. 27, pp. 100–108, 1957.

[40] P. R. Bunker and P. Jensen, *Molecular Symmetry and Spectroscopy*, 2nd ed. NRC Research Press, Ottawa, 1998.

[41] P. C. Cross, R. M. Hainer, and G. W. King, "II. Calculation of dipole intensities and line classification," *J. Chem. Phys.*, vol. 12, pp. 210–243, 1944.

[42] J. T. Hougen and J. K. G. Watson, "Anomalous rotational line intensities in electronic transitions of polyatomic molecules: Axis-switching," *Can. J. Phys.*, vol. 43, pp. 298–320, 1965.

[43] A. Held, B. B. Champagne, and D. W. Pratt, "Inertial axis reorientation in the $S_1 \leftarrow S_0$ electronic transition of 2-pyridone. A rotational Duschinsky effect. Structural and dynamical consequences," *J. Chem. Phys.*, vol. 95, pp. 8732–8743, 1991.

[44] A. M. Mebel, M. Hayashi, K. K. Liang, and S. H. Lin, "Ab initio calculations of vibronic spectra and dynamics for small polyatomic molecules: Role of Duschinsky effect," *J. Phys. Chem. A*, vol. 103, pp. 10 674–10 690, 1999.

[45] W. Demtröder, *Laserspektroskopie - Grundlagen und Techniken*, 4th ed. Springer Verlag, Berlin, 2000.

[46] M. Born and R. Oppenheimer, "Zur Quantentheorie der Molekeln," *Ann. Phys.*, vol. 4, pp. 457–484, 1927.

[47] M. Born and K. Huang, *Dynamical Theory of Crystal Lattices*, 1st ed. Oxford University Press, 1954.

[48] L. S. Cederbaum, "Born-Oppenheimer Approximation and Beyond," in *Conical Intersections: Electronic Structure, Dynamics & Spectroscopy*, W. Domcke, D. R. Yarkony, and H. Koppel, Eds. World Scientific Publishing, 2004.

[49] D. R. Yarkony, "Conical intersections: The new conventional wisdom," *J. Phys. Chem. A*, vol. 105, pp. 6277–6293, 2001.

[50] J. Michl and V. Bonačić-Koutecký, *Electronic Aspects of Organic Photochemistry*, 1st ed. Wiley, New York, 1990.

[51] M. Klessinger and J. Michl, *Excited States and Photochemistry of Organic Molecules*, 1st ed. Wiley, New York, 1995.

[52] F. Bernardi, M. Olivucci, and M. A. Robb, "Potential energy surface crossings in organic photochemistry," *Chem. Soc. Rev.*, vol. 25, pp. 321–328, 1996.

[53] A. L. Sobolewski and W. Domcke, "*Ab Initio* investigations on the photophysics of indole," *Chem. Phys. Lett.*, vol. 315, pp. 293–298, 1999.

[54] W. Domcke, D. R. Yarkony, and H. Koppel, Eds., *Conical Intersections: Electronic Structure, Dynamics & Spectroscopy*, 1st ed. World Scientific Publishing, 2004.

[55] N. J. Turro, V. Ramamurthy, and J. C. Scaiano, *Principles of Molecular Photochemistry*, 10th ed. University Science Books, 2009.

[56] F. Jensen, *Introduction to Computational Chemistry*, 1st ed. Wiley, New York, 1999.

[57] D. R. Yarkony, "Conical intersections: Their description and consequences," in *Conical Intersections: Electronic Structure, Dynamics & Spectroscopy*, W. Domcke, D. R. Yarkony, and H. Koppel, Eds. World Scientific Publishing, 2004.

[58] E. U. Condon, "Nuclear motions associated with electron transitions in diatomic molecules," *Phys. Rev.*, vol. 32, pp. 858–872, 1928.

[59] J. Franck, "Elementary processes of photochemical reactions," *Trans. Faraday Soc.*, vol. 21, pp. 536–542, 1926.

[60] G. Herzberg, *Molecular Spectra and Molecular Structure, III. Electronic Spectra and Electronic Structure of Polyatomic Molecules*, 1st ed. van Nostrand Reinhold Company, New York, 1966.

[61] J. N. Murrell and J. A. Pople, "The intensities of the symmetry–forbidden electronic bands of benzene," *Proc. Phys. Soc. A*, vol. 69, pp. 245–252, 1955.

[62] P. A. Geldorf, R. P. H. Rettschnick, and G. J. Hoytink, "Vibronic coupling and radiative transitions," *Chem. Phys. Lett.*, vol. 10, pp. 549–558, 1971.

[63] G. Orland and W. Sieband, "Mechanisms of vibronic intensity borrowing," *Chem. Phys. Lett.*, vol. 15, pp. 465–468, 1972.

[64] D. R. Yarkony, "Diabolical conical intersection," *Rev. Mod. Phys.*, vol. 68, pp. 985–1013, 1996.

[65] G. J. Atchity, S. S. Xantheas, and K. Ruedenberg, "Potential energy surfaces near intersections," *J. Chem. Phys.*, vol. 95, pp. 1862–1876, 1991.

[66] D. R. Yakony, "Conical intersections: Diabolical and often misunderstood," *Acc. Chem. Res.*, vol. 31, pp. 511–518, 1998.

[67] S. Gerstenkorn and P. Luc, *Atlas du Spectre d'Absorption de la Molecule d'Iodine.* Editions du Centre National de la Recherche Scientifique, Paris, 1978.

[68] W. Koechner, *Solid-State Laser Engineering*, 3rd ed., ser. Springer Series in Optical Sciences. Springer, Berlin, 1992.

[69] O. Svelto, *Principle of Lasers*, 1st ed. Heyden & Son Limited, London, 1976.

[70] Sirah Laser- und Plasmatechnik GmbH, *Matisse User´s Guide*, 1st ed.

[71] F. L. Pedrotti and L. S. Pedrotti, *Introduction to Optics*, 2nd ed. Prentice-Hall International, 1993.

[72] R. D. Suenram, F. J. Lovas, and G. T. Fraser, "Microwave spectrum and ^{14}N quadrupole coupling constants of indole," *J. Mol. Spectrosc.*, vol. 127, pp. 472–480, 1988.

[73] H. Gobrecht, Ed., *Optik*, 8th ed., ser. Bergmann Schäfer Lehrbuch der Experimentalphysik. de Gruyter, Berlin, 1987, no. III.

[74] Spectra-Physics LAS GmbH, *Wavetrain-User´s Manual*, 4th ed., 2002.

[75] R. W. P. Drever, J. L. Hall, F. V. Kowalski, J. Hough, G. M. Ford, A. J. Munley, and H. Ward, "Laser phase and frequency stabilization using an optical resonator," *Appl. Phys. B Laser Optic*, vol. 31, pp. 97–105, 1983.

[76] R. Campargue, Ed., *Atomic and Molecular Beams*, 1st ed. Springer, Berlin, 2000.

[77] D. H. Levy, "Laser spectroscopy of cold gas-phase molecules," *Annu. Rev. Phys. Chem.*, vol. 31, pp. 197–225, 1980.

[78] J. M. Hollas and D. Phillips, Eds., *Jet Spectroscopy and Molecular Dynamics*, 1st ed. Blackie Academic & Professional, London, 1995.

[79] G. Scoles, Ed., *Atomic and Molecular Beam Methods, Volumes I and II*, 1st ed. Oxford University Press, 1988 & 1992.

[80] D. R. Miller, "Free jet sources," in *Atomic and Molecular Beams.* Oxford University Press, 1988, vol. 1.

[81] R. H. Edwards and H. K. Cheng, *Distribution function and temperature in a monoatomic gas under steady expansion into a vacuum.* Academic Press, New York, 1967, vol. 1, pp. 819–835.

[82] Y. R. Wu and D. H. Levy, "Determination of the geometry of deuterated tryptamine by rotationally resolved electronic spectroscopy," *J. Chem. Phys.*, vol. 91, pp. 5278–5284, 1989.

[83] J. B. Anderson and J. B. Fenn, "Velocity distributions in molecular beams from nozzle sources," *Phys. Fluids*, vol. 8, pp. 780–787, 1965.

[84] A. Kantrowitz and J. Grey, "A high intensity source for the molecular beam. Part I. Theoretical," *Rev. Sci. Instrum.*, vol. 22, pp. 328–332, 1951.

[85] M. J. Böhm, "Rotationsaufgelöste elektronische Spektroskopie and flexiblen Molekülen und Molekülkomplexen," Ph.D. dissertation, Heine-Universität, Düsseldorf, 2010.

[86] J. Küpper, "Rotationsauflösende Laserspektroskopie, Beziehung zwischen Struktur und interner Dynamik von Molekülen," Ph.D. dissertation, Heine-Universität, Düsseldorf, 2000.

[87] J. Küpper, D. W. Pratt, W. L. Meerts, C. Brand, J. Tatchen, and M. Schmitt, "Vibronic coupling in indole: II. Investigation of the ^1L_a–^1L_b interaction using rotationally resolved electronic spectroscopy," *Phys. Chem. Chem. Phys.*, vol. 12, pp. 4980–4988, 2010.

[88] C. Darwin, *On the Origin of Species By Means of Natural Selection, or, the Preservation of Favoured Races in the Struggle for Life*, 1st ed. John Murray, London, 1859.

[89] H.-G. Beyer and H.-P. Schwefel, "Evolution strategies - a compresensive introduction," *Natural Computing*, vol. 1, pp. 3–52, 2002.

[90] L. J. Fogel, "Autonomous automata," *Industrial Research Magazine*, vol. 4, pp. 14–19, 1962.

[91] L. J. Fogel, A. J. Owens, and M. J. Walsh, *Artificial Intelligence through Simulated Evolution*, 1st ed. Wiley, New York, 1966.

[92] J. H. Holland, "Outline for a logical theory of adaptive systems," *J. AMC*, vol. 9, pp. 297–314, 1962.

[93] ——, *Adaptation in natural and artificial systems*, 1st ed.   The University of Michigan Press, Ann Arbor, 1975.

[94] I. Rechenberg, *Evolutionsstrategie: Optimierung technischer Systeme nach Prinzipien der biologischen Evolution*, 1st ed.   Frommann-Holzboog Verlag, Stuttgart, 1973.

[95] H.-P. Schwefel, "Evolutionsstrategie und numerische Optimierung," Ph.D. dissertation, TU Berlin, 1975.

[96] J. R. Koza, *Genetic Programming: On the Programming of Computers by Means of Natural Selection*, 1st ed.   The MIT Press, 1992.

[97] ——, *Genetic Programming II: Automatic Discovery of Reusable Programs*, 1st ed.   The MIT Press, 1994.

[98] F. H. E. Schöneburg and S. Feddersen, *Genetische Algorithmen und Evolutionsstrategien*, 1st ed.   Addison-Wesley, 1994.

[99] J. Heistermann, *Genetische Algorithmen*, 1st ed.   Teubner-Verlag, 1994.

[100] K. Weicker, *Evolutionäre Algorithmen*, 2nd ed.   Teubner-Verlag, 2007.

[101] I. Gerdes, F. Klawonn, and R. Kruse, *Evolutionäre Algorithmen*, 1st ed. Vieweg, Wiesbaden, 2004.

[102] H. Pohlheim, *Evolutionäre Algorithmen*, 1st ed.   Springer, Berlin, 1999.

[103] A. E. Eiben and J. E. Smith, *Introduction to Evolutionary Computing (Natural Computing Series)*, 2nd ed., 2003.

[104] J. A. Hageman, R. Wehrens, R. de Gelder, W. L. Meerts, and L. M. C. Buydens, "Direct determination of molecular constants from rovibronic spectra with genetic algorithms," *J. Chem. Phys.*, vol. 113, pp. 7955–7962, 2000.

[105] W. L. Meerts, M. Schmitt, and G. Groenenboom, "New applications of the genetic algorithm for the interpretation of high-resolution spectra," *Can. J. Chem.*, vol. 82, pp. 804–819, 2004.

[106] W. L. Meerts and M. Schmitt, "A new automated assign and analysing method for high-resolution rotationally resolved spectra using genetic algorithms," *Phys. Scr.*, vol. 73, pp. C47–C52, 2006.

[107] N. Hansen, "The CMA evolution strategy: a comparing review," in *Towards a new evolutionary computation. Advances on estimation of distribution algorithms*, J. A. Lozano, P. Larranaga, I. Inza, and E. Bengoetxea, Eds. Springer, Berlin, 2006.

[108] N. Hansen and A. Ostermeier, "Adapting arbitrary normal mutation distributions in evolution strategies: The covariance matrix adaptation," in *the 1996 IEEE Conference on Evolutionary Computation (ICEC '96)*, 1996, pp. 312–317.

[109] N. Hansen, *The CMA Evolution Strategy: A Tutorial*, 2009.

[110] S. Grimme and M. Waletzke, "A combination of Kohn-Sham density functional theory and multi-reference configuration interaction methods," *J. Chem. Phys.*, vol. 111, pp. 5645–5655, 1999.

[111] O. Christian, H. Koch, and P. Jørgensen, "The second-order approximate coupled cluster single and double model CC2," *Chem. Phys. Lett.*, vol. 243, pp. 409–418, 1995.

[112] C. Hättig and F. Weigend, "CC2 excitation enery calculatons on large molecules using the resolution of the identity approximation," *J. Chem. Phys.*, vol. 113, pp. 5154–5161, 2000.

[113] O. Vahtras, J. Almlöf, and M. W. Feyereisen, "Integral approximation for LCAO-SCF calculations," *Chem. Phys. Lett.*, vol. 213, pp. 514–518, 1993.

[114] B. O. Roos, M. Fülscher, P.-A. Malmqvist, M. Merchan, and L. Serrano-Andrés, "Theoretical studies of the electronic spectra of organic molecules," in *Quantum Mechanical Electronic Structure Calculations with Chemical Accuracy*, S. R. Langhoff, Ed. Springer Netherlands, 1995.

[115] W. D. Laidig, P. Saxe, and R. J. Bartlett, "The description of N_2 and F_2 potential energy surfaces using multireference coupled cluster theory," *J. Chem. Phys.*, vol. 86, pp. 887–907, 1986.

[116] I. Schavitt, "The method of configuration interaction," in *Modern Theoretical Chemistry Vol. 3: Methods of Electronic Structure Theory*, H. F. Schaefer III, Ed. Plenum, New York, 1977.

[117] P. Hohenberg and W. Sham, "Inhomogeneous electron gas," *Phys. Rev.*, vol. 136, pp. B864–B871, 1964.

[118] W. Kohn and L. J. Sham, "Self-consistent equations including exchange and correlation effects," *Phys. Rev.*, vol. 140, pp. A1133–A1138, 1965.

[119] R. G. Parr and W. Yang, *Density Functional Theory of Atoms and Molecules*, 1st ed. Oxford University Press, 1989.

[120] A. Nagy, "Density functional. Theory and application to atoms and molecules," *Phys. Rep.*, vol. 298, pp. 1–79, 1998.

[121] A. D. Becke, "Density-functional exchange-energy approximation with correct asymptotic behaviour," *Phys. Rev. A*, vol. 38, pp. 3098–3100, 1988.

[122] C. Lee, W. Yang, and R. G. Parr, "Development of the Colle-Salvetti correlation-energy formula into a functional of the electron density," *Phys. Rev. B*, vol. 37, pp. 785–789, 1988.

[123] C. D. Sherrill and H. F. Schaefer III, "The configuration interaction method: Advances in highly correlated approaches," *Adv. Quantum Chem.*, vol. 34, pp. 143–269, 1999.

[124] W. Caminati and S. di Bernando, "Microwave spectrum and amino hydrogen location in indole," *J. Mol. Struct.*, vol. 240, pp. 253–262, 1990.

[125] G. Berden, W. L. Meerts, and E. Jalviste, "Rotationally resolved ultraviolet spectroscopy of indole, indazole, and benzimidazole: Inertial axis reorientation in the $S_1(^1L_b) \leftarrow S_0$ transitions," *J. Chem. Phys.*, vol. 103, pp. 9596–9606, 1995.

[126] A. Lautié, M. F. Lautié, A. Gruger, and S. A. Fakhri, "Etude par Spectrométrie I.R. et Raman de l'Indole et de l'Indolizine. Liaison Hydrogéne $NH \cdots \pi^*$," *Spectrochim. Acta, Part A*, vol. 36, pp. 85–94, 1980.

[127] T. D. Klots and W. B. Collier, "Heteroatom derivatives of indene part 3. Vibrational spectra of benzoxazole, benzofuran, and indole," *Spectrochim. Acta, Part A*, vol. 51, pp. 1291–1316, 1995.

[128] S. Albert, K. K. Albert, P. Lerch, and M. Quack, "Synchrotron-based highest resolution fourier transform infrared spectroscopy of naphthalene ($C_{10}H_8$) and indole (C_8H_7N) and its application to astrophysical problems," *Faraday Discuss.*, vol. 150, pp. 71–99, 2011.

[129] S. D. Dieng and J. P. M. Schelvis, "Analysis of measured and calculated Raman spectra of indole, 3-methylindole, and tryptophan on the basis of observed and predicted isotope shifts," *J. Phys. Chem. A*, vol. 114, pp. 10 897–10 905, 2010.

[130] H. Takeuchi and I. Harada, "Normal coordiante analysis of the indole ring," *Spectrochim. Acta, Part A*, vol. 42, pp. 1069–1078, 1986.

[131] K. R. F. Somers, E. S. Kryachko, and A. Ceulemans, "Theoretical study of indole: protonation, indolyl radical, tautomers of indole, and its interaction with water," *Chem. Phys.*, vol. 301, pp. 61–79, 2004.

[132] M. Majoube and G. Vergoten, "Vibrational spectra of indole and assignments on the basis of ab initio force fields," *J. Raman Spectrosc.*, vol. 23, pp. 431–444, 1992.

[133] N. Glasser and H. Lami, "Nonradiative decay of indoles under collision-free conditions," *J. Chem. Phys.*, vol. 74, pp. 6526–6527, 1981.

[134] A. L. Sobolewski, W. Domcke, C. Dedonder-Lardeux, and C. Jouvet, "Excited-state hydrogen detachment and hydrogen transfer driven by repulsive $^1\pi\sigma^*$ states: A new paradigm for nonradiative decay in aromatic biomolecules," *Phys. Chem. Chem. Phys.*, vol. 4, pp. 1093–1100, 2002.

[135] C. Dedonder-Lardeux, C. Jouvet, S. Perun, and A. L. Sobolewski, "External electric field effect on the lowest excited states of indole: *ab initio* and molecular dynamics study," *Phys. Chem. Chem. Phys.*, vol. 5, pp. 5118–5126, 2003.

[136] B. C. Dian, A. Longarte, and T. S. Zwier, "Hydride stretch infrared spectra in the excited electronic states of indole and its derivatives: Direct evidence for the $^1\pi\sigma^*$ state," *J. Chem. Phys.*, vol. 118, pp. 2696–2706, 2002.

[137] Y. Yamamoto and J. Tanaka, "Polarized absorption spectra of crystals of indole and its related compounds," *Bull. Chem. Soc. Jpn.*, vol. 45, pp. 1362–1366, 1971.

[138] B. Albinsson and B. Nordén, "Excited-state properties of the indole chromophore. Electronic transition moment directions from linear dichroism measurements: Effect of methyl and methoxy substituents," *J. Phys. Chem.*, vol. 96, pp. 6204–6212, 1992.

[139] A. Mani and J. R. Lombardi, "Electronic absorption spectrum of the 2838 $\mathring{A}$ system of indole," *J. Mol. Spectrosc.*, vol. 31, pp. 308–317, 1969.

[140] L. A. Philips and D. H. Levy, "The rotationally resolved electronic spectrum of indole in the gas phase," *J. Chem. Phys.*, vol. 85, pp. 1327–1332, 1986.

[141] C. Kang, T. M. Korter, and D. W. Pratt, "Experimental measurement of the

induced dipole moment of an isolated molecule in its ground and electronically excited states: Indole and indole-H_2O," *J. Chem. Phys.*, vol. 122, pp. 174 301(1–8), 2005.

[142] C.-T. Chang, C.-Y. Wu, A. R. Muirhead, and J. R. Lombardi, "The dipole moment in the lowest singlet $\pi \to \pi^*$ state of indole determined by the optical stark effect," *Photochem. Photobiol.*, vol. 19, pp. 347–351, 1974.

[143] P. R. Callis, J. T. Vivian, and L. S. Slater, "Ab initio calculations of vibronic spectra for indole," *Chem. Phys. Lett.*, vol. 244, pp. 53–58, 1995.

[144] E. H. Strickland, J. Horwitz, and C. Billups, "Near-ultraviolet absorption bands of tryptophan. Studies using indole and 3-methylindole as models," *Biochemistry*, vol. 9, pp. 4914–4920, 1970.

[145] B. E. Anderson, R. D. Jones, and A. A. Rehms, "Polarized two-photon fluorescence excitation spectra of indole and benzimidazole," *Chem. Phys. Lett.*, vol. 125, pp. 106–112, 1986.

[146] A. A. Rehms and P. R. Callis, "Resolution of L_a and L_b bands in methyl indoles by two-photon spectroscopy," *Chem. Phys. Lett.*, vol. 140, pp. 83–89, 1987.

[147] R. Bersohn, U. Even, and J. Jortner, "Fluorescence excitation spectra of indole, 3-methyl indole, and 3-indole acetic acid in supersonic jets," *J. Chem. Phys.*, vol. 80, pp. 1050–1058, 1984.

[148] G. A. Bickel, D. R. Demmer, E. A. Outhouse, and S. C. Wallace, "The S_1–S_0 transition of indole and N-deuterated indole: Spectroscopy and picosecond dynamics in the excited state," *J. Chem. Phys.*, vol. 91, pp. 6013–6019, 1989.

[149] J. R. Cable, "Polarization resolved two-photon resonant ionization spectroscopy of indole and 3-methylindole," *J. Chem. Phys.*, vol. 92, pp. 1627–1633, 1989.

[150] D. M. Sammeth, S. Yan, L. H. Spangler, and P. R. Callis, "Two-photon fluorescence excitation spectra of indole in vapor and jet: ^1L_a states," *J. Phys. Chem.*, vol. 94, pp. 7340–7342, 1990.

[151] Y. Nibu, H. Abe, N. Mikami, and M. Ito, "Electronic spectra of hydrogen-bonded indoles in a supersonic free jet," *J. Phys. Chem.*, vol. 87, pp. 3898–3901, 1983.

[152] T. L. O. Barstis, L. I. Grace, T. M. Dunn, and D. M. Lubman, "Vibronic

analysis of indole and 1-H-Indole-d_6," *J. Phys. Chem.*, vol. 97, pp. 5820–5825, 1993.

[153] B. J. Fender, D. M. Sammeth, and P. R. Callis, "Site selective photoselection study of indole in argon matrix: location of the ^1L_a origin," *Chem. Phys. Lett.*, vol. 239, pp. 31–37, 1995.

[154] P. R. Callis, "Molecular orbital theory of the ^1L_b and ^1L_a states of indole," *J. Chem. Phys.*, vol. 95, pp. 4230–4240, 1991.

[155] L. S. Slater and P. R. Callis, "Molecular orbital theory of the ^1L_a and ^1L_b, states of indole. 2. An *ab Initio* study," *J. Phys. Chem.*, vol. 99, pp. 8572–8581, 1995.

[156] R. Berger, C. Fischer, and M. Klessinger, "Calculation of the vibronic fine structure in electronic spectra at higher temperatures. 1. benzene and pyrazine," *J. Phys. Chem. A*, vol. 102, pp. 7157–7167, 1998.

[157] M. Böhm, J. Tatchen, D. Krügler, K. Kleinermanns, M. G. D. Nix, T. A. LeGreve, T. S. Zwier, and M. Schmitt, "High-resolution and dispersed fluorescence examination of vibronic bands of tryptamine: Spectroscopic signatures for L_a/L_b mixing near a conical intersection," *J. Phys. Chem. A*, vol. 113, pp. 2456–2466, 2009.

[158] L. Serrano-Andrés and B. O. Roos, "Theoretical study of the absorption and emission spectra of indole in the gas phase and in a solvent," *J. Am. Chem. Soc*, vol. 118, pp. 185–195, 1996.

[159] A. C. Borin and L. Serrano-Andrés, "A theoretical study of the absorption spectra of indole and its analogs: indene, benzimidazole, and 7-azaindole," *Chem. Phys.*, vol. 262, pp. 253–265, 2000.

[160] L. Serrano-Andrés and A. C. Borin, "A theoretical study of the emission spectra of indole and its analogs: indene, benzimidazole, and 7-azaindole," *Chem. Phys.*, vol. 262, pp. 267–283, 2000.

[161] T. H. Dunning, "Gaussian basis sets for use in correlated molecular calculations. I. The atoms boron through neon and hydrogen," *J. Chem. Phys.*, vol. 90, pp. 1007–1023, 1989.

[162] R. Ahlrichs, M. Bär, M. Häser, H. Horn, and C. Kölmel, "Electronic structure calculations on workstation computers: The program system turbomole," *Chem. Phys. Lett.*, vol. 162, pp. 165–169, 1989.

[163] C. Hättig and A. Köhn, "Transition moments and excited-state first-order properties in the coupled cluster model CC2 using the resolution-of-the-identity approximation," *J. Chem. Phys.*, vol. 117, pp. 6939–6951, 2002.

[164] C. Hättig, "Geometry optimizations with the coupled-cluster model CC2 using the resolution-of-the-identity approximation," *J. Chem. Phys.*, vol. 118, pp. 7751–7761, 2003.

[165] A. Köhn and C. Hättig, "Analytic gradients for excited states in the coupled-cluster model CC2 employing the resolution-of-the-identity approximation," *J. Chem. Phys.*, vol. 119, pp. 5021–5036, 2003.

[166] F. Weigend, A. Köhn, and C. Hättig, "Efficient use of the correlation consistent basis sets in resolution of the identity MP2 calculations," *J. Chem. Phys.*, vol. 116, pp. 3175–3183, 2001.

[167] M. J. Frisch, G. W. Trucks, H. B. Schlegel, G. E. Scuseria, M. A. Robb, J. R. Cheesemana, J. A. Montgomery, Jr., T. Vreven, K. N. Kudin, J. C. Burant, J. M. Millam, S. S. Iyengar, J. Tomasi, V. Barone, B. Mennucci, M. Cossi, G. Scalmani, N. Rega, G. A. Petersson, H. Nakatsuji, M. Hada, M. Ehara, K. Toyota, R. Fukuda, J. Hasegawa, M. Ishida, T. Nakajima, Y. Honda, O. Kitao, H. Nakai, M. Klene, X. Li, J. E. Knox, H. P. Hratchian, J. B. Cross, C. Adamo, J. Jaramillo, R. Gomperts, R. E. Stratmann, O. Yazyev, A. J. Austin, R. Cammi, C. Pomelli, J. W. Ochterski, P. Y. Ayala, K. Morokuma, G. A. Voth, P. Salvador, J. J. Dannenberg, V. G. Zakrzewski, S. Dapprich, A. D. Daniels, M. C. Strain, O. Farkas, D. K. Malick, A. D. Rabuck, K. Raghavachari, J. B. Foresman, J. V. Ortiz, Q. Cui, A. G. Baboul, S. Clifford, J. Cioslowski, B. B. Stefanov, G. Liu, A. Liashenko, P. Piskorz, I. Komaromi, R. L. Martin, D. J. Fox, T. Keith, M. A. Al-Laham, C. Y. Peng, A. Nanayakkara, M. Challacombe, P. M. W. Gill, B. Johnson, W. Chen, M. W. Wong, C. Gonzalez, and J. A. Pople, *GAUSSIAN 03, revision a.1*, Gaussian, Inc., Pittsburgh, PA, 2003.

[168] M. J. Bearpark, M. A. Robb, and H. B. Schlegel, "A direct method for the location of the lowest energy point on a potential surface crossing," *Chem. Phys. Lett.*, vol. 223, pp. 269–274, 1994.

[169] B. J. Fender, K. W. Short, D. K. Hahn, and P. R. Callis, "Vibrational assignments for indole with the aid of ultrasharp phosphorescence spectra," *Int. J. Quant. Chem.*, vol. 72, pp. 347–356, 1999.

[170] E. Jalviste and N. Ohta, "Stark absorption spectroscopy of indole and 3-methylindole," *J. Chem. Phys.*, vol. 121, pp. 4730–4730, 2004.

[171] H. Köppel, W. Domcke, and L. S. Cederbaum, "Multi-mode molecular dynamics beyond the Born-Oppenheimer approximation," *Adv. Chem. Phys.*, vol. 57, pp. 59–246, 1984.

[172] W. B. Collier, "Vibrational frequencies for polyatomic molecules. I. Indole and 2,3-benzofuran spectra and analysis," *J. Chem. Phys.*, vol. 88, pp. 7295–7306, 1988.

[173] E. V. Doktorov, I. A. Malkin, and V. I. Man'ko, "Dynamical symmetry of vibronic transitions in polyatomic molecules and the Franck-Condon principle," *J. Mol. Spectrosc.*, vol. 64, pp. 302–326, 1977.

[174] A.Giussani, M. Merch, D. Roca-Sanju, and R. Lindh, "Essential on the photophysics and photochemistry of the indole chromophore by using a totally unconstrained theoretical approach," *J. Chem. Theory Comput.*, vol. 7, pp. 4088–4096, 2011.

[175] M. R. Eftink, L. A. Selvidge, P. R. Callis, and A. A. Rehms, "Photophysics of indole derivatives: Experimental resolution of the L_a and L_b transitions and comparison with theory," *J. Phys. Chem.*, vol. 94, pp. 3469–3479, 1989.

[176] J. W. Hager, D. R. Demmer, and S. C. Wallace, "Electronic spectra of jet-cooled indoles: Evidence for the ^1L_a state," *J. Phys. Chem.*, vol. 91, pp. 1375–1382, 1987.

[177] B. Fender and P. R. Callis, "^1L_a origin locations of methyl indoles in argon matrices," *Chem. Phys. Lett.*, vol. 262, pp. 343–348, 1996.

[178] Y. Huang and M. Sulkes, "Jet-cooled solvent complexes with indoles," *J. Phys. Chem.*, vol. 100, pp. 16 479–16 486, 1996.

[179] D. M. Sammeth, S. S. Siewert, L. H. Spangler, and P. R. Callis, "^1L_a transitions of jet-cooled 3-methylindole," *Chem. Phys. Lett.*, vol. 193, pp. 532–538, 1992.

[180] D. M. Sammeth, S. S. Siewert, P. R. Callis, and L. H. Spangler, "Methyl rotor effects in 3- and 5-methylindole," *J. Phys. Chem.*, vol. 96, pp. 5771–5778, 1992.

[181] K. Remmers, E. Jalviste, I. Mistrík, G. Berden, and W. L. Meerts, "Internal rotation effects in the rotationally resolved $S_1(^1L_b) \leftarrow S_0$ origin bands of 3-methylindole and 5-methylindole," *J. Chem. Phys.*, vol. 108, pp. 8436–8445, 1998.

[182] S. Arnold and M. Sulkes, "Spectroscopy of solvent complexes with indoles: Induction of ^1L_a–^1L_b state coupling," *J. Phys. Chem.*, vol. 96, pp. 4768–4787, 1992.

[183] O. Oeltermann, C. Brand, W. L. Meerts, J. Tatchen, and M. Schmitt, "Rotationally resolved electronic spectroscopy of 2,3-bridged indole derivatives: Tetrahydrocarbazole," *J. Mol. Struc.*, vol. 993, pp. 2–8, 2011.

[184] K. W. Short and P. R. Callis, "One- and two-photon spectra of jet-cooled 2,3-dimethylindole: ^1L_b and ^1L_a assignments," *Chem. Phys.*, vol. 283, pp. 269–278, 2002.

[185] Y. Huang and M. Sulkes, "Anomalously short fluorescence lifetimes in jet cooled 4-hydroxyindole. Evidence for excited state tautomerism and proton transfer in clusters," *Chem. Phys. Lett.*, vol. 254, pp. 242–248, 1996.

[186] C. K. Teh, A. Gharavi, and M. Sulkes, "Lifetime measurements in jet-cooled indoles: Additional evidence for the ^1L_a state," *Chem. Phys. Lett.*, vol. 165, pp. 460–464, 1989.

[187] M. Sulkes and I. Borthwick, "Enhanced photophysical effects in indole due to C-6 chemical group substitutions," *Chem. Phys. Lett.*, vol. 279, pp. 315–318, 1997.

[188] S. Arnold and M. Sulkes, "Fluorescence lifetimes of jet-cooled carbonyl-substituted indoles. Evidence of intramolecular charge transfer quenching," *Chem. Phys. Lett.*, vol. 200, pp. 125–129, 1992.

[189] O. Oeltermann, C. Brand, B. Engels, J. Tatchen, and M. Schmitt, "The structure of 5-cyanoindole in the ground and the lowest electronically excited singlet states, deduced from rotationally resolved electronic spectroscopy and ab initio theory," *Phys. Chem. Chem. Phys.*, vol. 14, pp. 10 266–10 270, 2012.

[190] J. L. Lin, S. Zhang, and W. B. Tzeng, "Mass analyzed threshold ionization spectroscopy of 5-methylindole and 3-methylindole cations and the methyl substitution effect," *J. Chem. Phys.*, vol. 120, pp. 5057–5063, 2004.

[191] T. A. A. Oliver, G. A. King, and M. N. R. Ashfold, "Position matters: competing O-H and N-H photodissociation pathways in hydroxy and methoxy-substituted indoles," *Phys. Chem. Chem. Phys.*, vol. 13, pp. 14 646–14 662, 2011.

[192] T. L. O. Barstis, L. I. Grace, T. M. Dunn, and D. M. Lubman, "Vibronic

analysis of 4-, 5-, and 6-fluoroindole," *J. Phys. Chem.*, vol. 98, pp. 4261–4270, 1994.

[193] T. Liu, P. R. Callis, B. H. Hesp, M. de Groot, W. J. Buma, and J. Boos, "Ionization potentials of fluoroindoles and the origin of nonexponential tryptophan fluorescence decay in proteins," *J. Am. Chem. Soc.*, vol. 127, pp. 4104–4113, 2005.

[194] P. R. Callis, "The theory of two-photon-induced fluorescence anisotropy," in *Topics in Fluorescence Spectroscopy*, J. Lakowicz, Ed. New York: Plenum Press, 1977, vol. 5, pp. 1–42.

[195] C. Brand, J. Küpper, D. W. Pratt, W. L. Meerts, D. Krügler, J. Tatchen, and M. Schmitt, "Vibronic coupling in indole: I. theoretical description of the ^1L_a-^1L_b interaction and the electronic spectrum," *Phys. Chem. Chem. Phys.*, vol. 12, pp. 4968–4979, 2010.

[196] C. Brand, O. Oeltermann, D. W. Pratt, R. Weinkauf, W. L. Meerts, W. van der Zande, K. Kleinermanns, and M. Schmitt, "Rotationally resolved electronic spectroscopy of 5-methoxyindole," *J. Chem. Phys.*, vol. 133, pp. 024 303(1–11), 2010.

[197] M. Schmitt, J. Küpper, D. Spangenberg, and A. Westphal, "Determination of the structures and barriers to hindered internal rotation of the phenol-methanol cluster in the S_0 and S_1 states," *Chem. Phys.*, vol. 254, pp. 349–361, 2000.

[198] A. Hellweg, S. A. Grün, and C. Hättig, "Benchmarking the performance of spin-component scaled CC2 in ground and electronically excited states," *Phys. Chem. Chem. Phys.*, vol. 10, pp. 4119–4127, 2008.

[199] "TURBOMOLE V6.1 2009, a development of University of Karlsruhe and Forschungszentrum Karlsruhe GmbH, 1989-2007, TURBOMOLE GmbH, since 2007; available from `http://www.turbomole.com`."

[200] V. Barone, "Anharmonic vibrational properties by a fully automated second-order perturbative approach," *J. Chem. Phys.*, vol. 122, pp. 014 108(1–10), 2005.

[201] A. Ostermeier, A. Gawelczyk, and N. Hansen, "Step-size adaptation based on non-local use of selection information," in *Lecture Notes in Computer Science: Parallel Problem Solving from Nature (PPSN III)*, 1994, pp. 189–198.

[202] N. Hansen and A. Ostermeier, "Completely derandomized self-adaptation in evolution strategies," *Evolutionary Computation*, vol. 9, pp. 159–195, 2001.

[203] W. L. Meerts and M. Schmitt, "Application of genetic algorithms in automated assignments of high-resolution spectra," *Int. Rev. Phys. Chem.*, vol. 25, pp. 353–406, 2006.

[204] O. M. Shir and T. Bäck, *The Second Harmonic Generation Case Study as a Gateway for ES to Quantum Control Problems*, ser. Proceedings of the Genetic and Evolutionary Computation Conference. London: ACM Press, 2007, pp. 713–721.

[205] R. Hoffmann, A. Imamura, and W. J. Hehre, "Benzynes, dehydroconjugated molecules, and the interaction of orbitals separated by a number of intervening sigma bonds," *J. Am. Chem. Soc.*, vol. 90, pp. 1499–1509, 1968.

[206] R. Hoffmann, E. Heilbronner, and R. Gleiter, "Interaction of nonconjugated double bonds," *J. Am. Chem. Soc.*, vol. 92, pp. 706–707, 1970.

[207] C. Brand, W. L. Meerts, and M. Schmitt, "How and why do transition dipole moment orientations depend on conformer structure?" *J. Phys. Chem. A*, vol. 115, pp. 9612–9619, 2011.

[208] A. E. Reed, R. B. Weinstock, and F. Weinhold, "Natural population analysis," *J. Chem. Phys.*, vol. 83, pp. 735–746, 1984.

[209] M. Martinaud and A. Kadiri, "Comparative sensibility of $S_1 \leftarrow S_0$ and $S_2 \leftarrow S_0$ indole electronic transitions to environment perturbations. The positions of the 0–0 bands in polar media," *Chem. Phys.*, vol. 28, pp. 473–485, 1978.

[210] G. M. Florio, R. A. Christie, K. D. Jordan, and T. S. Zwier, "Conformational preferences of jet-cooled melatonin: Probing trans- and cis-amide regions of the potential energy surface," *J. Am. Chem. Soc.*, vol. 124, pp. 10 236–10 247, 2002.

[211] S. Wiedemann, A. Metsala, D. Nolting, and R. Weinkauf, "The dipeptide cyclic(glycyltryptophanyl) in the gas phase: A concerted action of density functional calculations, S_0-S_1 two–photon ionization, spectral UV/UV hole burning and laser photoelectron spectroscopy," *Chem. Phys. Phys. Chem.*, vol. 6, pp. 2641–2649, 2004.

[212] A. Schäfer, C. Huber, and R. Ahlrichs, "Fully optimized contracted Gaussian

basis sets of triple zeta valence quality for atoms Li to Kr," *J. Chem. Phys.*, vol. 100, pp. 5829–5835, 1993.

[213] A. Suwaiyan and M. A. Morsy, "Ab initio calculations and vibrational spectra of 5-methoxy indole," *Spectrochim. Acta A*, vol. 53, pp. 575–588, 1997.

[214] R. Pariser, "Theory of the electronic spectra and structure of the polyacenes and of alternant hydrocarbons," *J. Chem. Phys.*, vol. 24, pp. 250–268, 1955.

[215] H. Tylli and H. Konshchin, "A Raman spectroscopic study of the low-frequency vibrations in anisole and anisole-d_3," *J. Mol. Struct.*, vol. 42, pp. 7–12, 1977.

[216] O. Oeltermann, C. Brand, M. Wilke, and M. Schmitt, "Ground and electronically excited singlet state structures of the syn and anti rotamers of 5-hydroxyindole," *J. Phys. Chem. A*, vol. 116, pp. 7873–7879, 2012.

[217] C. Brand, O. Oeltermann, M. Wilke, J. Tatchen, and M. Schmitt, "Ground and electronically excited singlet-state structures of 5-fluorindole deduced from rotaionally resolved electronic spectroscopy and *Ab Initio* calculations," *ChemPhysChem*, vol. 13, pp. 3134–3138, 2012.

[218] C. Brand, B. Happe, O. Oeltermann, M. Wilke, and M. Schmitt, "High resolution spectroscopy of several rovibronically excited bands of 5-cyanoindole - the effect of vibrational averaging," *J. Mol. Struct.*, 2012, http://dx.doi.org/10.1016/j.molstruc.2012.11.049.

[219] M. Schmitt, D. Krügler, M. Böhm, C. Ratzer, V. Bednarska, I. Kalkman, and W. L. Meerts, "A genetic algorithm based determination of the ground and excited (^1L_b) state structure and the orientation of the transition dipole moment of benzimidazole," *Phys. Chem. Chem. Phys.*, vol. 8, pp. 228–235, 2005.

[220] M. Schmitt, C. Ratzer, K. Kleinermanns, and W. L. Meerts, "Determination of the structure of 7-azaindole in the electronic ground and excited state using high-resolution ultraviolet spectroscopy and an automated assignment based on a genetic algorithm," *Mol. Phys.*, vol. 102, pp. 1605–1614, 2004.

[221] C. W. Kang, J. T. Yi, and D. W. Pratt, "High resolution electronic spectra of 7-azaindole and its Ar atom van der Waals complex," *J. Chem. Phys.*, vol. 123, pp. 94 306(1–7), 2005.

[222] H. Kang, C. Jouvet, C. Dedonder-Lardeux, S. Martrenchard, G. Grégoire, C. Desfrançois, J.-P. Schermann, M. Barat, and J. A. Fayeton, "Ultrafast

deactivation mechanisms of protonated aromatic amino acids following UV excitation," *Phys. Chem. Chem. Phys.*, vol. 7, pp. 394–398, 2005.

[223] S. R. Mercier, O. V. Boyarkin, A. Kamariotis, M. Guglielmi, I. Tavernelli, M. Cascella, U. Rothlisberger, and T. R. Rizzo, "Microsolvation effects on the excited-state dynamics of protonated tryptophan," *J. Am. Chem. Soc.*, vol. 128, pp. 16 938–16 943, 2006.

[224] J. R. Lakowicz, Ed., *Protein Fluorescence*, ser. Topics in Fluorescence Spectroscopy. Springer Verlag, Berlin, 2000, vol. 6.

[225] E. A. Permiakov, *Luminescent Spectroscopy of Proteins*, 1st ed. CRC Press Inc., 1992.

[226] D. P. Millar, "Time-resolved fluorescence spectroscopy," *Curr. Opin. Struct. Biol.*, vol. 6, pp. 637–642, 1996.

[227] C. A. Royer, "Probing protein folding and conformational transitions with fluorescence," *Chem. Rev.*, vol. 106, pp. 1769–1784, 2006.

[228] A. P. Demchenko, *Ultraviolet Spectroscopy of Proteins*, 1st ed. Springer Verlag, Berlin, 1986.

[229] T. R. Rizzo, Y. D. Park, L. Peteanu, and D. H. Levy, "Electronic spectrum of the amino acid tryptophan cooled in a supersonic molecular beam," *J. Chem. Phys.*, vol. 83, pp. 4819–4820, 1985.

[230] ——, "The electronic spectrum of the amino acid tryptophan in the gas phase," *J. Chem. Phys.*, vol. 84, pp. 2534–2541, 1986.

[231] T. R. Rizzo, Y. D. Park, and D. H. Levy, "A molecular beam of tryptophan," *J. Am. Chem. Soc*, vol. 107, pp. 277–278, 1985.

[232] ——, "Time-resolved spectroscopy of tryptophan conformers in a supersonic jet," *J. Chem. Phys.*, vol. 85, pp. 6945–6951, 1988.

[233] L. A. Philips, S. P. Webb, S. J. Martinez III, G. R. Fleming, and D. H. Levy, "Time-resolved spectroscopy of tryptophan conformers in a supersonic jet," *J. Am. Chem. Soc.*, vol. 110, pp. 1352–1355, 1988.

[234] G. Rouillé, M. Arold, A. Staicu, T. Henning, and F. Huisken, "Cavity ringdown laser absorption spectroscopy of jet-cooled L-tryptophan," *J. Phys. Chem. A*, vol. 113, pp. 8187–8194, 2009.

[235] L. C. Snoek, R. T. Kroemer, M. R. Hockridge, and J. P. Simons, "Conformational landscape of aromatic amino acids in the gas phase: Infrared and ultraviolet ion dip spectroscopy of tryptophan," *Phys. Chem. Chem. Phys.*, vol. 3, pp. 1819–1826, 2001.

[236] A. Lindinger, J. P. Toennies, and A. F. Vilesov, "High resolution vibronic spectra of the amino acids tryptophan and tyrosine in 0.38 K cold helium droplets," *J. Chem. Phys.*, vol. 110, pp. 1429–1436, 1999.

[237] J. Sipior and M. Sulkes, "Conformational analysis of jet cooled tryptophan analogs by molecular mechanics: Comparison with experiment," *J. Chem. Phys.*, vol. 98, pp. 9389–9398, 1993.

[238] C. K. Teh, J. Sipior, and M. Sulkes, "Spectroscopy of tryptophan in supersonic expansions: addition of solvent molecules," *J. Phys. Chem.*, vol. 93, pp. 5393–5400, 1988.

[239] L. Blancafort, D. González, M. Olivucci, and M. A. Robb, "Quenching of tryptophan $^1(\pi\pi^*)$ fluorescence induced by intramolecular hydrogen abstraction via an aborted decarboxylation mechanism," *J. Am. Chem. Soc.*, vol. 124, pp. 6398–6406, 2002.

[240] K. Y. Baek, Y. Fujimura, M. Hayashi, S. H. Lin, and S. K. Kim, "Density functional theory study of conformation-dependent properties of neutral and radical cationic L-tyrosine and L-tryptophan," *J. Chem. Phys. A*, vol. 115, pp. 9658–9668, 2011.

[241] J. R. Cable, M. J. Tubergen, and D. H. Levy, "Fluorescence spectroscopy of jet-cooled tryptophan peptides," *J. Am. Chem. Soc.*, vol. 111, pp. 9032–9039, 1989.

[242] M. J. Tubergen, J. R. Cable, and D. H. Levy, "Substituent effects on the electronic spectroscopy of tryptophan derivatives in jet expansions," *J. Chem. Phys.*, vol. 92, pp. 51–60, 1989.

[243] B. C. Dian, A. Longarte, P. R. Winter, and T. S. Zwier, "The dynamics of conformational isomerization in flexible biomolecules. I. hole-filling spectroscopy of N-acetyl tryptophan methyl amide and N-acetyl tryptophan amide," *J. Chem. Phys.*, vol. 120, pp. 133–147, 2004.

[244] B. C. Dian, A. Longarte, and T. S. Zwier, "Conformational dynamics in

a dipeptide after single-mode vibrational excitation," *Science*, vol. 296, pp. 2369–2373, 2002.

[245] K. Schwing, C. Reyheller, A. Schaly, S. Kubik, and M. Gerhards, "Structural analysis of an isolated cyclic tetrapeptide and its monohydrate by combined IR/UV spectroscopy," *ChemPhysChem*, vol. 12, pp. 1981–1988, 2011.

[246] M. Gerhards, "Spectroscopy of neutral peptides in the gas phase: structure, reactivity, microsolvation, molecular recognition," in *Principles of mass spectrometry applied to biomolecules*, J. Laskin and C. Lifshitz, Eds. Wiley Interscience, 2006.

[247] A. Abo-Riziq, J. E. Bushnell, B. O. Crews, M. P. Callahan, L. Grace, and M. S. de Vries, "Gas phase spectroscopy of the penta-peptide fdasv," *Chem. Phys. Lett.*, vol. 431, pp. 227–230, 2006.

[248] D. Řeha, H. Valdés, J. Vondrášek, P. Hobza, B. Crews, A. Abu-Riziq, and M. S. de Vries, "Structure and IR spectrum of Phenylalanyl-Glycyl-Glycine tripetide in the gas-phase: IR-UV experiments, ab initio quantum chemical calculations and molecular dynamic simulations," *Chem. Eur. J.*, vol. 11, pp. 6803–6817, 2005.

[249] G. Grégoire, H. Kang, C. Dedonder-Lardeux, C. Jouvet, C. Desfrançois, D. Onidas, V. Leperec, and J. A. Fayetonc, "Statistical vs. non-statistical deactivation pathways in the UV photo-fragmentation of protonated tryptophan-leucine dipeptide," *Chem. Phys. Phys. Chem.*, vol. 8, pp. 122–128, 2005.

[250] D. Nolting, T. Schultz, I. V. Hertela, and R. Weinkauf, "Excited state dynamics and fragmentation channels of the protonated dipeptide H_2N-Leu-Trp-COOH," *Phys. Chem. Chem. Phys.*, vol. 8, pp. 5247–5254, 2006.

[251] A. Fujihara, H. Matsumoto, Y. Shibata, H. Ishikawa, and K. Fuke, "Photodissociation and spectroscopic study of cold protonated dipeptides," *J. Phys. Chem. A*, vol. 112, pp. 1457–1463, 2008.

[252] W. Caminati, "The rotational spectra of conformers of biomolecules: tryptamine," *Phys. Chem. Chem. Phys.*, vol. 6, pp. 2806–2809, 2004.

[253] L. L. Connell, T. C. Corcoran, P. W. Joireman, and P. M. Felker, "Conformational analysis of jet-cooled tryptophan analogs by rotational coherence spectroscopy," *Chem. Phys. Lett.*, vol. 166, pp. 510–516, 1990.

[254] L. A. Philips and D. H. Levy, "Rotationally resolved electronic spectroscopy

of tryptamine conformers in a supersonic jet," *J. Chem. Phys.*, vol. 89, pp. 85–90, 1988.

[255] T. V. Nguyen, T. M. Korter, and D. W. Pratt, "Tryptamine in the gas phase. A high resolution laser study of the structural and dynamic properties of its ground and electronically excited states," *Mol. Phys.*, vol. 103, pp. 1603–1613, 2005.

[256] M. Schmitt, M. Böhm, C. Ratzer, T. B. C. Vu, I. Kalkman, and W. L. Meerts, "Structural selection by microsolvation: Conformational locking of tryptamine," *J. Am. Chem. Soc.*, vol. 127, pp. 10356–10364, 2005.

[257] J. R. Carney and T. S. Zwier, "The infrared and ultraviolet spectra of individual conformational isomers of biomolecules: Tryptamine," *J. Phys. Chem. A*, vol. 104, pp. 8677–8688, 2000.

[258] T. V. Nguyen and D. W. Pratt, "Permanent electric dipole moments of four tryptamine conformers in the gas phase: A new diagnostic of structure and dynamics," *J. Chem. Phys.*, pp. 054317(1–6), 2006.

[259] B. C. Dian, J. Clarkson, and T. S. Zwier, "Direct measurement of energy thresholds to conformational isomerization in tryptamine," *Science*, vol. 303, pp. 1169–1173, 2004.

[260] J. R. Clarkson, B. C. Dian, L. Moriggi, A. DeFusco, V. McCarthy, K. D. Jordan, and T. S. Zwier, "Direct measurement of the energy thresholds to conformational isomerization in tryptamine: Experiment and theory," *J. Chem. Phys.*, vol. 122, pp. 214311(1–15), 2005.

[261] M. Böhm, R. Brause, C. Jacoby, and M. Schmitt, "Conformational relaxation paths in tryptamine," *J. Phys. Chem. A*, vol. 118, pp. 448–455, 2009.

[262] T. A. L. Greve, E. E. Baquero, and T. S. Zwier, "Infrared and ultraviolet spectral signatures and conformational preferences of jet-cooled serotonin," *J. Am. Chem. Soc.*, vol. 129, pp. 4028–4038, 2006.

[263] T. A. LeGreve, W. H. James III, and T. S. Zwier, "Solvent effects on the conformational preferences of serotonin: Serotonin-$(H_2O)_n$, n=1,2," *J. Phys. Chem. A*, vol. 113, pp. 399–410, 2009.

[264] G. M. Florio and T. S. Zwier, "Solvation of a flexible biomolecule in the gas phase: The ultraviolet and infrared spectroscopy of melatonin-water clusters," *J. Phys. Chem. A*, vol. 107, pp. 974–983, 2003.

[265] T. B. C. Vu, I. Kalkman, W. L. Meerts, C. Brand, Y. N. Svartsov, S. Wiede-mann, R. Weinkauf, and M. Schmitt, "The conformational landscape of 5-methoxytryptamine studied by rotationally resolved fluorescence spectroscopy and resonant ionization spectroscopy," *Phys. Chem. Chem. Phys.*, vol. 11, pp. 2433–2440, 2009.

[266] P. A. Hepworth, J. McCombie, J. P. Simons, J. F. Pfanstiel, J. W. Ribblett, and D. W. Pratt, "High-resolution electronic spectroscopy of molecular con-formers. 3-hydroxy and 3-deuteroxy benzoic acid esters," *Chem. Phys. Lett.*, vol. 236, pp. 571–579, 1995.

[267] R. T. Kroemer, K. R. Liedl, J. A. Dickinson, E. G. Robertson, J. P. Simons, D. R. Borst, and D. W. Pratt, "Conformationally induced changes in the electronic structures of some flexible benzenes. A molecular orbital model," *J. Am. Chem. Soc.*, vol. 120, pp. 12 573–12 582, 1998.

[268] P. A. Hepworth, J. McCombie, J. P. Simons, J. F. Pfanstiel, J. W. Ribblett, and D. W. Pratt, "High resolution electronic spectroscopy of molecular con-formers. methyl- and ethyl-3-aminobenzoic acid esters," *Chem. Phys. Lett.*, vol. 249, pp. 341–350, 1996.

[269] P. W. Joireman, R. T. Kroemer, D. W. Pratt, and J. P. Simons, "Confor-mationally induced rotation of a molecular electronic transition moment," *J. Chem. Phys.*, vol. 105, pp. 6075–6077, 1996.

[270] J. A. Dickinson, P. W. Joireman, R. T. Kroemer, E. G. Robertson, and J. P. Simons, "Conformationally induced transition moment rotations in the $S_1 \leftarrow S_0$ electronic spectra of n-propylbenzene and n-butylbenzene," *J. Chem. Soc., Faraday Trans.*, vol. 93, pp. 1467–1972, 1997.

[271] J. A. Dickinson, M. R. Hockridge, R. T. Kroemer, E. G. Robertson, J. P. Si-mons, J. McCombie, and M. Walker, "Conformational choice, hydrogen bond-ing, and rotation of the $S_1 \leftarrow S_0$ electronic transition moment in 2-phenylethyl alcohol, 2-phenylethylamine, and their water clusters," *J. Am. Chem. Soc.*, vol. 120, pp. 2622–2632, 1998.

[272] M. R. Hockridge, S. M. Knight, E. G. Robertson, J. P. Simons, J. McCombie, and M. Walker, "Conformational landscapes in flexible organic molecules: 4-hydroxy phenyl ethanol (p-tyrosol) and its singly hydrated complex," *Phys. Chem. Chem. Phys.*, vol. 1, pp. 407–413, 1999.

[273] Y. D. Park, T. R. Rizzo, L. A. Peteanu, and D. H. Levy, "Electronic spec-

troscopy of tryptophan analogs in supersonic jets: 3-indole acetic acid, 3-indole propionic acid, tryptamine, and n-acetyl tryptophan ethyl ester," *J. Chem. Phys.*, vol. 84, pp. 6539–6549, 1986.

[274] R. Ahlrichs, M. Bär, H.-P. Baron, R. Bauernschmitt, S. Böcker, P. Deglmann, M. Ehrig, K. Eichkorn, S. Elliott, and F. Furche, *TURBOMOLE, version 5.6.*

[275] J. C. López, V. Cortijo, S. Blanco, and J. L. Alonso, "Conformational study of 2-phenylethylamine by molecular-beam fourier transform microwave spectroscopy," *Phys. Chem. Chem. Phys.*, vol. 9, pp. 4521–4527, 2007.

[276] S. Grimme and M. Parac, "Substantial errors from time-dependent density functional theory for the calculation of excited states of large π systems," *ChemPhysChem*, vol. 4, pp. 292–295, 2003.

[277] R. Weinkauf, F. Lehrer, E. W. Schlag, and A. Metsala, "Investigation of charge localization and charge delocalization in model molecules by multiphoton ionization photoelectron spectroscopy and DFT calculations," *Faraday Discuss.*, vol. 115, pp. 363–381, 2000.

[278] K. Kimura, S. Katsumata, Y. Achiba, T. Yamazaki, and S. Iwata, *Handbook of HeI Photoelectron Spectra of Fundamental Organic Compounds*, 1st ed. Japan Scientific Soc. Press, Tokyo, 1981.

[279] J. D. Pitts, S. Basu, and J. L. Knee, "3-ethylindole electronic spectroscopy: S_1 and cation torsional potential surfaces," *J. Chem. Phys.*, vol. 113, pp. 1857–1865, 2000.

[280] M. M. Posmyk and K. M. Janas, "Melatonin in plants," *Acta Physiol. Plant.*, vol. 31, pp. 1–11, 2009.

[281] J. Arendt, "Melatonin, circadian rhythms, and sleep," *N. Engl. J. Med.*, vol. 343, pp. 1114–1116, 2010.

[282] A. Carrillo-Vico, J. M. Guerrero, P. J. Lardone, and R. J. Reiter, "A review of the multiple actions of melatonin on the immune system," *Endocrine*, vol. 27, pp. 189–200, 2005.

[283] D. X. Tan, L. Chen, B. Poeggeler, L. Manchester, and R. Reiter, "Melatonin: a potent, endogenous hydroxyl radical scavenger." *Endocrine J.*, vol. 1, pp. 57–60, 1993.

[284] M. Mathé-Allainmat, J. Andrieux, and M. Langlois, "Recent developments in

melatonin receptor ligands," *Exp. Opin. Ther. Patents*, vol. 7, pp. 1447–1458, 1997.

[285] E. Fourmaintraux, P. Depreux, D. Lesieur, B. Guardiola-Lemaître, C. Bennejean, P. Delagrange, and H. E. Howell, "Tetrahydronaphthalenic derivatives as new agonist and antagonist ligands for melatonin receptors," *Bioorg. Med. Chem.*, vol. 6, pp. 9–13, 1998.

[286] B. C. Dian, G. M. Florio, J. R. Clarkson, A. Longarte, and T. S. Zwier, "Infrared-induced conformational isomerization and vibrational relaxation dynamics in melatonin and 5-methoxy-N-acetyl tryptophan methyl amide," *J. Chem. Phys.*, vol. 120, pp. 9033–9047, 2004.

[287] M. Kubota and T. Kobayashi, "Electronic structures of melatonin and related compounds studied by photoelectron spectroscopy," *J. Electron Spectrosc Relat. Phenom.*, vol. 128, pp. 165–178, 2003.

[288] W. A. Majewski, J. F. Pfanstiel, D. F. Plusquellic, and D. W. Pratt, *High Resolution Optical Spectroscopy in the Ultraviolet*, ser. Techniques of Chemistry. J. Wiley and Sons, 1995, vol. 23, pp. 101–148.

[289] H. C. Allen and P. C. Cross, *Molecular Vib-Rotors: The Theory and Interpretation of High Resolution Infrared Spectra.* New York: Wiley, 1963.

[290] I. Kalkman, T. B. C. Vu, M. Schmitt, and W. L. Meerts, "The tunneling splittings in the benzoic acid dimer S_0 and S_1 state determined by high resolution UV spectroscopy," *ChemPhysChem*, vol. 9, pp. 1788–1797, 2008.

[291] S. Ullrich and K. Müller-Dethlefs, "A REMPI and ZEKE spectroscopic study of a secondary amide group in acetanilide," *J. Phys. Chem. A*, vol. 106, pp. 9181–9187, 2002.

[292] V. A. Shubert, E. E. Baquero, J. R. Clarkson, W. H. James III, J. A. Turk, A. A. Hare, K. Worrel, M. A. Lipton, D. P. Schofield, K. D. Jordan, and T. S. Zwier, "Entropy-driven population distributions in a prototypical molecule with two flexible side chains: O-(2-acetamidoethyl)-N-acetyltyramine," *J. Chem. Phys.*, vol. 127, pp. 234 315(1–21), 2007.

[293] C. Jacoby and M. Schmitt, "Torsional barriers in aromatic molecular clusters as probe of the electronic properties of the chromophore," *ChemPhysChem*, vol. 5, pp. 1686–1694, 2004.

[294] T. Kojima, E. Yano, K. Nakagawa, and S. Tsunekawa, "Microwave spectrum of acetamide," *J. Mol. Spectrosc.*, vol. 122, pp. 408–416, 1987.

[295] D. F. Plusquellic and D. W. Pratt, "Probing the electronic structure of peptide bonds using methyl groups," *J. Phys. Chem. A*, vol. 111, pp. 7391–7397, 2007.

A. Supplementary Material

This chapter contains the cartesian coordinates of all molecules covered in this thesis. Furthermore, the supplementary material which was included in the publications is given.

Table A.1: Optimized (CC2/cc-pVTZ) Cartesian coordinates of indole (in Angström).

	S_0			^1L_b			^1L_a		
	x	y	z	x	y	z	x	y	z
C	2.13669403	-0.72104013	-0.00000771	2.16111917	0.71525175	0.00002201	2.15757049	-0.73289976	0.00002669
C	2.16152129	0.68835307	-0.00000654	2.16111917	0.71525175	0.00002201	2.19372312	0.64812287	0.00002197
C	0.98797951	1.42958702	0.00000454	0.94887817	1.48008694	-0.00000955	1.01676361	1.45586758	-0.00002367
C	-0.24333451	0.75265383	0.00001127	-0.27090646	0.77085026	-0.00003741	-0.22696851	0.76107772	-0.00003778
C	-0.24230000	-0.67041898	0.00001151	-0.22210764	-0.68858515	-0.00003700	-0.23240858	-0.65016178	-0.00003942
C	0.93655300	-1.42082196	0.00000387	0.96525147	-1.44478041	-0.00001224	0.89789782	-1.46070621	-0.00000872
H	1.01993302	2.51188807	0.00000805	0.97983036	2.56049799	-0.00001114	1.06402653	2.53569360	-0.00004694
H	3.06963027	-1.26896564	-0.00001912	3.13681254	-1.22059196	0.00004753	3.08366878	-1.29240486	0.00006781
H	3.11590419	1.19801318	-0.00001435	3.10373853	1.24794899	0.00004957	3.15878123	1.14016666	0.00005481
C	-1.61118483	1.16975477	-0.00000268	3.10373853	1.24794899	0.00004957	-1.58825073	1.17815862	0.00001826
H	-1.98616885	2.17943926	-0.00000889	3.10373853	1.24794899	0.00004957	-1.58825073	1.17815862	0.00001826
C	-2.37955294	0.02886562	-0.00000943	-2.41942699	0.00253014	0.00003167	-2.43172938	0.01621973	0.00004039
N	-1.55647124	-1.07761777	-0.00000045	-1.51969875	-1.09708677	0.00000394	-1.59039675	-1.03805586	-0.00000604
H	-3.45059409	-0.08733242	-0.00001990	-3.48230529	-0.15764499	0.00006907	-3.50158464	-0.09227437	-0.00000744
H	-1.87007702	-2.03285138	-0.00000415	-1.80794871	-2.06373894	0.00001811	-1.88955422	-2.00561671	-0.00002072
H	0.91989562	-2.50350965	0.00000710	0.95046924	-2.52605632	-0.00002002	0.85118224	-2.54052177	0.00000622

Table A.2: Optimized (SCS-CC2/cc-pVTZ) Cartesian coordinates of 5-cyanoindole (in bohr).

	S_0			S_1			S_2		
	x	y	z	x	y	z	x	y	z
C	2.35019781	-3.46398276	-0.06583061	2.34807092	-3.45121350	-0.06567041	1.2410487	-1.8388334	-0.0350051
C	1.28135652	-0.97281537	-0.00578832	1.31745932	-0.98607006	-0.00698208	0.6970113	-0.5115760	-0.0023882
C	-1.38961411	-1.25884087	-0.06860637	-1.42925839	-1.27098536	-0.07067684	-0.7171235	-0.6468323	-0.0352273
N	-1.89043978	-3.80593228	-0.16184733	-1.90275426	-3.83626947	-0.16247871	-0.9721944	-2.0166550	-0.0852949
C	0.36301331	-5.13025296	-0.16013315	0.34811237	-5.16343948	-0.16031102	0.1686789	-2.7682496	-0.0870437
C	2.31302511	1.46736094	0.09439528	2.41402094	1.45822464	0.09393837	1.2647933	0.7835091	0.0514377
C	0.67241128	3.52912870	0.12867474	0.70538740	3.58187038	0.12996315	0.3300143	1.8937713	0.0685636
C	-1.98699674	3.20244899	0.06483292	-2.00778801	3.23347115	0.06409216	-1.0466920	1.7243175	0.0353670
C	-3.04346320	0.80888173	-0.03428126	-3.10968351	0.78973714	-0.03755976	-1.6284286	0.4077290	-0.0190492
C	1.68504998	6.04595455	0.23055902	1.67494416	6.07294292	0.23293712	0.8633120	3.2192908	0.1218805
N	2.50559442	8.11020028	0.31366763	2.48621201	8.15247905	0.31986988	1.3282576	4.3020695	0.1658065
H	4.32368942	-3.96057592	-0.04256695	4.32112387	-3.95620480	-0.04261124	2.2857520	-2.1086299	-0.0229029
H	0.36148410	-7.16517968	-0.22675658	0.36191796	-7.19766887	-0.22525079	0.1470518	-3.8424047	-0.1227854
H	-3.61968003	-4.58790024	-0.22239344	-3.62911603	-4.62778158	-0.22186540	-1.9058414	-2.4069084	-0.1168937
H	4.33593391	1.76399170	0.14448228	4.43380807	1.74901566	0.14363946	2.3303580	0.9571404	0.0784388
H	-5.07329575	0.56211543	-0.08298895	-5.13799148	0.55595816	-0.08572679	-2.6984262	0.2575186	-0.0454691
H	-3.18826627	4.85539776	0.09458110	-3.19446532	4.89593403	0.09469290	-1.6875719	2.5947432	0.0505655

Table A.3: Optimized (CC2/cc-pVTZ) Cartesian coordinates of 5-fluoroindole (in bohr).

	S_0			S_1		
	x	y	z	x	y	z
C	2.47427550	-1.97522152	-0.00356764	2.55192659	-1.99198820	-0.00228773
C	1.37418190	0.42370064	0.04426603	1.38305032	0.40165244	0.04395637
C	-1.29011552	0.78948762	-0.00581221	-1.33307571	0.82369411	-0.00548684
C	-2.88649036	-1.33192455	-0.10724556	-2.94099383	-1.29509126	-0.10703228
C	-1.75619811	-3.68135634	-0.15280104	-1.72008448	-3.69374646	-0.15231083
C	0.86808393	-4.04829929	-0.10361135	0.91081533	-4.13181054	-0.10537395
N	2.47145703	2.78071821	0.14133233	2.43862857	2.73813801	0.13964635
C	0.61002559	4.59927062	0.15446887	0.58332485	4.68186232	0.15658219
C	-1.72338960	3.45249004	0.06572101	-1.73950385	3.49614724	0.06673760
F	-3.23879953	-5.76596209	-0.25025449	-3.23804353	-5.72202055	-0.24906297
H	-3.51806996	4.41174832	0.05378965	-3.54621857	4.43688729	0.05374482
H	1.09652233	6.57475869	0.22617522	1.12732945	6.63708890	0.22806980
H	4.33903000	3.12484555	0.19604331	4.31837709	3.05431879	0.19330055
H	-4.92278465	-1.16870052	-0.14903415	-4.97783295	-1.18635764	-0.15030057
H	4.50321825	-2.23101657	0.03530712	4.58329395	-2.19903072	0.03798564
H	1.59905320	-5.95453879	-0.14477712	1.59900678	-6.04974375	-0.14816813

Table A.4: Structural parameters of *syn* 5-methoxyindole in its electronic ground state and in the lowest two excited singlet states from the CC2/cc-pVTZ optimized structures in (bohr).

	S_0			S_1			S_2		
	x	y	z	x	y	z	x	y	z
C	-2.54512588	4.20517651	0.00663807	-2.54424575	4.24310362	-0.01955988	-2.53884198	4.14585426	0.00787187
C	-1.32443668	1.78844882	-0.03972559	-1.36491372	1.82073223	-0.08235955	-1.35512359	1.77085236	-0.09715657
C	1.32225644	2.25103219	0.06374419	1.34079410	2.22469542	0.04915823	1.28890391	2.24161155	0.04995983
N	1.66656546	4.84128108	-0.04984171	1.67529765	4.77305426	0.01882730	1.61726791	4.91688408	0.05600274
C	-0.67200037	6.00431301	-0.00324053	-0.67465593	6.07041226	-0.01916224	-0.63020589	6.07075580	0.01316837
C	-2.20013270	-0.70835609	0.04971379	-2.25614147	-0.68536711	0.07457020	-2.30787299	-0.75842815	-0.02467681
C	-0.45178265	-2.67349286	-0.01532529	-0.41829531	-2.66784170	0.00168634	-0.44869233	-2.69500937	-0.01082254
C	2.17128521	-2.18390228	0.04502663	2.24646040	-2.26293493	0.06883454	2.15267812	-2.18271377	0.06903947
C	3.07375806	0.28895700	-0.03750980	3.15292858	0.27319116	-0.07130790	3.15467678	0.35299612	-0.15112565
O	-1.46897292	-5.06965656	-0.01172022	-1.47708681	-5.00269207	0.00375380	-1.42900716	-5.10709297	0.09728889
C	0.26892940	-7.11838327	-0.01108357	0.17906604	-7.15650736	-0.02898718	0.32135261	-7.13662122	-0.04118825
H	-4.54907828	4.57364318	-0.04808196	-4.55115953	4.60761647	-0.06206724	-4.54420209	4.53192108	-0.02729312
H	-0.80814409	8.03863134	0.02131126	-0.73898896	8.10035589	0.09435912	-0.81185611	8.10143271	0.05155715
H	3.32100002	5.73020713	0.27020609	3.37791360	5.63202400	0.12365849	3.31581068	5.79430884	0.07976510
H	-4.19977370	-1.15128982	0.00410932	-4.24168410	-1.17850349	0.08637414	-4.29064204	-1.20099484	-0.24074967
H	5.09228558	0.64554789	-0.02530664	5.15999578	0.67745940	-0.03757938	5.15598986	0.72612340	0.04079986
H	3.52075834	-3.71699214	-0.00987335	3.55545924	-3.81888022	-0.09880037	3.49673295	-3.71905521	0.19781868
H	-0.88446676	-8.81804879	0.01858991	-1.06218861	-8.78666325	0.08516404	-0.81429600	-8.84943817	-0.02269243
H	1.44468921	-7.11514276	-1.71097313	1.25929556	-7.20185283	-1.78316855	1.43117987	-7.05667077	-1.78387898
H	1.47811547	-7.08076381	1.66467705	1.44676767	-7.10841728	1.59410817	1.59735448	-7.14797077	1.58586793

Table A.5: Structural parameters of *anti* 5-methoxyindole in its electronic ground state and in the lowest two excited singlet states from the CC2/cc-pVTZ optimized structures (in bohr).

		S_0			S_1			S_2	
	x	y	z	x	y	z	x	y	z
C	-2.93742831	3.55138472	0.01423863	-2.95470929	3.57329054	-0.01947283	-2.91313458	3.50630969	0.06648136
C	-1.25449811	1.43548925	-0.02992360	-1.29885133	1.43992433	-0.08322780	-1.26864705	1.41701799	-0.11297104
C	1.23572293	2.42080828	0.05600380	1.27432883	2.40187289	0.02059702	1.21378912	2.39761398	-0.01174223
N	1.05177237	5.02414485	-0.06181490	1.06492411	4.96491174	0.01351277	0.98776972	5.08739047	-0.00462040
C	-1.46886565	5.69768092	-0.00945164	-1.50294982	5.73714752	0.00057776	-1.43456076	5.79384017	0.04020350
C	-1.62619358	-1.20106364	0.09097232	-1.69621440	-1.18537816	0.13148877	-1.71221366	-1.25929163	0.05153425
C	0.49119429	-2.75503933	0.01065403	0.51947116	-2.74802957	0.03284536	0.51114597	-2.77075122	0.04074098
C	2.96243460	-1.73435525	0.03398200	3.03509838	-1.79576429	0.04765008	2.93744975	-1.75234833	0.04928232
C	3.35979643	0.84986573	-0.05130870	3.45107467	0.86737664	-0.09898241	3.41570761	0.93860152	-0.15443182
O	0.41665858	-5.35356941	0.03115114	0.38186440	-5.31010281	0.05077466	0.43409029	-5.37721818	0.18898390
C	-2.03019970	-6.46140445	-0.07467042	-2.06987931	-6.46798722	-0.09354129	-1.97637197	-6.50706619	-0.16270645
H	-4.97525540	3.50625356	-0.01970904	-4.99385640	3.51580608	-0.04482290	-4.95444184	3.46993682	0.14256043
H	-2.01252841	7.66239917	0.00391891	-1.99199066	7.71187043	0.02901632	-2.01198670	7.74839800	0.04818298
H	2.50220158	6.22923102	0.21060278	2.55151379	6.16074895	0.07965122	2.48581455	6.27972059	-0.04601598
H	-3.52579259	-1.95760660	0.07369384	-3.58053013	-1.96882212	0.19811177	-3.59507703	-2.00888156	-0.18602575
H	5.26345791	1.60945950	-0.06095682	5.33622645	1.66187720	-0.05366976	5.29547072	1.71812539	0.04713187
H	4.53778664	-3.04013546	-0.02814445	4.56900877	-3.14010055	-0.08866467	4.51140571	-3.06302181	0.10071160
H	-1.71993766	-8.49196261	-0.06656016	-1.70961931	-8.48719583	-0.02282567	-1.66904623	-8.53244710	0.00937997
H	-3.16274755	-5.93048691	1.57087557	-3.23208240	-5.90620677	1.51262063	-3.31384676	-5.89516859	1.28856436
H	-3.02598131	-5.91501201	-1.80176510	-3.00068095	-5.97011584	-1.86354879	-2.74536806	-6.07802883	-2.03292502
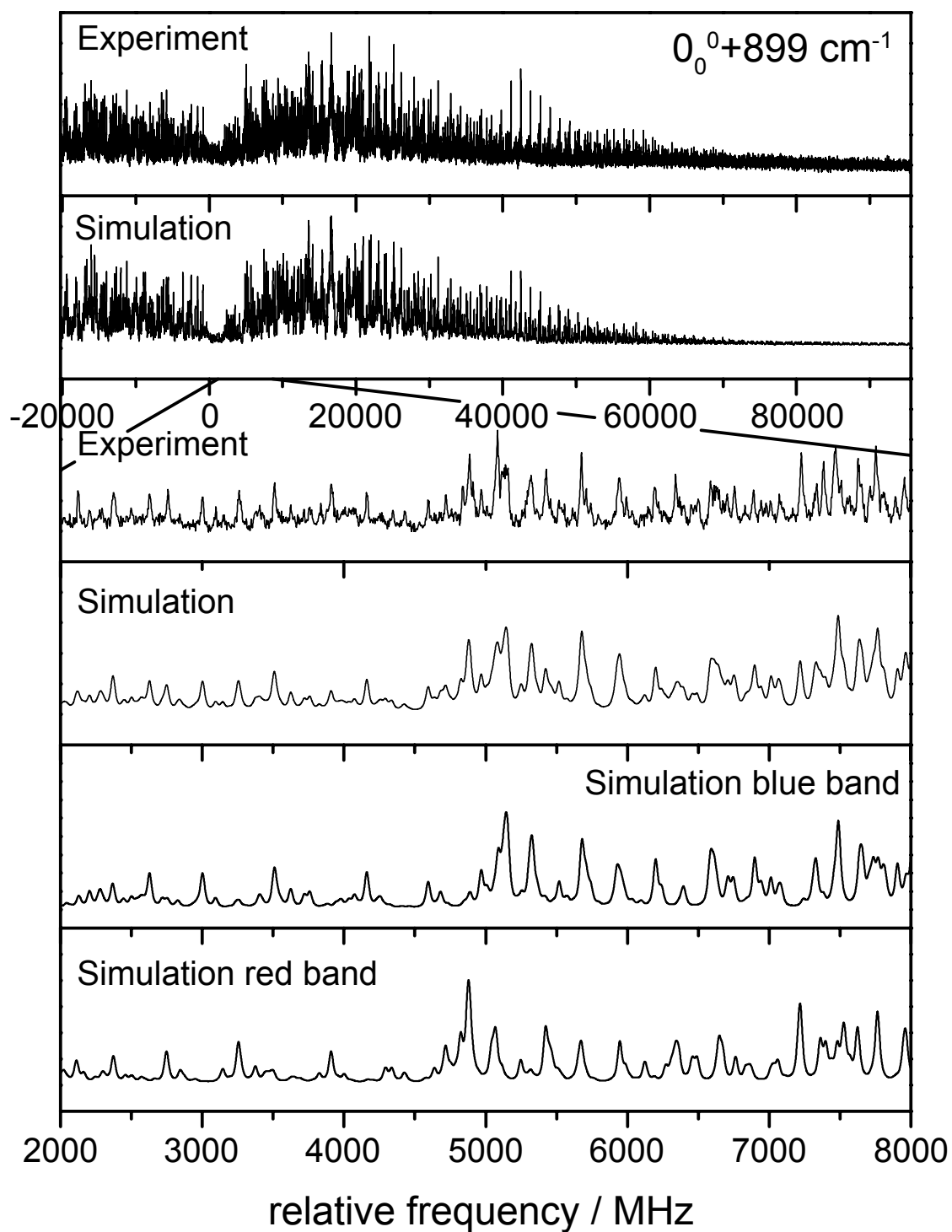
Figure A.1: Rovibronic spectrum of the vibrational band of 5-methoxyindole 899 cm^{-1} above the electronic origin.
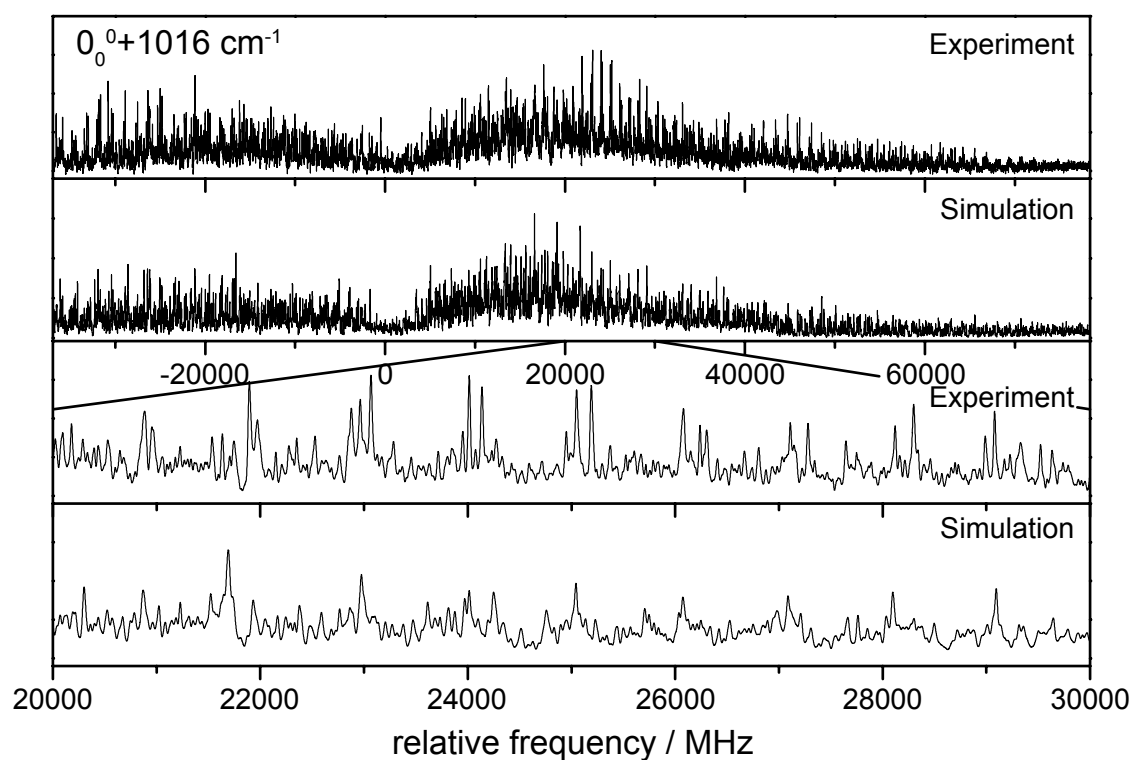
Figure A.2: Rovibronic spectrum of the vibrational band of 5-methoxyindole 1016 cm^{-1} above the electronic origin.
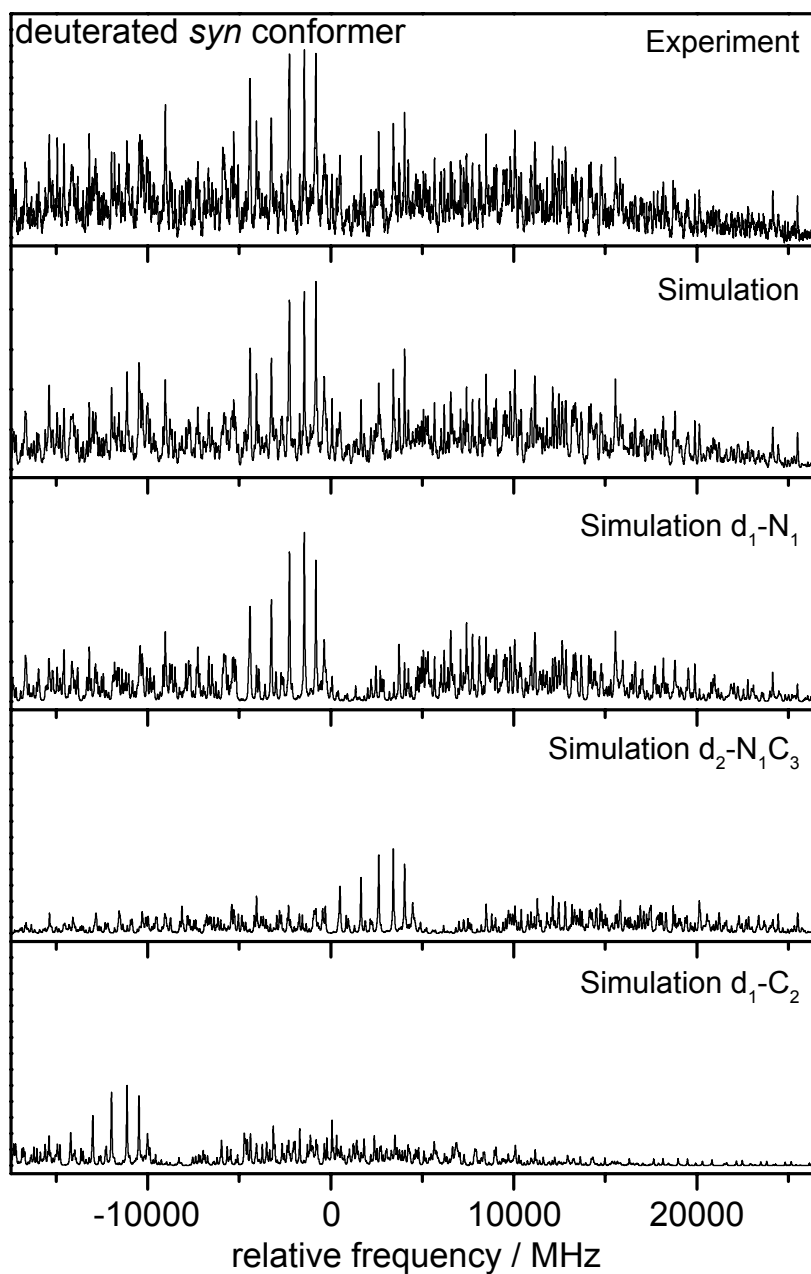
Figure A.3: Rotationally resolved electronic origin of the deuterated *syn* conformer of 6-methoxyindole
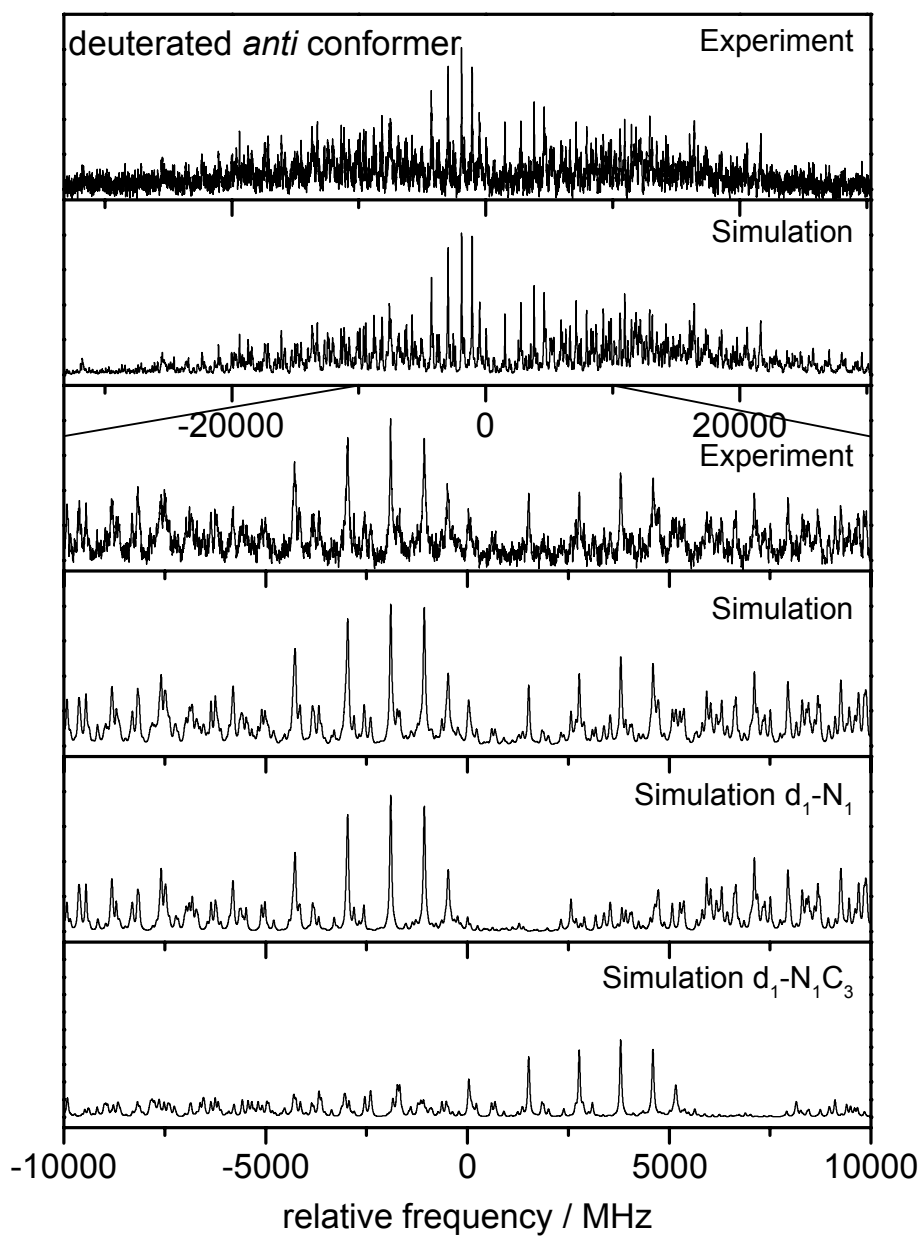
Figure A.4: Rotationally resolved electronic origin of the deuterated *anti* conformer of 6-methoxyindole

Table A.6: Structural parameters of *syn* 6MOI in its electronic ground state and in the lowest two excited singlet states from the SCS-CC2/cc-pVTZ optimized structures (in Angström).

	S_0			S_1			S_2		
	x	y	z	x	y	z	x	y	z
C	-2.74681463	-0.58928858	0.00000777	-2.72821262	-0.59305715	-0.00008270	-2.75226410	-0.58412721	-0.00066891
C	-1.31747155	-0.72791958	-0.00011966	-1.32320083	-0.74520705	0.00007934	-1.33259420	-0.74675023	-0.00020726
C	-0.77213088	0.57757348	-0.00021065	-0.76431493	0.60202877	0.00009401	-0.76294784	0.56261388	0.00059446
N	-1.82661416	1.46327105	0.00000715	-1.83657517	1.47905982	0.00001654	-1.83596584	1.44418060	0.00053455
C	-3.01840515	0.75721571	0.00010202	-3.01760047	0.77142823	-0.00008296	-3.05801739	0.79814259	-0.00046072
C	-0.42858861	-1.82241935	-0.00000481	-0.46245518	-1.88259378	0.00002965	-0.44826410	-1.85540168	-0.00055482
C	0.93369085	-1.58861375	0.00005286	0.94813196	-1.60791850	0.00000166	0.96280989	-1.58636535	-0.00012967
C	1.45231897	-0.26894455	0.00005266	1.45087650	-0.27173259	0.00001198	1.48030510	-0.30522428	0.00060669
C	0.60979013	0.83766581	-0.00000445	0.61615126	0.89390977	0.00008741	0.59690653	0.85798445	0.00094426
H	1.64213339	-2.40576016	0.00002520	1.68009284	-2.40347905	-0.00003384	1.66376049	-2.41123707	-0.00020827
H	-3.47967526	-1.37899036	0.00003045	-3.46394443	-1.38083375	-0.00020610	-3.48862736	-1.37319695	-0.00117216
H	-3.96148269	1.27797271	0.00018209	-3.96755387	1.27992952	-0.00011633	-3.98686475	1.33814848	0.00013673
H	-1.74749639	2.46431242	0.00053094	-1.76400704	2.48084888	-0.00000402	-1.73039223	2.44983415	0.00099201
H	-0.80331520	-2.83835947	0.00003068	-0.84642458	-2.89132922	-0.00002879	-0.81013462	-2.87412458	-0.00131984
H	0.98415185	1.85080300	0.00029094	0.99864675	1.90108235	0.00014291	0.95923452	1.87439239	0.00148618
O	2.82163875	-0.19824284	0.00008412	2.80715047	-0.19918915	-0.00004591	2.85365903	-0.18371529	0.00196802
C	3.38347773	1.10700683	-0.00006300	3.40155993	1.10129628	-0.00005962	3.38174958	1.13336506	-0.00246301
H	4.46068235	0.96787620	0.00002830	4.47378687	0.93098666	-0.00014315	4.46259117	1.01903011	-0.00255055
H	3.08773547	1.66479741	-0.89210341	3.11486917	1.65712443	0.89331116	3.07860838	1.68477429	-0.89625122
H	3.08761586	1.66505058	0.89178000	3.11473548	1.65716536	-0.89336094	3.07949900	1.69048465	0.88807597

Table A.7: Structural parameters of *anti* 6MOI in its electronic ground state and in the lowest two excited singlet states from the SCS-CC2/cc-pVTZ optimized structures (in Angström).

	S_0			S_1			S_2		
	x	y	z	x	y	z	x	y	z
C	2.64446005	-0.93343624	-0.00000195	2.61211699	-0.94109479	0.00004882	2.81477505	-0.91817508	-0.17217322
C	1.21481916	-0.77969202	0.00011536	1.21232196	-0.79578039	-0.00003335	1.38884915	-0.79643295	-0.17216271
C	0.94579069	0.61518884	0.00004167	0.95025383	0.62689501	-0.00005891	1.08664524	0.60616803	-0.17213504
N	2.16016084	1.26614383	0.00013029	2.18510169	1.26932278	-0.00007805	2.30285201	1.25424588	-0.17214879
C	3.18141801	0.32952380	-0.00008829	3.18504140	0.34037674	0.00001015	3.38461734	0.36673389	-0.17216307
C	0.12763308	-1.66550022	-0.00001817	0.12758759	-1.73377390	0.00001103	0.30118546	-1.70073910	-0.17215312
C	-1.17136737	-1.16562267	-0.00003724	-1.19841280	-1.19051042	-0.00001738	-1.04200168	-1.16849675	-0.17217569
C	-1.40642728	0.22876850	-0.00006376	-1.40317879	0.22819167	0.00003553	-1.28966643	0.19367613	-0.17217819
C	-0.34943079	1.13665664	-0.00004325	-0.34311704	1.18696835	0.00008923	-0.19481439	1.14827611	-0.17215030
H	-1.99796649	-1.85961123	-0.00003096	-2.04844200	-1.85442071	-0.00005407	-1.86064347	-1.87356960	-0.17219375
H	3.20281944	-1.85474021	-0.00004937	3.17074285	-1.86335702	0.00015290	3.37743509	-1.83898779	-0.17217048
H	4.21126431	0.64632805	-0.00016601	4.22138802	0.63569498	0.00003094	4.39981257	0.71771189	-0.17221007
H	2.28703453	2.26215100	-0.00049257	2.31836700	2.26521123	-0.00016466	2.39845081	2.26066372	-0.17214925
H	0.28843160	-2.73650668	-0.00026048	0.30018046	-2.79966707	0.00010051	0.45220791	-2.77156640	-0.17212367
H	-0.55682014	2.19856508	-0.00004732	-0.56118492	2.24384164	0.00028613	-0.39908129	2.20977628	-0.17216199
O	-2.65953791	0.79085762	-0.00005881	-2.63494697	0.79147608	0.00005850	-2.52506673	0.79548985	-0.17220963
C	-3.76402182	-0.10492120	0.00008030	-3.77661552	-0.07411950	-0.00007480	-3.63734586	-0.08717815	-0.17211969
H	-4.65117141	0.52209926	0.00014555	-4.63795350	0.58665686	-0.00001701	-4.52226326	0.54321794	-0.17213715
H	-3.76546027	-0.73579871	-0.89160919	-3.78489791	-0.69825428	-0.89334293	-3.63628229	-0.72047024	-1.06320271
H	-3.76528007	-0.73573294	0.89181601	-3.78494721	-0.69847171	0.89304131	-3.63622630	-0.72034808	0.71904994

Table A.8: Structural parameters of *syn* 6MOI in its electronic ground state and in the lowest two excited singlet states from the genuine CC2/cc-pVTZ optimized structures (in Ångström).

	S_0			S_1			S_2		
	x	y	z	x	y	z	x	y	z
C	-2.73974241	0.58959820	0.00012379	-2.70695831	-0.59615761	-0.00004150	-2.75656180	-0.57641555	-0.00043633
C	-1.31636032	0.72925149	-0.00001832	-1.31375357	-0.74620619	-0.00001810	-1.32926854	-0.74357222	0.00041801
C	-0.76764967	-0.57897628	-0.00008496	-0.76328950	0.58999624	0.00004110	-0.75730031	0.56069231	0.00095181
N	-1.82192031	-1.46110591	-0.00017823	-1.83820232	1.47559672	0.00001043	-1.82561037	1.43910875	0.00032293
C	-3.01179431	-0.75836580	0.00011335	-3.00693929	0.78079921	-0.00001153	-3.05970361	0.79572521	-0.00116276
C	-0.42954047	1.82142431	-0.00005049	-0.45099763	-1.88911796	-0.00005968	-0.45373384	-1.85392384	-0.00032426
C	0.93304802	1.58734183	-0.00004500	0.95176107	-1.61096764	0.00006247	0.95797721	-1.58249464	-0.00025415
C	1.45152748	0.27185348	-0.00000518	1.44184584	-0.27573957	0.00005861	1.47926477	-0.30115028	0.00038047
C	0.61025281	-0.83702877	-0.00006127	0.61400727	0.89057088	0.00005144	0.60593608	0.85972031	0.00085619
H	1.64184024	2.40421546	-0.00008244	1.69295812	-2.39805661	0.00012139	1.66048892	-2.40635342	-0.00061297
H	-3.47320009	1.37844438	0.00018813	-3.44428427	-1.38298786	-0.00009141	-3.48981654	-1.36841779	-0.00070265
H	-3.95420153	-1.27984831	0.00021124	-3.95951812	1.28433675	-0.00001113	-3.98349412	1.34344284	0.00133983
H	-1.74257936	-2.46329839	0.00064016	-1.75946811	2.47858848	0.00014652	-1.71482918	2.44594888	0.00035576
H	-0.80435918	2.83715125	-0.00007163	-0.83930924	-2.89611130	-0.00010482	-0.81659977	-2.87189409	-0.00104377
H	0.98769543	-1.84924458	-0.00005977	0.99737293	1.89740622	-0.00001888	0.96721764	1.87652154	0.00151076
O	2.81917250	0.19892461	0.00007752	2.79481757	-0.19100313	0.00002396	2.85237967	-0.18910744	0.00095343
C	3.36734658	-1.10942074	0.00005151	3.37684576	1.11500422	-0.00009774	3.37247036	1.12831066	-0.00158637
H	4.44519353	-0.98224592	0.00010660	4.44952991	0.95394634	-0.00010936	4.45334820	1.02175647	-0.00206891
H	3.06471208	-1.66467299	-0.89088482	3.08209911	1.66557701	-0.89301045	3.06450419	1.67973545	-0.89332193
H	3.06463501	-1.66474217	0.89091956	3.08214017	1.66573508	0.89273046	3.06571328	1.68273545	0.88870617

Table A.9: Structural parameters of *anti* 6MOI in its electronic ground state and in the lowest two excited singlet states from the genuine CC2/cc-pVTZ optimized structures (in Ångström).

	S_0			S_1			S_2		
	x	y	z	x	y	z	x	y	z
C	-2.63629320	0.93536794	-0.00007087	-2.59519397	0.94222708	-0.00007051	-2.66816595	0.91534615	-0.00008802
C	-1.21296138	0.78102585	0.00001100	-1.20317038	0.79466936	0.00007401	-1.23658751	0.79208355	0.00000633
C	-0.94399081	-0.61681966	0.00003569	-0.94760628	-0.61312582	0.00010547	-0.93163720	-0.61246084	0.00007494
N	-2.15824379	-1.26253555	0.00026609	-2.18742453	-1.25946057	-0.00003422	-2.14186224	-1.25444291	0.00005786
C	-3.17661499	-0.32799008	-0.00012746	-3.18407906	-0.34738344	-0.00014409	-3.23525386	-0.35698506	-0.00003768
C	-0.12544732	1.66370420	0.00004265	-0.11398025	1.73234370	0.00009767	-0.15453957	1.69611263	0.00004907
C	1.17173553	1.16091197	0.00001365	1.20424104	1.18555418	0.00001319	1.18637530	1.15919088	0.00002575
C	1.40496642	-0.23153668	-0.00002518	1.39603363	-0.22271022	0.00005371	1.43867862	-0.20878543	-0.00001599
C	0.34778281	-1.13865661	0.00000913	0.33733921	-1.18328562	0.00013552	0.35341147	-1.15811192	0.00001623
H	2.00024401	1.85269216	-0.00000310	2.05960440	1.84292579	-0.00013874	2.00678278	1.86251628	0.00002813
H	-3.19359706	1.85705749	-0.00001655	-3.15266332	1.86582031	-0.00013432	-3.22447837	1.83975249	-0.00018330
H	-4.20652438	-0.64376575	-0.00021269	-4.22069500	-0.64035449	-0.00023731	-4.24801137	-0.71384008	-0.00012206
H	-2.28675958	-2.25950735	-0.00122702	-2.31370539	-2.25861990	-0.00007045	-2.23795557	-2.26191285	0.00012233
H	-0.28436535	2.73483636	0.00003003	-0.28721516	2.79830087	0.00014068	-0.30324131	2.76685370	0.00011318
H	0.55619159	-2.20053939	0.00001243	0.55538769	-2.24020815	0.00029081	0.55457132	-2.22019773	-0.00005827
O	2.65632984	-0.79299015	-0.00009482	2.62104469	-0.79893239	-0.00001155	2.68090069	-0.79379143	-0.00009207
C	3.75192929	0.10984405	0.00003043	3.76271920	0.06542818	-0.00015053	3.77509472	0.10669920	0.00002068
H	4.64395390	-0.50875309	0.00004915	4.62355931	-0.59447813	-0.00011582	4.67078796	-0.50684713	-0.00005624
H	3.74750745	0.74147690	-0.89064342	3.76489314	0.69006536	-0.89241473	3.76388982	0.74096183	-0.89008736
H	3.74738600	0.74136550	0.89078287	3.76496380	0.69026141	0.89197595	3.76388097	0.74073594	0.89029006

Table A.10: Structural parameters of the antiph, antipy, and antiup conformers of tryptamine in their electronic ground state from the genuine CC2/cc-pVTZ optimized structures (in bohr).

	antiph			antipy			antiup		
	x	y	z	x	y	z	x	y	z
N	-7.71007807	-1.79266321	-0.42915941	7.80998642	-1.60321956	0.47350191	-7.79326664	-1.76785564	-0.69352042
H	-8.47173297	-2.70042474	-1.93453826	8.62882695	-2.41028082	2.00612186	-7.75835435	-3.05289026	0.72864654
C	-5.22698977	-0.77519466	-1.10916685	5.24295542	-0.78182242	1.10930522	-5.24757600	-0.77030242	-1.08637589
H	-5.25688010	0.57587448	-2.68156572	5.36717018	0.58702938	2.64613398	-5.31705542	0.59222448	-2.63323543
H	-4.02747828	-2.34778429	-1.69076365	3.99597055	-2.30604514	1.75522143	-4.04020074	-2.31550300	-1.72425064
C	-4.03398978	0.51257346	1.17935638	4.03908944	0.50326121	-1.17406344	-4.02578629	0.49961253	1.21732303
H	-5.20732994	2.11776868	1.74442031	5.22804077	2.09045638	-1.73920672	-5.19943656	2.09493348	1.80732482
H	-4.04969612	-0.82615405	2.75087973	4.02777077	-0.83033180	-2.75677510	-4.01392349	-0.84852642	2.78656334
C	-1.40865033	1.38523220	0.64576238	1.40988837	1.36644292	-0.64177893	-1.40191236	1.37479374	0.67941638
C	-0.60201472	3.82228752	0.20465695	0.61133936	3.80897459	-0.21565093	-0.60762746	3.81403588	0.22433843
H	-1.66089892	5.56361446	0.22979144	1.67860927	5.54495845	-0.24703571	-1.67209742	5.55189555	0.25448101
C	0.77887358	-0.19236192	0.38545322	-0.78431739	-0.20123113	-0.37868280	0.78812751	-0.19618989	0.40071906
N	1.95579006	3.83318126	-0.31335233	-1.94717015	3.83237232	0.29628489	1.94538449	3.83222280	-0.31407141
H	2.99972825	5.38356855	-0.65483629	-2.98476286	5.38841782	0.63167341	2.97930541	5.38469353	-0.67656634
C	2.86146109	1.39957621	-0.21069594	-2.86249870	1.40248325	0.20390595	2.86035976	1.40234008	-0.21472633
C	1.18456563	-2.80570459	0.61978940	-1.20387841	-2.81359128	-0.59952910	1.20717679	-2.80747725	0.63360406
H	-0.36307906	-4.06276387	1.08494299	0.33880638	-4.08245598	-1.04900511	-0.33127775	-4.07313709	1.10601614
C	5.30169410	0.45992395	-0.57486669	-5.30760071	0.47554013	0.56773137	5.30067289	0.47125211	-0.59929429
H	6.87114596	1.69357260	-1.02531959	-6.87199573	1.71889795	1.00892384	6.86105069	1.71032253	-1.06583033
C	3.60760278	-3.74788542	0.25938997	-3.63184021	-3.74372733	-0.24156085	3.63020737	-3.74169947	0.25406005
H	3.94911900	-5.75611699	0.43636284	-3.98185626	-5.75138980	-0.40855929	3.97984754	-5.74879560	0.42741399
C	5.64177066	-2.13368909	-0.33327945	-5.66005466	-2.11737921	0.33790526	5.65301015	-2.12054804	-0.35773067
H	7.50661643	-2.92748807	-0.60360683	-7.52924348	-2.90108217	0.60738062	7.51818649	-2.90775772	-0.64402276
H	-8.90077874	-0.33964475	-0.04526648	7.71338545	-2.98789084	-0.84931197	-8.94029245	-0.35747021	-0.08459431

Table A.11: Structural parameters of the gphin, gphout, and gphup conformers of tryptamine in their electronic ground state from the genuine CC2/cc-pVTZ optimized structures (in bohr).

	gphin			gphout			gphup		
	x	y	z	x	y	z	x	y	z
C	5.40574766	-2.01776892	-0.22485313	5.44838966	-1.77323210	-0.25960129	-5.50260331	-1.67385133	0.33066146
C	5.03135485	0.55108599	-0.61587974	4.91814158	0.75859640	-0.71332642	5.83657384	-0.73442674	0.55083848
C	2.58525447	1.48347928	-0.26906770	2.43882031	1.56744529	-0.30088983	-2.40188428	1.58441348	0.31577249
C	0.51762451	-0.08629898	0.43785125	0.49687750	-0.09335654	0.54079113	-0.53021119	-0.11797343	-0.59981690
C	0.95952104	-2.67941324	0.80297215	1.09355004	-2.64630258	0.98085084	-1.21740279	-2.64363992	-1.05690259
C	3.39028068	-3.61146225	0.47750028	3.55790251	-3.45337287	0.57696646	-3.68824991	-3.39325863	-0.59033852
N	1.67232070	3.90611142	-0.49567483	1.37012557	3.92059824	-0.56798344	-1.26015326	3.90268026	0.57465567
C	-0.87073581	3.91766147	0.07222452	-1.14984995	3.80165040	0.09113508	1.23774430	3.72059533	-0.15064360
C	-1.67059656	1.50383173	0.65099011	-1.77737900	1.36663587	0.78202297	1.77606236	1.27689016	-0.88700747
C	-4.31354900	0.81646268	1.36836663	-4.33281173	0.45582959	1.56738222	4.28895683	0.27600654	-1.68994581
C	-5.82948290	-0.45565988	-0.73724343	-5.81948008	-0.71325179	-0.61300231	-4.88867168	0.83703773	0.79400397
N	-4.94784602	-3.04843275	-1.13343293	-4.51959367	-2.97183702	-1.53881905	4.67900187	-2.78355161	1.98891110
H	-5.71165382	-3.76715055	-2.73600029	-2.83311271	-2.45416721	-2.29464652	5.36876346	1.76290121	-2.63572745
H	-7.84734839	-0.33487325	-0.27177384	-7.67887689	-1.28685731	0.07256830	7.67359416	-1.38580221	-0.12691361
H	-5.53636654	0.59346693	-2.48691881	-6.10871312	0.74426087	-2.06138860	6.19180748	0.82701720	1.85260812
H	-5.30846108	2.53453499	1.94012828	-5.41574608	2.03518686	2.33899711	2.92272620	-2.24516075	2.54304880
H	-4.30598601	-0.43244149	3.01807381	-4.14381554	-0.95760077	3.05981393	4.02384950	-1.24234252	-3.06756489
H	-1.93171424	5.65824284	0.04533743	-2.31346757	5.47451482	0.04049633	2.45035260	5.35828413	-0.10271517
H	2.70798108	5.43688693	-0.93577604	2.29481516	5.49680681	-1.08934545	-2.12049870	5.49521027	1.15404756
H	-0.59081868	-3.92507500	1.26493163	-0.35920346	-3.95500821	1.58098381	0.15566529	-3.98313853	-1.77018213
H	6.57715352	1.77628196	-1.16195732	6.37342781	2.04572481	-1.35641007	-6.28822895	2.15503785	1.49524046
H	3.74969189	-5.60610452	0.75087907	4.04345427	-5.41226166	0.90627866	4.41323419	-4.29666418	0.84203541
H	7.27534047	-2.80821051	-0.47338234	7.34881908	-2.46672261	-0.55737261	-7.41081109	-2.31931541	0.68025844
H	-5.58998347	-4.15528793	0.29465683	-5.52410040	-3.75665042	-2.96957736	-4.23899856	-5.33167492	-0.93685998

Table A.12: Structural parameters of the gpyin, gpyout, and gpyup conformers of tryptamine in their electronic ground state from the genuine CC2/cc-pVTZ optimized structures (in bohr).

	gpyin			gpyout			gpyup		
	x	y	z	x	y	z	x	y	z
C	1.57791203	-0.19441733	-0.17034624	-0.70214173	-0.36947758	-0.58503405	-5.74139432	-1.23223315	0.71121440
C	-1.08771960	-0.67342814	-0.10530042	1.73291436	0.68528642	-1.13629499	-4.85345382	1.23711420	0.82753928
C	-2.33723792	1.70433795	0.03645367	-2.31454158	1.65409264	0.14921129	-2.33059704	1.64808138	0.16734947
N	-0.48995388	3.52841790	0.04787384	-0.89834978	3.83100726	0.05451095	-0.94158165	3.84351128	0.09579661
C	1.85863077	2.39791180	-0.08168760	-1.68949461	-2.83339694	-0.65977148	-0.69810503	-0.34541343	-0.60082680
C	-2.55245032	-2.88743128	-0.14424130	1.52681195	3.24881983	-0.71388478	-1.65407549	-2.82061887	-0.70091352
C	-5.16757428	-2.68333400	-0.04060978	5.20229668	-2.12669456	0.38131820	-4.16098214	-3.23785782	-0.04580355
C	-6.36156154	-0.30700302	0.10079980	4.05561261	-0.73368584	-1.87318272	1.48609988	3.30003671	-0.69248973
C	-4.96595595	1.91871622	0.14214410	-4.84561849	1.28237599	0.80113188	1.72163258	0.74495566	-1.15146271
C	3.59305551	-2.17251959	-0.30278298	-4.20485641	-3.21146023	-0.01221920	4.05086319	-0.64903847	-1.90171528
C	6.08008776	-1.44809784	0.94951040	-5.76399053	-1.17721023	0.71204280	5.19793952	-2.10065469	0.33948243
N	7.29405687	0.63656094	-0.42016718	5.96805016	-0.27950962	2.29186878	5.95186422	-0.54188817	2.48649255
H	8.97848509	1.05037202	0.39472843	4.39375515	0.62906906	2.90782660	4.43798441	0.49900469	3.04220984
H	5.69840749	-0.80400574	2.87104994	3.83340914	-3.52456205	1.06893845	3.82339770	-3.48123973	1.01671994
H	7.27103713	-3.13909909	1.08264567	6.88279398	-3.15001861	-0.23622618	6.84991311	-3.15564839	-0.30257521
H	3.97100245	-2.69494354	-2.27249169	5.46723762	0.57317020	-2.61720925	5.45682426	0.67860543	-2.63125667
H	2.88748079	-3.88753615	0.60743072	3.60813956	-2.09547327	-3.36042107	3.62158689	-1.97751300	-3.42750416
H	3.57271560	3.49247516	-0.12022672	2.93694503	4.70697653	-0.90923805	2.86776036	4.78481826	-0.89404324
H	-0.79335658	5.40189110	0.13901709	-1.53698190	5.57845860	0.44154561	-1.60141270	5.57817335	0.50405225
H	-1.66138933	-4.72691366	-0.26083210	-0.51210459	-4.41134237	-1.22019287	-0.46044745	-4.37741126	-1.28562056
H	-5.88939383	3.74195270	0.25128161	-6.05167504	2.84079672	1.35307725	-6.07549783	2.77307889	1.40631287
H	-6.31633608	-4.37484122	-0.07083463	-4.99005030	-5.09876529	-0.06276615	-4.92237550	-5.13419261	-0.11439122
H	-8.40262401	-0.21131271	0.17810015	-7.71577581	-1.53499324	1.20517683	-7.68560511	-1.62074708	1.21075306
H	7.70345465	0.05458084	-2.20159232	6.68509522	-1.18873701	3.81835318	7.26486029	0.73176856	1.90803809

Table A.13: Structural parameters of the anti conformers of 2-phenylethylamin in their electronic ground state from the genuine CC2/cc-pVTZ optimized structures (in bohr).

	anti(out)			anti(up)		
	x	y	z	x	y	z
C	2.27738349	-0.37510047	-1.40432492	2.27244888	-0.40589060	-1.40682356
C	2.27546689	0.29587486	-3.95330129	2.27898789	0.29127677	-3.94841020
C	-0.00781784	0.61804037	-5.23180823	0.00008905	0.64300559	-5.22731211
C	-2.28230672	0.26271969	-3.94570544	-2.27888224	0.29148672	-3.94856885
C	-2.26714923	-0.40755754	-1.39702408	-2.27254383	-0.40573872	-1.40696250
C	0.00982892	-0.73778684	-0.09253262	-0.00013923	-0.76890397	-0.10291191
C	0.01015727	-1.34367918	2.67826508	-0.00023174	-1.38175580	2.66569113
C	-0.00542250	1.05950886	4.27170096	0.00042633	1.03042595	4.27812098
N	-0.10354114	0.40603986	6.95847805	-0.00007435	0.64695436	7.01158045
H	-0.17626050	2.00500180	8.01121718	-1.52829920	-0.39808971	7.50795660
H	1.53024690	-0.46660178	7.45279215	1.52682285	-0.39988162	7.50826741
H	1.62595142	2.22111874	3.73229430	1.65320305	2.16162330	3.78324262
H	-1.69666964	2.14699219	3.81218323	-1.65143035	2.16276235	3.78278603
H	1.68606986	-2.45524405	3.15421938	1.66450323	-2.50662927	3.14608740
H	-1.64158273	-2.46985305	3.18174262	-1.66556149	-2.50562409	3.14612520
H	4.05534381	-0.63591493	-0.42069537	4.04724378	-0.68695269	-0.42294386
H	4.04775292	0.55792018	-4.93949851	4.05467492	0.55218354	-4.92860696
H	-0.01469753	1.13154641	-7.21047573	0.00015855	1.17866110	-7.20004541
H	-4.06118933	0.49824987	-4.92660424	-4.05465748	0.55245377	-4.92859576
H	-4.03699617	-0.69240045	-0.40572818	-4.04747310	-0.68660891	-0.42325847

Table A.14: Structural parameters of the gauche conformers of 2-phenylethylamin in their electronic ground state from the genuine CC2/cc-pVTZ optimized structures (in bohr).

	gauche(in)			gauche(out)			gauche(up)		
	x	y	z	x	y	z	x	y	z
C	2.44136422	-0.10512629	1.57609073	2.43144886	-0.10867633	1.31011276	2.41433219	-0.05639677	1.26744378
C	1.78109859	-0.82136530	4.02544236	1.92874418	-0.93686460	3.76038634	1.97249697	-0.93542091	3.71090202
C	-0.72348274	-0.62485185	4.82359081	-0.50410653	-0.71708741	4.75594327	-0.44201281	-0.76653893	4.76084672
C	-2.55140205	0.29268135	3.15866081	-2.42124262	0.33952685	3.28704152	-2.40188333	0.29195416	3.35273487
C	-1.88172901	1.00211247	0.71074677	-1.90747932	1.16873570	0.83646097	-1.94694977	1.16886112	0.90661089
C	0.62502719	0.81662113	-0.11157540	0.52443785	0.95654209	-0.18452930	0.46407504	1.01106705	-0.16964595
C	1.36405277	1.49116786	-2.76659916	1.05458392	1.73143777	-2.86361921	0.93271219	1.81692523	-2.84666461
C	0.92332385	-0.68093953	-4.62271591	0.83134304	-0.51567178	-4.66430350	0.82619227	-0.45003134	-4.66341563
N	-1.78834170	-1.11964019	-4.94575009	-1.75572331	-1.49056353	-4.62145312	-1.56989422	-1.81188080	-4.73850343
H	-2.07996346	-2.74053865	-5.92248267	-1.91910637	-2.93845276	-5.86524580	-2.97279310	-0.60885756	-5.24989285
H	-2.53142034	0.28364952	-6.01987458	-2.10799243	-2.23892737	-2.89045158	-2.01366404	-2.40454849	-2.96888913
H	1.75844079	-2.39684687	-3.84143058	2.27002605	-1.91939544	-4.14950040	2.29983787	-1.79349379	-4.13366996
H	1.91611856	-0.26125425	-6.39344436	1.24315930	0.11798173	-6.58265129	1.25836459	0.19358014	-6.57446900
H	3.36147945	2.00950892	-2.81450888	2.95734016	2.51830090	-3.00215547	2.78541125	2.71758895	-3.00059273
H	0.29485766	3.13798211	-3.41258291	-0.28727402	3.17919874	-3.45796561	-0.48350854	3.20632181	-3.42174094
H	4.39242534	-0.24827509	0.96650857	4.32632666	-0.27325200	0.54840699	4.29459007	-0.18621698	0.46413492
H	3.21519473	-1.51999489	5.30526331	3.42974269	-1.74223200	4.89211878	3.50666340	-1.74265828	4.79562436
H	-1.24358417	-1.17109652	6.72386749	-0.89752166	-1.35306967	6.65853900	-0.78772187	-1.44329350	6.65846739
H	-4.49825045	0.45152995	3.76482848	-4.31067200	0.52367682	4.04777632	-4.27717589	0.43961374	4.15504162
H	-3.30780518	1.68506208	-0.58448736	-3.39691449	1.98442459	-0.30646815	-3.46991740	2.00911711	-0.17410049

Table A.15: Structural parameters of the Anti(trans-out)/in & Anti(trans-out)/anti conformers of melatonin in their electronic ground state from the CC2/cc-pVTZ optimized structures (in bohr).

	Anti(trans-in)/anti			Anti(trans-out)/anti		
	x	y	z	x	y	z
N	2.77482877	-5.79911861	0.12253213	1.49597230	1.38445077	-0.29908382
C	4.20323280	-3.62821021	0.24718108	3.43905904	3.12008234	0.04790839
C	2.57352966	-1.57269171	-0.30413294	4.67297028	-1.97267963	0.05494736
C	0.11280698	-2.59201900	-0.77751378	2.13561622	-1.19827516	-0.29143589
C	0.32174937	-5.17747748	-0.49165126	1.49597230	1.38445077	-0.29908382
C	3.53450286	0.91121410	-0.32002118	5.96911174	2.32424899	0.39023801
C	6.08522113	1.25583475	0.21429578	6.61716955	-0.21412375	0.39718552
C	7.67952565	-0.81708679	0.76293725	0.63652273	-3.42914229	-0.59885760
C	6.76554671	-3.26954507	0.78355576	2.27537208	-5.45102763	-0.42317138
O	7.27748386	3.55655343	0.26312907	-4.92439485	2.17963020	-0.30052289
C	5.73033575	5.67439802	-0.28598457	-2.15571523	-3.41518007	-0.95580418
C	-2.23096183	-1.12804565	-1.31632423	-3.49424969	-2.52762364	1.45820362
C	-3.27981707	0.07700141	1.09767758	0.55486474	6.50056072	-0.23273635
N	-5.55429709	1.54178451	0.65098576	4.70088430	-4.57732763	-0.03004037
C	-7.83197170	0.36918547	0.34612251	-6.60018087	0.59177393	0.07307489
C	-10.03277232	2.08517464	-0.25979222	-9.34697643	1.13398728	-0.47834220
O	-8.07861050	-1.93891772	0.57259567	-0.45166886	1.95584230	-0.55160573
H	2.30438265	2.48356178	-0.75373482	7.39474652	3.76601217	0.65060349
H	9.64494113	-0.42643722	1.16488491	8.56384648	-0.78778222	0.66021694
H	8.01078756	-4.83828118	1.20248510	1.90322048	-7.44994092	-0.56390030
H	-1.10510863	-6.61973451	-0.68430186	-2.49269435	-0.89997533	2.22081214
H	-1.86779017	1.30189071	1.96348477	-2.84927665	-5.27964225	-1.50670341
H	-3.68949043	-2.35242508	-2.10491578	-2.64981496	-2.09284109	-2.46405884
H	-1.84640855	0.35942219	-2.69986037	0.60665756	8.54810736	-0.11830811
H	6.95546101	7.31545383	-0.17003062	-0.67426137	5.74212602	1.23971795
H	4.19855279	5.85677471	1.08706468	-0.18341960	5.91915925	-2.06944471
H	4.92774457	5.54234929	-2.18382286	-3.47942290	-4.01655990	2.88064163
H	-3.75086837	-1.41697715	2.43326266	6.24582101	-5.67148279	0.12830223
H	3.42246678	-7.56397467	0.39822981	-7.49582214	-3.02041504	1.12763105
H	-5.42258029	3.40124233	0.28024292	-9.87242796	2.87691844	0.47507810
H	-10.80817804	1.53895199	-2.08422237	-9.56297264	1.43853970	-2.50095994
H	-11.49649090	1.79158859	1.15300540	-10.61123924	-0.37512226	0.11707230
H	-9.52775415	4.07856029	-0.30736403	-0.45166886	1.95584230	-0.55160573

Table A.16: Structural parameters of the Anti(trans-up)/in & Gph(trans-in)/anti conformers of melatonin in their electronic ground state from the CC2/cc-pVTZ optimized structures (in bohr).

	Anti(trans-up)/anti			Gph(trans-in)/anti		
	x	y	z	x	y	z
N	5.11238823	-3.89932860	-0.00393307	-0.25400497	-5.83666267	0.68765165
C	5.39535495	-1.32048981	0.19163309	1.60936598	0.40472099	-1.14919289
C	3.00631216	-0.21843677	-0.32115018	4.08489829	0.56876998	-0.28547964
C	1.27853115	-2.23306862	-0.84484811	1.48537206	-3.90439829	0.53527959
C	2.64336812	-4.44642478	-0.62514774	0.28222574	-1.85829426	-0.70563470
C	2.73005776	2.42991139	-0.26253296	5.25674875	-1.48340597	0.96628323
C	4.84548113	3.88355019	0.30518968	3.98379979	-3.73444352	1.38392601
C	7.21095177	2.74997881	0.81449975	-2.24242358	-2.62432094	-1.29826601
C	7.51471241	0.15088164	0.76187980	-2.48832300	-5.07269565	-0.42057661
O	4.85881603	6.47244984	0.42589752	5.56933649	2.67498058	-0.53277931
C	2.51495663	7.66741621	-0.08293936	-4.20708962	-0.96090825	-2.44550863
C	-1.47679411	-1.98290397	-1.36681066	-5.80591464	0.38907075	-0.42890486
C	-2.95048972	-1.45774744	1.06879358	4.46397888	4.70360306	-1.91472528
N	-5.64420715	-1.17733153	0.64022535	-0.25400497	-5.83666267	0.68765165
C	-7.13879683	-3.24908339	0.28016605	-2.85922190	3.57079894	1.22300253
C	-9.88197425	-2.70677129	-0.29965477	-1.12770669	4.24068291	3.38965022
O	-6.30584899	-5.42175128	0.43893641	-2.94391916	4.81142400	-0.75703968
H	0.91710802	3.28050211	-0.66663293	0.68933074	1.96067171	-2.09916584
H	8.78391102	3.98168426	1.24547416	7.19012182	-1.24510003	1.58597620
H	9.33938952	-0.68933363	1.15130132	4.91259893	-5.29073125	2.33412172
H	2.02964467	-6.37431512	-0.86951015	-4.08163653	-6.34095271	-0.51321023
H	-2.24828229	0.25039044	1.98146058	-7.11439032	-0.94824894	0.43290405
H	-2.22021883	-3.71408986	-2.20260327	-5.47883579	-2.03360757	-3.66772406
H	-1.81723712	-0.44455700	-2.70553401	-3.29052356	0.46822550	-3.61408982
H	2.85831670	9.68247262	0.08761481	5.86863006	6.19807158	-1.93190974
H	1.07267540	7.09409520	1.27941433	2.73256526	5.37952500	-1.01917480
H	1.85462655	7.23670012	-1.99129437	4.03427636	4.12651315	-3.84933566
H	-2.68405861	-3.04005582	2.35837134	-6.89429736	1.90401981	-1.30126901
H	6.49384493	-5.18241352	0.23147987	0.08445750	-7.57342083	1.38082658
H	-6.37592739	0.54813083	0.32444385	-3.85895207	0.35362469	3.06611695
H	-10.32775286	-3.48332862	-2.15075627	0.73394152	3.44118216	3.00678664
H	-11.04614202	-3.68448187	1.08356313	-0.95509380	6.28430638	3.49318221
H	-10.34271699	-0.70225072	-0.27699677	-1.79877740	3.50951067	5.19211675

Table A.17: Structural parameters of the Gpy(trans-in)/anti & Gpy(trans-out)/anti conformers of melatonin in their electronic ground state from the CC2/cc-pVTZ optimized structures (in bohr).

	Gpy(trans-in)/anti			Gpy(trans-out)/anti		
	x	y	z	x	y	z
C	3.05894138	-1.10123718	0.68695034	-0.57109214	3.98344699	-0.57799483
C	5.26973421	-0.26605429	-0.46777707	-0.74427903	1.71880337	0.84828178
C	1.43931950	3.21575896	0.32346103	-3.37188689	1.28464118	1.35306211
C	1.10937916	0.66889825	1.09830818	-4.66824752	3.25893355	0.23685946
H	2.83217738	-3.03701596	1.29769611	1.36515558	-1.39216372	2.47367788
C	5.56481941	2.28197207	-1.21634730	1.46621074	0.34551172	1.41210550
O	7.31598074	-1.76897565	-0.97704828	6.03206922	0.07677928	0.85492842
C	3.66766636	4.04386815	-0.82936139	3.76159799	1.25379469	0.50505675
H	7.32845228	2.81649240	-2.10009723	5.73310544	4.13951498	-1.54610687
H	3.92372653	5.98908427	-1.41071138	1.87037718	6.63923190	-2.54149551
C	-1.35037014	0.47011358	2.20589961	3.89341838	3.52310112	-0.90255005
C	-2.42026579	2.84424904	2.04887720	1.74330667	4.91003857	-1.45457596
N	-0.75048143	4.49363227	0.91494941	-2.99109344	4.88766261	-0.90488691
H	-4.27224337	3.45963210	2.63803240	-6.67331684	3.62429717	0.19089538
C	-2.65167416	-1.87336539	3.06227828	5.92012855	-2.29921427	2.12630176
C	-3.09802902	-3.70197573	0.83416304	-4.55724037	-0.89949947	2.69641642
H	-4.60416857	-5.01989631	1.31586061	-5.00234913	-4.93943046	2.21233698
H	-4.47225953	-1.37449596	3.88166509	-6.60377718	-0.77958172	2.44702559
H	-1.55352037	-2.85927442	4.50832309	-4.20837175	-0.80533401	4.73049267
C	7.08373428	-4.33566133	-0.23602230	-3.61044285	-3.48768611	1.75591680
H	8.84380711	-5.24038585	-0.77455020	7.84397002	-3.01032817	2.13748239
H	5.50897790	-5.25348329	-1.20645944	4.67780807	-3.61263046	1.13506414
H	6.81433117	-4.50289996	1.80380145	5.26657085	-2.06043207	4.07037133
H	-1.39577375	-4.78798280	0.43466339	-1.84881015	-4.02790439	2.67297112
H	-1.02377758	6.36359542	0.71161123	-3.46057537	6.47683824	-1.83464614
C	-5.88065877	-0.90977803	-1.54674788	-0.73639960	-4.13482064	-1.80570658
O	-7.53004829	-1.02223978	0.09940849	0.75945511	-5.39719526	-0.53194225
H	-2.32562180	-1.86263693	-2.60785181	-3.99076097	-2.12838378	-1.96307032
N	-3.77210522	-2.40545527	-1.48981397	-3.08013311	-3.45433053	-0.93580375
C	-6.01827635	0.88858905	-3.75977941	-0.09462807	-3.15565560	-4.40301712
H	-5.17889137	2.68320883	-3.19009579	1.14563483	-4.49020720	-5.34812684
H	-5.00241053	0.18460094	-5.40450085	-1.76554753	-2.81578722	-5.55563985
H	-7.98712541	1.21092935	-4.24050804	0.91829031	-1.37336117	-4.16163086